KU LEUVEN

ARENBERG DOCTORAL SCHOOL
FACULTY OF ENGINEERING SCIENCE

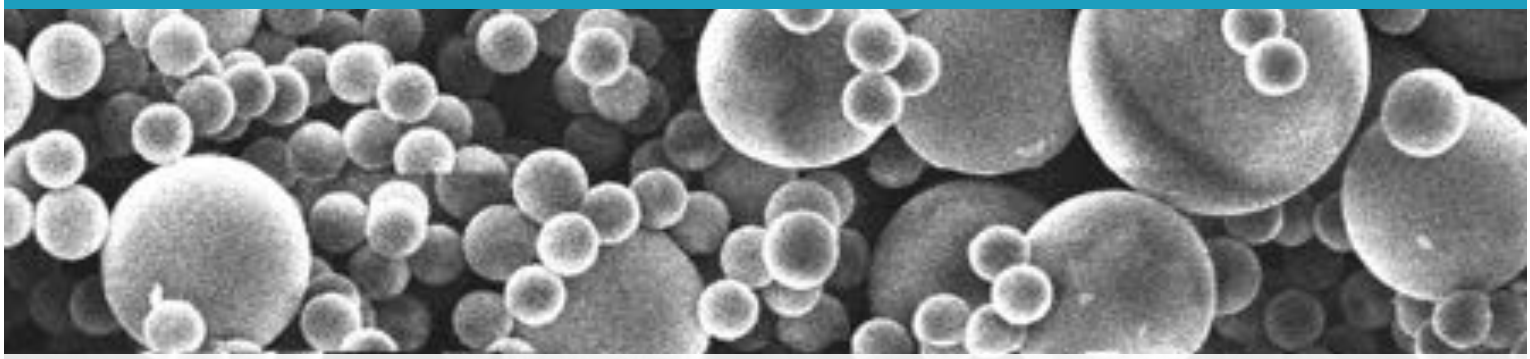

# Expanding the polymer material palette for laser sintering

## The importance of powder flowability

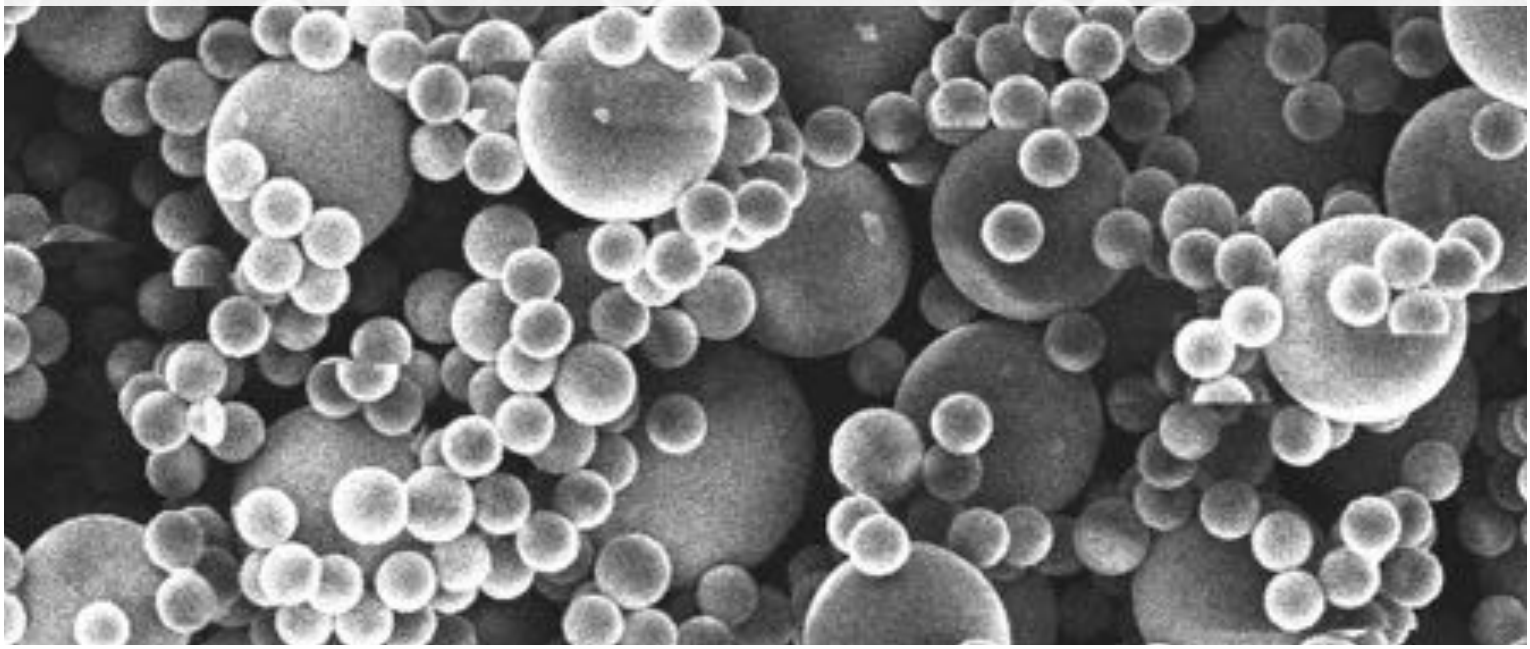

**Michael Van den Eynde**

Supervisor:
Prof. Peter Van Puyvelde

Dissertation presented in partial fulfilment of the requirements for the degree of Doctor of Engineering Science (PhD): Chemical engineering

October 2018

# Expanding the polymer material palette for laser sintering: The importance of powder flowability

**Michael VAN DEN EYNDE**

**Examination committee:**
Prof. dr. ir. Patrick Wollants, chair
Prof. dr. ir. Peter Van Puyvelde, supervisor
Prof. dr. Bart Goderis
Dr. ir. Tom Craeghs
(Materialise NV)
Prof. dr. ir. Simon Kuhn
Prof. dr. Geoffroy Lumay
(Université de Liège)

Dissertation presented in partial fulfilment of the requirements for the degree of Doctor of Engineering Science (PhD): Chemical engineering.

October 2018

© 2018 KU Leuven – Faculty of Engineering Science
Uitgegeven in eigen beheer, Michael Van den Eynde, Celestijnenlaan 200F box 2424, B-3001 Leuven (Belgium)

Alle rechten voorbehouden. Niets uit deze uitgave mag worden vermenigvuldigd en/of openbaar gemaakt worden door middel van druk, fotokopie, microfilm, elektronisch of op welke andere wijze ook zonder voorafgaande schriftelijke toestemming van de uitgever.

All rights reserved. No part of the publication may be reproduced in any form by print, photoprint, microfilm, electronic or any other means without written permission from the publisher.

# Preface

The past four years have been an interesting academic and personal journey. Therefore, I would like to take some time to thank everyone who contributed to the successful completion of this thesis work and helped in making my general work life at the SMaRT lab of KU Leuven so enjoyable. As my thesis turned out to be a bit longer than foreseen, I tried to be brief for a change. However, the gratitude I have for the past few years of PhD cannot be captured in these mere few pages.

First and foremost, I would like to thank my promotor, Peter Van Puyvelde. From my master's thesis onwards he managed to captivate me in the exciting research field of polymers and 3D printing. Not only was he always available for scientific advice, but he always made sure that his PhD students had all the possibilities for personal growth as well. He was very supportive when I still wanted to do an internship in my final PhD year, which eventually led to a job offer. I can honestly say that my life would have been very different without him as my mentor. He is not only an amazing promotor, but also a wonderful person.

Next, I want to express gratitude to my jury for reading my (long) thesis and giving valuable and constructive feedback. In particular, I want to thank Bart Goderis and Tom Craeghs, who also followed up on my research as my assessors during my entire PhD track.

Good research is also never performed alone. Within the framework provided by SIM-VLAIO, I had the opportunity to work with a lot of people both within and outside KU Leuven: Leander, my colleague at Chemical Engineering who paved the way for my research; the PMA division at Mechanical Engineering, especially Dieter, Sasan and prof. Jean-Pierre Kruth, who performed sintering tests and provided valuable discussions on laser sintering; the MSC group of Chemistry, especially Olivier, who helped with the structural analysis of the polymers; my colleagues at Materialise, Toon and Giovanni, who provided many insights into both the technical and commercial aspects of LS; Stijn who helped with particle analysis; my students Nicky, Manu and Kevin; and everyone else within the WAVE-POLYFORCE consortium, who are too numerous to all name.

Many of the set-ups described in this thesis would also not have been possible without the needed technical support. A very big thank you therefore is in place for Herman and Hanne, who spent many hours with me tinkering on mechanical set-ups, creating electrical circuits and finding creative solutions. Also, thanks to Anja and Nico, who always provided the needed support in the SMaRT labs and were always available for technical discussions, safety advice or just a general talk. Besides the practical lab-work, a lot of administration is often needed. Thanks to Marie-Claude and Beatrice for always getting everything sorted out in time.

And what would a PhD be without a pleasant working environment? I had the pleasure of meeting numerous delightful colleagues over the past four years and I will keep countless wonderful memories, both scientific and other. We have been a quite sporty division, which always appealed to me. I think of the long running trips with Jasper or the bouldering with our own personal bouldering guru Irene or Zumba classes with Roberta and An-Sofie. I will also never forget my Alma gang: Ava, Jan, Steffen, Akanshya, Sebastian, Maya, Moritz and Frank. Thanks for clearing up my mind each workday with an interesting lunch break and lively discussion topics. Keep the Alma tradition going long after I have left the KU Leuven! And thanks to my office mates Stijn, Manish, Gert, Annelies and Robin. It was a pleasure coming to work each and every day. Also thanks to Dries, who now has the hard but interesting task to keep the 3D-printing research going at our labs. And thanks to everyone else at the SMaRT/MSC group, Bram, Yannick, Helene, Susa, Karel, Taisir, Kristien, Jeroen, Maarten, Charlotte, Christian, Paula, Erin, Els, Mathieu, Greet, Wouter S, Wouter M, Ward, Youri, Ruth, Naveen, Venkat, Eline, Bruke, Josefina, Lien and Dorien, for all the pleasant memories that I will keep with me.

I also had the pleasure of being the ombudsman for all the students of Chemical Engineering. Though this sometimes took up a lot of my research time, it was a job I loved doing. Supported by my fellow ombudsmen Senne and Bart, program director Ilse Smets and my supervisor, we formed a good team and I believe we got a lot done for our students.

Also a big thank you to my parents for always supporting me. You were always there for me, no matter how busy it sometimes was. For that, I am really grateful. I am certain I would not be were I am now without your care and I am happy that I can now share the experience of my PhD defence with you.

Finally I would like to thank all my friends for the amazing time I had in Leuven. You gave me the needed distraction from research, to start all refreshed the next day. Thanks for all the great game nights, movies, trips, sports,… Without any particular order, thank you Kristof, Kwinten, Ellen, Robby, Roos, Mustafa, Stijn, Marijke L, Beeleke, Stef, Eline, Liza, Sam, Philip, Ann, Hanne, Glen, Astrid, Marijke G,

Prerna, Pieter, Jan, Vincent, Leroy, Felicia, all my former colleagues at Sagio.be and everyone else I was lucky enough to meet during my time in Leuven. I would however like to spend a moment on thanking one person in particular. Robin, thank you for supporting me throughout my master's and PhD. You were always there for me and helped me a lot on so many things. For that I will foverver be grateful.

*Michael Van den Eynde*

# Abstract

Laser sintering (LS) is a form of additive manufacturing (AM), a group of innovative production processes that are commonly referred to as 3D-printing. All AM techniques produce parts in an additive, layer-wise fashion, which enables unchallenged design freedom, as well as high manufacturing flexibility. As a result, these techniques have gained importance at an exponential rate in the last few decades. AM techniques are available for various material classes ranging from polymers to metals and ceramics. LS, more specifically, uses powders as its base material. In this technique, a thin layer of powder is spread, in which a laser sinters the cross-section of the desired product. A new layer is then deposited on top and the process continues until the final product is completed. A critical bottleneck for this application is the lack of commercially available, processable polymer powders. More specifically, one polymer family, namely polyamide, fully dominates the laser sintering market. This market unbalance does not only limit the achievable product properties. It also creates a monopoly for the producers of LS grade polyamides. This research, therefore, aims to expand the material palette with new grades and new polymer families.

To introduce new materials to the laser sintering market, two important steps are required. The first step is the identification of a processing route that creates powders within a desirable size range, i.e. around 25 µm to 80 µm. This work opts for the cryomilling route, due to its universal applicability. The second step is the definition of a relevant lab-scale screening methodology for the polymer pellets prior to milling and for the powder prior to full scale sintering tests. This screening intends to not only prevent unnecessary full-scale milling or sintering trials. It also aids in finding the correct LS processing parameters. One of the largest gaps of the currently available screening methodologies is the limited prediction of powder flowability, which is thus a focal topic of this research. As a result, this research is built up into three major parts: (1) optimisation of the screening methodology, with a focus on powder flowability, (2) investigation of cryomilling as a viable production route for laser sintering powders and (3) application of the former two parts to add new polymers to the laser sintering market.

The first part expands the currently available screening methodology for LS polymers. The methodology includes most of the LS processing cycle, namely coalescence, solidification, powder recyclability and mechanical properties. This research adds upon it by introducing three powder flowability measurements: the dynamic angle of repose, the powder rheometer and the powder spreader, which is a newly developed set-up that mimics the spreading step of an industrial LS machine. Temperature control is a crucial factor in the correct evaluation of powder flow for LS, thus it is added to all three techniques. To form a baseline for the evaluation of new materials, all techniques are tested on both commercial sintering powders, such as PA 2200, and ideal spherical reference powders. These tests show that each technique fills its own niche within the screening methodology. The dynamic angle of repose is a quick and easy screening tool for general flow trends, such as the variation in additive content. The powder rheometer provides the most accurate prediction of thermal effects. And finally, the powder spreader provides the most useful ranking of the final powders due to its direct link to the process.

The second part applies the expanded screening methodology to cryomilled grades of existing LS polymers, namely polyamide and thermoplastic polyurethane. The flow behaviour of these milled grades is compared to that of smooth reference powders to assess the viability of cryomilling. Furthermore, coalescence and solidification behaviour of the TPU grades is compared before and after milling to evaluate the effect of cryomilling on the base polymer properties. The analysis shows that cryomilling succeeds in producing viable powders for LS within some limitations. All milled powders show a rough particle morphology, which results in generally poorer flowability, compared to the reference LS grades. In most cases, however, smooth and defect-free powder layers are deposited, though the decreased flowability results in a lower packing density for these layers. Some changes are also noted between the pellet and powder properties, which include nucleation for crystallisation due to the addition of flow enhancers and post-condensation of grades that possess this phenomenon. These changes thus need to be accounted for in the screening of the polymer pellets.

The final part studies three polymers that are currently uncommon or not used in LS applications for full-dense parts. These materials are PLA, PB-1 and a coPA. Each of them is cryomilled and examined by the full screening methodology. Powder flow at elevated temperatures proves to be a crucial aspect in the sinterability of these materials. In the case of PLA and PB-1, this powder flow behaviour is improved by optimising the crystal structure of the polymers via annealing treatments. This finding has consequences for the screening methodology, as other materials that are currently deemed unsinterable in their base form, may become viable for laser sintering after a simple and scalable annealing step. This opens up new possibilities for the further expansion of the LS material palette.

# List of symbols and abbreviations

## Symbols

### Roman

| Symbol | Description | Units |
|---|---|---|
| $a$ | Approach distance | [m] |
| A | Constant in the Arrhenius equation | [Pa s] |
| ---$A_h$ | Hamaker constant | [J] |
| $A$ | Area | [m] |
| $A_p$ | Projected area of the particle | [m] |
| b | Generic fitting constant | [various] |
| Bo | Bond number | [/] |
| ---$Bo_{VdW}$ | Bond number based solely on VdW force | [/] |
| ---$Bo_{VdW,s-s}$ | Bond number for sphere-sphere contact | [/] |
| ---$Bo_{VdW,s-w}$ | Bond number for sphere-wall contact | [/] |
| $c$ | Convexity | [°] |
| C | Compressibility (index) | [/] |
| $d$ | Diameter | [m] |
| ---$d_p$ | Particle diameter | [m] |
| $D_i$ | $i$-th percentile of the PSD | [m] |
| $E$ | Young's modulus | [Pa] |
| $E_{flow}$ | Flow energy | [J] |
| $E_a$ | Activation energy | [J/mol] |
| ED | Energy density | (see below) |
| ---$ED_A$ | Energy density (area based) | [J/m$^2$] |
| ---$ED_V$ | Energy density (volume based) | [J/m$^3$] |
| EG | Energy gradient | [J/m] |
| f | Generic function | [various] |
| $ff_c$ | Flow function | [/] |

| Symbol | Description | Units |
|---|---|---|
| $F$ | Force | [N] |
| ---$F_{\mathrm{Cap}}$ | Capillary force | [N] |
| ---$F_{\mathrm{Coulomb}}$ | Coulomb force | [N] |
| ---$F_{\mathrm{g}}$ | Gravitational force | [N] |
| ---$F_{\mathrm{N}}$ | Normal force | [N] |
| ---$F_{\mathrm{VdW}}$ | Van der Waals force | [N] |
| Fr | Froude number | [/] |
| g | Gravitational acceleration (9.81 m/s$^2$) | [m/s$^2$] |
| $h$ | Layer thickness | [m] |
| HR | Hausner ratio | [/] |
| $l$ | Length | [m] |
| $M$ | Torque | [Nm] |
| $n$ | Amount of taps | [/] |
| $P$ | Laser power | [W] |
| $q$ | Scattering vector | [Å$^{-1}$] |
| $Q$ | Charge | [C] |
| $r$ | Drum radius | [m] |
| R | Universal gas constant (8.3145 J/mol K) | [J/mol K] |
| $s$ | Surface charge | [C/m$^2$] |
| $\mathrm{S_f}$ | Shape factor | [/] |
| $\mathrm{S_a}$ | Aspect ratio | [/] |
| $t$ | Time | [s] |
| ---$t_{\mathrm{x}}$ | Reference time | [s] |
| $T$ | Temperature | [K] |
| ---$T_{\mathrm{c}}$ | Crystallisation temperature (peak) | [K] |
| ---$T_{\mathrm{g}}$ | Glass transition temperature | [K] |
| ---$T_{\mathrm{m}}$ | Melting temperature (peak) | [K] |
| ---$T_{\mathrm{s}}$ | Stickiness temperature | [K] |
| $U$ | Particle perimeter (projected) | [m] |
| $v$ | Speed | [m/s] |
| ---$v_{\mathrm{scan}}$ | Beam speed | [m/s] |
| $V$ | Volume | [m$^3$] |
| $w$ | Width | [m] |
| ---$w_{\mathrm{spacing}}$ | Beam spacing | [m] |
| $z$ | Vertical coordinate | [m] |

## Greek

| Symbol | Description | Units |
|---|---|---|
| $\beta$ | Liquid bridge half angle | [rad] |
| $\Gamma$ | Surface tension | [N/m] |
| $\delta$ | AoR profile width | [°] |
| $\epsilon$ | Porosity | [/] |
| $\epsilon_{\mathrm{p}}$ | Electric permittivity | [F/m] |
| $\eta_0$ | Zero-shear viscosity | [Pa s] |
| ---$\eta_{00}$ | Constant in the Arrhenius relation for $\eta_0$ | [Pa s] |
| $\theta$ | Contact angle | [rad] |
| $\lambda$ | Wavelength | [m] |
| $\rho$ | Density | [kg/m$^3$] |
| ---$\rho_{\mathrm{b}}$ | Powder bulk density | [kg/m$^3$] |
| ---$\rho_{\mathrm{m}}$ | Material density | [kg/m$^3$] |
| ---$\rho_{\mathrm{p}}$ | Particle density | [kg/m$^3$] |
| ---$\rho_{\mathrm{pk}}$ | Packing density | [/] |
| $\sigma$ | Normal stress | [Pa] |
| ---$\sigma_{\mathrm{c}}$ | Unconfined yield strength | [Pa] |
| $\tau$ | Shear stress | [Pa] |
| $\chi$ | Logarithmic viscosity increase | [/] |
| $\phi$ | Angle of repose/average angle | [rad] |
| ---$\phi_{\mathrm{a}}$ | Avalanche angle | [rad] |
| $\phi_{\mathrm{e}}$ | Effective angle of internal friction | [rad] |
| $\phi_{\mathrm{i}}$ | Internal friction angle | [rad] |
| $\Psi$ | Sphericity | [/] |
| $\omega$ | Rotational speed | [rad/s] |

# Abbreviations

| Abbreviation | Description |
|---|---|
| 3DP | Three-dimensional printing |
| 3DW | Three-dimensional welding |
| ABS | Acrylonitrile butadiene styrene |
| A-DAoR | Ambient dynamic angle of repose (set-up) |
| AFM | Atomic force microscopy |
| AM | Additive manufacturing |
| AoR | Angle of repose |
| BER | Bed expansion ratio |
| BPM | Ballistic particle manufacturing |
| CAD | Computer aided design |

| Abbreviation | Description |
|---|---|
| coPA | Copolyamide |
| DAoR | Dynamic angle of repose |
| ---A-DAoR | Ambient DAoR |
| ---T-DAoR | Thermal DAoR |
| DLP | Digital light projection |
| DSC | Differential scanning salorimetry |
| EAB | Elongation at break |
| EBM | Electron beam melting |
| FDM | Fused deposition modelling |
| FTIR | Fourier transformed infra-red |
| HR | Hausner ratio |
| HSM | Hot stage microscopy |
| HSS | High speed sintering |
| IM | Injection moulding |
| LENS | Laser engineered net shaping |
| LLM | Layer laminated manufacturing |
| LOM | Laminated object manufacturing |
| LS | Laser sintering |
| MDK | Material development kit |
| MJP | Multijet printing |
| PA | Polyamide |
| PAEK | Polyaryletherketone |
| PB-1 | Polybutene-1 |
| PBT | Polybutene terephthalate |
| PC | Polycarbonate |
| PID controller | Proportional-integral-derivate controller |
| PLA | Polylactic acid |
| PMMA | Polymethylmethacrylate |
| POM | Polarised optical microscopy |
| PP | Polypropene |
| PS | Polystyrene |
| PSD | Particle size distribution (normalised) |
| PVA | Polyvinyl alcohol |
| RAM | Radiation absorbing material |
| SAoR | Static angle of repose |
| SDL | Selective deposition lamination |
| SEM | Scanning electron microscopy |
| SFF | Solid freeform fabrication |
| SFP | Solid foil polymerisation |
| SIM-Flanders | Strategic Initiative Materials in Flanders |
| SLA | Stereolithography |

| Abbreviation | Description |
|---|---|
| SLM | Selecive laser melting |
| SLS | Selective laser sintering |
| STREAM | Structural engineering materials through additive manufacturing |
| TC | Thermocouple |
| T-DAoR | Thermal dynamic angle of repose (set-up) |
| TGA | Thermogravimetric analysis |
| TMA | Thermo-mechanical analysis |
| TPU | Thermoplastic polyurethane |
| UTS | Ultimate tensile strength |
| VLAIO | Flemish agency innovation & entrepreneurship (Vlaams agentschap innoveren & ondernemen) |
| WAXS | Wide angle X-ray scattering |

# Contents

**Preface** i

**Abstract** v

**List of symbols and abbreviations** vii

**Contents** xiii

**1 Introduction** 1

1.1 Motivation ---- 1

1.2 Context ---- 2

1.3 Aim ---- 3

1.4 Outline ---- 3

**2 State of the art** 7

2.1 Introduction to laser sintering ---- 7

2.1.1 Additive manufacturing ---- 8

2.1.2 Laser sintering ---- 10

2.1.3 LS material selection ---- 13

2.2 Fundamentals on powder flow ---- 20

2.2.1 Forces affecting powder flowability ---- 20

Van der Waals forces ---- 21

Electrostatic forces ---- 23

Moisture related forces ---- 25

Other forces hindering flowability ---- 26

Conclusions ---- 26

2.2.2 Particle characterisation ---- 27

2.3 Measuring powder flow ---- 30

2.3.1 Shear cell ---- 31

2.3.2 Hausner ratio ---- 33
2.3.3 Hall Flowmeter ---- 35
2.3.4 Angle of repose (AoR) ---- 35
2.3.5 Powder rheometer ---- 39
2.3.6 Other techniques ---- 43
2.3.7 Comparison of the techniques ---- 44
2.3.8 Selection of techniques for LS ---- 46
2.4 Conclusions ---- 47

**3 Development of powder flow characterisation techniques 49**
3.1 Methods for assessing LS applicability ---- 49
3.1.1 PSD analysis ---- 50
3.1.2 Thermogravimetric Analysis (TGA) ---- 51
3.1.3 Differential Scanning Calorimetry (DSC) ---- 51
3.1.4 Melt Rheology ---- 52
3.1.5 Moisture determination ---- 52
3.2 Reference materials ---- 53
3.2.1 Polyamide (PA) ---- 54
3.2.2 Polystyrene spheres (PS) ---- 56
3.2.3 Polymethylmethacrylate spheres (PMMA) ---- 58
3.3 Dynamic angle of repose ---- 59
3.3.1 Software ---- 60
3.3.2 A-DAoR ---- 66
3.3.3 T-DAoR ---- 73
3.3.4 Comparison of the set-ups ---- 76
3.4 Powder rheometer ---- 77
3.5 Powder spreader ---- 81
3.5.1 Semi-automated powder spreader ---- 81
3.5.2 Thermal control ---- 88
3.5.3 Automated powder spreader ---- 90
3.6 Conclusions ---- 92

**4 Cryomilled powders in laser sintering 97**
4.1 Powder production – Cryogenic milling ---- 98

4.2 Methods 99
4.2.1 Hot stage microscopy (HSM) 100
4.2.2 Tensile testing 100
4.3 Polyamide (PA) 101
4.3.1 Powder characterisation 101
4.3.2 Powder flowability 103
4.3.3 Coalescence and solidification 108
4.3.4 Recyclability 108
4.3.5 LS proof of concept 108
4.3.6 Conclusions 109
4.4 Thermoplastic polyurethane (TPU) 110
4.4.1 General introduction on TPU 110
4.4.2 First selection: general sintering criteria 115
4.4.3 First selection and milling 121
4.4.4 Powder flowability 124
4.4.5 Evaluation of cryomiling process for TPU 126
4.4.6 Proof of concept 128
4.4.7 Conclusions 134
4.5 Conclusions 135

**5 New materials for LS: flow at elevated temperature 137**

5.1 Materials & methods 137
5.1.1 Summary of materials 138
5.1.2 Hausner ratio 139
5.1.3 Wide angle X-ray scattering (WAXS) 139
5.1.4 Dilatometry 140
5.2 Polylactic acid (PLA) 140
5.2.1 Powder characterisation 141
5.2.2 Powder flowability 145
5.2.3 Coalescence 147
5.2.4 Solidification 148
5.2.5 Recyclability 149
5.2.6 LS proof of concept 178
5.2.7 Conclusions 152

5.3 PB ---- 153
5.3.1 PB-1 polymorphism and thermal treatments ---- 153
5.3.2 Powder flowability ---- 159
5.3.3 Coalescence ---- 161
5.3.4 Solidification ---- 163
5.3.5 Recyclability ---- 164
5.3.6 LS proof of concept ---- 164
5.3.7 Conclusions ---- 167
5.4 Copolyamide (coPA) ---- 168
5.4.1 Powder characterisation ---- 169
5.4.2 Powder flowability ---- 171
5.4.3 Coalescence and solidification ---- 172
5.4.4 Recyclability ---- 173
5.4.4 LS proof of concept ---- 175
5.4.6 Conclusions ---- 178
5.5 Conclusions ---- 179

**6 Conclusions and outlook 181**

6.1 Final conclusions ---- 181
6.1.1 Successful expansion of the screening methodology ---- 181
6.1.2 Viability of cryomilling ---- 183
6.1.3 Evaluation of three new polymers and various new TPU grades ---- 184
6.1.4 Thermal treatments to improve LS viability ---- 184
6.2 Future outlook ---- 185
6.2.1 Cryomilling optimisation and deeper understanding ---- 185
6.2.2 Investigation of unexplained sintering issues ---- 186
6.2.3 Further expansion of the material palette ---- 186
6.3 Concluding statement ---- 187

**Appendix 189**

**References 193**

**Curriculum vitae 203**

**List of publications 205**

# Chapter 1

# Introduction

Additive manufacturing (AM), more commonly referred to as 3D printing, is gaining interest in many aspects of society. AM techniques have existed since the 1980's and their applications have grown tremendously [1,2]. As a result, research on AM technologies and materials has a potentially large impact on the current manufacturing industry. This thesis focusses on the addition of new materials to the AM market. The work presented in this thesis is therefore applied research with a strong link to the (Flemish) additive manufacturing industry. Consequently, the work mainly handles with real, commercial, non-idealised powder systems.

This chapter provides a brief overview of the motivation, context and goals of this work, as well as an overview of the structure of the following chapters. A more detailed and technical explanation of all concepts that are introduced in this chapter is found in Chapter 2.

## 1.1 Motivation

This work focuses on one AM technique, namely Laser Sintering (LS), which is explained in detail in Section 2.1.2. In LS a final product is formed by selectively sintering powder particles. One of the major bottlenecks of this technique is the limited availability of suitable polymer grades. Currently, one polymer, namely polyamide 12 (PA12) is used in roughly 95 % of all LS polymer applications [3,4]. This lack in material choice thus limits the attainable product properties, and moreover puts a monopoly on the limited set of LS PA grades that dominate the

materials market. A need therefore exists to (1) gain a better understanding on why these PA grades are so viable for the LS process and (2) find new polymers that have similar sinterability. Fundamental knowledge on what makes a polymer appropriate for LS has been investigated in previous work [5]. This work adds upon this knowledge and applies it to the selection of new materials.

Besides the availability of sinterable polymers and the knowledge to identify these materials, a second bottleneck exists for the addition of new materials to the LS market. This second bottleneck is the limited availability of the correct polymer grades in a powder form. An extra production step is thus needed to create a processable material for LS. Furthermore, additional screening is needed to not only assess the base polymer material, but also the quality of the produced powder. Powder flowability has become an important and still much elusive factor in this assessment.

As the research in this work is directly linked to the industrial application, it has a clear valorisation potential. The global LS materials market is responsible for about a quarter of the AM materials turnover, which in 2015 amounted to 191 billion dollars. Furthermore, as the AM industry has known exponential growth in the previous years, a strong continuation of growth is forecast for the following years [2]. Increased understanding of the needed LS powder properties and the addition of new materials to the available material palette thus have a potentially huge economic impact.

## 1.2 Context

The research performed in this thesis is situated in the additive manufacturing framework of the Strategic Initiative Materials in Flanders (SIM-Flanders). In 2009, SIM-Flanders started as a virtual research centre, which was created as a collaboration between the Flemish materials industry and universities. It aims to form a collaborating environment both among and between these two partner groups and stimulate materials research within Flanders. In 2017, it partnered with the Flemish Agency Innovation & Entrepreneurship (VLAIO) to become the “spearhead cluster materials” in Flanders [6].

SIM-Flanders supports multiple research programs within the topic of materials research and industry in Flanders. The research of this thesis is situated more specifically within the additive manufacturing program STREAM (structural engineering materials through additive manufacturing). STREAM aims to further develop AM technologies for and in Flanders. Within the framework of STREAM, multiple smaller project groups exist, spanning various types of AM technologies. Two of these projects, named POLYFORCE and WAVE, focus on the laser

sintering of polymers. The main goals of POLYFORCE are fundamental understanding of the material requirements for LS polymers and the development of an adequate screening methodology to systematically assess these requirements for potential new LS polymers. The aims of WAVE are slightly less fundamental and more applied than those of POLFORCE. WAVE intends to use the knowledge build-up of POLYFORCE to add more powders to the LS market via the cryomilling production route. This thesis work is mainly related to the WAVE project, but has strong connections to POLYFORCE as well. The link to these projects enables a close collaboration with stakeholders in the entire LS production chain, from polymer powder creation to part production.

## 1.3 Aims

The aims of this research are, evidently, closely related to those of POLYFORCE and WAVE. This thesis focuses more specifically on the following three inter-related aims:

1. Expansion of the POLYFORCE screening methodology with a focus on powder flowability.
2. Evaluation of the cryomilling process as a viable powder production route for LS.
3. Addition of new polymers to the LS material palette via the cyromilling process.

The first aim is based on a noted gap in the available screening methodology for LS materials, namely powder flow assessment. As powder flow requirements are quite stringent for the intended application, as further elaborated on in Section 2.1.3, it is crucial to detect flowability issues early on in the material development cycle. This knowledge becomes even more crucial when evaluating milled powder samples, as their rough particle morphology tends to hinder flowability. The second aim is therefore the application of the developed flowability measurements to evaluate whether cryomilling, which is elaborated on in more detail in Section 4.1 forms a viable processing route for LS materials. Following a positive evaluation, this processing route is then utilised to reach the final aim, namely the addition of new materials to the LS palette.

## 1.4 Outline

This thesis is built up of five more chapters. Chapter 2 discusses the state of the art on laser sintering and granular material. Chapters 3 to 5 then aim to accomplish the

goals defined in Section 1.3. Finally, Chapter 6 provides a general overview of the conclusions of this work, as well as some recommendations for future projects. The final paragraphs of this chapter shortly introduce content of Chapters 2 to 5 and their links to the project context and among each other. Figure 1-1 provides a visual summary of this information.

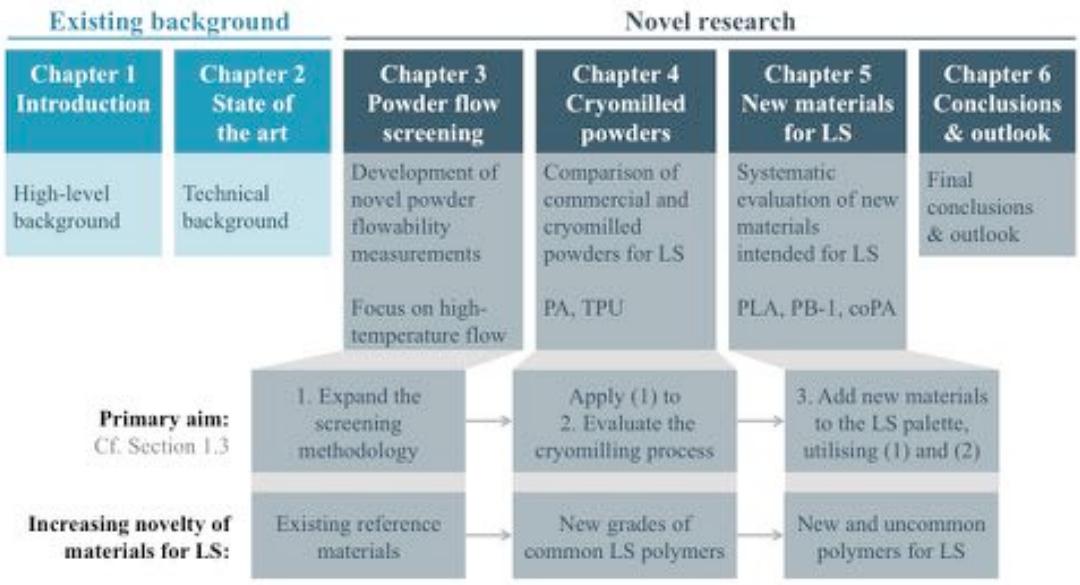


**Figure 1-1:** Visual summary of the structure of this thesis.

Chapter 2 summarises the available knowledge that is relevant for reaching the aims that have been set in Section 1.3. The chapter first evaluates the current knowledge on the laser sintering process and, more specifically, the material requirements for powders used in this process. The focus for these requirements lies on adequate powder flowability. Next, some basic principles of granular materials are explained. This section attempts to provide better insights into the inter-particle interactions that influence powder flowability and the characterisation techniques that are used to define particle size and shape. Finally, a literature review is provided on powder flowability measurements and their relevance for laser sintering is assessed. The techniques that are deemed relevant are further applied to powders intended for laser sintering in the next chapters.

The focus of Chapter 3 is the expansion of the polymer screening methodology that is introduced in Chapter 2. This expansion focuses on flowability measurements, as these have been missing from the previous studies within the POLYFORCE project. Based on the flowability knowledge that is summarised in Chapter 2, techniques that are relevant for LS are selected and developed. The usefulness of the techniques is then evaluated on current laser materials. These reference materials form an evaluation base for the resulting indices of each technique. Besides these laser

sintering powders, idealised spherical powders are used to evaluate the powder flowability measurements. The powder flow testing protocol, as well as the rest of the screening methodology, is then applied to various powders with increasing innovation levels in the subsequent two chapters.

Chapter 4 applies the powder testing methodology of Chapters 2 and 3 to new, cryomilled grades of current LS polymers, namely polyamides (PA) and thermoplastic polyurethanes (TPU). The results for both material families are then compared to reference LS grades of each family. This comparison yields an evaluation for the viability of cryomilling as a processing route for LS powders, which is the second major aim of this research.

Finally, Chapter 5 fully utilises the cryomilling process (Chapter 4) and the aforementioned screening methodology (Chapters 2 and 3) to expand the LS material palette with new polymers. The chapter thoroughly investigates the viability of polylactic acid (PLA), polybutene-1 (PB-1) and a copolyamide (coPA). This chapter thus focuses around the third aim of this project and the core objective of the WAVE project.

# Chapter 2

# State of the art

Granular matter is a multiphase aggregation state consisting of solid particles and an interstitial gas or liquid [7]. For particles in the size range of 5-500 µm the granular matter is typically called a powder [8]. As the size range of the solid particles and the type of interstitial fluid strongly influence the governing interactions, strongly different behaviour is seen in different granular systems. This work focuses on dry powder systems, i.e. granular matter in the powder size range with air as the interstitial fluid.

This chapter first discusses the application of interest, i.e. laser sintering (LS), to illustrate its particle requirements, with a focus on powder flowability. Secondly, the general concepts of powder flow are reviewed to assess what forces affect powder flow in this application. Finally, the third section summarises the state-of-the-art powder flowability measurements and discusses their relevance for LS.

## 2.1 Introduction to laser sintering

This thesis handles on the selection of new polymer powders for laser sintering (LS), a form of additive manufacturing (AM). Therefore, this section provides some insights into the LS process, in order to evaluate the exact requirements for any new material and to illustrate their possible impact to the LS industry. The next paragraphs first shortly introduce AM in general and then zoom in on the LS process and the specific powder requirements in LS, with a focus on the need for good powder flowability.

### 2.1.1 Additive manufacturing

Additive manufacturing (AM) processes build a final product by adding material in a layer-wise fashion [1]. In recent years, AM is often referred to as "3D printing", though this term is originally meant for one specific AM process, which is further discussed in section 2.1.2 [9]. Multiple techniques, besides LS and 3D printing, fall under the concept of AM, but their basic working principle is the same: First, a three-dimensional drawing of the desired product is made via computer aided design (CAD) [9]. A slicer software then cuts this 3D drawing into slices. Next, optimisation software computes the scan path in each slice, i.e. the movement of a laser, printing head or extruder to create the product cross-section in each layer. This information is uploaded to the AM device, which then builds each of these slices sequentially. Afterwards, the part is removed and post-processing is performed. Post-processing includes processing steps such as the removal of support structures, surface finishing or colouring, which in many cases still are manual processing steps [10,11,4].

Two of the most common AM processes, besides laser sintering, are stereo-lithography (SLA), in which a UV laser selectively cures a photocurable resin, and fused deposition modelling (FDM), in which a polymer filament is molten and then deposited by an extrusion head (cf. Figure 2-1) [12,13,14]. Table 2-1 lists a few other AM processes, based on the base material and the building mechanism. The list includes electron beam melting (EBM) [9], laminated object manufacturing (LOM) [12,13], 3D welding (3DW) [12], digital light projection (DLP) [15], laser engineered net shaping (LENS) [9] and Polyjet [1]. These processes are not further discussed in this research, as the focus is on LS powders. Other polymer powder bed based techniques, such as 3D printing (3DP) and high speed sintering (HSS) are briefly discussed in section 2.1.3, as they are more closely related to LS. The research results obtained for LS may therefore have additional impact for these processes.

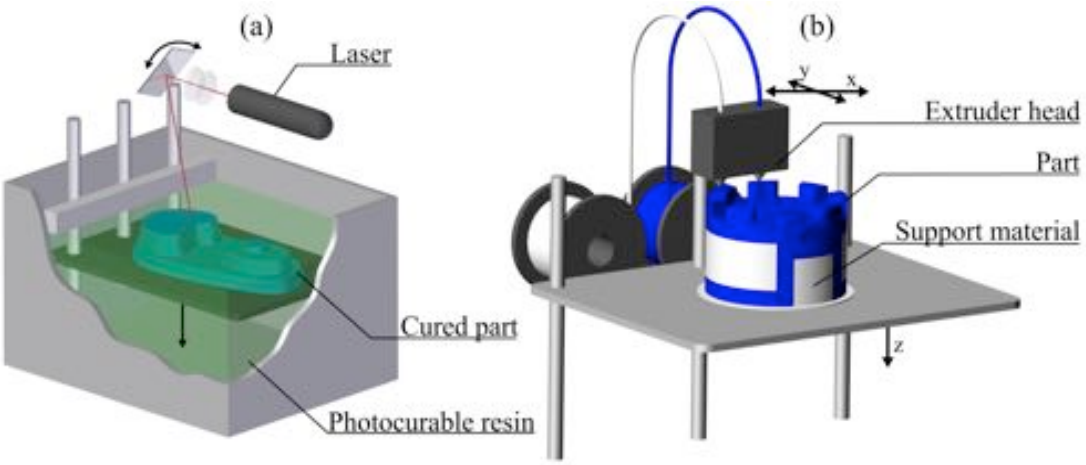


**Figure 2-1:** SLA (a) and FDM (b) processes (adapted from own publication [14]).

**Table 2-1:** Examples of AM techniques categorised by building mechanisms and base material.

| Base material | Building mechanism | | |
|---|---|---|---|
| | **Laser/light** | **Adhesive** | **Conduction** |
| **Powder** | LS/ SLM [4,12], HSS [16,17], EBM [9], LENS [9] | 3DP [12,9] | |
| **Liquid / resin** | SLA [12,13], MJP [1], PolyJet [1], DLP | | |
| **Solid** | SFP [12] | LOM/LLM [12,13] SDL [1] | FDM [12,9] 3DW [12], BPM [12] |

In the early years of AM, i.e. in the 1980's, the processes were primarily used to rapidly create prototypes for product development. Hence, it received the name rapid prototyping (RP). The main motivation for this particular use is the lack of product-specific tools, such as moulds, to create the final part. As a result, any shape can be produced in a small quantity, without a large overhead cost and with a short delivery time [13,18,12,19]. The concept of "free customisation" is therefore often seen as one of the main advantages of AM (cf. Figure 2-2) [1]. This advantage further expanded the use of AM in later years to actual production applications that require strong customisation, such as patient specific implants [20,21].

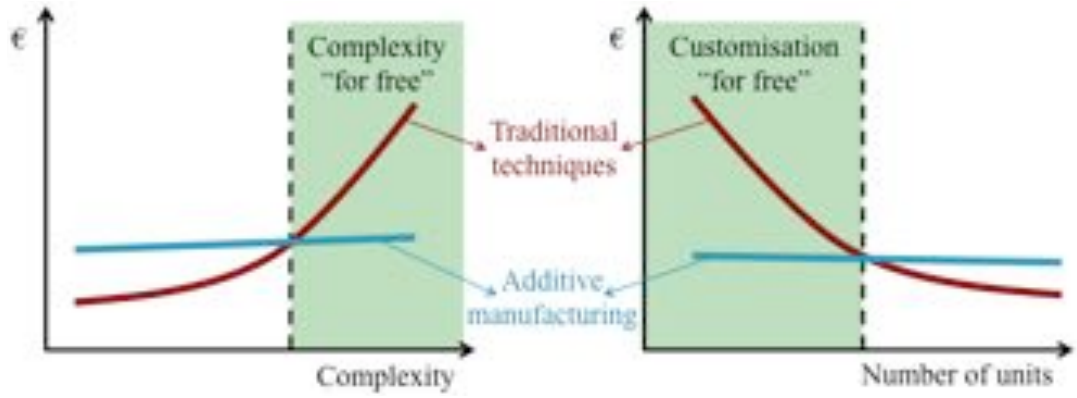


**Figure 2-2:** Illustration of the advantages of AM (adapted from Amado [22]).

Another advantage of these additive processes is the concept of freeforming. This concept refers to the fact that the complexity of the final part plays a much lesser role compared to traditional manufacturing, since material can be freely added anywhere to the final build. This design freedom does not only enable designs that are impossible with traditional manufacturing processes, but it also strongly

simplifies the production of existing designs by minimising post-production assembly. The result is a cost reduction for very complex parts (cf. Figure 2-2) [1]. As a result, AM is sometimes referred to as solid freeform fabrication (SFF) [23,24]. There are, however, some limitations to this "free complexity" concept, as the material being added needs sufficient support from the rest of the structure during the build. This often leads to additional support columns that need to be incorporated in the build and require, often manual, removal afterwards [1,10].

Besides support removal and other post-processing steps, AM has additional disadvantages. Some major drawbacks include the limited building speed, the lack of available materials for some AM processes and the often reduced strength of parts (primarily in the z-direction), due to the layer-wise strategy of AM [9,25]. Therefore, not all products are suited for production via AM processes. Typically the biggest gain is found for high complexity, low quantity product with a high added value.

Between 2010 and 2015, the AM industry had an annual growth rate of roughly 30 %, further indicating how it is continuously developing as a state of the art industrial manufacturing route, rather than just a prototyping technique. Furthermore, materials sales are expected to reach $8 billion by 2025 [26]. Vasquez et al. note similar growth numbers, focussing on the high economical value of AM materials, which they claim represent about 20% of the AM industry [27]. These sales and growth trends illustrate the possible economic impact of introducing new AM materials to the market.

### 2.1.2 Laser sintering

The LS creates the product by selectively sintering powder particles in sequential layers. Similar to all other AM techniques, a CAD model is created and sliced into thin layers. The typical thickness of a layer for LS is in the order of 100 µm, which is roughly 1.5 to 2.5 times the average particle diameter [28,29]. A sintering machine, as illustrated in Figure 2-3, then deposits powder layers of the same thickness. In each of these layers a laser sinters the cross-section of the final products. The process of powder spreading and sintering is repeated until all layers are formed. For economical reasons, an LS build typically contains multiple products, stacked next to and above each other. After building all the layers, the products are removed from the unsintered powder, which is recycled for new builds [3,30,10].

LS was originally developed at the University of Texas (Austin) and the process was patented in 1986 [31]. In the following years, 3D systems trademarked the process and corresponding machine under the name selective laser sintering (SLS). As a result, both LS and SLS are found in literature to describe the same process, though technically SLS was only applicable for the LS machines or processes of 3D

systems. The trademarks for both the machine and process description have expired in 2016, making it common to use SLS as a general terminology [32,33,34,35]. Currently, there are two main manufacturers for LS machines, namely 3D Systems Corporation and EOS GmbH [36].

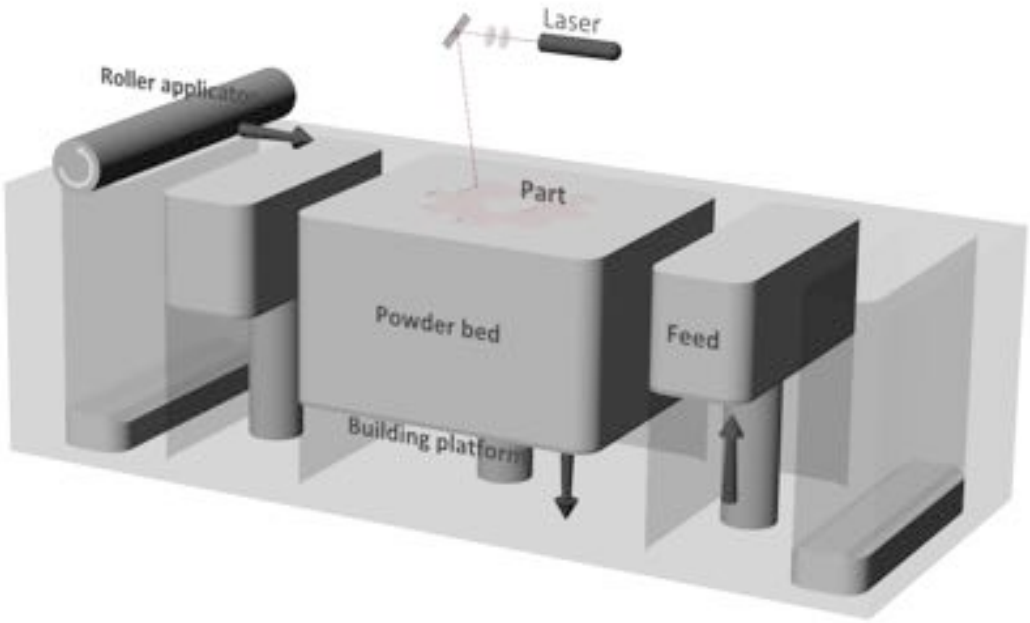


**Figure 2-3:** Schematic representation of the laser sintering process as applied in 3D Systems' brand of LS machines.

LS has multiple advantages over the other aforementioned AM processes. Firstly, parts with typically better mechanical strength are produced, compared to e.g. SLA or FDM [4]. This makes the technique more suitable for load bearing parts [37]. This improvement is not only due to the superior inter-layer fusion, but also due to the typically higher-strength polymers used in LS. Secondly, the surrounding powder bed can carry a load, thereby functioning as a support material. This makes LS a true freeforming technique as no support columns need to be build and removed afterwards [21]. Finally, control over the porosity of the product is possible, making this a useful technique for applications such as porous scaffold [38,39] or even membrane production [40]. Drawbacks, compared to other AM techniques, include the inherently poor surface finish of the product, which often requires a further coating step, the limitation of single-material builds and the limited palette of available polymers [1]. The latter issue is one of the main drives behind the research performed in this thesis.

From a broad perspective, the material palette for LS is extensive. The process is available for polymers, ceramics and metals, though in the case of metals it is typically called selective laser melting (SLM) [1]. The focus of this research lies on polymers. Within this sub-class of materials, a strong hindrance is the lack of

available grades, compared to traditional polymer processing techniques. One polymer, namely polyamide-12 (PA12), makes up about 95 % of the LS polymer market [3,4]. For applications that require more flexible materials, thermo-plastic polyurethane (TPU) sintering powders exist. Their market share is, however, not as large as that of PA [41]. The limited range in (mechanical) properties that are attainable for these polymer families forms a major hurdle for LS, as it hinders the technique from fully meeting the market needs [42]. Other materials are researched, including polycarbonate (PC) [43,44], polypropene (PP) [45,46,] polybutene terephthalate (PBT) [47], polycaprolactone (PCL) [38,39] and poly(aryl ether ketone) (PAEK) [48,49,50,51]. Their market share, however, cannot compete with that of PA [4]. The addition of new polymers to the LS market is therefore valuable for the AM industry.

Other powder bed based AM processes exist, such as the aforementioned SLM process for metals. As each of these processes have steps in common with LS, especially the layer deposition step, the research performed in this thesis may also benefit these techniques. The next paragraphs therefore shortly introduce the concept of two powder bed based techniques that are available for polymers, namely high speed sintering (HSS) and three-dimensional printing (3DP).

High speed sintering (HSS), as the name indicates, is a faster variant of the LS process. The speed increase is obtained by replacing the slow laser scanning by a radiant source that reaches the entire bed surface at once. The selective sintering then occurs by locally varying the absorbance of the powder. This is possible by using a mask in front of the radiation source or by adding a radiation absorbing material (RAM) locally to the powder bed to improve absorbance [16,17]. The RAM is typically added by inkjet heads, not unlike those used in paper printers. Particles that are not jetted by the RAM do not absorb enough energy to melt and thus remain unsintered [17]. In 2016 HP commercialised the technique as Multi Jet Fusion and added besides the RAM also a “detailing agent” to minimise heating of the powder adjacent to the part [52,53,54].

Three-dimensional printing (3DP) shows some similarities to both LS and HSS, mainly related to powder spreading. The binding mechanism is, however, different. Rather than fusing the particles by melting, inkjet heads jet a binder material that glues the particles together. The technique, licenced by MIT, has been applied to metals, ceramics and polymers [55,56,57,9]. The research on powder flowability should however be applicable to this technique as well, as the typical deposition mechanism for dry powder spreading is also the counter-rotating roller set-up. Opposed to the dry spreading, there are also 3DP systems that deposit the layers in a wet slurry form. The flow mechanisms in this case will be significantly different to the layer deposition in LS [56].

### 2.1.3 LS material selection

A good sintering powder needs to possess various properties, as summarised in Figure 2-4. This section clarifies all the selection criteria that need to be taken into account for the evaluation of a new material. Materials in the LS process undergo four distinct steps. (1) First, a layer of powder is deposited on the building platform. (2) Next, the powder melts and coalesces upon absorbing the laser energy. (3) The formed polymer melt then solidifies again. (4) The final step is split into two parts depending on the state of the material: (4a) Part of the powder will, through steps 2 and 3, have formed an end product, which needs to adhere to certain standards. (4b) However, as not all powder is sintered, the remainder of the powder should preferably be re-usable in subsequent builds [27,3,58]. The next paragraphs illustrate the working principle of each step more in detail, focussing on semi-crystalline polymers, which are the most common in LS. The final paragraphs add some remarks on the differences between the use of semi-crystalline versus amorphous materials.




**Figure 2-4:** Requirements for the different steps within the laser sintering process.

**Step 1: layer deposition**

First, the powder needs to flow well to be deposited into thin layers. The exact thickness of the layer depends on the material used and the desired resolution versus building speed, but it is typically in the order of magnitude of 100 µm [36]. The layers should be smooth, defect-free and preferably dense. The latter is relevant, as denser powder layers are known to lead to denser final parts, which typically possess better mechanical properties, such as higher strength [59,60].

The need for powder flowability in the LS process is visible at two steps. The first step is the delivery of powder to the applicator system. Two common practices are used to achieve this: (1) A movable platform pushes up a fixed powder volume, as illustrated in Figure 2-3. This is typical for the machines of 3D Systems [36]. (2) A

hopper drops down a fixed amount of powder in front of the applicator. This is the strategy in EOS machines [36]. However, as the former strategy has very limited requirements on powder flow and the hopper flow of the latter strategy is well established, the research performed in this work focuses on flow in the second step. The second step is the deposition of powder onto the building platform. As this step results in a very particular flow field, flow requirements in this step are much less known. The requirements on this step are, however, very stringent, as all layers need to be dense and defect-free. Again, two strategies exist for this deposition step. (1) a counter-rotating roller pushes the powder over the bed. In some set-ups, a co-rotating motion to further densify the layer follows. (2) A blade scrapes powder over the platform. The blade typically has an inclined base to aid the compression of powder into the layer [36,22].

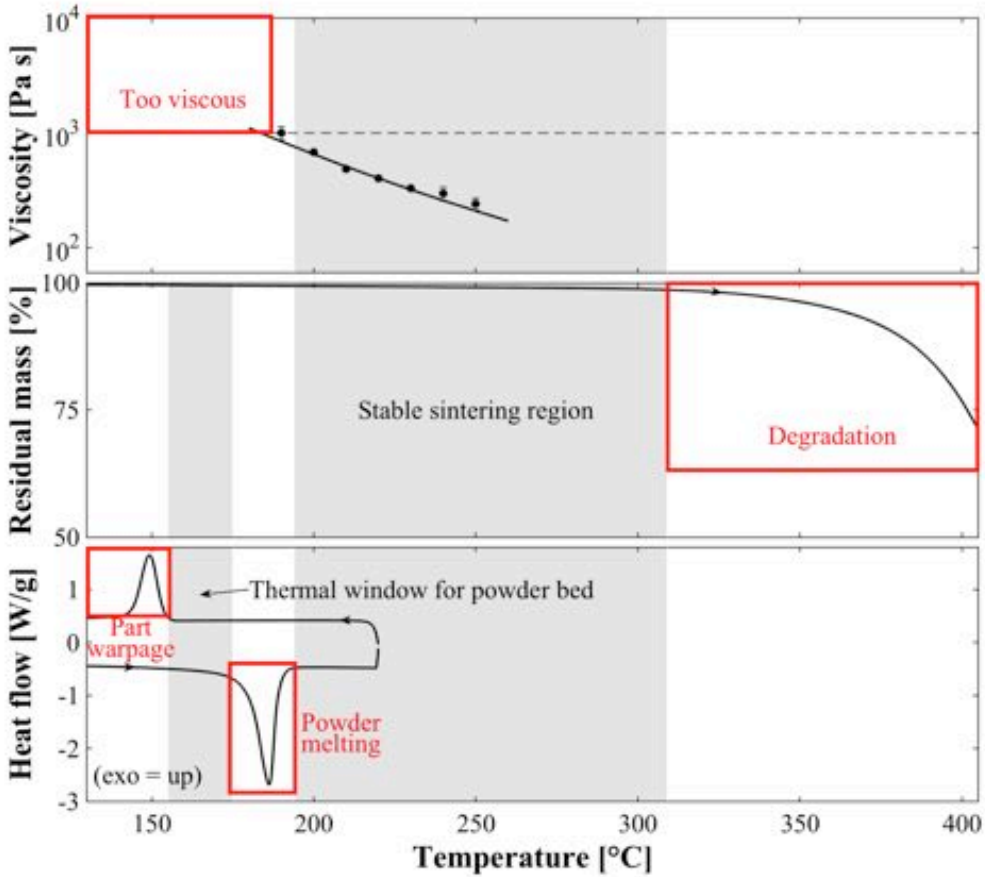


**Figure 2-5:** Illustration of the thermal windows (grey), measured for the market dominating PA12 grade (PA 2200).

The boundary conditions of the layer thickness and required powder flowability place some limitations on the usable particle size ranges for LS. One the one hand, to enable good powder flowability, fine particles (< 30 µm) are undesirable due to their strong Van der Waals interactions [29,60], as further discussed in Section 2.2.1.

On the other hand, particles that are larger than the layer thickness evidently result into spreading issues. As a result, Schmid et al. propose an ideal LS size range of 20 µm to 80 µm [29]. Goodridge et al. place these limits from 45 µm to 90 µm [28], which is quite similar. In the case of poorly spreading powders, e.g. due to an inherent rough particle morphology, an option is to increase the layer thickness. Goodridge et al. illustrate this for a milled glass-ceramics sample that requires a 250 µm layer thickness to allow adequate spreading [61]. This increase, evidently, reduces part accuracy and is thus preferentially avoided.

Temperature adds another level of complexity to the powder flow analysis for LS. The entire powder bed is heated to delay crystallisation and related shrinkage of the sintered cross-section. This temperature increase is expected to have a strong effect on the powder flowability [3,62,63]. The main reason to deter shrinkage lies in the layer-wise fabrication mechanism. By keeping the bed above the crystallisation onset, the material that is molten by the laser (cf. step 2: coalescence), is kept from crystallising and thus shrinking. If this melt would instantly start crystallising in each layer, the volume contraction associated with this phase change would pull on the layers below it, thus warping the part and possibly destroying the entire build. If the bed temperature would, however, be too high, the entire powder bed starts to stick or even melt, thus creating an upper limit for the powder bed temperature. This temperature range is called the thermal window for the powder bed (cf. Figure 2-5) [4,3]. The use of this thermal window has the added advantage, that the laser only needs to add the energy required to heat the material slightly above the melting peak, rather than the complete heating from ambient conditions [3].

Heating in the LS system is performed in various ways and is often dependent on the brand of the device. In all devices, infrared heaters are placed above the powder bed to control the temperature of the bed surface. In some devices, conductive heating is also present at the sidewalls of the powder bed, to avoid the bed from cooling too fast. Other devices only have insulations placed at these sidewalls. Finally, also the powder in the feeders is heated in some devices. This prevents the freshly deposited powder from cooling the layer below it too much upon spreading [3].

**Step 2: coalescence**

After the deposition step, the powder needs to coalesce fast and completely when hit by the laser. As a result, only thermoplastic polymers, i.e. polymers that are melt-processable, are usable in LS. Besides a low viscosity, this requirement implies good absorption at the laser wavelength, a sharp and clear melting peak for semi-crystalline polymers and either a degradation onset well-above the melting temperature or glass transition temperature for semi-crystalline or amorphous polymers respectively [64,58].

The laser adds energy to the material, to increase the temperature from the powder bed temperature to a point at which the melt flows well enough to coalesce. This flow, or rather the resistance to flow, is given by the melt viscosity $\eta$, which is strongly temperature dependent. For many semi-crystalline polymers, it is sufficient to raise the temperature above the melting peak, hence reaching a fully molten state (cf. Figure 2-5). For other polymers, additional heating is required to further lower the viscosity of the melt. The melt viscosity follows an Arrhenius type dependency on temperature (Eq. 1.1), with $E_\mathrm{a}$ the activation energy for viscous flow and $\eta_{00}$ a constant that expresses the molecular mobility [36]. As the only driving force for coalescence is surface tension (and gravity), the shear rates in this process are rather low. Consequently, the zero-shear viscosity $\eta_0$ is the most representative indicator for coalescence in LS. Studies on typical LS PA show that a viscosity below 1000 Pa s is desirable [58].

$$\eta_0 = \eta_{00} e^{\frac{E_\mathrm{a}}{RT}} \tag{1.1}$$

Another common method to assess coalescence behaviour is hot stage microscopy (HSM). In HSM, powder particles are loaded onto a transparent plate with a controllable temperature. A microscope then optically monitors the coalescence behaviour. The coalescence should be fast and complete [27,65]. As a typical conductive hot stage is not able to reach the heating profiles seen in LS, this technique is very indicative. To get a more quantitative interpretation, the necking of two touching, molten polymer particles is often studied. This necking is promoted by the surface tension $\Gamma$ of the polymer melt and hindered by the (zero-shear) viscosity $\eta_0$, as described by the Frenkel-Eshelby model (Eq. 1.2), with $w$ the neck width and $d_\mathrm{p}$ the particle radius [27,65]:

$$\frac{w}{d_\mathrm{p}} = \sqrt{\frac{2\Gamma t}{\eta_0 d_\mathrm{p}}} \tag{1.2}$$

This simple model holds for round particles. However, as the necking speed is not only influenced by the bulk material properties $\Gamma$ and $\eta_0$, but also by the shape of the particles and the resulting contact, the practical implementation of this model for irregular particles is more limited.

As the laser provides an intense burst of energy to the material, temperature overshoots are almost inevitable. Therefore, the degradation onset of the polymer should be well above the desired temperature for coalescence. This defines a second thermal window, namely that for the laser heating, which sits between the required temperature for adequate melt flow and the start of the degradation onset (cf. Figure 2-5). This is sometimes referred to as the stable sintering region. Vasquez et al suggest the point at which 1 % of the material mass has disappeared as the end of the stable sintering region [66].

The amount of energy added by the laser is typically described by the energy density (ED), which is the amount of energy added per unit area [3,67,68] (Eq. 1.3a). In this equation $P$ is the laser power, $v_{\text{scan}}$ is the traveling speed of the laser beam and $w_{\text{spacing}}$ is the spacing between adjacent beam paths. In some studies, the energy density is defined per unit volume, including the effect of the layer thickness $h$ (Eq. 1.3b) [69]. Though this is also a correct measurement of the energy addition that the powder experiences, it is less commonly used.

$$\text{ED}_A = \frac{P}{v_{\text{scan}}\, w_{\text{spacing}}} \quad [\text{J/m}^2] \tag{1.3a}$$

$$\text{ED}_V = \frac{P}{v_{\text{scan}}\, w_{\text{spacing}}\, h} \quad [\text{J/m}^3] \tag{1.3b}$$

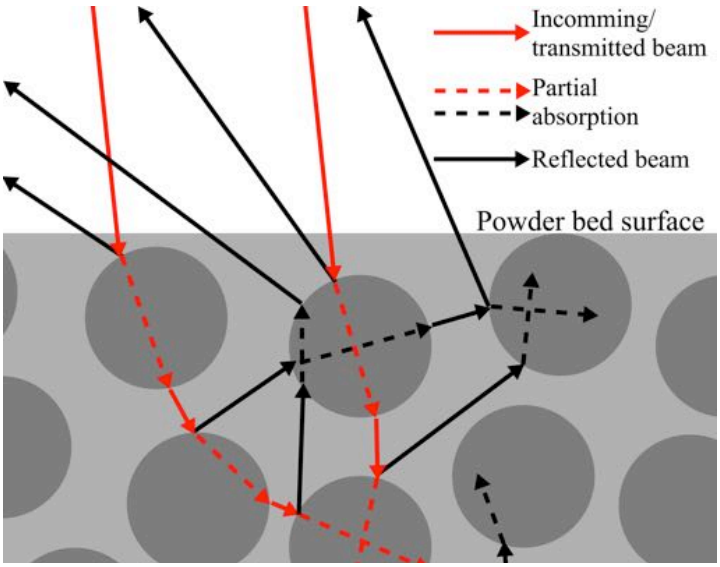


**Figure 2-6:** Internal reflection of the laser beam (adapted from Laumer [70]).

LS machines typically use $CO_2$ lasers, which have a wavelength of 10.6 µm, because polymers tend to have high absorption rates at long wavelengths [30,36]. This behaviour contrasts with metals, which typically absorb better at lower wavelengths. As a result, some SLM machines carry a Nd:YAG laser, which has a wavelength of 1.06 µm [30]. The laser interacts with the powder material in three ways: (1) reflection, (2) absorption and (3) transmission. The net effect of these components is complex, as internal reflections in the powder bed result in additional absorption and thus also affect the penetration depth (cf. Figure 2-6). This yields a much higher absorbance than a solid block of the same material would [70,71]. Studies show that the typical PA 2200 powder bed reflects only 5-6 % of the incoming $CO_2$ laser at the bed surface, thus yielding a high absorbance of 94-95% [70]. To correctly compare materials with different reflective properties, the energy density is sometimes described as the amount of energy taken up by the material, rather than the energy

input by the laser. This is done by multiplying the energy density described in Eq. 1.3 by a conversion factor which is smaller than unity [72]. All reported ED values in this work, however, report the energy input by the laser, i.e. in case of a conversion factor of unity.

**Step 3: solidification**
After coalescence, the polymer melt needs to solidify with minimal shrinkage during the process. As mentioned in step 1, shrinkage is detrimental, as the layer-wise production of LS would then yield part warpage, which consequently destroys the build [3,58]. Again, multiple techniques exist to study the solidification behaviour. Besides aforementioned DSC measurements, which determine the thermal window for the powder bed, dilatometry provides more insights into the expected shrinkage upon crystallisation.

The most fundamental way to look at the issue of shrinkage, is to directly measure the thermal expansion via dilatometry. Verbelen et al. developed a set-up to easily assess the volumetric change of polymers on a thermomechanical analysis (TMA) device. Their measurements showed that the shrinkage upon crystallisation for typical LS PA is 4-5 % [73,5]. New materials intended for LS thus ideally have similar or less shrinkage.

**Step 4a: final product**
Finally, the end-state of the material needs to be taken into account. On the one hand, the final product needs to possess desirable properties for a market application and hold dimensional stability upon further cooling after the build. Many of these parameters can be measured on injection-moulded parts of the base material. However, loss of these properties by poor coalescence or degradation by the laser in LS needs to be taken into account.

**Step 4b: unsintered powder recycling**
Besides final products, a lot of unsintered powder remains in the build. In order to re-use the powder for new builds, this powder cannot have significantly changed in its properties [74]. Reported ratios of unsintered powder volume to part volume are as high as 10:1, thus re-usability of this unsintered powder is economically crucial [19]. To regain some powder properties after recycling, the recycled powder is mixed with new powder. The ratio of new to used powder is called the refresh rate. Refresh rates of 30 % to 70 % are applied for PA powders to prevent poor surface finishing in the final parts [75]. After a few recycles, however, the powder is typically discarded to prevent over-aging of the oldest particles in the recycled fraction [19].

One of the major hurdles that limit recyclability of LS powders is post-condensation. Many polymers, including PA, are polymerised via a condensation reaction, i.e. reactive groups on the molecules interact and form covalent bonds. As a result, after

polymerisation, the ends of the polymer chains still contain reactive groups. These unreacted groups may lead to further polymerisation, thus increasing the molecular weight and thereby the viscosity. A too high viscosity increase results in coalescence issues and poor surface quality, often described as "orange peel" [29]. At room temperature, post-condensation is limited. However, the prolonged exposure to high temperatures in the powder bed promotes the post-condensation reaction. Acierno and Van Puyvelde propose Eq. 1.4 for the post-condensation viscosity increase, with $\chi$ the logarithmic viscosity increase and $t_x$ a characteristic time constant [76]:

$$\log(\eta_0(t)) = \log(\eta_0(t=0)) + \chi(1 - e^{-\frac{t}{t_x}}) \quad (1.4)$$

Post-condensation can be avoided by end-capping the polymer molecules at the end of the polymerisation process. However, post-condensation may also be beneficial for LS in some cases. It enables the use of a relatively low molecular weight polymer, with thus a relatively low viscosity. Upon melting, the high temperatures strongly increase the molecular weight to values that may otherwise yield coalescence issues. The final part thereby has a higher molecular weight and possible inter-layer linkage due to the continued polymerisation reaction, which typically results in a higher strength [29].

**Amorphous versus semi-crystalline powders**

LS polymers are typically split into two categories, namely semi-crystalline and amorphous materials [77]. Semi-crystalline polymers have a melting temperature $T_m$ and crystallisation temperature $T_c$. As mentioned in the previous section, these limit the thermal window for the powder bed. Upon melting the viscosity of the material typically drops significantly. For PA 2200 this means that upon fully melting the powder, the viscosity is already sufficiently low for coalescence, as illustrated in Figure 2-5. The stable sintering region is thus determined by the melting endotherm (DSC) and the degradation onset (TGA). This, however, is not the case for all polymers, as some grades will require (limited) additional heating above the melting peak. In that case, the temperature at which the viscosity becomes sufficiently low (rheometry) determines the lower limit of the stable sintering region.

Amorphous materials behave differently. They do not possess a melting temperature, as they have no crystals to melt. Amorphous materials only have a glass transition temperature $T_g$, below which they are in an immobile, glassy state. When heated above their glass transition temperature, the molecules regain their mobility and the material can flow. However, this increase in mobility is much more gradual, resulting in a need for a large temperature increase to sufficiently lower the viscosity according to Eq. 1.1. As a result, the solicitation step is much less problematic for amorphous polymers, as the lack of a phase transition due to crystallisation also means limited shrinkage. The trade-off is a more difficult

coalescence step, which is hindered by the higher viscosity, typically resulting in inferior part density and mechanical strength of the final parts [3,30]. Due to their high dimensional stability and low part density, these materials are often used as lost cores in precision casting [78]. The class of amorphous polymers is mainly represented by polycarbonate (PC) [77].

## 2.2 Fundamentals on powder flow

To fully understand powder flowability in LS, some fundamental concepts of particle characterisation and particle interactions are needed. The following paragraphs provide some insights in what forces affect powder flowability and which particle and process parameters have an influence on them.

### 2.2.1 Forces affecting powder flowability

*Passages from this section, including figures, have been adapted from an own, published lab course manual [79].*

Powder flowability results from the governing inter-particle interactions. These interactions are categorised into three main groups: (1) steric repulsion (2) friction forces and (3) attractive forces [80].

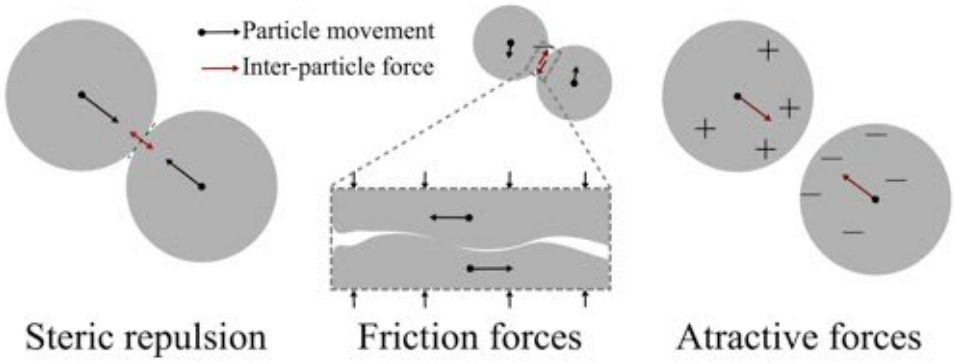


**Figure 2-7:** Governing inter-particle interactions: steric repulsion, friction forces and attractive forces.

Steric repulsions and friction forces are the dominant interactions for non-cohesive powders. Steric repulsions result from the geometrical properties of the powder and the fact that two powder particles cannot take up the same space. Friction forces are the result of particles sliding over each other and mechanically interlocking [81]. As a result, the behaviour of non-cohesive powders is mainly dominated by the geometry and surface structure of the grains [80]. For cohesive powders on the other hand, the

attractive forces are much more dominant. As most powders in this thesis can be seen as mildly to strongly cohesive, the next few paragraphs focus on the nature of these attractive forces. The most common attractive forces to take into account are Van der Waals, electrostatic, capillary and magnetic forces [80,81,82,83]. As this thesis discusses only polymeric powders, magnetic forces are not discussed further.

**Van der Waals forces**

Van der Waals forces are attractive forces on a molecular level. They are the electromagnetic forces resulting from the dipoles in the material. These dipoles can be of a permanent nature, as is the case in polar molecules, or they can be induced in inherently non-polar molecules [81,82]. As a consequence, the London dispersion force, i.e. the force between two induced dipoles, is the most fundamental contributor to the overall Van der Waals interaction, as it is present in all materials [81]. As the Van der Waals force acts on a molecular scale, computations to a net force on macroscopic bodies are required for practical use. The most relevant, and generic, case for investigating powders is that of two spheres, which yields Eq. 1.5, with $A_h$ the Hamaker constant, $a$ the approach distance between the two particles and $d_{pi}$ the respective particle diameters [83]:

$$F_{VdW} = \frac{A_h}{12a^2} \frac{d_{p1} d_{p2}}{d_{p1}+d_{p2}} \tag{1.5}$$

As spherical bodies are a strong simplification of real powder systems, the Van der Waals force computed by Eq. 1.5 is often an overestimation of the actual interactions. This difference is due to surface asperities, which change the contact area between the interacting particles. The equation further explains why compaction increases powder cohesion, as this lowers the approach distance $a$ [84].

In dry, non-charged powder systems of small particle size, the Van der Waals force is most often dominant for determining flowability [81]. This dominance is explained by looking at the ratio of the attractive force, in this case the Van der Waals force, to the inertia force of the two-particle system. For spheres of equal size, Eq. 1.5 shows a linear dependence of the Van der Waals force with particle diameter. The inertia force is proportional to the particle weight, and thus the sphere volume, which is dependent on the third power of the particle diameter. As a result, the Van der Waals force decreases much slower with particle size, compared to the inertia force, thus becoming dominant at small particle diameters [85]. The inertia force is typically represented by the gravitational force (Eq. 1.6), with $\rho_p$ the particle density and g the gravitational acceleration.

$$F_g = \frac{\pi}{6} d_p^3 \rho_p g \tag{1.6}$$

For the case of a particle sticking to a wall ($d_{p2} = \infty$), the ratio of the attractive Van der Waals force to the gravitational force is often called the adherence (Eq. 1.7a) [85]. This equation can, however, be extended for a sphere-sphere contact, in which the average inertial force for the two particles is taken (Eq. 1.7b). The ratio of the attractive forces between particles to their weight is called the particle Bond Number (Bo). The Bond number technically includes all attractive forces, but in this section is limited to Van der Waals interactions.

$$\text{Adherence} = \frac{F_{\text{VdW}}(d_{p1},\infty)}{F_g(d_{p1})} \tag{1.7a}$$

$$\text{Bo}_{\text{VdW,s-s}} = \frac{F_{\text{attraction}}}{F_{\text{inertia}}} = \frac{F_{\text{VdW}}(d_{p1},d_{p2})}{\left(F_g(d_{p1})+F_g(d_{p2})\right)/2} \tag{1.7b}$$

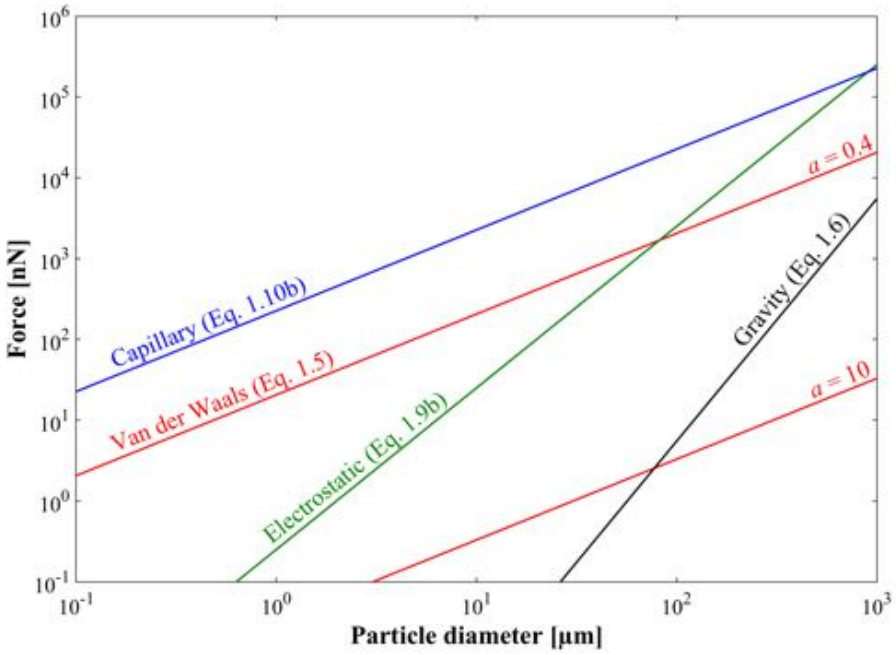


**Figure 2-8:** Illustration of the inter-particle forces between two equally-sized spheres: $\rho_p$ = 1.07 g/cm$^3$, $A_h$ = 7.9 10$^{-20}$ J, $\varepsilon$ = 8.8 10$^{-12}$ F/m; $s$ = 26.5 µC/m$^2$ and $\Gamma$ = 0.072 N/m (adapted from Masuda et al. [86]).

Figure 2-8 illustrates the order of magnitude of the Van der Waals and inertial forces for typical LS PA powder, based on the following material properties. Thio et al. computed the Hamaker constant of PA12 in air as $7.9\,10^{-20}$ J [87]. Own measurements on the PA 2200 powder show a density of 1.07 g/cm$^3$ and an average particle diameter of about 60 µm. This leaves only the approach distance unknown in Eq. 1.5. However, the value of the approach distance is difficult to assess. As the van der Waals force acts over a distance of roughly 10 nm [88] and the irregular powder surface of real powders typically results in an overestimation by the sphere-sphere model, a maximal approach distance of 10 nm is chosen. This example yields

a Van der Waals force of about 2 nN and a Bond number of about 1.7. A Bond number around unity is found for particles of 77 µm. This means that for the particles used in laser sintering, the Van der Waals force is quite dominant on the flow behaviour. The lower limit for the approach distance, i.e. 0.4 nm, is also plotted. Real Van der Waals forces will lie somewhere between these two limits, depending on the particle geometry.

The previous paragraphs discussed the Bond number for a two-particle system. The next step is to apply the concept of Van der Waals forces to a bulk of powder with a known particle size distribution (PSD). To obtain an average Bond number, each interaction between two particle sizes needs to be multiplied by the probability of these two particle sizes meeting. This yields Eq. 1.8 for the average Bond number. This equation can be used to predict flow behaviour of micron-sized powders, solely based on their normalised PSD. This definition of the average Bond number is an approximation for real systems, as it does not yet take into account that particles of different sizes may have different probabilities to interact. E.g. electrostatics can cause smaller particles to preferentially attract to larger ones.

$$\mathrm{Bo}_{\mathrm{VdW}} = \int_0^\infty \int_0^\infty \mathrm{Bo}_{\mathrm{VdW,s-s}}(d, d')\ \mathrm{PSD}(d)\ \mathrm{PSD}(d')\ \mathrm{d}d\ \mathrm{d}d' \qquad (1.8)$$

**Electrostatic forces**

Electrostatic forces are the result of powders obtaining a net charge. These forces are generally the effect of triboelectrification, also named contact electrification. In triboelectrification, the dynamic contact between different materials results in a transfer of charge from one material to the other (cf. Figure 2-9) [89]. After separating the materials, charge relaxations starts. For insulator materials such as polymers, this relaxation can take minutes to hours [90]. The charges transferred between polymers and metal surfaces is typically in the range of $10^{-4}$ C/m$^2$ [89]. In case of powders, charge transfer is not only possible between different materials, but also between different particles of the same material. In the latter case, electrons tend to transfer from larger to smaller particles [91]. In some cases, also ions can transfer.

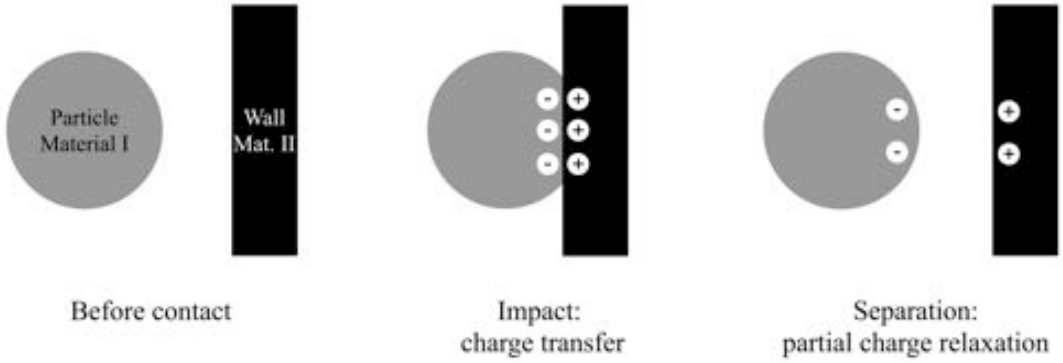


**Figure 2-9:** Schematic illustration of triboelectrification, based on Matsusyama et al. [89].

The resulting force, the Coulomb force, is directly proportional to the net charge of the particles. Assuming point charges, the Coulomb force is expressed by Eq. 1.9a, with $Q_i$ the net charge of each particle, $a$ the approach distance and $\epsilon_\mathrm{p}$ the electric permittivity of the medium [81,83,22]. Expansions for this equation exist for particles of finite size. Assuming insulator particles with a constant charge per surface area $s$ and an approach distance that is orders of magnitude smaller than the particle size, this yields Eq. 1.9b [86]. As polymer particles are insulators, their tendency to hold the transferred charge is high, often resulting in severe flowability issues, resulting from the attractive Coulomb force [92]. Figure 2-8 further illustrates the dominance of the Coulomb force in charged systems.

$$F_{\mathrm{Coulomb}} = \frac{Q_1 Q_2}{4\pi\epsilon_\mathrm{p} a^2} \tag{1.9a}$$

$$F_{\mathrm{Coulomb}} = \frac{\pi s^2 d_\mathrm{p}^2}{\epsilon_\mathrm{p}} \tag{1.9b}$$

Charge transfer is a complex phenomenon, with a lot of parameters. Not only the particle properties, such as the material, particle size, shape at the contact and purity, but also the environment play a huge role [90]. An increase in the relative humidity or moisture content of the powder can therefore sometimes improve powder flow by facilitating charge dissipation [93]. Besides flowability issues, charging may also induce explosion hazards for dry powders [94]. Precautions, such as sufficient grounding of the equipment, therefore need to be taken.

Multiple methods to measure the electrostatic charge on particles exist. They are typically divided in direct and indirect methods. Indirect methods study the motion of a charged particle in an electro(magnetic) field. Direct methods measure a change in potential or current due to contact of the charged particles with a conducting surface. A simple and direct method to measure charge is a Faraday cup measurement [95]. A Faraday cup consists of two concentric, conducting containers with an insulation material in between. The insulation prevents electrical contact and thus charge transfer between the two containers. The powder is placed in the inner container and induces charges on it. A voltmeter can then measure the voltage between the inner container and the grounded outer container. Via the capacitance of the system, the charge in the powder can be calculated [96]. The charge density, i.e. the charge per unit mass, logically follows from weighing the sample.

The Faraday cup can only indicate the amount of charge already present in a sample. On its own, it tells nothing on how much the powder will actually charge in a real system. Therefore, first a protocol has to be applied in which the powder is subjected to triboelectrification. There are some requirements to a good triboelectrification protocol: (1) The powder should be collected as soon as possible after charging, to avoid charge dissipation to the humid air. Humidity control during

the experiment aids in the reproducibility of the measurements [94]. Ideally, the powder could be collected on-line in the actual process, or directly after the charge protocol in the lab. (2) As charge acquisition is a system property, the wall material used for triboelectrification on lab scale should be the same as in the industrial application. (3) The way of charging should mimic the industrial application. E.g. a difference is typically seen between charging by sliding friction versus charge transfer upon impact. Stauffer et al. suggest the use of a tilted slide to induce frictional charging and collect the powder in a faraday cup at the bottom [94]. Some techniques therefore try to incorporate both mechanisms to get a generalised powder ranking. An example of a commercial set-up for inducing and measuring the triboelectrification of powders is the GranuCharge by Granutools. In this set-up the powder is poured in a pipe at a 45° angle. After flowing through this pipe, the powder drops into a second 45° angle pipe to also include the impact charging mechanism [97].

**Moisture related forces**

The effect of moisture on powder flowability is complex. Moisture interferes with the previous forces, resulting in a decrease or increase of the attractive force. On the other hand, moisture can create entirely new interactions between the particles. As the system of interest is still a "dry" powder, particle systems that mainly consist out of liquids, such as suspensions, will not be discussed. The net effect of adding moisture to a system will depend on the amount of moisture, the nature of the material and the dominant attractive forces present in the system.

Firstly, moisture can improve the flowability in some cases. It can act as a lubricant, thus lowering the friction force, or aid in charge dissipation for insulating materials, thus decreasing the Coulomb force [93,98]. As the powders in this research are non-conductive plastics, the effect of charge dissipation plays a large role.

Secondly, moisture can deteriorate flowability by increasing Van der Waals forces. Two mechanisms for this effect exist. (1) Van der Waals forces are very dependent on surface irregularities that increase the approach distance. Adsorbed layers of moisture could be seen as a smoother particle surface, thus decreasing the approach distance [98]. A remark, however, needs to be made that the Hamaker constant described earlier is dependent on the fluid between the particles. As the Hamaker constant is typically larger for particle-air-particle systems compared to particle-liquid-particle [99,100], this may also result in a slight decrease of the Van der Waals force. (2) In plastics moisture may act as a plasticiser, thus increasing deformability upon contact [101]. This increase in deformability leads to an increase in the contact area, or a decrease in the approach distance, thus increasing the Van der Waals force.

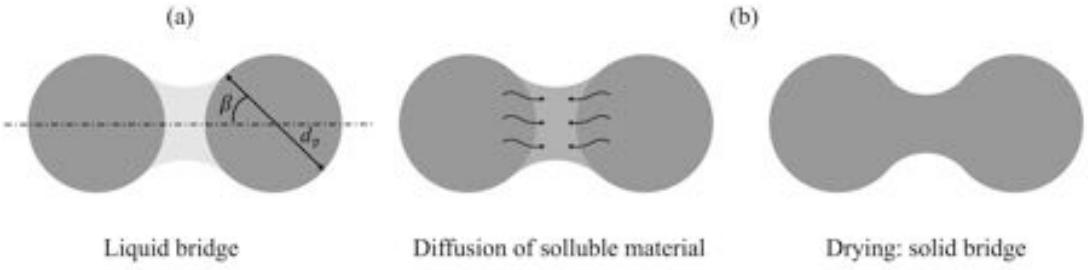


**Figure 2-10:** Illustration of (a) capillary bridges between powder particles and (b) solid bridge formation.

Finally, new interactions may occur due to the presence of moisture. Above a critical moisture content, liquid bridges appear and connect the particles (cf. Figure 2-10a) [98]. These bridges exert an attractive capillary force, as described in Eq. 1.10a [102], with $\Gamma$ the surface tension of the liquid, $\theta$ the contact angle and $\beta$ the bridge half angle. When the contact area of the liquid bridge is significantly smaller than the particle radius, as is expected in low moisture concentrations, this equation can be simplified to Eq. 1.10b, with $\theta$ the contact angle [102]. If the particles are water soluble, the liquid bridge may give rise to a solid bridge upon evaporation [102]. As none of the materials used in this research are water soluble, solid bridge formation is not further discussed. It should, however, not be neglected for water-soluble polymers, such as PVA, or in food and pharmaceutical powders [102,25,103].

$$F_{\mathrm{Cap}} = \frac{\pi \Gamma d_{\mathrm{p}} \cos(\theta)}{1+\tan\left(\frac{\beta}{2}\right)} \tag{1.10a}$$

$$F_{\mathrm{Cap}} = \pi \Gamma d_{\mathrm{p}} \cos(\theta) \tag{1.10b}$$

**Other forces hindering flowability**

Some other attractive forces than described above can be present in powder systems. These include the magnetic force, whose contribution when present is often dominant [98] and chemical bonding of the powder surface, including hydrogen bonding [98]. As the systems of interest are unreactive plastic powders, these forses are deemed negligible. In some polymers, e.g. polyamides, hydrogen bonding may play a role. However, the specific physics of this contribution are not further discussed, as modification of the polymer structures is outside of the scope of this work. It should, however, be noted that for applying this research to other systems, the contributions of these forces should be re-evaluated.

**Conclusions**

In conclusion, the powder behaviour is strongly dependent on the governing inter-particle forces. The type of powder and its surroundings strongly affect which forces are dominant for the given system. As a result, solutions to improve powder flow

should be tailored to the problem at hand. E.g. a charge issue could be remediated by increasing humidity, but if the flow issue is the result of capillary bridging, the increase in humidity will further deteriorate powder flow.

### 2.2.2 Particle characterisation

The aforementioned particle interactions are influenced by the material properties of the bulk polymer, such as the Hamaker constant, hardness and elasticity on the one hand, and particle properties, such as the size and shape distribution on the other hand. This section focuses on measuring and interpreting particle properties to provide a better understanding of the underlying mechanisms of powder flow.

Particle properties are more difficult to describe than bulk properties, as their values are distributions rather than simple constants. Furthermore, the concept of particle size becomes more difficult to describe if the given sample contains particles of irregular shapes. This shape irregularity leads to multiple descriptions of the particle size. The choice of the size definition depends on the application, as well as the measurement.

The different definitions for particle size can be split into two groups: (1) the sizes based on a certain equivalency to a perfect sphere and (2) sizes based on the direct dimensions of the irregular particle. The first group is the easiest to understand. In this case, the particle is given the diameter of a perfect sphere that shares one attribute with the irregular particle. This can be a sphere of the same volume, the same projected surface area or the same external surface.

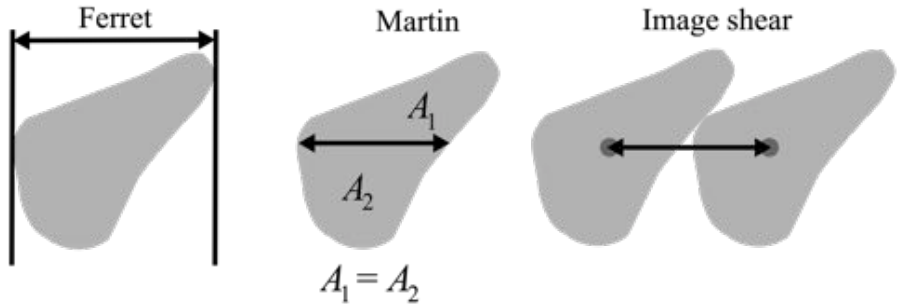


**Figure 2-11:** Illustration of the Ferret, Martin and shear image diameter.

The second set takes specific geometrical attributes of the particle. Examples are the Ferret, Martin and image shear diameter (cf. Figure 2-11). The Ferret diameter is the distance between two parallel lines that are tangent to the particle on opposite sides. The orientation of these lines is typically determined up front [104]. By looking at all possible directions, a minimal and maximal Ferret diameter can be defined. The Martin diameter equals the length of a line that splits the projected area into two equal areas. Again, the orientation of this line needs to be set in advance [104]. The

shear diameter is the minimal distance the projection of the particle needs to be translated in order to have no overlap with the original projection. As with the previous two definitions, the direction of translation is determined up front [104]. Other definitions of the diameters are possible, depending on the technique used. An example is the sieving diameter, which is determined by the smallest mesh of a sieve that the particle can still pass.

Particle shape can also be expressed in many ways (cf. Figure 2-12). Most of these definitions come from microscopy measurements and are thus based on the projected image of the particle rather than the 3D shape. One definition is that of sphericity $\Psi$. The sphericity is defined as the ratio of the projected area of the particle to the ratio of the smallest inscribed circle into which the entire particle fits (Eq. 1.11) [105].

$$\Psi = \frac{A_\mathrm{p}}{A_{\text{inscribed circle}}} \leq 1 \tag{1.11}$$

Another way of expressing the irregularity of a particle is the shape factor $S_f$, which is defined in Eq. 1.12. In this equation, $U$ is the perimeter of the projected particle area. The sphericity and shape factor thus have a maximum value of unity for perfect spheres.

$$S_\mathrm{f} = \frac{4\pi A_\mathrm{p}}{U^2} \leq 1 \tag{1.12}$$

Finally, the aspect ratio $S_a$ is defined as the ratio of the longest dimension, $l_\mathrm{p}$, to the shortest dimension, $w_\mathrm{p}$, (Eq. 1.13). Multiple definitions exist on what these dimensions are for irregular particles. They can, for example, be the maximal and minimal Ferret diameter or the longest dimension through the centre of the particle and the length of the line perpendicular to this direction [106].

$$S_\mathrm{a} = \frac{l}{w} \geq 1 \tag{1.13}$$

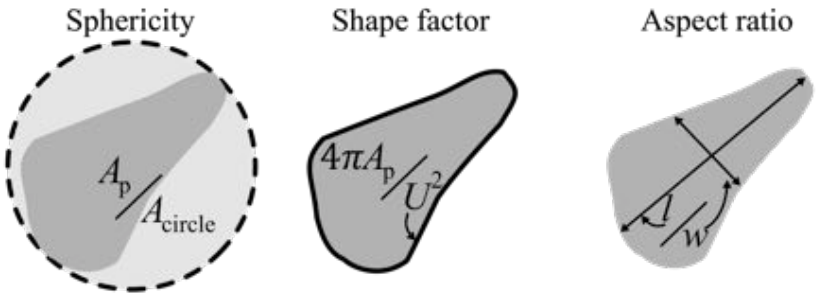


**Figure 2-12:** Illustration of the sphericity, shape factor and aspect ratio.

All the aforementioned particle characteristics are measurable for individual particles. For a bulk powder, they thus form distributions. These distributions are typically number- or weight-based. For powders that contain only particles of a single density, the latter equals a volume-based distribution. A volume-based distribution gives a higher weight to larger particles, compared to a number-based approach. Size distributions are typically described by $i^{\text{th}}$ percentile values, $D_i$. The width of the distribution is typically expressed by the relative span (Eq. 1.14).

$$\text{span} = \frac{D_{90} - D_{10}}{D_{50}} \tag{1.14}$$

Different methods exist to find the particle size. Depending on the chosen method, another value of the particle size may be found. This section discusses some common techniques, namely sieving, microscopy, scattering and sedimentation. Sieving methods use a calibrated grid and a shaking motion to separate particles. Particles that fall through the sieve have a dimension smaller than the grid's mesh size. By using a stack of different mesh sizes, the particle size distribution can be approximated by discrete ranges. The shortest two dimensions determine whether the particle can pass the grid. E.g. a 2x2x10 mm particle can pass a 3 mm grid, even though the largest dimension is much larger than the grid size. The separated fractions are then weighed.

Optical microscopy or scanning electron microscopy can be used to determine particle size via image analysis. Besides the PSD, these techniques indicate the shape distribution as well. Software then computes the size, based on a sphere with the same projected area. A downside of this technique is that the 3D shape thus has to be computed from a 2D projection of the particles. Dispersion of the particles is very important to get representative results. Two main dispersion mechanisms exist: (1) the particles are spread over a transparent plate or (2) the particles are dispersed in a gas in front of the microscope lens. The latter method has the advantage that the particles are viewed from a random direction. This is not the case for the former, as flat particles will always orient in a way that the shortest dimension is perpendicular to the lens.

Light scattering is a fast technique to analyse a large amount of particles. The basic principle of this technique is that particles of different sizes interact differently with a laser, thus yielding a distinct scattering pattern. The downside compared to optical methods, is that less information on the particle shape is obtained. The same requirement for good dispersion of the particles is present as is the case for optical methods [107].

Sedimentation techniques are based on the relation between settling time under gravity and particle size. The concentration of particles at a certain height or the settling rate at the bottom is monitored. The resulting diameter is the Stokes diameter, thus assuming Stokes' law is obeyed during the measurement [108].

## 2.3 Measuring powder flow

*Passages from this section, including figures, have been adapted from an own, published lab course manual [79].*

Measuring powder flow is often challenging. An important reason for this challenge is that almost all techniques measure indices rather than intrinsic material properties. An index is a system property, which means that its value is not only dependent on the evaluated powder, but also on the used geometry and resulting flow field. This dependence is in contrast with intrinsic material properties, such as the liquid viscosity, which are independent of the exact geometry used, if measured correctly. An index can thus only be used to relatively compare powders for flow and stress fields that are similar to those of the measurement.




**Figure 2-13:** Typical powder flow measurements categorized by their flow/stress state.

As the flow and stress fields are thus important factors [63], measurement techniques can be categorised by the type of flow and the level of stress they apply (cf. Figure 2-13) [109]. On the one extreme there is dense or consolidated flow. In this category, the powder is in a compacted state, often experiencing high stresses. On the other side of the spectrum there are the fluidised systems. In this category the powder is strongly agitated and packed very low dense. As a result the flow is mostly dominated by single particle contacts. Between these, there are the freely flowing applications, in which the powder is mildly agitated. These applications include processes such as pouring or spreading of powders. Devices that enable

measurements over the entire spectrum exist; an example is the powder rheometer. The next paragraphs discuss some typical powder flowability measurements, namely the shear cell, Hausner ratio, Hall flowmeter, angle of repose and powder rheometer.

### 2.3.1 Shear cell

The shear cell is one of the oldest, most fundamental and most well-established techniques for assessing the flowability of consolidated powders. The technique measures the friction between particles or the friction between particles and a wall, among other parameters. It is commonly used for the design of hoppers [110].

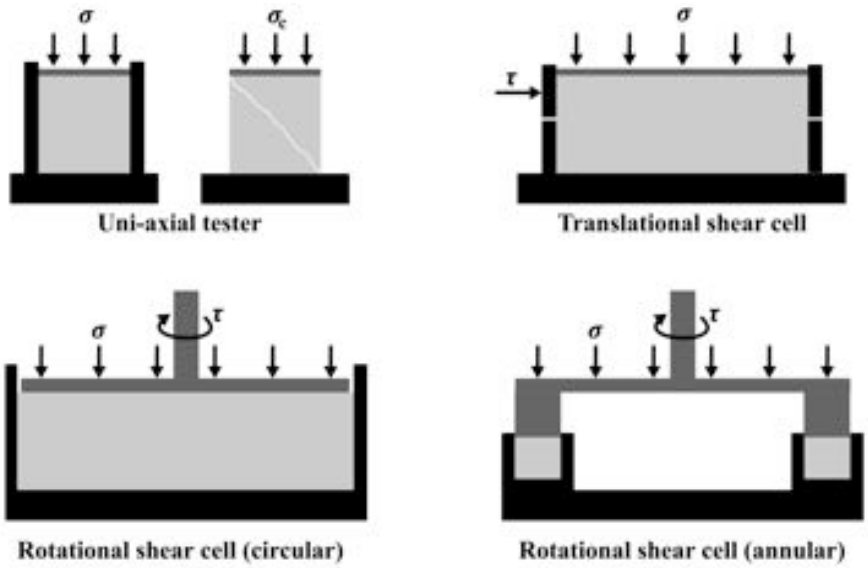


**Figure 2-14:** Illustration of different shear cell set-ups.

The basic principle of the shear cell is simple. First a sample is consolidated and then the stress needed to break the consolidated mass is measured. The conceptually simplest way of doing this is a uniaxial tester, which is technically not a shear cell (cf. Figure 2-14). In this case powder is loaded into a container and a normal stress is applied. The container walls are then removed and the stress to break the powder block is measured. This index is called the unconfined yield strength, $\sigma_c$ [111]. Though the principle is simple, there are other set-ups that are better from a practical standpoint and provide more insights into the materials.

The concept of the uniaxial tester was further expanded to the translational shear cell, e.g. the Jenike Shear cell, and the rotational shear cell, which can be either circular or annular (cf. Figure 2-14) [111]. The concept however remains similar. For the rotational shear cell, the procedure is illustrated in Figure 2-15. First, powder is loaded into the holder and a consolidation normal stress, $\sigma_{\text{consolidation}}$, is applied. During this consolidation a certain shear is imposed until a constant shear stress is

reached for a predetermined time, typically in the order of a few seconds. Next, a lower normal stress, $\sigma$, is applied and the sample is again sheared. This shear is continued until failure, i.e. slip, occurs. The shear stress, $\tau$ at which the failure occurs is then noted. This process is repeated for various normal stresses below the consolidation stress. The $(\sigma, \tau)$-couples form the yield locus or failure envelope, which determines the stress states at which the material fails. A Mohr circle through the origin in the $(\sigma, \tau)$-plane that touches the yield locus then indicates the unconfined yield strength that was found in the uniaxial tester [112].

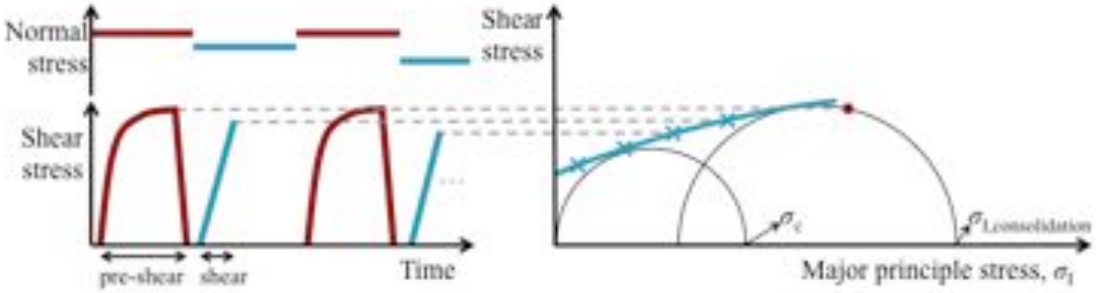


**Figure 2-15:** Conceptual representation of a shear cell experiment (adapted from Schwedes [112]).

The shear cell provides multiple material properties, besides the unconfined yield strength (cf. Figure 2-16). A first property is the cohesion, defined as the extrapolated intercept of the yield locus. As the name indicates, this property provides information on how cohesive the powder is. The second property is the friction angle, defined as either the effective angle of internal friction $\phi_e$ or the internal friction angle $\phi_i$. The tangent of these angles can be seen as a friction coefficient for inter-particle shear. Depending on the geometry used to apply the shear, failure within the powder or at the wall can be studied. Similar to the internal angle of friction, a wall friction angle can thus be determined. Finally, the flow function $ff_c$ is defined as the ratio of the major principle stress during consolidation, $\sigma_{I,consolidation}$, to the unconfined yield stress, $\sigma_c$. It indicates how freely flowing the powder is and how this flowability varies with increasing consolidation [113,114]. As the powder is technically static until failure, no assumptions of the flow field are necessary. As a result, the properties found are material parameters, as opposed to the aforementioned indices. However, in practice, issues such as sidewall effects influence the measured values, thus resulting in slightly different values depending on the equipment and protocol used.

Though the shear cell is a very fundamental and well-established measurement technique, it is not further considered for this research. The main reason for its exclusion is the need for a relatively high pre-consolidation stress. E.g. shear cell measurements on a commercial Freeman FT4 with 25 mm cell show that the sensitivity of the measurement becomes problematic below 2 kPa. Shear cells with

larger contact areas may enable measurements at lower consolidations stresses. However, as there is almost no consolidation present in the layer deposition process in LS, the relevance of this measurement technique is more limited. The technique may, however, still be useful for the hopper design in some LS machines.

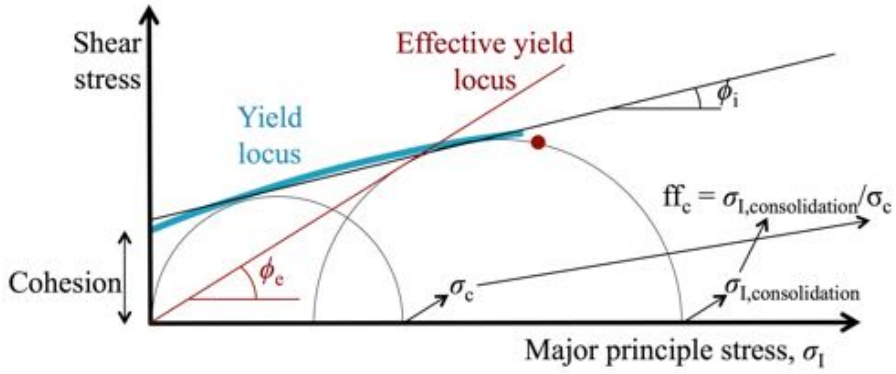


**Figure 2-16:** Illustration of the shear cell indices.

## 2.3.2 Hausner ratio

The Hausner ratio (HR) is the ratio between the (conditioned) bulk density of a powder and the density of the same powder after tapping (Eq. 1.15) [115]. It is often used as a flowability indicator. The reasoning behind this use is the following. As powder is poured into a container, inter-particle forces prevent the powder particles to settle in their densest packing (cf. Figure 2-17). By vibrating or tapping the powder, the inter-particle forces are temporarily overcome, allowing the powder to increase its packing. After a certain time, an equilibrium density is obtained, called the tapped density. The more the powder contracts in this process, the stronger the flow limitations by the inter-particle forces are and thus the poorer the powder flowability [116]. A major drawback of this technique is the strong dependence of both densities on the conditioning protocol and tapping time, frequency and intensity respectively [117,80]. Therefore, Hausner ratio measurements are typically standardised.

$$\mathrm{HR} = \frac{\rho_{\mathrm{b,tapped}}}{\rho_{\mathrm{b,initial}}} \tag{1.15}$$

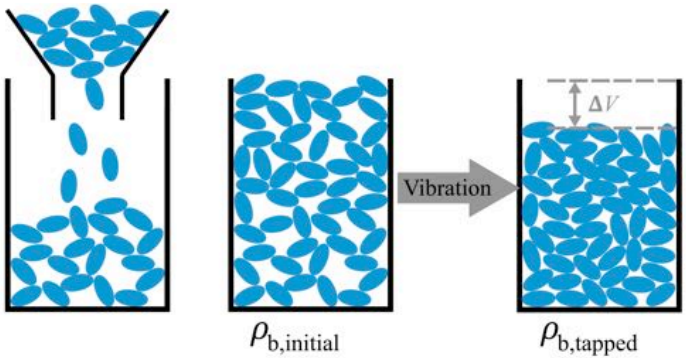


**Figure 2-17:** Schematic illustration of the Hausner ratio principle.

Other indices that describe the same densification by tapping exist. The compressibility, also called the compressibility index (C), is a common alternative to the Hausner ratio, based on the normalised density difference, rather than the ratio (Eq. 1.16a) [109]. As it is based on the same bulk density data as the HR, the two indices are interchangeable (Eq. 1.16b). Ranges for flowability have been proposed in literature (cf. Table 2-2) [118]. These ranges are, however, only indicative due to the aforementioned dependence on the powder conditioning.

$$\mathrm{C} = \frac{\rho_{\mathrm{b,tapped}} - \rho_{\mathrm{b,initial}}}{\rho_{\mathrm{b,tapped}}}\ 100\ \% \tag{1.16a}$$

$$\mathrm{C} = \left(1 - \frac{1}{\mathrm{HR}}\right) 100\ \% \tag{1.16b}$$

**Table 2-2:** Indicative ranges of flowability based on the Hausner ratio or compressibility [118].

| | **HR** [/] | **C** [%] |
|---|---|---|
| **Free flowing** | 1 – 1.25 | 0 – 20 |
| **Decreased flow** | 1.25 – 1.4 | 20 – 29 |
| **Cohesive** | >1.4 | >29 |

Kawakita and Lüdde [119] suggest that Eq. 1.17 provides a useful relation between the compressibility and the amount of applied taps $n$. It shows a simple linear relationship between the inverse of the compressibility and the inverse of the number of taps. The constant $\mathrm{C_h}$ in this equation is related to the cohesiveness of the powder [109]. Another approach is that of Heckel, who proposes an exponential decrease of the change in density as a function of the number of taps (Eq. 1.18). Both equations predict a plateau value of the density or corresponding compressibility at an infinite amount of taps, denoted by the subscript $\infty$ [116].

$$\frac{1}{\mathrm{C}} = \frac{1}{\mathrm{C}_\infty} + \frac{1}{n\ \mathrm{C}_\infty\ \mathrm{C_h}} \tag{1.17}$$

$$\rho_{\mathrm{b}} = \rho_{\mathrm{b}\infty} - \left(\rho_{\mathrm{b}\infty} - \rho_{\mathrm{b,aerated}}\right) e^{-\frac{n}{N_x}} \tag{1.18}$$

Schmid et al. evaluated the HR via a standardised Round Robin test on four LS polyamides. They concluded that the simple HR method was able to correctly distinguish between the different flow behaviour of the examined powders. Furthermore, the ability of a powder to pack densely is directly relevant for LS, as it improves the mechanical properties of the final part [63]. The tapped bulk density found in this simple test, also provides a relevant packing limit for the powder within the layers deposited in LS. The HR is therefore further studied within this

research. Ziegelmeier et al. examined the HR of PA12 2200 and several TPU powders intended for LS. They concluded that the deviations of the HR are significantly higher than those of other valid flow indices, such as the angle of repose and basic flow energy. They, however, also indicate the useful correlation of the HR with the real density of the powder in an LS feeder system [120].

### 2.3.3 Hall Flowmeter

A Hall flowmeter is a device which measures the time needed for a known quantity of powder to flow through a standardised funnel [121]. It is a very common technique in the research of metal powder flowability, including SLM research [122,123,124]. For polymers, however, the device is not commonly used. Their lower weight, compared to metal powders, makes it much more difficult for cohesive polymer powder to generate a flow rate through the funnel. Adaptations to the Hall flow meter exist, such as the GranuFlow (GranuTools). This device uses differently sized orifices instead of a funnel, but the working principle remains similar [125].

Spears et al. indicated that the Hall flowmeter provides a very simple ranking for metal powders, but that this index is not directly relevant for the SLM process [126]. Due to the limited link to the LS process and the difficulty to use this technique for more cohesive polymer powders, this technique was not further examined in this research.

### 2.3.4 Angle of repose (AoR)

The Angle of Repose (AoR) is another common indexer for powder flow. In this test, the angle of inclination of a heap of powder is measured. This angle is called the angle of repose. Higher angles result from stronger inter-particle forces and thus poorer powder flowability. There are two distinct versions of the angle of repose: the static and dynamic angle of repose [127].

**Static angle of repose (SAoR)**
The static angle of repose (SAoR) is the angle of a powder heap at rest. Various methods exist to form the needed powder heap. This text only discusses three non-limiting, but very common methods as an illustration of the principle (cf. Figure 2-18). The simplest way of measuring this angle is by pouring powder through a funnel and measuring the angle of the heap formed below it. This is referred to as the funnel method or poured angle of repose. A downside of this technique is that very cohesive powders show issues with flowing through the funnel, similar to the issues described for the Hall flowmeter [127,128]. Another method is to move a box of powder with a hole in it upwards. In this so-called ejection method or drained angle of repose, the angle of interest is that of the heap remaining inside the box [129,128]. A

third option is to place an amount of powder on a table and tilt this until the powder starts sliding [127]. This method is useful for more cohesive powders that do not flow through the funnel or orifice of the previous two methods.

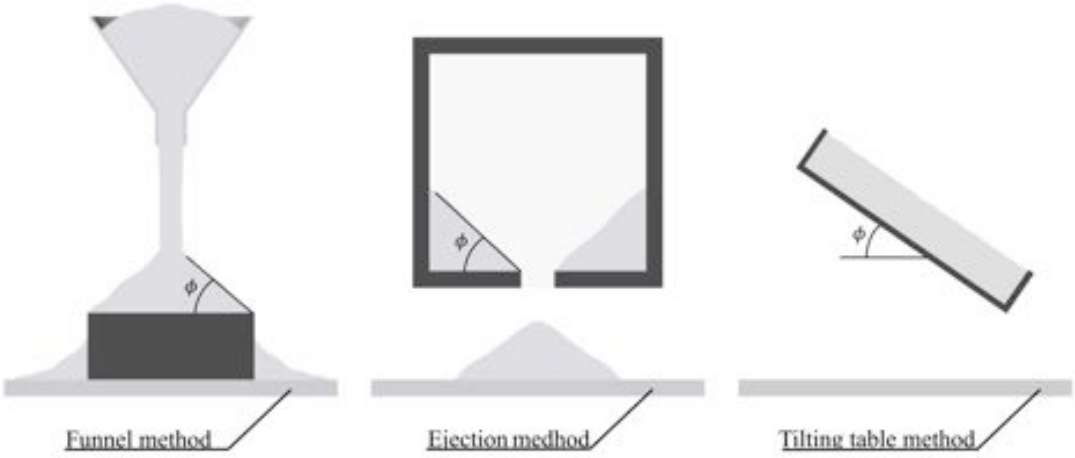


**Figure 2-18:** Different methods to measure the angle of repose.

A strong downside is that the obtained angle intrinsically differs between each of the methods. This makes it more difficult to compare values found in literature [127]. The funnel method, for instance, typically yields lower angles than the ejection method [129]. The difference in angles is possibly the result of the different powder interactions in the three methods. In the funnel method powder particles are poured on the heap. This means the particles are already in motion during the heap formation and the friction is determined by a dynamic friction coefficient. In the tilting table method, on the other hand, the entire powder mass is at rest up until failure. This means that the static friction coefficient is dominant. The ejection method sits somewhat in between these limits, as powder is now flowing away from the remaining powder mass that stays at rest. As typically the static friction coefficient is higher than the dynamic friction coefficient, this may explain the difference in attainable heap angles.

**Dynamic angle of repose (DAoR)**

The dynamic angle of repose (DAoR) is very similar to its static counterpart, with the difference that the powder heap is not at rest, but is continuously agitated. The typical set-up for measuring this index is the rotating drum. In this test, a cylindrical drum filled for 50% with powder is rotated around its own axis. The inclination angle of the powder heap at which the cohesive forces and the forces of gravity are in balance, is called the dynamic angle of repose [130]. To enable registration of the powder angle in time, both sides of the drum are made of transparent material. A backlight, placed on one side of the drum, provides the needed contrast for the camera on the other side (cf. Figure 2-19).




**Figure 2-19:** Schematic illustration of the rotating drum (dynamic angle of repose) set-up.

The flow field in the rotating drum is much more complex than that of the static angle of repose. Henein et al. describe six different flow regimes depending, on the one hand, on the rotational speed, dimensions and roughness of the drum and, on the other hand, on the particle properties (cf. Figure 2-20) [131]. The effect of the rotational speed and drum diameter is captured in the Froude number (Fr), as defined in Eq. 1.19 [18,132]. At low Fr, slipping with the wall dominates. With increasing Fr, the wall pulls up the material before a lump of solids detaches and slides down, resulting in a minimum and maximum for the inclination angle, referred to as the lower and upper angle of repose [131,133]. At higher speeds a continuous rolling motion is seen. Slip now occurs continuously in the top layer of the powder, yielding a rather constant inclination angle [131]. At even higher Fr, the cascading regime starts, in which powder builds up near the apex of the bed before detaching [131]. At even higher Fr, this regime transitions into the cataracting regime, in which powder is thrown due to the inertia. Finally, at extreme rotational speeds the centrifugal force dominates [131].

$$\mathrm{Fr} = \frac{\omega^2 r}{g} \tag{1.19}$$

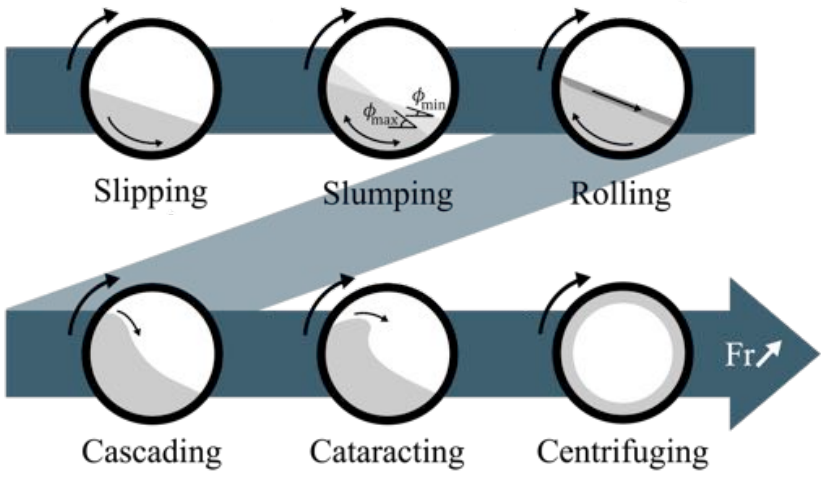


**Figure 2-20:** Flow regimes in the rotating drum (adapted from Henein et al. [131]).

It has to be noted, however, that these regimes are typically only described for grains in the millimetre size range, and, as stated earlier, the regimes are also dependent on the particle properties. As the interaction forces for cohesive micron sized powders are very different, it is possible that not all regimes can be distinguished for cohesive powders. Furthermore, as the interaction forces may differ for powders of unequal size or composition, various powders may exhibit different regimes at the same Froude number. Pirard et al. further showed that the filling degree also influences the transitions between the different regimes for carbon nanotubes [134].

Multiple indices follow from this rotating drum experiment. Firstly, the inclination angles, namely the aforementioned dynamic angle of repose or the lower and upper angle of repose, can be noted [131,133]. The maximum angle attained right before an avalanche, i.e. the upper angle of repose in the slumping regime, is typically called the avalanche angle. It should be noted that all these angles are also a distribution, rather than a constant value [135]. Secondly, the avalanching time is an index for cohesiveness. More cohesive powders have a larger avalanche build-up, thus resulting in a larger time between avalanches. The avalanche time distribution or the slope of the cumulative amount of avalanches in time is therefore sometimes taken as a flowability index. This index is evidently directly dependent on the rotational speed [136]. Thirdly, the roughness of the powder surface provides an indication of the flowability. A surface fractal can quantify this powder surface irregularity. Finally, some more well-flowing powders have a tendency to fluidise at high enough flow rates. The fluidised volume or height in the drum is thus a measure of how well the powder flows [137,22].

Amado et al. suggest that the flow field of the rotating drum measurement is very similar to that found in a counter-rotating roller set-up (cf. Figure 2-21) [137]. In both cases a wall pulls up the powder on one side and a free flow of powder sliding down on the other side. Forsyth et al. further concluded that the found angles increase linearly with inter-particle force, though this linear relation is not feasible when approaching high angles, as the angle cannot exceed 90°, except very locally [84].

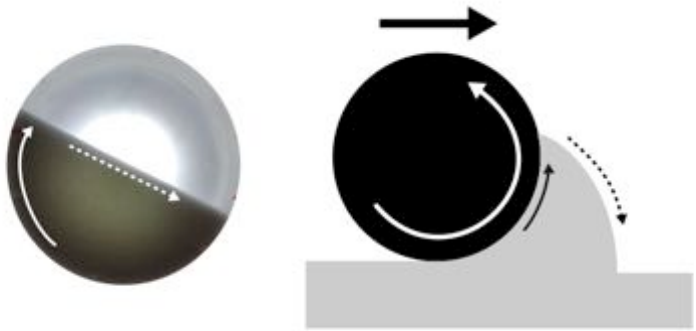

**Figure 2-21:** Comparison of the flow field in the dynamic angle of repose and in front of a roller coater.

Amado et al. have further made an attempt to modify the rotating drum set-up to include temperature control. They concluded that there is a powder dependent effect of temperature on flowability, which can be either positive or negative. The glass transition temperature is a distinct transition point for these changes in flowability [135]. At this time, however, there are no commercial devices including temperature control. More research is thus needed to assess the effect of temperature on the measured angles for different types of materials.

### 2.3.5 Powder rheometer

Similar to liquid rheometers, powder rheometers are gaining interest for the evaluation of powder flow properties. The application of powder rheometry is possible as an add-on cell for liquid rheometers, such as the powder cell of Anton Paar [138]. However, powder specific devices also exist, such as the Freeman powder rheometer [139]. Multiple types of tests exist on commercial powder rheometers. These tests range over the entire stress range, going from fluidised to highly compressed systems (cf. Figure 2-13). The next few paragraphs discuss the most common tests per regime.

**Consolidated measurements**
Rheometers are able to perform measurements on the consolidated side of the stress spectrum. Three of the most common tests on this side of the spectrum are compressibility, permeability and shear tests. Besides these tests, stickiness measurements are also possible on a rheometer. This section describes each of these four tests more in detail.

Compressibility tests measure the densification upon applying stress. This is not directly a flowability measurement, but the densification has a direct impact on inter-particle contact and thus flowability. Powder is loaded into a cup, after which an air permeable piston compresses it and the volume contraction is noted. Prior to this test a certain conditioning is applied by stirring the powder with a blade, thus also this conditioned bulk density could be used as a flowability indicator, similar to the Hausner ratio. Literature suggests many empirical fitting functions for this correlation, as illustrated in Eq. 1.20a-c, in which $b_i$ represent empirical fitting parameters [140].

$$\rho_b = \rho_{b0} + b_1 \sigma_I^{b_2} \tag{1.20a}$$

$$\rho_b = \rho_{b0}\, e^{b_1 \sigma_I^{b_2}} \tag{1.20b}$$

$$\rho_b = \rho_{b0}(1 + b_1 \sigma_I)^{b_2} \tag{1.20c}$$

Permeability measurements assess the resistance for air to flow through a powder column at various consolidation stresses. This is a relevant measurement for flow, as airflow rates in dense powder flow, such as hoppers, often form a limit for the powder mass flow. The reason for this is the need for powders to dilate upon shearing (cf. Figure 2-22). In dense systems, air availability often becomes problematic [141].

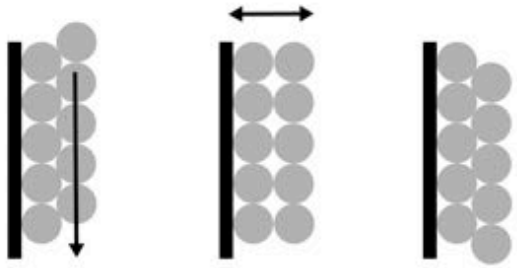

**Figure 2-22:** Illustration of powder dilation.

Finally, due to the ability of rheometers to apply deformation and measure stresses (or vice versa), all shear cell measurements are possible on a powder rheometer, provided the correct tools and protocols are available. The working principles of these types of measurements are identical to those described in Section 2.3.1.

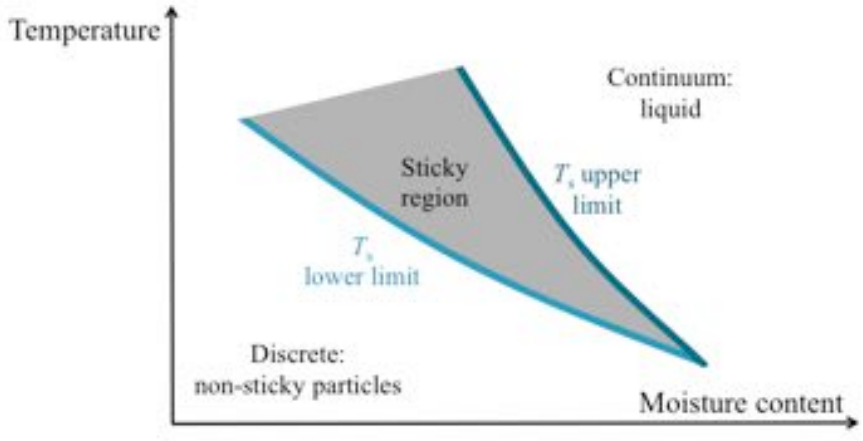


**Figure 2-23:** Illustration of the sticky region and sticky point temperature for tomato powder (adapted from Bhadra et al. [142]).

Another type of consolidated measurement performed on rheometers is the so-called stickiness measurement. This measurement, which is typically applied to food powders, is used to study caking phenomena due to moisture or elevated temperature [142]. In this technique, developed by Lazar et al. in the 1950's, a multi-bladed vane tool is pushed into a sample cup. The propeller then rotates a quarter turn at the time and the needed torque or motor voltage is registered. The sample cup is then heated and the experiment repeats until a discrete jump in the torque is seen. The temperature at which this jump occurs is called the sticky point temperature $T_s$,

which has been shown to correlate with the glass transition temperature of the powder [142,143,144,145]. The sticky point temperature for typical food powders, however, appears to be higher than the actual glass transition temperature [146]. The sticky point temperature is typically dependant on the moisture content, resulting in a sticky region in the temperature-moisture space (cf. Figure 2-23) [142]. This measurement can thus be seen as a strain-controlled variant of a yield stress measurement in liquid rheology.

The consolidated state tests could be relevant for laser sintering in two ways. Firstly, these measurements aid in the hopper design for the feeder systems of EOS machines. Secondly, compressibility knowledge is directly relevant to study the caking phenomena in the deposited powder bed. Stickiness measurements are potentially useful for gaining additional insights into caking of the powder bed in a sintering device. The effect of moisture content may be less pronounced for LS powders, as polymers tend to take up a lot less moisture than food powders. The effect of moisture on caking is also known to be much stronger for amorphous powders [145]. Furthermore, in an LS machine, most sintering powders are exposed to high temperatures, at which moisture has already evaporated.

**Free flowing tests**

At lower stress states, the measurements enter the free-flowing regime. In this regime, the basic principles remain the same as for liquid systems. A certain deformation is applied, at which the needed torques and forces are measured, or vice versa. Higher torques and forces mean a stronger resistance to the applied deformation and thus poorer flowabililty. There is, however, a strong difference between liquid and powder rheometry. In liquid rheometers geometries are chosen to obtain a simple flow field for which the deformation at every point is known, and thus also the resulting stress in each point can be computed. For powder systems this is not the case, as the flow and stress fields are typically unknown and not uniform. As a result, the relation between stress and strain fields is undetermined and it is impossible to obtain intrinsic material parameters, such as a viscosity. In this regime, powder rheometers also become indexers.

The simple free flow experiment is to rotate a propeller in a sample filled cup and measure the resulting torque. This, however, yields a problem, as cohesive powders will form bridges, thus resulting in a torque drop. A solution is to use the principle of Freeman, in which a propeller rotates while moving up or down through a powder sample, thus following a helicoidal path (cf. Figure 2-24). The resulting index of this measurement is called the flow energy, which is the total amount of work performed by the propeller moving through the entire powder mass (Eq. 1.21) [139]. This work is split up into a torque ($M$) component and a normal force ($F_{\mathrm{N}}$) component. Their relative contributions are dependent on the angle of the helicoidal propeller path, which is defined by the axial and rotational velocity, $v$ and $\omega$.The derivative with

the propeller height, i.e. the instantaneous work, is called the energy gradient (EG). It is evident that this is an index, as the amount of work is dependent on the propeller path and the propeller geometry.

$$E_{\text{flow}} = \int \text{EG}\, \mathrm{d}z \tag{1.21a}$$

$$\text{EG} = \frac{\omega}{v} M(z) + F_{\text{N}}(z) \tag{1.21b}$$

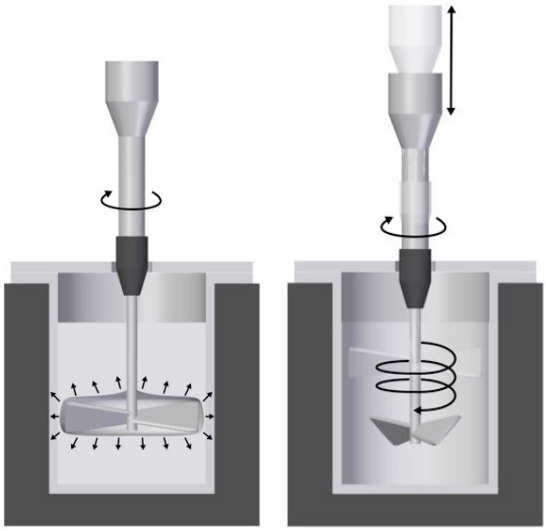

**Figure 2-24:** Illustration of bridging in a powder rheometer and the solution by applying a helicoidal propeller path.

Variations on the aforementioned test exist. These include the use of either the upward or downward path. Another adaptation is the so-called stability test. In this test the helicoidal motion is repeated multiple times. A change in the resulting flow energy is then usually the result of triboelectrification, making this a useful technique to assess the charging of powders.

For the layer deposition in LS, this regime of measurements is deemed the most interesting. However, as all results obtained here are indices, rather than material parameters, care needs to be taken in their interpretation. As the flow fields of spreading layers is vastly different than that of a propeller moving through a cup of powder, the direct relevance for LS needs to be further investigated. This thesis therefore presents research on an adapted liquid rheometer to include these free flow measurements at elevated temperatures.

**Fluidisation tests**

Tests in the fluidisation regime are only possible on rheometers with an aeration unit, which blows a gas through the base of the powder filled cup. Different indices can then be obtained, such as the gas velocity or pressure needed for fluidisation or the expansion of the powder bed upon fluidisation, i.e. the bed expansion ratio

(BER) [147]. Some tests also exist where after fluidisation the resistance or apparent viscosity of the fluidised powder is measured by an impeller [148]. Fluidisation tests are not further discussed, as the fluidisation regime is the least relevant for LS.

### 2.3.6 Other techniques

Besides the aforementioned techniques, some lesser-known techniques for measuring powder flowability exist, either directly or via cohesive forces. This section provides a non-limiting list of a few techniques that provide different insights, compared to the previous tests.

A powder tensile strength tester measures the force needed to separate two powder layers. This force is the result of the cohesiveness between the particles. In practice this measurement is performed by adhering a layer of powder to a surface, which is hung from a load cell. The particle-coated surface is then pushed onto the surface of the powder bed of the same material. The load cell then measures the force needed to separate the two elements again [149]. This resembles the pull-off force measurement in an atomic force microscope (AFM) measurement, in which the force to separate two particles is measured [150]. AFM, however, has strong reproducibility issues for irregular particles, as the shape at the inter-particle contact strongly influences the results. By looking at an entire powder layer, rather than individual particles, this issue is averaged out for the powder bulk.

Zafar et al. evaluated the drop test method for assessing the adhesion properties of particles. In this set-up particles are dispersed on a glass stub, which is hung in a tube. The stub is then dropped. The fall is halted by a stopper, which does not touch the glass surface. Upon the sudden deceleration, the particles feel a tensile force and some will disconnect from the glass surface. An optical microscope records the particles before and after the drop, thus noting the detachment [103]. The principle, working with the tensile properties of powders, is thus similar to the powder tensile tester, but the focus is on adhesion to walls, rather than inter-particle cohesion.

In 2017, HP released their Material Development Kit (MDK), which assesses the spreadability of powders for AM powder bed applications (cf. Figure 2-25). The kit is primarily intended for HP's Multi Jet Fusion, but it is also applicable for LS. In the test, a counter-rotating roller spreads a fixed amount of powder on a heated metal plate. A layer thickness between 0.1 mm and 1 mm is achievable [151]. The deposited layer is then assessed for defects. Limitations of the kit include the qualitative nature of the layer assessment, as well as the limitation of only spreading one layer of powder onto a metal plate. This hinders the study of powder-on-powder deposition, which is more relevant for both the LS and Multi Jet Fusion processes. The commercialisation of the MDK, however, further illustrates the industrial need

to evaluate powders in flow fields specific to the application on the one hand and the importance of temperature on the spreadability of powders on the other hand. In the course of this PhD, a similar set-up with a blade instead of a counter-rotating roller is developed. This newly developed set-up, which quantitatively studies powder-on-powder deposition, is further discussed in Chapter 2.

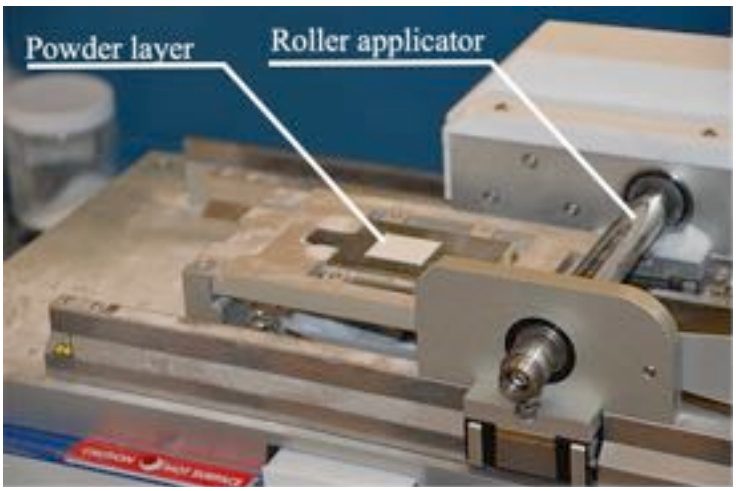


**Figure 2-25:** HP material development kit (MDK) spreader tester (adapted from Molitch-Hou [151]).

### 2.3.7 Comparison of the techniques

The multitude of the tests available, result in even more indices to compare. Table 2-3summarises the indices of the discussed measurement techniques. Care needs to be taken when selecting a technique for a specific application, as inconsistencies in the different rankings of the different indices form issues. Not only do different tests provide different rankings, also the pre-conditioning of the powders within the test strongly influences the results [147].

Krantz et al. compared the static angle of repose, avalanche angle, BER and cohesion for various polyester-epoxy and polyurethane powders with a $D_{50}$ between 20 µm and 30 µm. Similar techniques, such as the static angle of repose and the avalanche angle, form a good correlation for all powders, though both angles differ. Techniques at different stress states, such as the angle of repose, cohesion and BER are not interchangeable and may even provide contradicting rankings. However, they all indicate the same trends with particle size, i.e. poorer flowability for smaller particles. The resulting conclusion is that the applied stress field should match the application as close as possible to provide interpretable results and that for powder undergoing multiple flow operations multiple tests may be required [147].

**Table 2-3:** Summary of flowability indices of methods discussed in this thesis.

| Technique | Index | Available standardisation |
|---|---|---|
| **Shear cell** | Angle of internal friction [114]<br>Wall friction angle [114]<br>Cohesion [114]<br>Unconfined yield strength [112]<br>Flow function [112,114] | ASTM D6773 [137] |
| **Tapping test** | HR or compressibility [115]<br>Tapped bulk density [115] | ASTM D7481 [137] |
| **Hall flowmeter** | Flow time [121] (metals) | ASTM B213-3 [121,123] |
| **AoR/Rotating drum** | Static angle of repose [127]<br>Avalanche angle [137]<br>Average angle<br>Volume expansion ratio [152,137]<br>Surface fractal [137]<br>Angle variation<br>Upper and lower AoR [133]<br>Fluidised volume height [137]<br>Fluidised volume slope [137]<br>Final settling time [137]<br>Avalanching time [136] | DIN ISO 4324 [137] |
| **Powder rheometer** | Conditioned bulk density<br>Flow energy [139]<br>Specific energy<br>Stability index<br>Permeability [140]<br>Fluidisation energy [148]<br>Apparent powder "viscositity" [148]<br>Bed expansion ratio [147] | |
| **Tensile tester** | Powder tensile strength [149] | |

Grey and Beddow describe a relation between the Hausner ratio on the one hand and the static angle of repose and the maximum and minimum angles in a rotating drum measurement on the other hand. However, they indicate that even for their limited set of copper samples, exceptions were seen [115]. Geldart et al. further describe a positive linear correlation between the static angle of repose, measured in their proprietary set-up, and the Hausner ratio [153]. However, they only demonstrated this

for a variation in PSD for one material class, rather than for strongly differing powders. As indicated by Krantz et al. similar trends with only varying particle size are expected [147].

Leturia et al. further demonstrate the need for multiple characterisation methods to fully understand the flow properties of a powder. They also indicate how the difference of the stress condition, especially between the compacted, free-flowing and aerated states yields completely different flow properties [109]. Lumay et al. propose the same reasoning regarding the difference between the (quasi-)static conditions or dynamic conditions, i.e. free-flowing [80].

Tay et al. looked at the correlation between the different indices for different lactose samples of which particle size and shape were noted. Principle component analysis (PCA) split the evaluated indices into two groups. On the one hand a correlation was seen between the density measurements, flow energy curvature of avalanches and the flow function. On the other hand, a second group of somewhat correlated indices was noted, namely the angle of repose, Hausner ratio, avalanche time, angle of internal friction and cohesion [154].

In conclusion, while many techniques could be used for a first quick screening of trends in e.g. particle size, not all techniques provide a relevant ranking for the envisioned application. The next section further evaluates the examined techniques with respect to LS and makes a selection to further evaluate in this thesis.

### 2.3.8 Selection of techniques for LS

Based on the technique descriptions of the previous sections three techniques are chosen to use for the powder flow evaluation in LS. This choice is based on the relevance of the flow and stress fields on the one hand and the known correlations to LS found in literature. The chosen techniques are the dynamic angle of repose, the Hausner ratio and the powder rheometer.

The dynamic angle of repose is chosen for three main reasons. Firstly, it is a simple to use technique, meaning it can provide quick insights early on in the powder development. As the volume of the drum can easily be adjusted, this enables the study of powder flow in early stage powder development, when material may still be scarce. Secondly, it is a well-known technique in LS research. As a result, a good comparison to literature can be made. As proven by Amado [137], it is directly relevant for the flow field in the spreading step of the LS process. Finally, as the sample container in this test is closed, it enables the measurement of pre-conditioned powder to evaluate effects of humidity. Section 3.3 further shows how this technique is implemented in the LS screening methodology.

The Hausner ratio is chosen because it is a technique based on powder density. As shown by Ziegelmeier [60], the density of the powder bed has a direct influence on the final part density and resulting properties. Furthermore, this is a well-standardised technique, making comparison to earlier studies simpler. A commercial set-up is further applied to the powders of Chapters 4 and 5.

Powder rheometry is chosen for its versatility. The free-flowing regime is deemed the most interesting for LS, but the relevance of the suggested indices needs to be assessed. On the other hand, the concept of the stickiness measurement is interesting for both caking phenomena in the powder bed and stickiness issues upon spreading the powder. Section 3.4 therefore introduces an adaptation on a liquid rheometer that incorporates the stickiness concept to the free flowing regime.

Finally, as none of the aforementioned techniques have a specific focus on the LS spreading mechanism, a new technique is developed in Chapter 3. Section 3.5 introduces this spreading-based measurement and proves the necessity for mimicking the industrial flow field in the screening methodology.

## 2.4 Conclusions

This chapter provided some basic insights in the LS process to aid in the material selection. Four main steps within the sintering process were identified, namely powder spreading, coalescence, solidification and evaluation of the resulting product or unsintered powder. A focus lies on the powder flowability step, for which the basic principles, as well as some typical measurement techniques were researched. Based on the literature study, four powder flowability set-ups were selected to further assess flow in the LS process. These are the Hausner ratio, the dynamic angle of repose, the powder rheometer and an in-house build spreading device.

# Chapter 3

# Development of powder flow characterisation techniques

This chapter discusses three techniques that were developed in this PhD work for the study of powder flowability, with a focus on laser sintering (LS). The first set-up is the dynamic angle of repose, which is useful for a quick first screening of the powder. This set-up is further expanded to include temperature control. Next, a liquid rheometer is adapted to enable the measurement of powders. This set-up mainly serves to check for temperature effects of the flowability. The final set-up is the powder spreader. This set-up mimics the flow field of a sintering machine as close as possible, in order to get the most directly relevant results for the application. The results of this set-up are used to validate the applicability of the other two set-ups for LS.

Section 3.1 first describes all auxiliary methods used to evaluate the powders of this chapter, such as particle size analysis and differential scanning calorimetry (DSC). Section 3.2 then introduces some reference powders, including laser sintering polyamides (PA) and ideal spherical reference systems, which are used to evaluate the flowability measurements proposed in this chapter. Finally, Sections 3.3–3.5 discuss the three powder flowability set-ups and apply them to the references.

## 3.1 Methods for assessing LS applicability

A good LS powder needs to fulfil many requirements, as discussed in Chapter 1. Figure 3-1 summarises the techniques that are used to assess the sinterability criteria that are listed in Section 2.1.3. As all powders in this chapter are either already

available as commercial sintering powders or are solely intended as a flowability reference, not all techniques shown in Figure 3-1 are discussed for these powders. A brief screening on the thermal windows for the LS process is performed by DSC, TGA and melt rheology. The other techniques from this summary are further discussed in the following chapters when they are applied to new sintering powders. This chapter puts a focus on the dynamic angle of repose (DAoR), powder rheometer and powder spreader set-ups which were developed in the course of this research. Besides the actual flowability measurements, PSD, moisture and charge analysis are used to gain more insights in the observed flow phenomena. The thermal window of the powder bed, obtained via DSC, is further utilised to determine relevant testing temperatures for the powder flowability measurements at elevated temperatures.

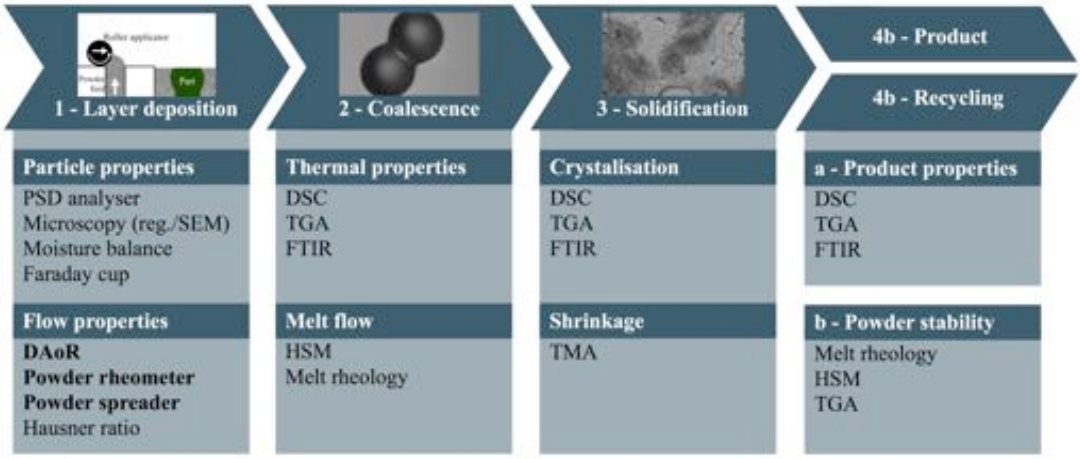


**Figure 3-1:** Summary of techniques used to assess the LS applicability of powders.

### 3.1.1 PSD analysis

Particle size analysis is performed by an external partner. A QICPIC Particle Size Analyser (Sympatec GmbH) with a RODOS/L dispersion unit is used. This device uses optical images to determine the particle diameter. As discussed in Section 2.2.2, multiple definitions of a particle diameter exist for irregular particles. Furthermore, the limitation of only seeing two dimensions also means an assumption needs to be made on the third dimension. The software approximates the particle volume by taking a cylinder with length $l_{i,\max}$ and diameter $l_{i,\min}$. Eq. 2.1 then provides the diameter of a sphere with the same volume as the cylinder.

$$d_i = \sqrt[3]{\frac{3}{2} l_{i,\min}^2 l_{i,\max}} \tag{2.1}$$

$l_{i,\max}$ and $l_{i,\min}$ are the longest and shortest dimension of the 2D projection, respectively. Again, multiple definitions of these dimensions exist. Examples are the

discussed minimal and maximal Ferret or Martin diameters. The QICPIC software, however, utilises the longest connected length for the skeletonisation of the particle as $l_{i,\max}$. $l_{i,\min}$ then follows as the ratio of the projected area of the particle to $l_{i,\max}$. As different skeletonisation algorithms may provide slightly different values for $l_{i,\max}$, the final diameter is dependent on the algorithm of Sympatec GmbH. Figure 3-2 provides a visualisation of skeletonisation for a spherical and potato shaped particle. In the case of the spherical particle, the diameter computed by Eq. 2.1 is the real particle diameter. An advantage of this skeletonisation approach is that it is straightforward to incorporate rod- or fibre-like particles, as further discussed in Chapter 4. After applying the algorithm to all particles, the software generates a number based PSD.




**Figure 3-2:** Theoretical visualisation of skeletonisation performed on a spherical (e.g. PS Dynoseeds, PMMA Spheromers CA) and potato-shaped (e.g. PA 2200) particle.

### 3.1.2 Thermogravimetric Analysis (TGA)

Thermogravimetric analysis (TGA) is applied to indicate the stable sintering region. The measurements are performed on a Q500 TGA (TA Instruments), following a standardised protocol. Around 10 mg of sample is loaded onto an aluminium pan and placed in the TGA oven. The sample is then heated to 550 °C at a rate of 10 °C/min under a nitrogen atmosphere. As discussed in Chapter 1, the degradation onset should be well-above the melting peak, thereby defining the stable sintering region. Samples were not pre-dried due to the fast and uncontrollable uptake of moisture by the small sample volume during the loading of the TGA. Weight losses <1% below 100 °C are therefore attributed to moisture evaporation and are excluded from the 1% weight loss limit to determine the stable sintering region, as discussed in Section 2.1.3.

### 3.1.3 Differential Scanning Calorimetry (DSC)

Differential scanning calorimetry (DSC) measurements indicate the available thermal window for the powder bed. The used device is a Q2000 DSC (TA Intstruments), which is operated with the following protocol. First, a sample mass of

7±0.5 mg is loaded into an aluminium pan, with is sealed by a non-hermetic lid. The sample is then equilibrated for 5 minutes at the lowest temperature of interest. Next, the powder is heated at 10 °C/min until the fully molten state is reached. The setpoint for this final temperature is limited by the degradation onset found in the TGA measurements. This final temperature is maintained for 5 minutes. Finally, the powder is again cooled to the starting temperature at a rate of -10 °C/min. The found thermal window for the powder bed, as defined in Section 1.1.3 provided a good indication on the ease of process control in sintering, as well as an indication of the temperatures of interest for the assessment of powder flowability.

### 3.1.4 Melt Rheology

Melt rheology measurements assess the coalescence behaviour of the powders. An ARES strain-controlled rheometer (TA Instruments) with 25 mm steel plates determines the viscosity of the sample in the fully molten state. The device is used in steady shear mode at low shear rates to mimic the coalescence of particles under no external shear. Steady measurements are preferable, as the long measurement time needed for oscillatory measurements at low frequencies may degrade some samples. First, a ratesweep is performed just above the melting temperature to determine the plateau value of the viscosity at low shear rates. This plateau value is referred to as the zero-shear viscosity. Based on this measurement, a shear rate well below the onset of shear thinning is chosen to allow for slight variation of this plateau within the temperature range of the following measurements. The shear rate, however, needs to be sufficiently high to register torque values above the sensitivity limit of the rheometer. Next, steady shear measurements at this chosen shear rate are performed at various temperatures. Prior to each individual measurement, the sample is heated at least 10 °C above the end of the melting peak to erase the thermal history of the sample and ensure no crystals are present in the sample. In the case of materials that exihibit a time dependent viscosity, e.g. due to degradation during the measurement, a new sample is taken for each test. Hot Stage Microscopy (HSM) measurements are used to further link this viscosity to actual coalescence behaviour. Those measurements are further discussed in Chapter 3.

### 3.1.5 Moisture determination

Thermogravimetrical measurements on an HX204 moisture balance (Mettler Toledo) determine the moisture content of each powder. The working principle of this moisture balance is similar to a TGA, but a larger bulk of powder can be loaded quickly. As a result the moisture loss or uptake during loading is minimised. The set-up consists of a weighing chamber, which is heated by a halogen ring shaped radiator. A disposable aluminium tray is placed directly below this radiator and is

dried by pre-heating at 100 °C for 15 minutes. A powder sample of 10±0.5 g is then spread evenly over the tray and subsequently undergoes a pre-defined heating protocol. During the entire heating protocol, the sample mass is monitored. To avoid thermal overshoot, which may melt the top layer of the powder and hinder moisture from escaping the rest of the sample bulk, a gentle heating protocol is performed. First the powder is heated 30 °C below the melting onset temperature for semi-crystalline polymers or the glass transition temperature for amorphous polymers. After an equilibration of 5 minutes, the temperature is raised 20 °C. The device then maintains this temperature until the mass decrease over 140 s is less than 1 mg.

## 3.2 Reference materials

Two sets of reference materials are chosen to assess the applicability of the powder flowability measurements developed in this research. The first set consists of laser sintering polyamide (PA) grades, as these currently dominate the LS material palette. The set of sintering PA provides a benchmark for the type of flow that is adequate for LS, as the grades in this set have proven to be industrially usable. These results will therefore be further utilised in Chapters 3 and 4. The second set of materials contains relatively monodisperse, spherical powders of various sizes. These powders are idealised systems, which enable the evaluation of the influence of particle size on the proposed flow measurements. Furthermore, as most of the powders in this set show rather high flowability, they pose an idealised limit to which to compare the other powders. Two different materials are evaluated within this set, namely polystyrene (PS) and polymethylmethacrylate (PMMA).

**Table 3-1:** Physical properties of the different materials used in this chapter.

| Sample | $\rho_m$ [kg/m$^3$] | $A_h$ [J/10$^{20}$] |
|---|---|---|
| **PA 12 2200** | 1.07±0.001 | 7.9 [87] |
| **PA 12 Orgasol** | 1.02±0.001 | 7.9 [87] |
| **PA 12 Vestosint** | 1.02* | 7.9 [87] |
| **PA 11 Rilsan** | 1.08±0.003 | 7.9 [87] |
| **PA 6 Sinterline** | 1.18±0.001 | 7.9 [87] |
| **PS Dynoseeds** | 1.05±0.002 | 9.4 [87] |
| **PMMA Spheromers** | 1.18±0.002 | 6.3 [155] |

*data from manufacturer

The physical properties of interest of the base polymer grades are listed in Table 3-1. The complete list of powders used in this chapter, as well as their particle properties, is shown in Table 3-2. Most powders have Bond numbers around or above unity. As

a result these systems, including commercial sintering PA powders, are in a regime that is strongly affected by Van der Waals interactions. The material density $\rho_m$ is determined through Archimedes' method (ISO 1183-1). The values of the Hamaker constant, $A_h$, are approximated from literature on similar materials. As a result, the computed Bond numbers are only indicative.

**Table 3-2:** Particle properties of the different samples used in this chapter.

| Sample | $D_{10}$ [µm] | $D_{50}$ [µm] | $D_{90}$ [µm] | relative span [/] | $\Psi$ [/] | Bo [/] |
|---|---|---|---|---|---|---|
| **PA 2200** | 39.5 | 63.4 | 82.2 | 0.67 | 0.86 | 1.49 |
| **PA Orgasol** | 31.9 | 42.3 | 56.5 | 0.58 | 0.87 | 3.28 |
| **PA Vestosint** | 38.6 | 55.4 | 79.4 | 0.74 | 0.87 | 1.81 |
| **PA Rilsan** | 20.6 | 44.2 | 80.1 | 1.35 | 0.86 | 2.89 |
| **PA Sinterline** | 26.9 | 57.9 | 107.2 | 1.39 | 0.79 | 1.51 |
| **PS 20 µm** | 12.0 | 23.4 | 37.3 | 1.08 | 1.00 | 12.85 |
| **PS 40 µm** | 36.2 | 47.6 | 58.9 | 0.48 | 1.00 | 3.06 |
| **PS 80 µm** | 64.0 | 88.2 | 105.4 | 0.47 | 1.00 | 0.95 |
| **PS 140 µm** | 118.8 | 145.3 | 176.0 | 0.39 | 1.00 | 0.33 |
| **PMMA 20 µm** | 19.2* | 19.6* | 20.0* | 0.04* | 1.00 | 11.27 |
| **PMMA 30 µm** | 28.6* | 29.1* | 29.6* | 0.03* | 1.00 | 5.11 |
| **PMMA 40 µm** | 39.9* | 40.8* | 41.7* | 0.04* | 1.00 | 2.60 |
| **PMMA 60 µm** | 58.6* | 59.7* | 60.7* | 0.03* | 1.00 | 1.21 |

*data from manufacturer

### 3.2.1 Polyamide (PA)

The set of reference sintering polyamides (PA) focuses on Polyamide 12 2200, which is further abbreviated as PA 2200. This specific powder is the reference sintering PA of EOS GmbH. The commercial powder consists of relatively smooth, often potato shaped particles (cf. Figure 3-3) and an undisclosed amount of micron-sized flow improvers, as illustrated in Figure 3-4. HSM measurements on virgin PA 2200 samples, i.e. samples that have not been recycled yet, show that these flow improvers are not evenly distributed over all particles. The melt pools of some PA 2200 particles show large amounts of smaller unmelted particles, while others have none. The measured sample has an average particle size of 63.4 µm. The other size and shape characteristics are found in Table 3-2.

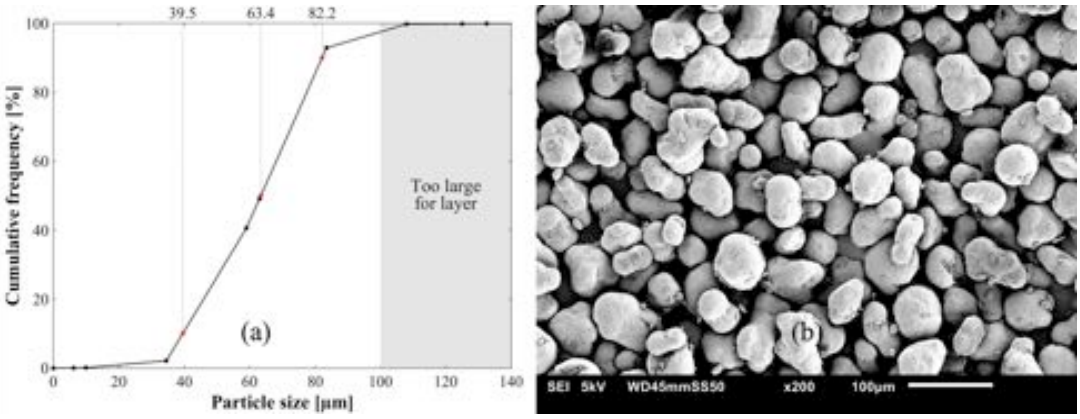


**Figure 3-3:** PSD (a) and SEM image (b) of a typical PA 2200 sample.

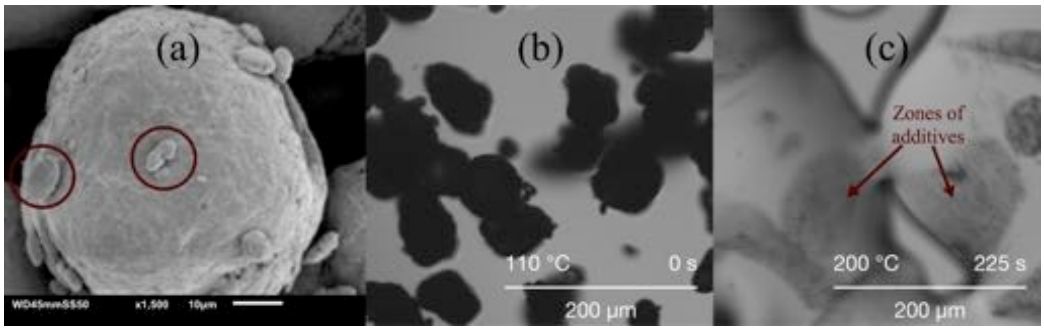


**Figure 3-4:** SEM image (a) of a PA 2200 particle with micron-sized particles adhered to the surface. Hot stage optical microscopy of PA 2200 particles before (b) and after melting (c).

To provide a larger frame of comparison, four other PA powders are tested, namely PA12 Vestosint 2157 (Evonik Industries AG) and Orgasol (Arkema), PA11 Rilsan (Arkema) and PA6 Sinerline (Solvay). These powders have varying particle size and morphology, as shown in Figure 3-5. The Vestosint and Orgasol samples are similar to PA 2200. They are both quite smooth powders with a relatively regular shape. The Vestosint powder closely resembles PA 2200 in terms of particle shape, most likely as a result from the similar production route [5,156]. The Orgasol sample is made in a different production route, which results in much rounder and significantly smaller particles [5,157]. This smaller particle size translates to a much higher Bond number (3.28), which indicates more difficult powder flow. The Rilsan and Sinterline powders, on the other hand, show a more irregular particle shape and a larger PSD span. For the Sinterline powders, the $D_{90}$ is larger than the layer thickness of 100 µm that is used in this work. This is expected to influence the deposition of the particles significantly. Besides a difference in particle size, these commercial PA powders contain various and undisclosed amounts additives. The Rilsan sample contains carbon black particles, which do not only affect laser absorption and thermal conductivity of the powder bed, but also powder flowability. Furthermore, titanium dioxide is often added to commercial PA powders to avoid

yellowing upon sintering [158]. All these powders are already available as commercial sintering powders and their sinterability was already assessed in prior research [5]. Therefore, only their flowability properties are discussed in this work.

Based on the results of Thio et al. the Hamaker constant of all PA samples is approximated by $7.9\ 10^{-20}$ J [87]. Berretta et al. computed a Hamaker constant of $7.65\ 10^{-20}$ J [50]. There is thus a slight uncertainty on the Hamaker constant, depending on the computation or measurement method, but the results should be in the same order of magnitude. A difference between the different grades is also expected. However, due to the irregular particle size and the varying amounts of additives, it is only possible to give an indicative Bond number. The error made by approximating the Hamaker constant is therefore deemed less significant to this research. A difference in material density is also seen, as shown in Table 3-1. Vestosint and Orgasol are the lightest materials at 1.02 g/cm$^3$. PA 2200 and Rilsan are slightly heavier with densities of 1.07 and 1.08 g/cm$^3$ respectively. Finally, Sinterline has a material density of 1.18 g/cm$^3$.

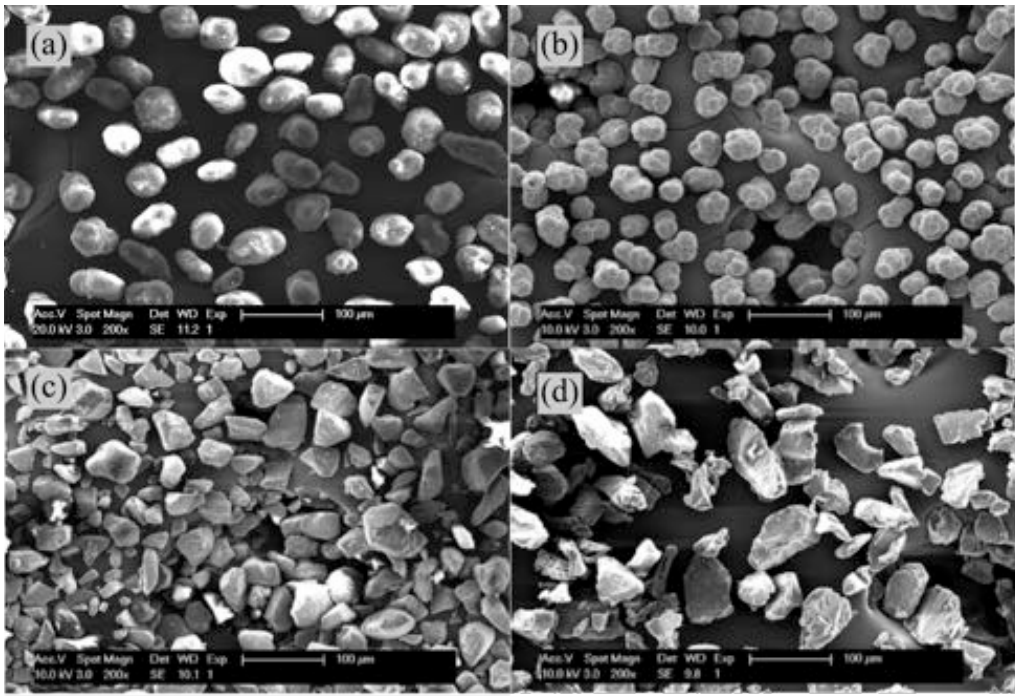


**Figure 3-5:** SEM images of PA12 Vestosint (a) and Orgasol (b), PA11 Rilsan (c) and PA6 Sinterline (d) [5].

### 3.2.2 Polystyrene spheres (PS)

Polystyrene (PS) spheres with a relatively narrow, monodisperse particle size distribution are examined as one of the two spherical reference systems. The used spheres are Dynoseeds TS (Microbeads), which have target particle sizes of 20, 40,

80 and 140 µm. These powders are not commercially used for sintering applications, but form an idealised reference for powder flow measurements. However, Strobbe et al. have performed sintering tests on these powders [159]. Figure 3-6 shows the measured PSD as well as SEM images of the different samples. While the samples are monodisperse, it is seen that there is still quite some variation notable in the particle size. These systems are pure PS and do not contain any flow improvers or other additives.

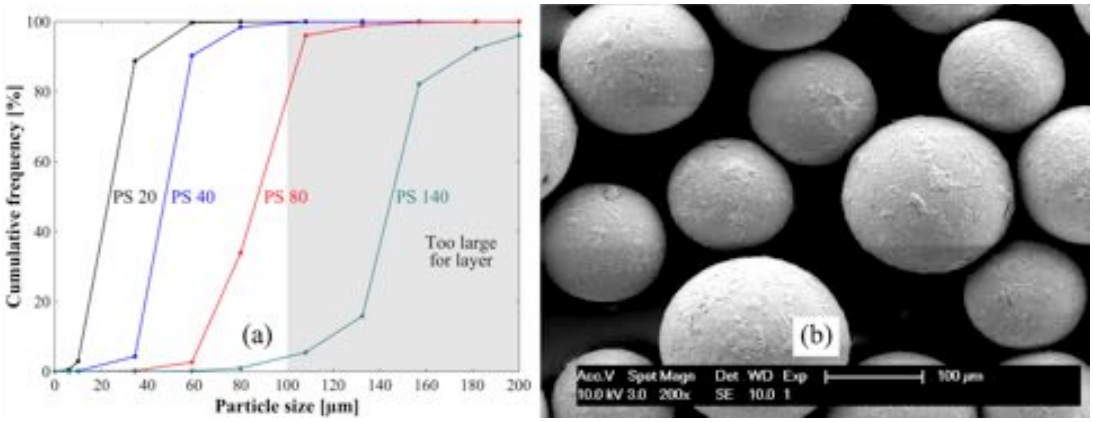


**Figure 3-6:** PSD of all PS samples (a) and SEM image of PS 140 µm(b).

Thio et al. provide a Hamaker constant of $9.4\ 10^{-20}$ J for PS [87]. This is again an approximation for this particular grade. However, as all PS systems are made from the same base material and are perfectly spherical, the Bond number provides a good flow indication between the different sizes. No density difference is noted between the different samples, which al have a density of 1.05 g/cm$^3$ (cf. Table 3-1).

PS Dynoseeds is currently not used as an LS powder. Therefore, the applicability of this particular powder is further evaluated in addition to its use as a flow reference. Figure 3-7 shows the thermal processing windows obtained via DSC, TGA and melt rheology. As PS is an amorphous polymer, no crystallisation and associated shrinkage is present. As a result, DSC measurements do not indicate a lower limit for the thermal window of the powder bed. At around 100 °C the grade passes its glass transition temperature, marking the upper limit of the thermal window of the powder bed. As there are no crystals present to keep the polymer solidified, the particles start coalescing at this temperature. Rheological measurements, however, show that the viscosity at this point is still extremely high (above 10 000 Pa s), resulting in the powder forming a sticky mass. This high viscosity thus determines the lower limit for the stable sintering region. At around 186 °C the viscosity reaches the 1000 Pa s limit for adequate coalescence. As a result, the laser power needs to bridge a large temperature gap, which hinders sinterability. The 1%-degradation limit is found at 269 °C. Strobbe et al. researched the sinterability of the

40 µm PS Dynoseeds powder. They concluded that single layers could be manufactured, albeit with a low relative density after sintering (0.94) [159]. The low density is likely a result of the mentioned viscosity issues.

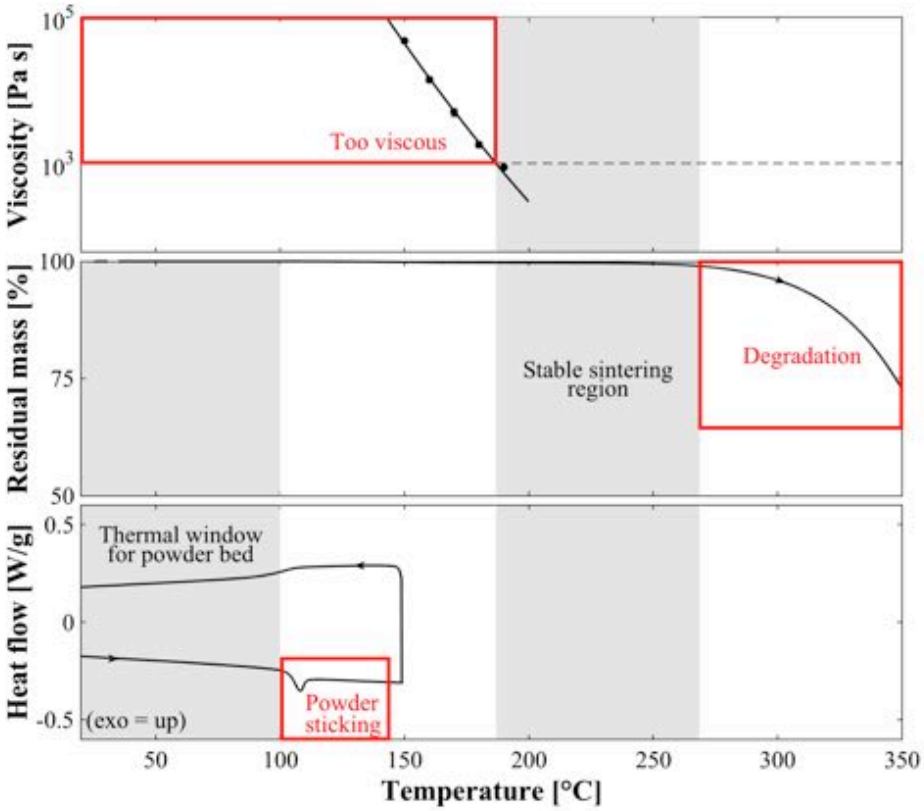


**Figure 3-7:** Thermal processing windows for Dynoseeds TS PS. The data is obtained for the 40 µm powder, but no difference is seen between the samples of different particle size.

### 3.2.3 Polymethylmethacrylate spheres (PMMA)

Finally, polymethylmethacrylate (PMMA) spheres serve as a second, independent set of spherical powder to validate the flow results. These spheres are Spheromers CA (Microbeads). Four samples with target particle sizes of respectively 20, 30, 40 and 60 µm are evaluated. Similar to the PS samples, these are pure materials, not containing any additives. The PSD curves are based on the manufacturer's information. The SEM images confirm that these particles are rather monodisperse (Figure 3-8).

The PMMA samples are only used as a reference material for evaluating the powder flow set-ups. It is not under consideration for use in LS due to two main reasons. First and foremost, there is a strong lack of a stable sintering region, as illustrated in Figure 3-9. Significant mass loss starts as early as 160 °C. This is only slightly

above the glass transition temperature (130 °C). As a result the polymer is still too viscous to coalesce sufficiently. An exact viscosity determination has not been performed as the coalescence temperature is too close to the degradation onset and the large mass loss is undesirable in the rheometer. Secondly, PMMA is known to be a very brittle material. Even if sintering parameters could be found, the porosity obtained in LS due to the high material viscosity or gas bubble formation by degradation would be detrimental for the brittleness of the final product.

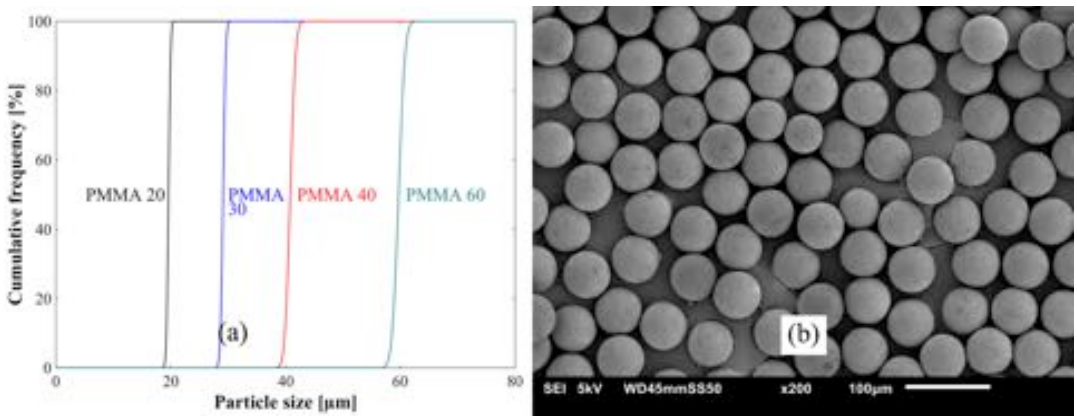


**Figure 3-8:** PSD of all PMMA samples (a) and SEM image of PMMA 60 µm (b).

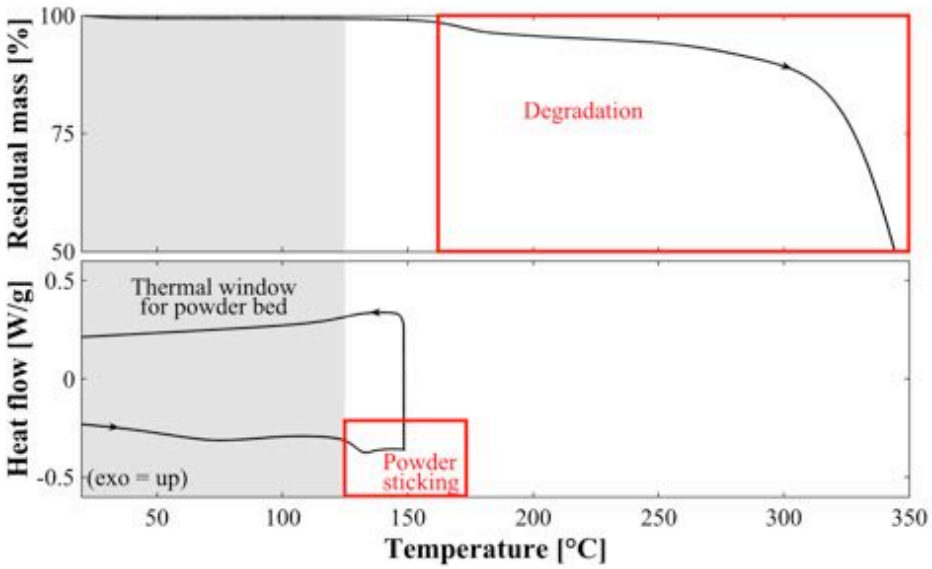


**Figure 3-9:** Thermal processing windows for Spheromers CA PMMA. The stable sintering region is absent.

## 3.3 Dynamic angle of repose

Two versions of the dynamic angle of repose are built for this research, based on the rotating drum set-up, described in Chapter 1. The first set-up, further referred to as the ambient dynamic angle of repose (A-DAoR), measures the angle of repose at

ambient conditions. Ambient conditions are defined as the conditions present in the lab, which is kept at roughly 20 °C and 50 % to 60 % relative humidity. The second set-up, further called the thermal dynamic angle of repose (T-DAoR), is able to measure the angle of repose at elevated temperatures. Besides the design of the hardware, dedicated software is written to obtain the necessary indices from the measurements. Section 3.3.1 describes this software, which is compatible for both set-ups. Sections 3.3.2 and 3.3.3 then describe the development of the individual set-ups and compare the results obtained by both.

### 3.3.1 Software

The angle of repose image analysis software is written in Matlab and exported as a standalone application. The goal of this software is to compute powder flowability indices based on a movie of the powder heap in the rotating drum. The software has several distinct steps, which maximise automation to limit user variability:

- Selecting frame range
- Drum localisation
- Converting to grey tones
- Edge detection
- Angle computation
- Profile analysis

First, the movie is selected and the desired frame range is indicated. This enables the removal of frames at the start or end of the measurement for which the lighting is suboptimal due to operator interference. Furthermore, for longer timed movies, this facilitates the study of time effects such as charge build-up. Next, the powder drum is located within the first frame of the selected time-range. This facilitates the use of the software for different set-ups with different distances between the camera and the sample drum. As the drum is round, it is located via a circular Hough transform (cf. Appendix A). Based on the location of the drum, an analysis window is taken, as shown in Figure 3-10. This allows local or global analysis of the heap angle. In this research, the global analysis window (Figure 3-10a) is chosen, as this provides the most complete and reproducible edge analysis.

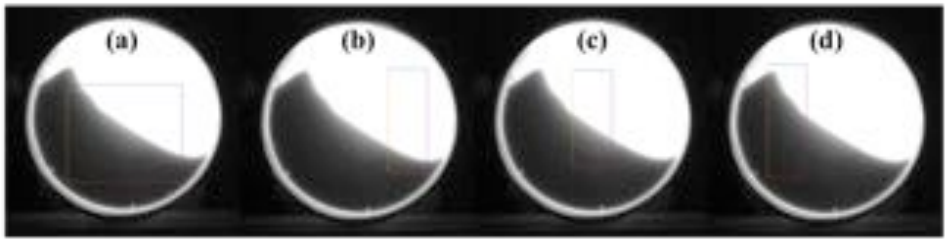


**Figure 3-10:** Automatic analysis windows: (a) global, (b-d) local.

Next the image is converted to grey tones based on the intensity of each pixel. In this image the edge is detected via the Canny method. The Canny method convolutes the image with the derivative of a Gaussian filter to obtain the gradient image. If this image gradient exceeds a certain threshold value, the location of this point is seen as an edge [160]. Figure 3-11 illustrates the Canny method for a 1D example. The solid black line in the upper panel represents the expected intensity profile of the image. An edge, i.e. a distinct change in intensity, is visible at 200 pixels and 700 pixels respectively. However, in reality, noise on the image complicates the definition of the edge, as represented by the grey curve. Convolution of the real, noisy image by the derivative of a Gaussian curve (shown in the middle panel) results in the signal of the bottom panel. This convolved signal shows two clear peaks at 200 and 700 pixels respectively. Furthermore, it is evident that the edge at 700 pixels is much stronger, due to the larger intensity difference. This also translates into a higher peak for the convolved signal. By selecting a threshold value, it can be chosen which edges are taken into account. In practice, the highest peak is normalised to unity, resulting in a threshold range from zero to unity. Similarly, an upper threshold can be defined to exclude strong edges. The expansion of this example to 2D is straightforward by applying the convolution twice, once in the x-direction, and once in the y-direction.

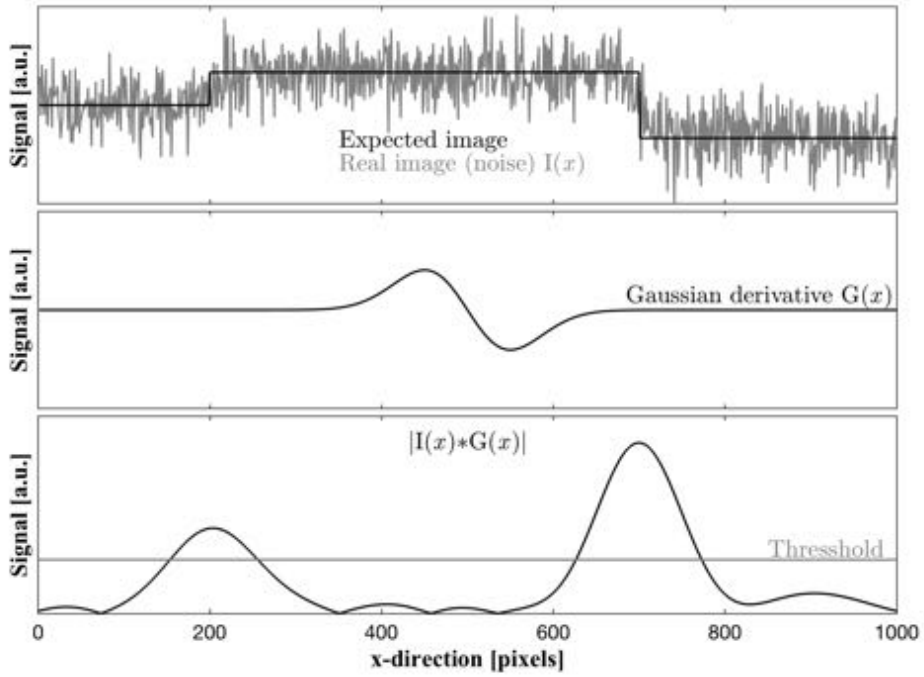


**Figure 3-11:** Canny edge detection method illustrated in 1D with $\boldsymbol{\sigma = 50}$ pixels.

The threshold is inputted manually, based on the edges detected in the first image of the movie. This enables the exclusion of false edges, such as those from powder outside the focus distance of the camera or defects in the uniformity of the light source. As the backlight, however, creates a strong contrast at the interface,

threshold values between 0.5 and 0.9 give the same results for almost all measurements, as illustrated in Figure 3-12, indicating the robustness of the software. For practical use, also an optimisation of the backlight has been performed in the updated set-up. A default threshold of 0.6 is used for most movies. The standard deviation of the Gauss curve is set to 6 pixels, as this in practice provided a good trade-off between preventing false edge detection due to noise on the one hand and processing speed limitations due to the time needed for the convolution algorithm on the other hand. The final software algorithm, including all processing steps, has a processing rate of around 15 fps for a typical measurement with a two megapixel resolution and a screen fill as shown in Figure 3-12. This speed is deemed sufficiently high for practical use. A lower camera resolution or a smaller coverage of the frame by the powder drum strongly speeds up the analysis as this reduces the amount of pixels in the analysis window.

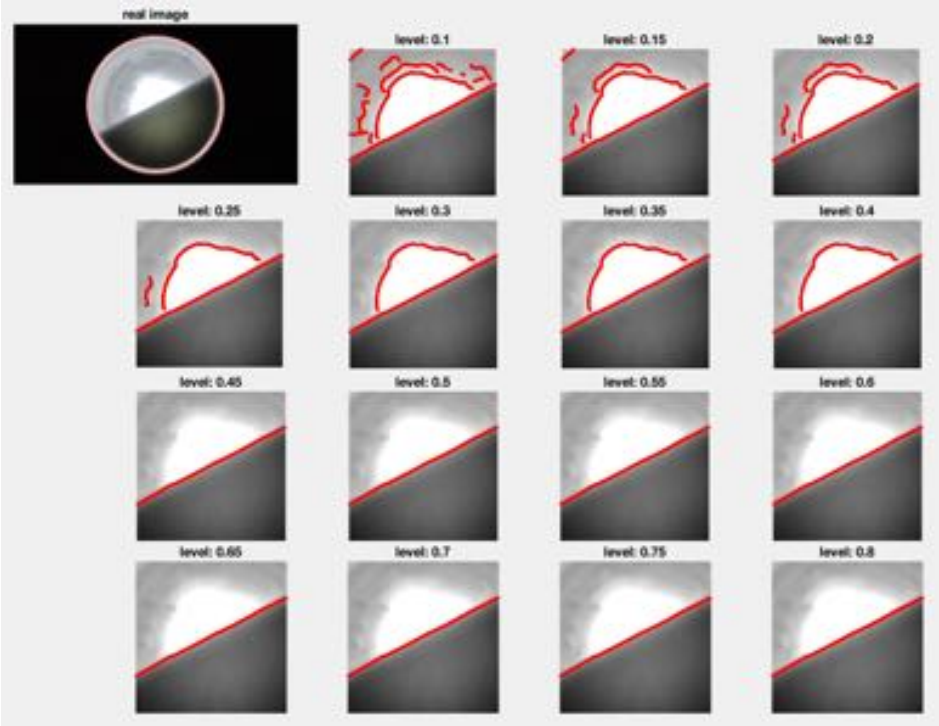


**Figure 3-12:** Illustration of the robustness of the Canny edge detection method for a set-up with uneven backlighting.

The Canny method was compared to the Sobel [161] and Prewitt methods [162], which will not be further discussed in this text. Also the Marr-Hildreth method, which uses the Laplacian of a Gaussian [163,164], was tested. However, for the given images the noise sensitivity of this method was much higher, due to the use of a second derivative, compared to the robust Canny method. As the Canny method was able to correctly detect the edge in all assessed measurements, this was taken as the default strategy for the software.

Once the edge is detected, the next step is the angle computation. For a straight edge, this computation is evident. For an irregular or curved edge, on the other hand, there are multiple definitions possible for the angle. Based on techniques applied in literature, three methods are used to determine the heap angle (cf. Figure 3-13). The first is the connection method, which is the simplest and thus also least time-consuming method. This method connects the pixels at both ends of the edge by a straight line. The slope of this line then determines the angle. The second method computes a linear regression over the edge. This is the most frequently applied approach in literature [137,165]. The final method is based on the heap determination in the commercial set-ups for computing the static angle of repose, such as the GranuHeap measurement. The angle of the powder heap is determined by the angle of an isosceles triangle which has the same base and surface area as the heap [80]. For the rotating drum measurement, the same approximation is possible by taking a right-angled triangle with the same base as the width of the detected edge and the same surface as the integral below the edge. In the determination of this integral, the lowest pixel of the edge is taken as the zero-height reference. To have an unambiguous definition for the numerical integral, the lowest pixel of the edge at each horizontal coordinate is taken when the edge contains multiple y-values at a single x-coordinate.

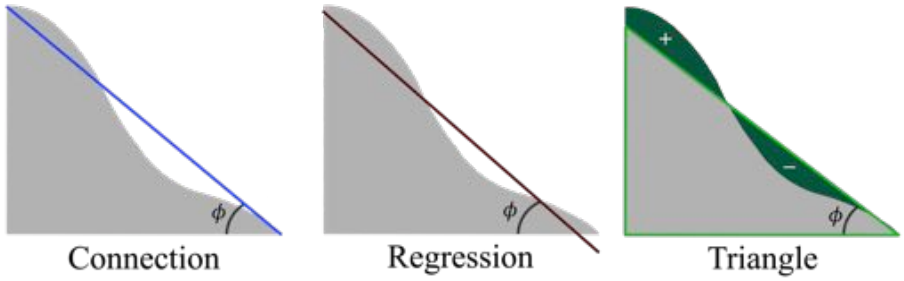


**Figure 3-13:** Conceptual illustration of the angle determination by the three methods: connection, regression and triangle method.

Extensive use of the software has proven that the angles from all three methods show similar trends for most samples, but each method has its advantages. The connection method is computationally the fastest. It, however, neglects most of the powder edge and is very sensitive to powder sticking to the circumference of the drum. The regression method is therefore preferable due to its inclusion of the entire powder edge. This provides the most complete information on the powder behaviour. It should, however, be noted that for most powders in the cascading or rolling regime, both angles typically only differed about 2° on average. Finally, the triangle method is also much less affected by powder sticking to the drum, but on its own is unable to take into account the high local angles typically found near the top of a cascading powder edge. In the rest of the text, the mentioned angles are those of the regression method, unless explicitly stated otherwise.

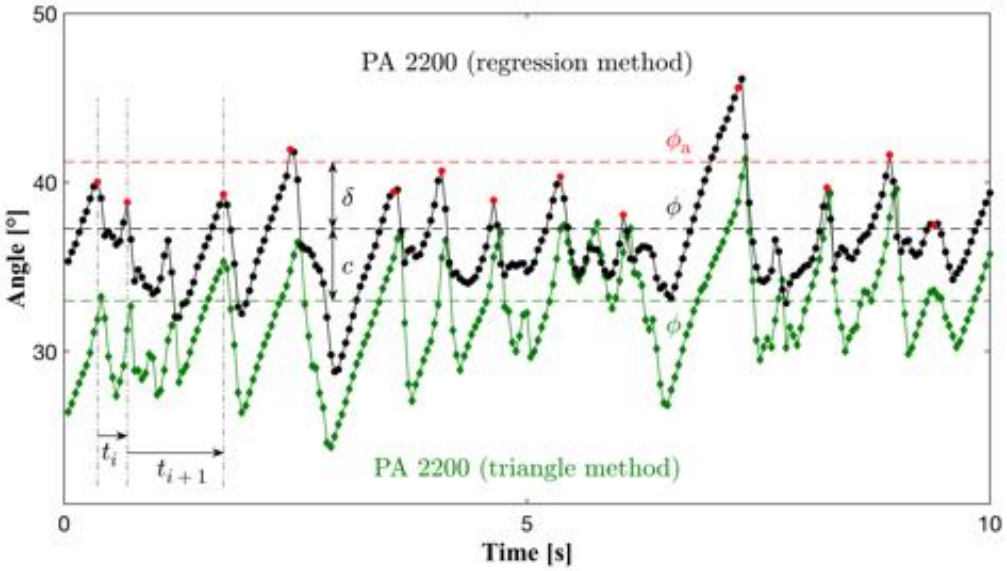


**Figure 3-14:** Example of the angle profile in time for PA 2200 at 3 rpm, zoomed in on the first 10 s for a 120 s measurement.

The angle computation is performed on every frame within the selected range, resulting in an angle profile in time (cf. Figure 3-14). This graph illustrates how the angle builds up in time, followed by an avalanche at which the angle drops down again. As seen on the graph, there can be a strong variation in the attainable avalanche angle. Based on this profile, multiple indices can be obtained, in correspondence to the AoR review of Section 2.3.4 (cf. Table 3-3). The first index is the average angle in time $\phi$, which forms a direct index for powder flowability. Larger angles mean that there is stronger interaction between the particles, which hinders them to flow down due to gravity. The second index is the average avalanche angle in time $\phi_a$, which corresponds to the average of the maxima in the angle profile. $\phi_a$ has a similar interpretation as $\phi$. The difference $\delta$ between both angles is a third indicator on the flow behaviour. The stronger the two angles differ, the stronger the avalanching behaviour is and thus the less smooth the powder flows. Other equivalent indices for expressing this variation are the minimum angle of repose, similar to the upper and lower angle of repose discussed in Chapter 1, or the standard deviation of the angle in a single measurement. However, to limit the amount of indices, only $\delta$ is reported in this research. A fourth index is the convexity $c$, which is a new index, defined as the difference between the average angles of the regression and triangle method. The higher this value, the more curved the edge is. For the ideal slumping or rolling regime, the convexity equals zero. For the cascading and cataracting regimes the convexity has a positive value. Surfaces with high convexity values typically are very sensitive to the exact location of the analysis window. Finally, also the average time between avalanches is noted. The longer the time between avalanches is, the stronger the avalanche build-up is. Avalanche times can only be compared correctly for identical rotational speeds, as

an increased rotation speed decreases the time for avalanches of the same magnitude to build-up. This decrease of the avalanche with increasing rotational speeds does not indicate an increase in flowability.

**Table 3-3:** Indices reported by the DAoR software.

| Name | Symbol | Units |
|---|---|---|
| Average angle in time | $\boldsymbol{\phi}$ | [°] |
| Maximum angle (= avalanche angle) | $\boldsymbol{\phi_a}$ | [°] |
| Width ($\boldsymbol{\phi_a - \phi}$) | $\boldsymbol{\delta}$ | [°] |
| Convexity | $\boldsymbol{c}$ | [°] |
| Avalanching time | $\boldsymbol{t_a}$ | [s] |

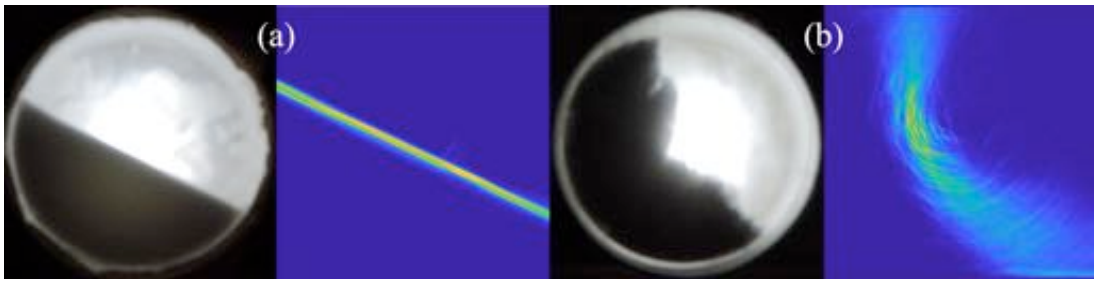


**Figure 3-15:** Powder edge heat map for a well flowing powder in the rolling regime (a) and a strongly avalanching powder (b).

The analysis steps of the previous paragraphs enable an extensive evaluation of the powder flow behaviour in the drum. The next paragraphs describe some extra features that were added to the analysis to improve both robustness and ease of interpretation. An example of a robustness issue is the adherence of powder to the container wall. This creates an extra edge, which is thus also indicated by the software and contributes to the linear regression. Three indications are available in the software to recognise issues in the results. (1) The software is able to generate a processed movie with the edge and angles plotted on each frame. This provides the most complete information, but is very time consuming in both computing time, as well as operator time. (2) Out of the three angle computation methods, the regression method is affected the strongest by such false edges. By comparing the different angles of each frame, issues with false edge detections are in some cases visible. Not only should the occurrence of avalanches be roughly the same for the three methods, for powders that do not experience strong avalanching behaviour, the connection and regression methods provide angles that typically differ less than 2°. (3) The software generates a heat map of how often each pixel on the screen contained the powder edge, as illustrated in Figure 3-15. This edge heat map gives a fast visualisation of the flow behaviour during the entire measurement. False edges,

created by powder sticking to the wall are easily seen as long circular lines above the actual powder edge. This quick visualisation also provides a simple tool to easily distinguish between the different flow regimes described in Section 2.3.4. The thin, straight band on Figure 3-15a clearly shows that the sample is in the rolling regime for all frames of the movie. The circular lines that form the powder edge on Figure 3-15b on the other hand show that the powder rotates as a static body until a heap of powder crashes down.

The software described in this section is applicable to any rotating drum set-up. It is applied for the two set-ups that are built in the course of this research. Sections 3.3.2 and 3.3.3 discuss the A-DAoR and T-DAoR respectively and the results obtained for the reference powders. To enable an easier visual comparison between the angles resulting from set-ups with opposite rotational directions, the software mirrors all images from measurements in the counter-clockwise direction. The rotational direction is automatically determined by the software from the sign of the slope of the linear regression of the powder surface.

### 3.3.2 A-DAoR

The ambient dynamic angle of repose (A-DAoR), shown in Figure 3-16, consists of a PS drum, with an inner diameter of 52 mm and an axial length of 12 mm. These dimensions were chosen to (1) minimise the variation in the axial direction and (2) limit the amount of powder needed for a DAoR test in early powder development. During a measurement, the drum is filled for 50%, resulting in a sample volume of approximately 12.7 ml at poured bulk density. The sample drum is mounted on a support cylinder to which the motor transfers its rotational movement. This cylinder contains a backlight, which provides the needed contrast for the camera. This camera records the avalanching at a frame rate of 25 fps. The drum is fully sealed after the powder is loaded, thereby limiting moisture transfer to or from the powder. This enables the study of moisture on powder flow by pre-conditioning the powder prior to the measurement.

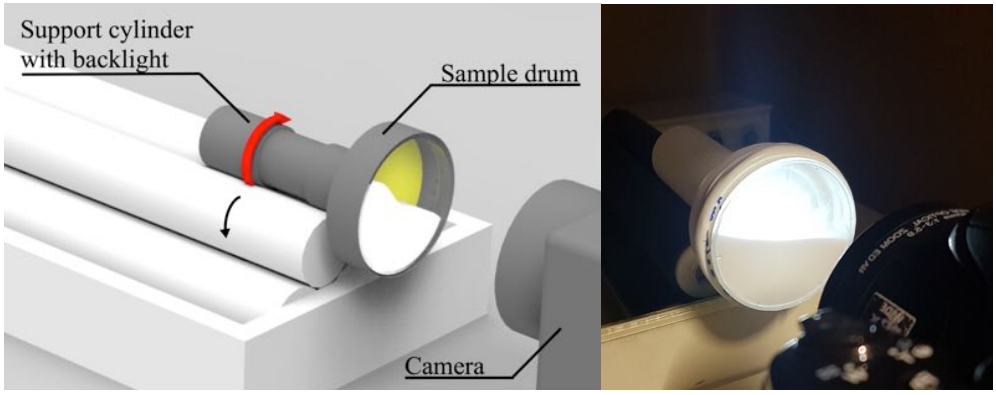


**Figure 3-16:** Schematic and picture of the A-DAoR setup.

Rotational speeds up to 30 rpm are feasible on this device. Multiple aspects play a role in the choice of rotational speed. One methodology is to mimic the velocity of the drum velocity of the counter-rotating roller in an LS machine. This reasoning builds on the concept that the flow field in front of a spreading tool in an LS machine is very similar to that of a rotating drum, as discussed in section 2.3.4. Two routes exist for creating this velocity equivalence. (1) The angular velocity of the drum can be chosen similarly to the angular velocity of the roller. For a Sinterstation 2000 with a 50 mm diameter roller this would result in a rotational speed of 35 to 80 rpm [22]. These speeds are currently out of the device specifications. (2) A more accurate speed equivalence is that of the circumferential velocity, as this is the velocity the powder feels via the interaction with the drum or roller wall. In the case of this geometry, both routes lead to approximately the same rotational speeds due to the choice of the drum size. At these rotational speeds, many powders are typically in the fluidisation regime [22].

Within research however, most work is based on the blade spreading mechanism of EOS GmbH. In this case there is no upward force that agitates the powder. Therefore, it is deemed that measurements at low rotational speeds, in the flowability regime rather than the fluidisation regime, are more representative. Furthermore, very cohesive powders do not tend to fluidise at higher rotational speeds, but rather create a strong cataracting motion, in which lumps of powder are thrown. The low rotational speeds facilitate the measurement of these powders as the lower inertia limits the cataracting motion. Earlier work shows that a rotational speed of 3 rpm provides a reproducible measurement condition for all typical LS powders [166].

**Assessing reference materials**

All materials in this chapter are assessed on the angle of repose. The relevance of the found DAoR indices is further discussed in 3.5.1 by comparing these results to spreading experiments. The resulting indices and edge heat maps are found in Table 3-4 and Figure 3-17, respectively.

Firstly, the link to the Bond numbers, computed in Table 3-2, is assessed. It is seen that for the spherical powders, the Bond number provides a good first indication on the flowability behaviour. For the PMMA spheres, the relation between the observed angles and the Bond number is almost linear, with the exception of PMMA 60 µm, which scores almost identical to PMMA 40 µm. A possible explanation is that at these low Bond numbers, the Van der Waals force is no longer the dominant force and increasing the particle size further has no significant effect. For PS a similar linear trend is seen for the smaller, Van der Waals dominated powders. The PS 140, however, scores significantly better than a linear trend would predict. Furthermore the PS and PMMA spheres do not lie on a master curve, even when scaling for the

uncertainty of the Hamaker constant. This indicates that the defined Bond number is not a universal parameter for ranking flow behaviour in the DAoR. Parameters such as hardness, elasticity and surface roughness of the particles are not included, resulting in different particle interactions. A similar trend is seen between the Bond number and the DAoR indices of the PA powders. E.g. the two powders with the highest Bond numbers, i.e. PA Orgasol and Sinterline, score the largest angles, which indicates that the Bond number is still viable at giving a first estimate. However, it does not hold for all samples. The particle shape/roughness is namely an important variable that contributes the final flowability. This effect is even more pronounced for the strongly irregular, milled samples of Chapters 4 and 5.

**Table 3-4:** DAoR results for the reference powders.

| | **Bo** [/] | $\boldsymbol{\phi}$ [°] | $\boldsymbol{\phi_a}$ [°] | $\boldsymbol{\delta}$ [°] | $\boldsymbol{c}$ [°] | $\boldsymbol{t_a}$ [s] |
|---|---|---|---|---|---|---|
| **PA 2200** | 1.49 | 36.9 ± 1.8 | 40.6 ± 2.1 | 3.6 ± 0.4 | 4.5 ± 0.7 | 0.71 ± 0.04 |
| **PA Orgasol** | 3.28 | 44.1 ± 0.6 | 50.7 ± 0.1 | 6.6 ± 0.8 | 3.2 ± 0.2 | 1.34 ± 0.03 |
| **PA Vestosint** | 1.81 | 30.7 ± 0.6 | 32.1 ± 0.5 | 1.4 ± 0.7 | 3.4 ± 0.4 | 0.61 ± 0.03 |
| **PA Sinterline** | 2.89 | 43.9 ± 1.3 | 52.6 ± 1.5 | 8.7 ± 1.7 | 3.3 ± 1.2 | 0.68 ± 0.05 |
| **PA Rilsan** | 1.51 | 40.0 ± 0.8 | 43.9 ± 1.0 | 3.9 ± 0.5 | 7.1 ± 1.4 | 0.60 ± 0.01 |
| **PS 20** | 12.85 | 35.6 ± 0.4 | 43.9 ± 1.4 | 8.3 ± 1.6 | 7.4 ± 1.8 | 1.21 ± 0.00 |
| **PS 40** | 3.06 | 31.3 ± 1.6 | 39.1 ± 3.0 | 7.8 ± 1.7 | 6.2 ± 1.2 | 1.24 ± 0.03 |
| **PS 80** | 0.95 | 29.8 ± 1.6 | 37.5 ± 2.2 | 7.7 ± 0.6 | 1.8 ± 0.1 | 1.19 ± 0.04 |
| **PS 140** | 0.33 | 26.5 ± 0.5 | 26.9 ± 0.4 | 0.3 ± 0.1 | 0.6 ± 0.3 | 0.59 ± 0.00 |
| **PMMA 20** | 11.27 | 35.1 ± 0.9 | 40.4 ± 0.8 | 5.3 ± 0.3 | 7.2 ± 0.9 | 1.01 ± 0.03 |
| **PMMA 30** | 5.11 | 27.5 ± 0.8 | 32.2 ± 0.2 | 3.7 ± 0.3 | 5.5 ± 0.4 | 1.05 ± 0.03 |
| **PMMA 40** | 2.60 | 25.6 ± 0.3 | 27.6 ± 0.2 | 2.0 ± 0.2 | 1.6 ± 0.2 | 0.87 ± 0.02 |
| **PMMA 60** | 1.21 | 25.6 ± 0.4 | 26.8 ± 0.3 | 1.2 ± 0.1 | 0.9 ± 0.1 | 0.80 ± 0.02 |

Next, the powders can be split up into three classes depending on their flowability, as illustrated in Table 3-4. PMMA 40 µm and 60 µm and PS 140 µm are clearly in the rolling regime. This is seen by the low $\delta$ and $c$ values, as well as the thin, straight band in the edge heat maps. A quite smooth and continuous flow is seen. PA Orgasol shows very strong avalanching behaviour. As illustrated in Figure 3-18c, this yields local powder angles of 90° or higher, making the definition of an average angle less meaningful for this regime. The smaller PS and PMMA spheres and the other PA powders lie in an intermediate cascading regime.

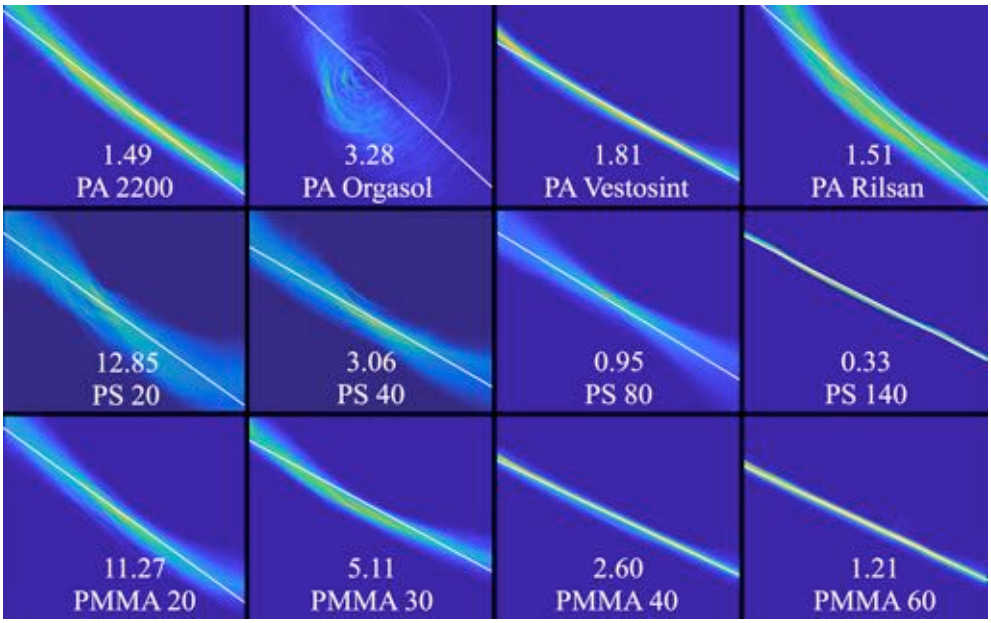


**Figure 3-17:** Edge heat map illustration of the examined powders, listed with their respective Bond numbers.

The avalanche time furthermore shows a distinct difference between the rolling and cascading regime of the spherical powders. However, the polyamides have significantly lower avalanche times than the PMMA powders, though the PA powders are flowing less smoothly. A possible explanation is that in the rolling regime the continuous rolling of the material gives rise to fewer discrete disturbances in the powder surface and thus fewer actual avalanches. For this reason, the avalanche time is deemed less useful when comparing powders that are in different flow regimes.

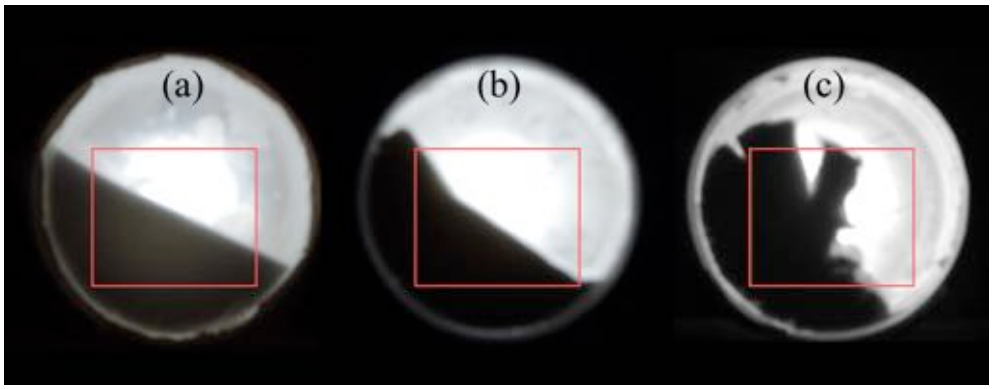


**Figure 3-18:** Regimes seen in the samples (a) rolling, PMMA 60, (b) cascading, PA 2200 and (c) strong avalanche lumps, PA Orgasol. The red rectangle indicates the analysis window.

**Assessing effects of humidity and charge**

One of the major advantages of the A-DAoR set-up, besides its simple use, is the fact that the measurement happens in a fully closed system. This enables an easy measurement of the relative effect of humidity by conditioning of the powder prior to loading.

Pre-conditioning is achieved in two ways. (1) To obtain a stable moisture content in the powder, the powder is equilibrated in a humidity chamber for 24 hours at 25 °C and 60% relative humidity. The powder is spread on a wide petri dish to maximise the contact with the surrounding air. Directly after pre-conditioning the powder is loaded in the sealed DAoR cells. (2) To assess the effect of removing humidity, the powder is dried in a vacuum oven for 24 hours at 60 °C. The sample is loaded into the DAoR cell and measured immediately. After this measurement the sample continues to rotate on the DAoR for another hour and is subsequently shaken vigorously to distribute the charge.

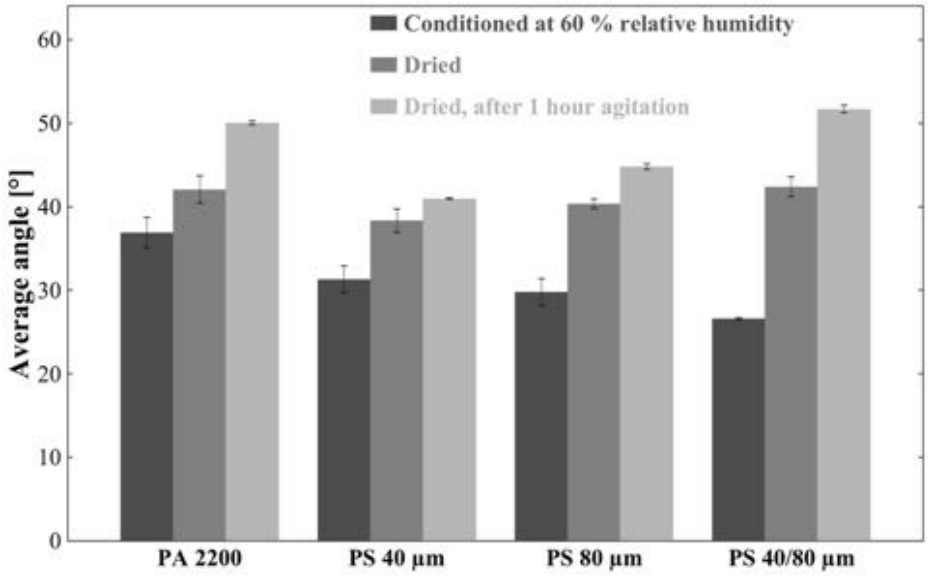


**Figure 3-19:** Effect of triboelectrification on PA 2200 and PS samples. The PS 40 µm/80 µm mixture had a 50/50 composition.

The conditioning steps mentioned in the previous paragraphs are applied to PA 2200, PS 40 µm, PS 80 µm and a 50/50 mixture of the two PS samples. The results for these powders are shown in Figure 3-19. All four samples show deterioration in flowability due to drying. After inducing more friction in the samples, the angle shoots up further. This added increase indicates that the flow deterioration is at least partially due to triboelectrification. This triboelectrification is also seen in charge measurements with a Coulombmeter and Faraday cup. A clear increase in charge is seen, though the absolute values of the charge are difficult to measure and reproduce. Furthermore, it is also the charge difference between particles that causes attraction, rather than the net charge of the sample. It should be

noted that the PS particles also exhibit triboelectrification, even though they are only in contact with themselves and the PS drum. This further demonstrates that for powders the size difference is a source for charge transfer between the same materials [91], as discussed in Section 2.2.1. This effect is amplified by an increase in the particle size difference, as shown for the 40 µm/80 µm mixture, which has a much larger increase of its angle. The actual amount of moisture present at equilibrium at 60% relative humidity also differs strongly between the PA and PS samples. PA 2200 has an equilibrium moisture content of about 0.68 %, while the PS samples only contain 0.060 % to 0.065 %. As a conclusion, a limited amount of moisture, even as little as that of PS, is thus desirable to avoid triboelectrification issues.

Figure 3-20 further illustrates the reversibility of this triboelectrification process for PA 2200 and the change in flow regime. It shows the edge heat maps of four PA 2200 measurements under different triboelectrification and humidity conditions. The heap angle of the dried sample shows an increase of 5°. This is likely the result from tribo-electification during the DAoR measurement. After rotating the sample for one hour, the angle has increased another 7° and the flow regime has changed from rather smooth flow to a more irregular flow pattern that is dominated by chunks of powder sliding down. This observation further supports the hypothesis of electrification issues. After re-humidifying and letting the sample rest for a day, the same angle as that of the pre-conditioned sample is re-obtained.

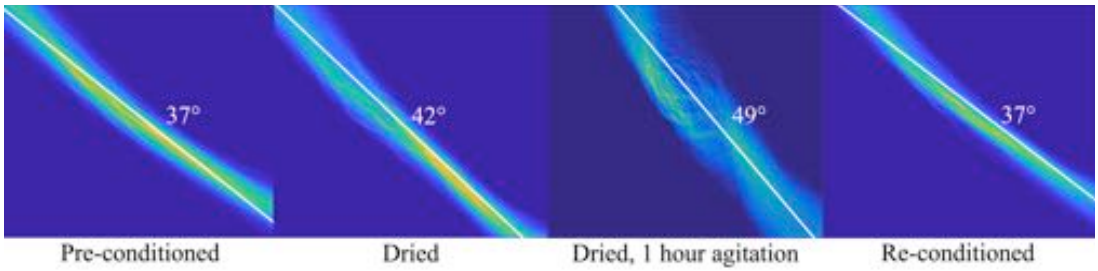


**Figure 3-20:** Edge heat maps for PA 2200 measurements under different tribo-electrification and humidity conditions. Indicated angles are the average angles for all samples of the given condition and may differ slightly to the angle of the individually plotted samples.

Next, the effect of additional moisture is assessed by pre-conditioning the samples at different relative humidity values between 50 % and 90 %. Therefore, the link between humidity and moisture content needs to be known. This was examined via thermo-gravimetrical analysis on a moisture balance directly after pre-conditioning. Figure 3-21 shows the moisture content of PA 2200 and PS 40 µm as a function of the relative humidity. PA 2200 takes up relatively high amounts of moisture in comparison to the PS. The latter has a moisture content that is an order of magnitude smaller. However, the effect on flow is quite opposite, as shown in Figure 3-22. The

PA 2200 sample seems rather unaffected by a raise in the moisture content. The PS 40 µm sample, in contrast, has a steady rise in the angles. A reason for this difference may lie in the way the moisture is taken up by the polymer. The PA is more hydrophilic, taking up the moisture. The flow additives present in the commercial sample may also further attract the moisture, preventing it from forming capillary bridges on the PA surface. The PS on the other hand only takes up very small amounts of moisture. It is therefore possible that most of this moisture is adsorbed on the spheres instead, resulting in a stronger capillary effect, compared to the moisture present in PA 2200.

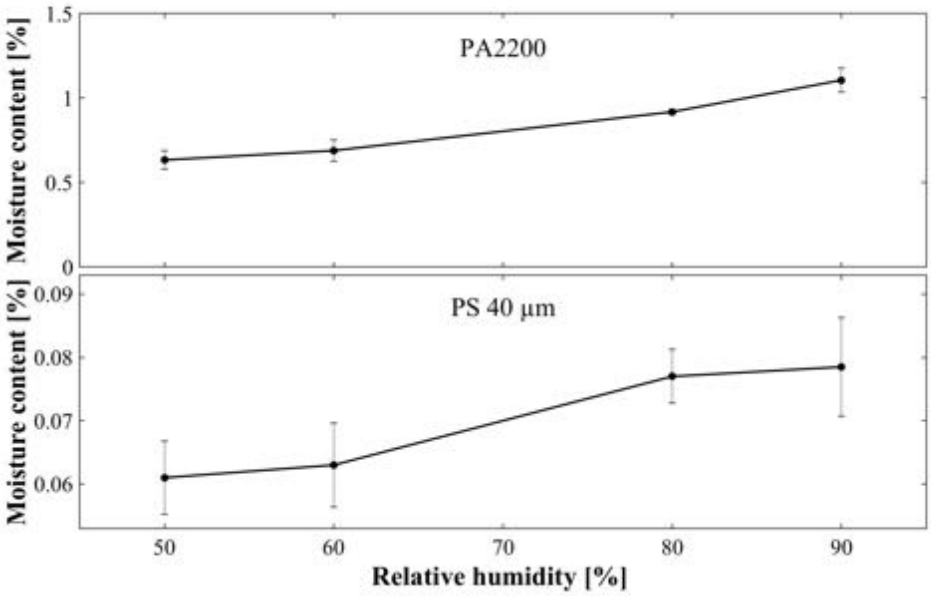


**Figure 3-21:** Moisture content of PA 2200 and PS 40 µm in function of the relative humidity at 20 °C.

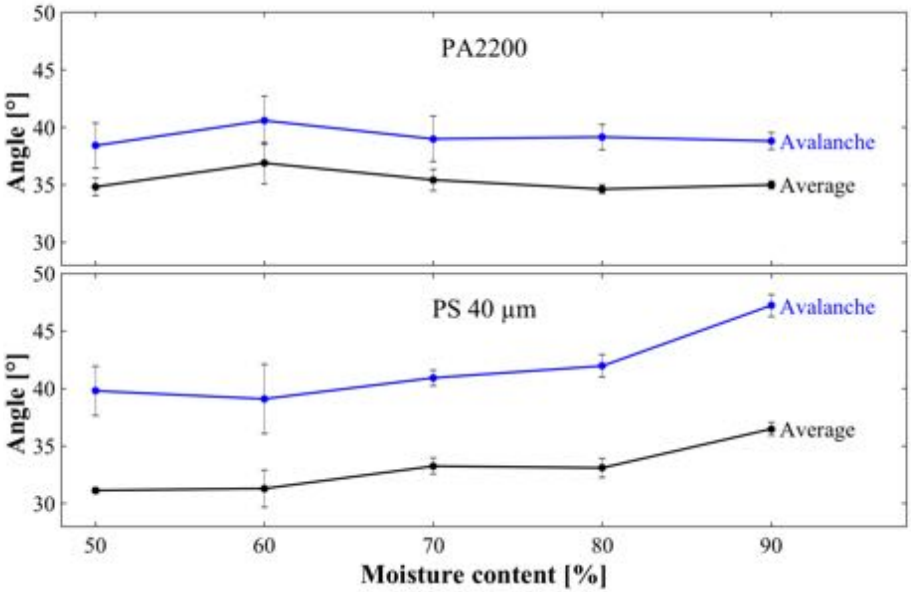


**Figure 3-22:** Effect of humidity on the angle of repose of PA 2200 and PS 40 µm.

Finally the addition of micron-sized silica additives is assessed. Three silica-based additives are added to PA 2200 in various amounts. Figure 3-23 shows the effect on the average and avalanche angles. For additive A and B an optimum around 0.5 % is seen, beyond which the system becomes oversaturated and the poor flowability of the additives themselves starts to dominate. It needs to be noted that this is the amount of additives added to the undisclosed amount of flow improvers already present in the commercial sample. For additive C also an improvement is seen, but the oversaturation is much less pronounced. As the previous measurements showed that the effect of moisture on the PA 2200 sample was already limited, the effect of the additional additives is likely not due to their potential to absorb moisture. Rather, the additives sit on the surface of the particles, changing the inter-particle contact.

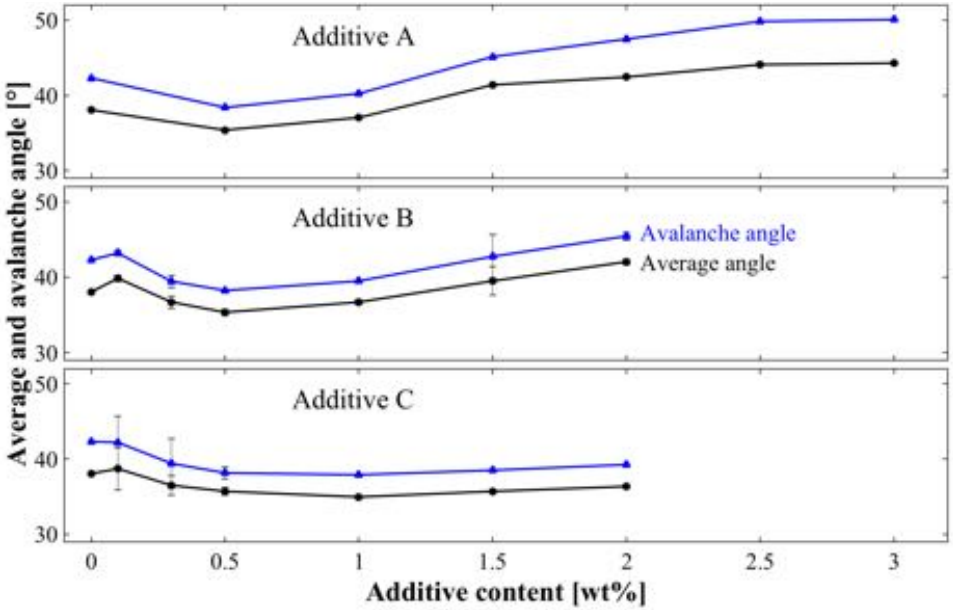


**Figure 3-23:** Effect of silica-based flow improvers on the avalanche angle of PA 2200.

In conclusion, the A-DAoR is able to distinguish changes in flowability based on moisture or additive content. It is furthermore a quick screening method to get some first insights into the flow behaviour of a wide variety of samples. The next section further expands upon this set-up by creating a new design to include thermal control.

### 3.3.3 T-DAoR

The thermal dynamic angle of repose (T-DAoR) forms an expansion on the A-DAoR setup to include heating effects. In this set-up, the sample drum is enclosed in a convection oven, thus enabling temperature control. This convection oven consists of two concentric boxes, as shown in Figure 3-24. In between these two boxes a layer of insulation is placed to minimise heat loss to the environment. Two cylinders are mounted within the oven. The axes of both cylinders are driven by an externally

placed stepper motor to allow precise rotational control. The sample holder is then placed on top of these two cylinders. On opposite sides of the oven two glass windows are present to allow light from the backlight to pass through the sample and into the camera. The backlight and camera are both placed outside of the oven box to avoid heat damage.

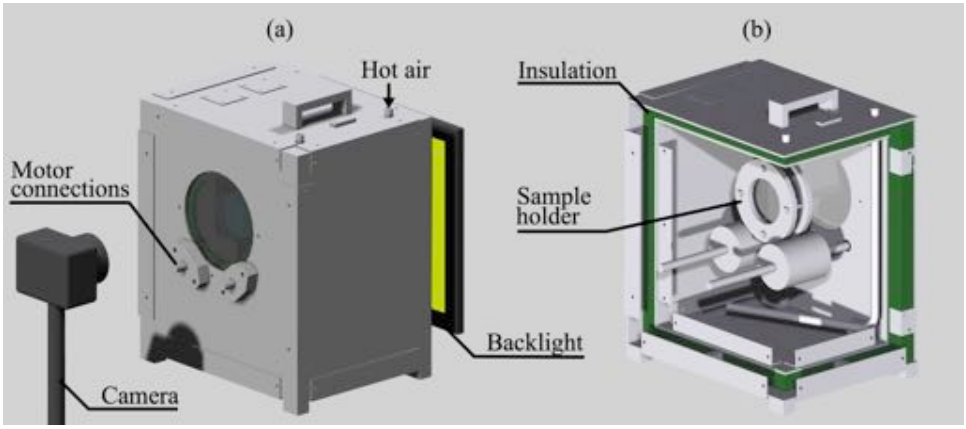


**Figure 3-24:** T-DAoR setup: (a) outer box and camera set-up. (b) inner structure and sample holder.

The sample holder, as shown in Figure 3-25, consists of two materials. The drum, which is in contact with the powder, is made of glass. The change in material from PS to glass is expected to have an effect on the interaction with the powder and thus also the measured angles. This effect is therefore evaluated in Section 3.3.4. The glass drum consists out of a cup and a lid (Figure 3-25a), which are pushed together by two aluminium rings (Figure 3-25b). These aluminium rings contact the rolling cylinders that are driven by the stepper motor. A flexible thermocouple is placed against the top of the glass drum, as shown in Figure 3-25c. During the rotation it maintains contact with the drum, except for brief periods when the screws that hold together the aluminium rings pass. This way, the temperature of the sample drum is monitored as close as possible.

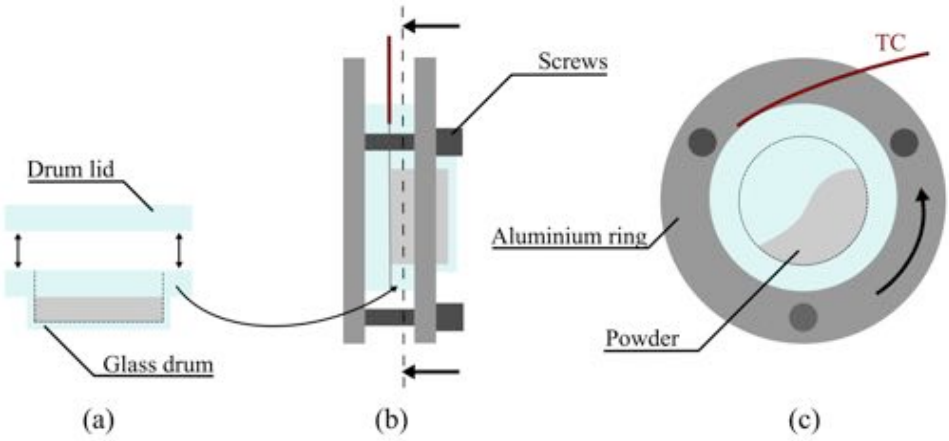


**Figure 3-25:** Placement of the glass drum (a) and the thermocouple (TC) in the sample holder: Side view (b) and front section view with a cutting plane at the dotted line (c).

Figure 3-26 shows the effect of temperature on the average and avalanche angle for PA 2200. Between 20 °C and 40 °C a jump in the angles is seen. This jump is related to static charging of the powder, as discussed in the next paragraph. Past this jump, the angles seem relatively stable up to around 80 °C, after which a gradual increase of the avalanche angle is seen. This is in correspondence to the findings of Amado et al., who see no difference in the avalanche angle between 30 and 70 °C and a small increase at 110 °C [167]. Upon cooling the sample again, the angles return to the plateau value. As the device has no active cooling mechanism, it was not feasible to cool down the sample to 20 °C without opening the oven.

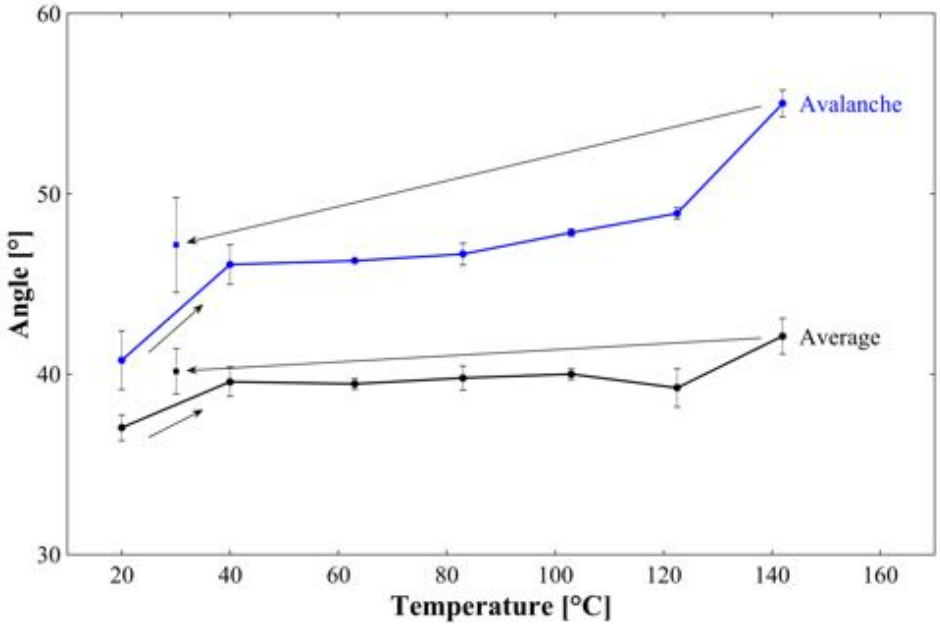


**Figure 3-26:** Average and avalanche angle of PA 2200 as a function of increasing temperature. ■ denotes the values obtained after cooling the sample again.

As stated in the previous paragraph, the triboelectric charging of the powder forms a strong influence on measuring the angle of repose values. This effect is illustrated on PA 2200 and PS 40 µm in Figure 3-27. The same protocol is applied as for the charging tests on the A-DAoR and the data of Figure 3-19 is added for the ease of comparison. No significant difference is seen in the behaviour in the two set-ups. The same angles are found for the conditioned sample on the one hand and the dried, agitated samples on the other hand. As a result, the charging effect seems to be primarily due to inter-particle friction, rather than contact with the drum wall. It also proves that the increase in the average angle of PA 2200 during the thermal measurements is a result from electrostatic charging. The increase at 140 °C on the other hand, is far above the expected increase by charging and is thus likely also influenced by softening of the polymer. The effect of softening is further discussed for the powder rheometer in Section 3.5.2.

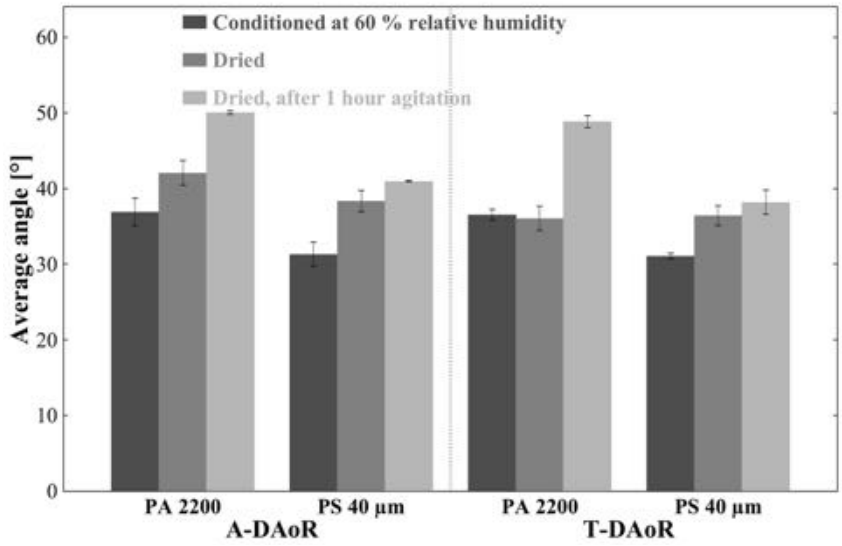


**Figure 3-27:** Effect of triboelectrification in the T-DAoR set-up.

### 3.3.4 Comparison of the set-ups

At ambient conditions, both set-ups are functionally the same, except for the drum material, which is PS for the A-DAoR and glass for the T-DAoR, as well as a negligible difference in the drum dimensions. The difference in material leads to a difference in roughness of the walls as well as a difference in electrostatic interaction. Figure 3-28 shows the average and avalanche angle for all samples that were tested under ambient conditions on both devices. These include data points for some cryogenically milled TPU powders that are further discussed in Chapter 4 and cryomilled PB-1, which is discussed in Section 5.3. The correspondence of both devices is quite high at lower angles. At higher angles, a small deviation towards lower angles is seen for the T-DAoR set-up. The effect is, however, limited.

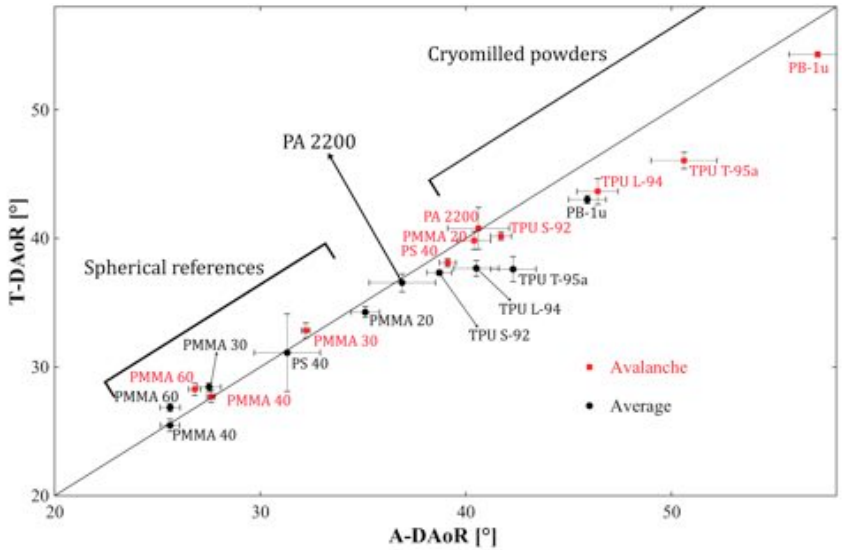


**Figure 3-28:** Comparison of the avalanche and average angles of the two DAoR set-ups. The cryomilled powders are defined in Chapters 4 and 5.

## 3.4 Powder rheometer

The powder rheometer is an adaptation of an existing liquid rheometer. The adaptation enables a measurement protocol that is similar to that of the basic flow energy of a Freeman FT4 rheometer (cf. Section 2.3.5). During the course of the research, the rheometer adaptation was tested on an AR-G2 and a DHR-3 stress controlled rheometer (TA instruments). The main goal of the powder rheometry measurements is to evaluate changes in powder flowability with temperature, which is currently not possible on commercial rheometers, such as the FT4. This thus extends the idea of the stickiness temperature, discussed in Section 2.3.5, to the free flowing regime.

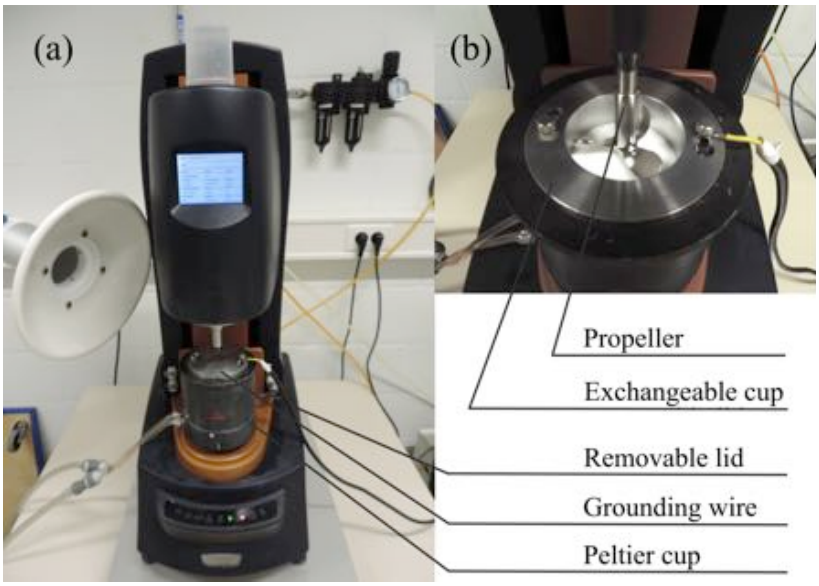


**Figure 3-29:** Illustration of the powder rheometer expansion for the DHR-3 (a). The lid is removed on the close-up (b) in order to show the propeller and powder loading.

Both devices use the same interchangeable powder cell and are operated by the same protocol. The powder cell, shown mounted on the DHR-3 rheometer in Figure 3-29, consists of a Peltier cup holder, fitted with an aluminium cup with an inner diameter of 52 mm and a height of 75 mm. The Peltier system enables temperature control from -20 °C up to 150 °C. A two-piece lid is screwed onto the cup after loading the powder and inserting the propeller, leaving a small hole for the propeller shaft to pass through without friction. This lid aids in creating a microenvironment within the cup. A custom geometry holder enables the use of various propeller geometries. The measurements in this research are performed with a three-bladed propeller with a blade length of 25 mm and a blade inclination of 45°. This geometry was empirically chosen to provide sufficient resistance with the powder mass. Other, smaller, two-bladed propellers have been tested. These, however, tend to slice more through the powder, rather than pushing it, which yields in a lower sensitivity. The

resulting index is thus strongly dependent on the chosen propeller, as is inherent to indexing measurements. However, the evolution with temperature is similar for the tested reference materials.

A grounding wire is added to the aluminium cup to avoid issues with static charge build-up. As shown in the DAoR measurements (Sections 3.3.2 and 3.3.3) static charging of powders, especially during heating, is detrimental for powder flowability. Preliminary tests show torque increases in time of up to 200 % for the PA 2200 powder when the grounding wire is removed. The conductivity of the powder cup and addition of the grounding wire are able to avoid the charge build-up that was present in the DAoR measurements and create stable measurements in time, even for dried powders.

To ensure reproducibility, the following protocol is followed. A fixed mass of powder is loaded for each measurement, as opposed to the fixed volume approach of the FT4 rheometer. The reason for this choice is the difficulty of setting a fixed volume due to thermal expansion during the measurement. To compensate for the difference in volume, the computation of the flow energy happens over a fixed penetration depth of the propeller, rather than the entire propeller path. A mass of 40 g was chosen, as this provided a sufficiently high powder column without overfilling upon thermal expansion for all examined powders.

After loading the powder and equilibrating the temperature, the propeller moves 15 cycles in a downward and subsequent upward helicoidal motion, with a rotational speed of 2 rad/s and an axial speed of 2 mm/s. The data of the downward motion is taken to compute the flow energy. The first cycle serves as a pre-conditioning cycle. The subsequent 14 cycles are averaged out and used to compute the energy gradient. As stated in the previous paragraph, the flow energy is computed over a fixed axial length, starting from the height at which the propeller hits the powder surface. This starting height is determined a posteriori as the point at which the torque component of the energy gradient reaches 0.5 % of its maximum value during the cycle. This way, the fixed-volume methodology of the FT4 rheometer is maintained.

One of the biggest differences between both set-ups is the location of the normal force transducer. For the AR-G2, this transducer is located on the bottom, and thus records the force transferred to the cup. For the DHR-3, on the other hand, the force transducer is located at the head of the rheometer, thus directly registering the force on the propeller. Comparative measurements on both devices show that the AR-G2 set-up is unable to reproducibly measure the normal force, as it is dampened out by the sample. Therefore only the torque component of the flow energy is measurable. As seen in Eq. 1.21b, the relative contribution of the torque and normal force components are dependent on the axial and rotational velocity. The measurements indicate that the contribution of the normal force for the chosen propeller speeds and

geometry is negligible compared to the torque contribution, as shown in Figure 3-30, resulting in the same powder ranking for both devices. The negligible normal force contribution is seen for all examined powders.

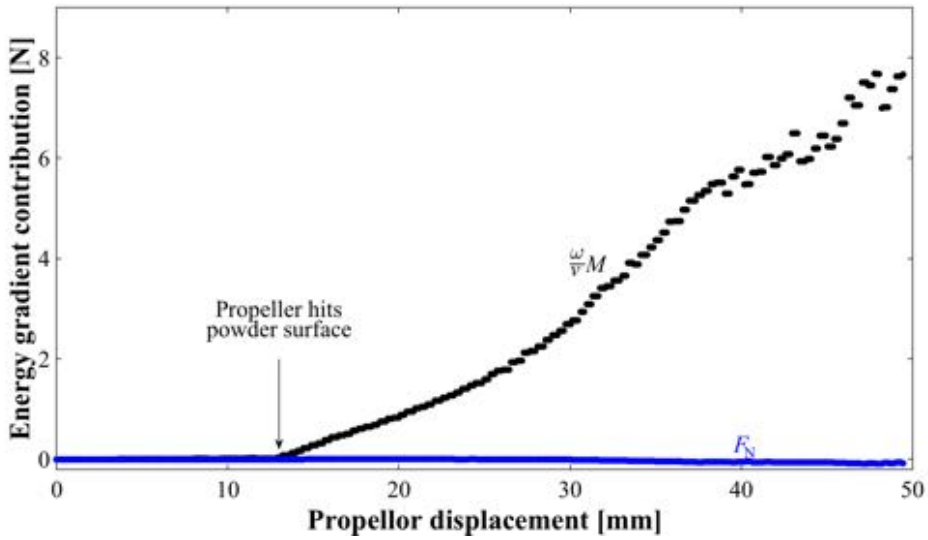


**Figure 3-30:** Relative contributions of the torque and normal force components during one downward cycle of a typical powder rheometry measurement.

A remark needs to be made on the negative sign of the normal force component in Figure 3-30. Due to the relatively fast rotation of the propeller, the powder that hits the inclined surface of the propeller blade in the horizontal plane pushes the propeller down, thus aiding the vertical movement. Therefore, the net energy gradient (Eq. 1.21b) is slightly smaller than the torque contribution. The torque and normal force needed to compute the energy gradient follow directly from the Trios software of TA Instruments. The averaging procedures over the multiple cycles, the powder surface detection and EG computation are automated in Matlab to avoid operator errors.

$$\mathrm{EG} = \frac{\omega}{v} M(z) + F_{\mathrm{N}}(z) \qquad (1.21b)$$

PA 2200 follows the expected behaviour with temperature, as shown in Figure 3-31. At low temperatures, below the glass transition, the flow energy is independent of temperature. The glass transition then marks a distinct change, as the flow energy continuously increases beyond this temperature. This distinct effect of the glass transition temperature is in correspondence with the observations of Amado et al. for the behaviour of the surface fractal in the rotating drum experiment [167]. The results also correspond with the findings of Verkinderen et al. on polyamides. They found that above the glass transition the rigid fraction decreases, while the mobile amorphous fraction increases [168]. This may explain the softening effect, which was also discussed for the T-DAoR (Cf. Section 3.3.3).

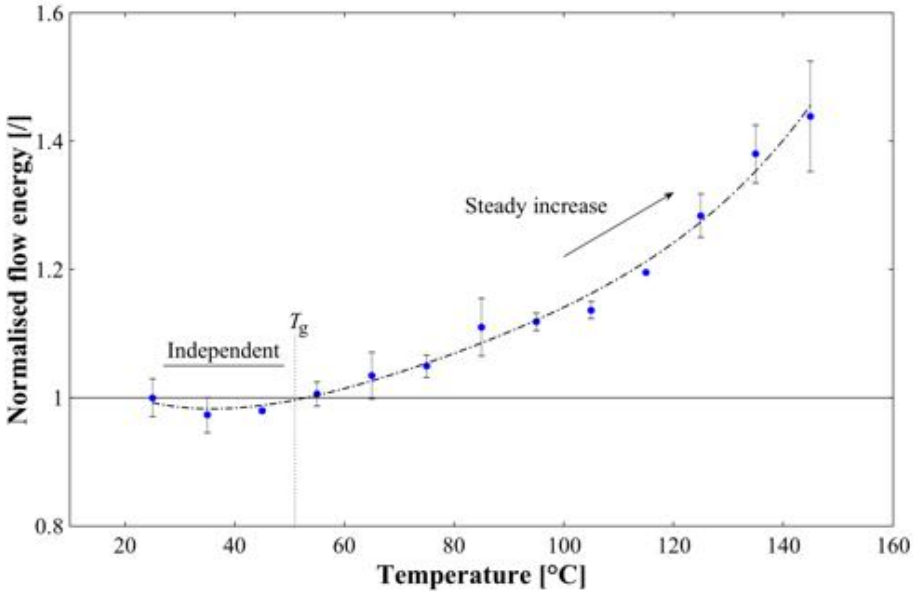


**Figure 3-31:** Normalised flow energy of PA12 2200 with increasing temperature.

Similarly, PS 40 µm has only limited temperature dependence below its glass transition, as shown in Figure 3-32. As stated in the description of the grounding wire, an important difference with the temperature results found in the angle of repose experiments is the limited contribution of triboelectrification effects. The conductivity of the metal tools that are in contact with the powder is most likely the cause.

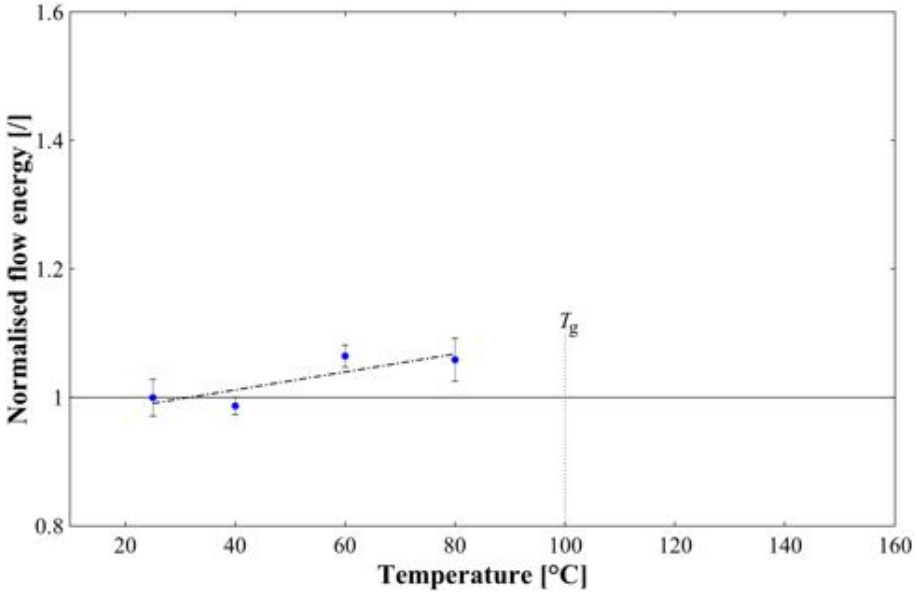


**Figure 3-32:** Normalised flow energy of PS 40 µm with increasing temperature.

## 3.5 Powder spreader

Finally, the powder spreader is created to mimic the flow fields present in an LS machine as closely as possible on a reduced scale. The powder spreader was developed particularly for this research, as no such device existed commercially prior to this research. Two designs of the powder spreader are created. The first is a semi-automated version that still requires operator input during the measurement. The second version is a fully automated set-up that requires no operator interaction during the measurement. Both set-ups include temperature control.

### 3.5.1 Semi-automated powder spreader

*Passages from this section, including figures, have been adapted from an own, published journal paper [169] and conference paper [170].*

The semi-automated powder spreader, shown in Figure 3-33, has the following working principle. A powder sample is loaded manually in front of an interchangeable spreading blade. A translational motor then pushes this blade across the measurement platform. A vertical positioning stage, located below the measurement platform, enables vertical movement of the platform with a precision of 10 µm. This movement does not only enable control over the deposited layer thickness, it also enables the study of powder on powder deposition by allowing the deposition of sequential powder layers. Between two sequential layers, the operator is required to reset the blade to the starting position and load a fresh amount of powder. This makes this set-up semi-automatic. The automatic version improves this by removing this manual step.

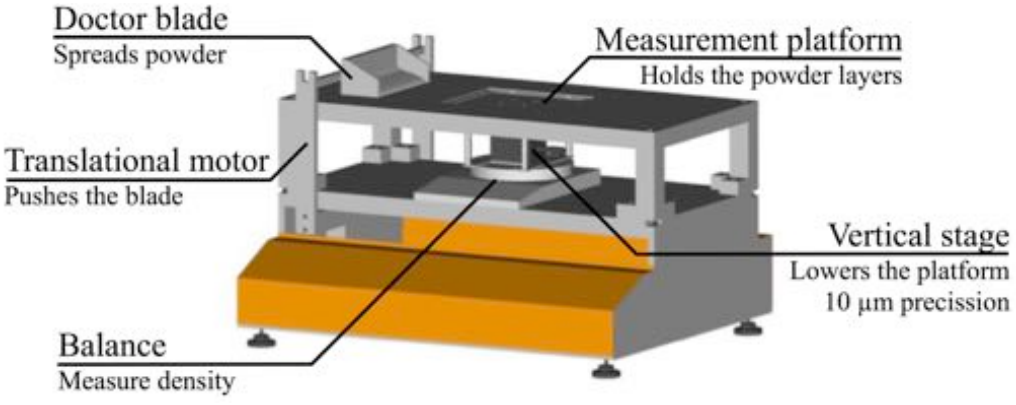


**Figure 3-33:** Semi-automated powder spreader.

The set-up provides both a qualitative and quantitative evaluation of the deposited powders. Firstly, the occurrence of defects in each layer is qualitatively observable. This yields a pass/fail assessment of the powder, similar to the assessment of HP's MDK [151]. Secondly, for the powders that pass the qualitative criterion, a quantitative

index is measured. A balance, which carries the measurement platform and the vertical positioning stage, determines the weight of each individual powder layer. Via the known platform dimensions and layer thickness, the bulk density of the powder layer is determined.

As the density itself is more difficult to compare directly between different powders, two dimensionless indices are derived. The first is the packing density $\rho_{\mathrm{pk}}$, which expressed the volume fraction of the layer that is filled with particles (Eq. 2.1). This facilitates the comparison of powders made of different polymers. The complement of the packing density is the porosity $\epsilon$. Lower porosities facilitate coalescence within the layer, thus generally yielding denser products. The packing density is therefore a directly useful index for LS, as discussed in Section 2.1.3.

$$\rho_{\mathrm{pk}} = \frac{\rho_{\mathrm{b,layer}}}{\rho_{\mathrm{m}}} = 1 - \epsilon \tag{2.1}$$

The packing density is determined by two factors. On the one hand it is limited by the geometrical packing of the powders. E.g. monodisperse, incompressible, spherical powders only reach packing densities up to 60 % to 64 % in their densest configuration [171,7]. On the other hand, the packing density is influenced by the powder flowability, which determines whether the powder can flow into its densest geometrical packing under the given flow conditions. To evaluate both effects separately the following reasoning is made. It is assumed that the ideal, densest geometrical packing is achieved at the end of a Hausner ratio measurement. The tapped bulk density thus serves as an approximation of the geometrical packing limit $\rho_{\mathrm{pk,geom}}$ (Eq. 2.2). The actual, theoretical closest packing may not be achievable within the tapping protocol. However, from a practical standpoint, this approximation is deemed sufficient.

$$\rho_{\mathrm{pk,geom}} = \frac{\rho_{\mathrm{b,tapped}}}{\rho_{\mathrm{m}}} \tag{2.2}$$

How close the layer packing approximates its maximum limit is expressed in a second, new index, the packing ratio PR (Eq. 2.3). A packing ratio below unity means that flow is limiting the particles to fall into their densest packing. A packing ratio above unity means that the stress applied by the blade or the roller applicator deforms the particles, which results in an increased packing. The definition of the packing ratio yields a strong resemblance to the Hausner ratio, described in Section 2.3.2. For both indices the bulk density of a powder is compared to the powder's tapped density. The difference lies in the definition of the bulk density, which for the Hausner ratio results from funnel flow and for the packing ratio results from a spreading procedure (Eq. 2.4).

$$\rho_{\mathrm{pk}} = \mathrm{PR}\,\rho_{\mathrm{pk,geom}} \tag{2.3}$$

$$\mathrm{PR} = \frac{\rho_{\mathrm{pk}}}{\rho_{\mathrm{pk,geom}}} = \frac{\rho_{\mathrm{b,layer}}}{\rho_{\mathrm{b,tapped}}} \tag{2.4a}$$

$$\frac{1}{\mathrm{HR}} = \frac{\rho_{\mathrm{b,initial}}}{\rho_{\mathrm{b,tapped}}} \tag{2.4b}$$

The set-up (cf. Figure 3-33) is an adjustment of a commercial Elcometer 4340 Motorised Film Applicator. The Film Applicator consists of a translational motor and a horizontal plate on which to deposit liquid films. A second horizontal plate is built on top of the existing device to create room for the vertical stage and weighing mechanism. This second horizontal plate is further referred to as the support plate. It has a rectangular hole of 14 cm by 17 cm with rounded corners to minimise edge effects upon layer deposition. Inside this hole the vertical stage is fitted, as shown in Figure 3-34. The vertical stage consists of a Newport manual vertical stage element with a precision of 10 µm. The Newport stage moves the measurement platform within a rectangular ring, which closely fits to the platform. This close fit keeps powder from falling down. The rectangular ring has a width of 1 cm, thus resulting in a measurement platform of 12 cm by 15 cm. The rectangular ring fits within the support plate, but a much wider gap is present. This wider gap makes sure that there is no friction between the support plate and the vertical stage, which sits on the balance. This enables accurate weight determination. As powder may fall through this gap or get stuck in it causing friction, the gap needs to be screened. Therefore, a thin plate with a hole that is exactly the same size as the measurement platform is placed on top of the support plate. In rest, this thin plate does not touch the rectangular ring. However, as the blade passes, it pushes the thin plate closer to the ring, creating a better seal. After the blade has passed, the thin plate relaxes again and lifts from the ring. This way the added weight of the layer can now be measured, without any external stresses on the framework.

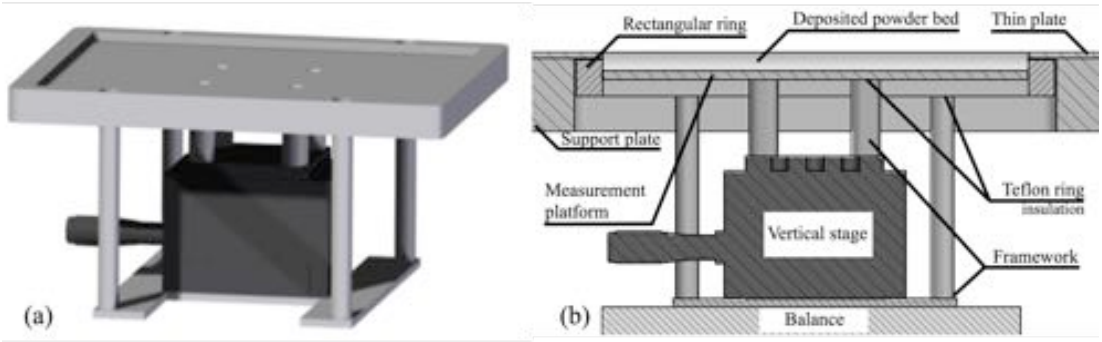


**Figure 3-34:** Illustration of the vertical stage framework (a) and its positioning within the support plate (b).

The semi-automated powder spreader has the option to exchange the used blade. Two types of blades were tested, as illustrated in Figure 3-35. The first is a simple doctor blade intended for spreading liquid films. The second is a box-type spreader, mimicked from an industrial EOS sintering machine.

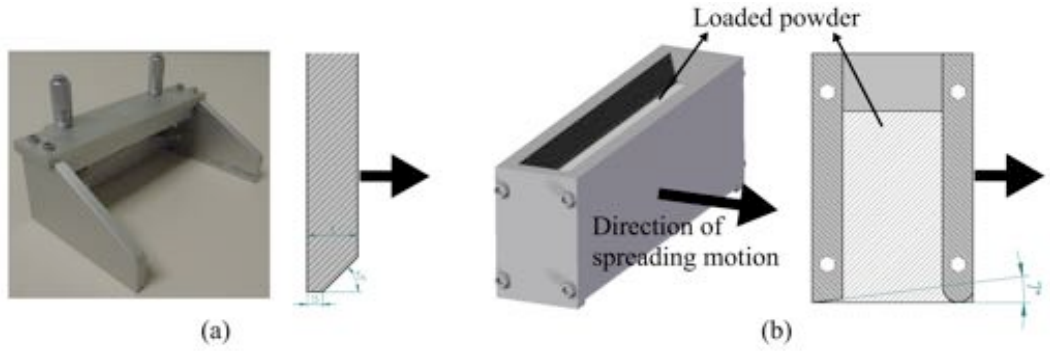


**Figure 3-35:** Blades used on the powder spreader: (a) doctor blade (b) mimicked EOS spreading box. Indicated dimensions are in mm.

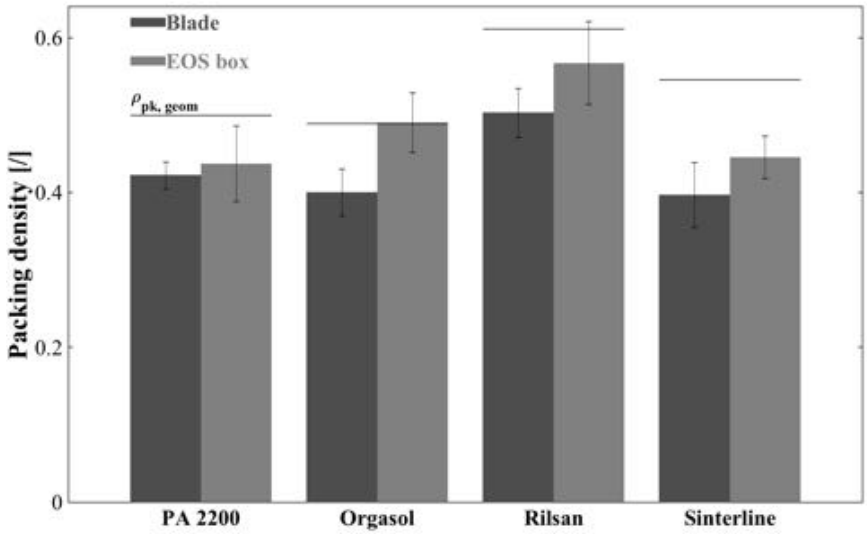


**Figure 3-36:** Packing density of individual layers for the two tested spreading tools for four polyamide powders. The error bars indicate the variation in apparent density between the different layers of a single measurement.

Tests on the polyamide powders show that the packing density is systematically higher when using the mimicked EOS spreading box in comparison to the doctor blade, as shown in Figure 3-36. In these tests, 30 layers of powder were deposited sequentially and the packing density of each layer is determined. While there is some inherent variation in the layer packing, the results clearly show an increase of the packing density for all tested powders. The reason for this difference is the compressive capabilities of the thicker wall with the inclined base, compared to the doctor blade. The inclined bottom pushes the particles into the layer and further densifies it. The improvement is the largest for the poorer flowing powders, such as

the Orgasol, which are strongly limited from achieving their densest packing due to flow limitations. The Orgasol sample is able to reach its densest packing and thus a packing ratio of unity by this blade improvement. The other powders also exhibit a denser packing, but the values of the PR remain between 82% and 93%. For the rest of this research, unless specified otherwise, the mimicked EOS spreader box is used as the default spreading tool.

Table 3-5 shows the powder spreader results for the examined powders. The spherical powders have very high PR, which means that they are able to approach their densest geometrical packing closely within the applied flow field. This is an expected result as these powders showed to flow well in the angle of repose. The PS 80 µm showed a strong variation in the packing ratio between sequential layers. For some individual layers, the packing ratio even passed unity. The reason for this phenomenon is that the 80 µm spheres are too large to fill a 100 µm layer. As a result, the layer cannot be completely filled by the spheres. The next layer therefore has the extra space of the previous layer to deposit the powder. As a result the density is seemingly higher than the closest geometrical packing. The PA samples are much more limited by flow, with the exception of Orgasol. It should, however, be noted that the spherical systems are much less affected by the chosen spreading tool, as the doctor blade provided very similar results.

**Table 3-5:** Powder spreader results for the examined powders without prior conditioning.

| Sample | $\rho_{tapped}$ [g/cm$^3$] | PR [/] | $\rho_{pk}$ [/] | Layer quality |
|---|---|---|---|---|
| **PA 2200** | 0.53 | 0.87 | 0.44 | Smooth surface |
| **PA Orgasol** | 0.50 | 1.00 | 0.49 | Smooth surface |
| **PA Vestosint** | N/A | N/A | N/A | N/A |
| **PA Sinterline** | 0.64 | 0.82 | 0.45 | Rough surface |
| **PA Rilsan** | 0.66 | 0.93 | 0.57 | Rough surface |
| **PS 20 µm** | 0.64 | 0.93 | 0.57 | Smooth surface |
| **PS 40 µm** | 0.64 | 0.97 | 0.59 | Smooth surface |
| **PS 80 µm** | 0.65 | 0.94 | 0.58 | Alternating quality |
| **PS 140 µm** | N/A | N/A | N/A | Larger than layer |
| **PMMA 20 µm** | N/A | N/A | N/A | N/A |
| **PMMA 30 µm** | N/A | N/A | N/A | N/A |
| **PMMA 40 µm** | 0.75 | 0.98 | 0.62 | Smooth surface |
| **PMMA 60 µm** | N/A | N/A | N/A | N/A |

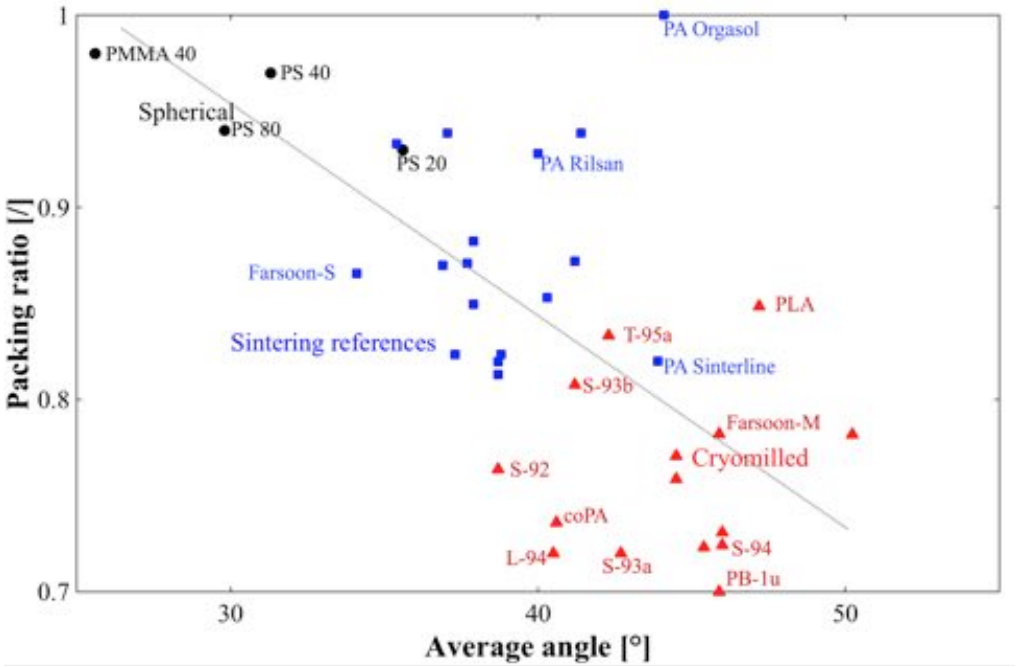


**Figure 3-37:** Comparison of the packing ratio and average angle. Powders of Chapters 4 and 5 are included. Unlabeled markers represent undisclosed sintering powder that are not further discussed in this work.

A comparison of the results on the DAoR and powder spreader now allows the evaluation of the DAoR as a flow analysis tool for LS. Figure 3-37 shows the comparison of indices obtained in both techniques. The figure includes also the powders examined in Chapters 4 and 5 to provide a more extensive evaluation of the techniques. Details on the results of those powders can be found in their respective chapters. It is seen that the angle of repose gives a first indication on flowability, as powders with a low angle of repose tend to have higher packing densities. There is however a large spread to this relation, as illustrated further by the Orgasol powder that achieves very dense packing, although it has poor flow behaviour in the rotating drum. Both techniques also tend to sort the powders in their three different groups. The spherical powders are found in the top left corner of the graph, with low angles and high packing. The strongly irregular, cryomilled powders, which are further discussed in Chapter 4, group at the bottom right of the graph at high angles and relatively low packing. Finally, the reference sintering powders, which are typically more smooth, such as the precipitated PA samples, score in between the other two groups. PA Sinterline sits among the cryomilled powders, as it is also an irregular, likely milled sample.

The relation between the DAoR and powder spreader is further investigated by looking at the effect of flow improvers on powder flowability of PA 2200. The effect of additives is tested with the doctor blade set-up, as earlier tests showed the largest improvement being possible for this tool. The same three additives were used

as in the DAoR measurements of Section 3.3.2. Similar results are, however, expected for the EOS spreader box. The addition of very small amounts of flow improvers creates a significant improvement of the packing, as shown in Figure 3-38. Similar trends are seen as in the DAoR measurements. Additives A and B again show an optimum concentration around 0.5-1 wt%. Additive C also creates an improvement on the packing, but the optimum is not seen within the tested concentrations. A final remark has to be made on the strong variation of the data points. This is the variation between individual layers. It indicates that there is a strong fluctuation in the measured layer density, which could be the result of suboptimal distribution of the additives in the powder. The additives were added to 200 g of the base powder, after which this was agitated for several hours on a rotating bench. An improvement in this mixing procedure could involve two adjustments: (1) The additive could be added to the mixture through a sieve to avoid agglomeration of the micron-sized particles and thus create a better distribution. (2) Instead of adding the flow improvers to the entire mixture, it could be mixed with a smaller amount of powder before adding to the rest of the batch. This generally improves the distribution and avoids the additive particles from sticking together after adding them.

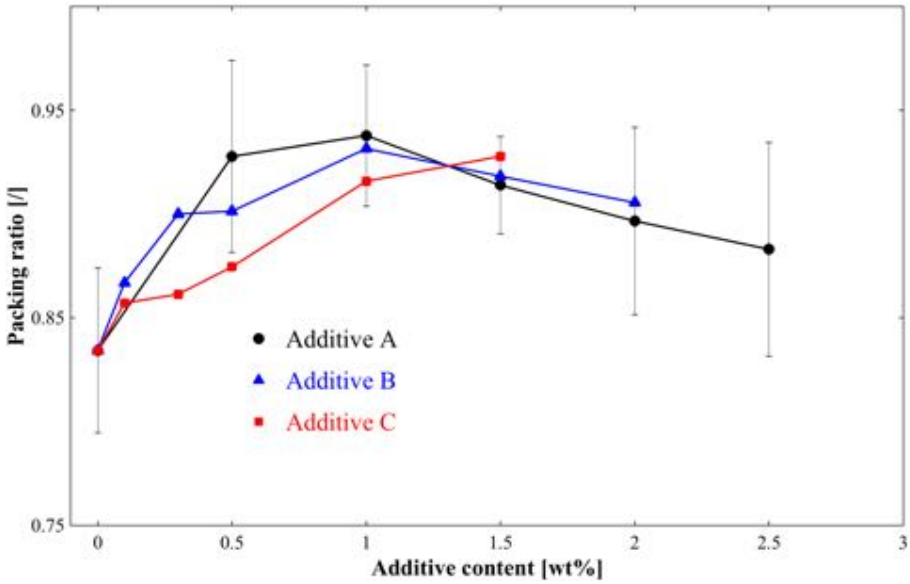


**Figure 3-38:** Effect of additives on the packing of PA 2200. Error bars are only added for additive A to improve readability. The error bars of the other additives are similar in magnitude.

In conclusion, the DAoR provided a useful first screening of powders. It can indicate certain flowability trends, such as the effect of adding flow improvers. However, on its own, the DAoR did not succeed in fully predicting the achievable layer density for LS, due to the limited relevance of the flow field. This relevance may be higher for a roller, as discussed in Section 2.3.4. Therefore, the powder

spreader is a useful addition to the testing protocol, as it gives directly applicably indices to rank the powders for blade-based spreading mechanisms.

### 3.5.2 Thermal control

*Passages from this section, including figures, have been adapted from an own, published conference paper*[170].

As discussed in Chapter 1, the spreading of powders in an actual LS machine happens at strongly elevated temperatures. Therefore, the powder spreader set-up is expanded to include thermal control. To have similar thermal control as in an LS machine, radiant heaters were chosen. Two 650 W ceramic heaters are placed above the powder bed to provide the best possible heat distribution over the bed surface. A thermocouple is positioned at the top layer of the powder bed. To ensure a steady location when lowering the measurement plate, the thermocouple is inserted between the support plate and the thin plate. This thermocouple provides an input signal for a PID control loop that controls the heaters via a solid-state relay. The control is set to a desired setpoint, with alarm limits at 3 °C above and below this setpoint. The powder is loaded next to the measurement platform. Thereby, due to the radiation of the heaters, this powder is also slightly heated, but to a lower temperature than the powder bed. This is deemed representative for the LS process, as LS machines either preheat the powder to a lower temperature, or have no active preheating for the powder. In the latter case the powder tends to heat up slightly due to the radiation from the heaters and/or the conduction from the powder bed. A glass box encases the entire device, with an opening in the front for operator interaction. This encasing improves the temperature control.

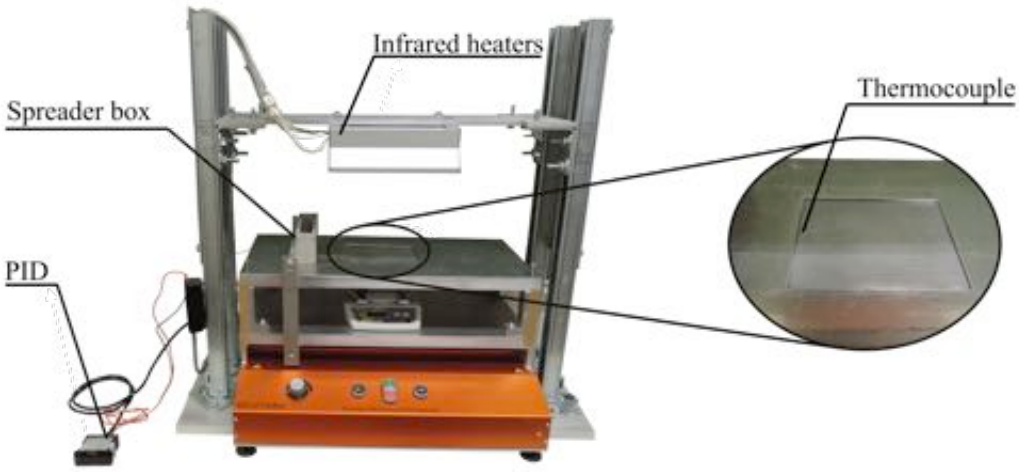


**Figure 3-39:** Picture of the powder spreader temperature expansion.

The uniformity of the heating was tested for various setpoints. One thermocouple, placed as shown in Figure 3-39, forms the input for the PID controller. An external

thermocouple measures the temperature at various spots in the layer. The results for 90 °C and 120 °C are shown in Figure 3-40. It is seen that close to the thermocouple of the PID control the temperature is in the range of the setpoint. Some variation on the measurement of the external thermocouple is expected, as the recorded temperature is dependent of its penetration depth in the bed. However, the general trends of the surface temperature are the same for both setpoints. Hot spots are seen directly below the lamps. The temperature distribution is, however, deemed sufficient to obtain a first indication of flowability at elevated temperatures. To get a more detailed indication of exact temperatures at which flow changes, the temperature control of the powder rheometer thus still provides an added advantage for LS powder flowability evaluation.

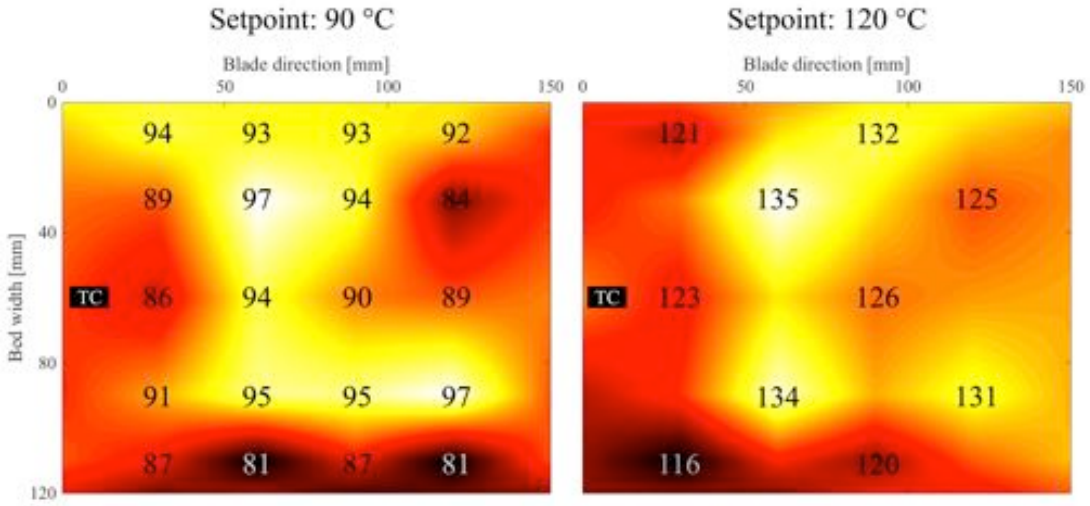


**Figure 3-40:** Thermal control of the powder bed surface. Measured temperatures at fixed locations are indicated in degrees Celsius and temperatures at other locations are interpolated to form a full thermal mapping. "TC" indicates the location of the PID thermocouple.

The effects of temperature and moisture on powder flow in the powder spreader have a certain interaction. Figure 3-41 illustrates this interaction for PA 2200. At ambient conditions, each layer has a packing density around 0.44, as was shown in Table 3-5. Upon drying, however, the packing increases to 0.50, which corresponds to the PR limit of unity. This indicates that the moisture content at ambient conditions hinders flowability significantly and that charging is not problematic. The latter is likely due to the extensive contact with conductive parts and the short spreading times resulting in limited friction. However, after spreading 30 layers, which takes roughly 30 minutes, the powder has taken up the moisture again, as illustrated in Figure 3-41b. As a result also the packing density drops down to the value of the sample that was not pre-dried. Layers that are spread at 90 °C also show a packing density of 0.50. At these temperatures, the radiant heating

evaporates the moisture from the powder. As a result, there is no drop to lower packing densities in time. Due to the drying effect during layer deposition, there is no significant difference between pre-dried or non-conditioned powder, as long as the powder can equilibrate near the heaters. This example thus shows that care needs to be taken when comparing the effect of temperature. At 140 °C, a slight drop in flowability is seen, likely due to softening of the particles.

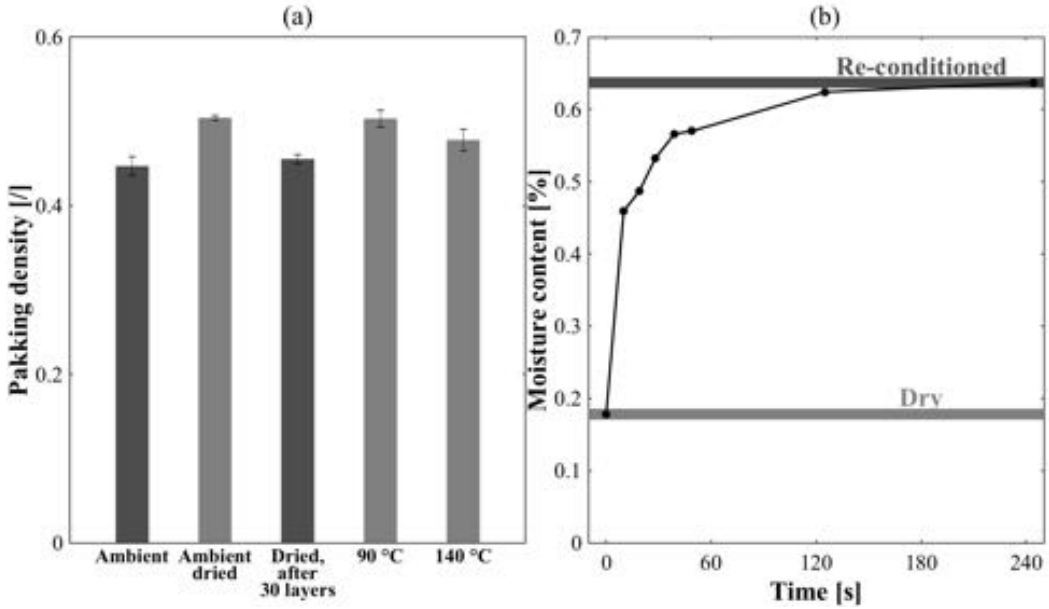


**Figure 3-41:** Results of PA 2200 powder flow on the powder spreader at elevated temperatures (a) and the relation to moisture content (b).

The drop in packing density occurs at higher temperatures than the onset of the increase in the flow energy that was measured in the powder rheometer. In those measurements, a continuous decrease in flowability was seen past the glass transition. A possible explanation for this difference is the actual difference in the powder temperature. In the powder rheometer, all powder is equilibrated at the same temperature. In the powder spreader, however, only the already deposited layer is at the setpoint temperature. The powder that is being spread is at a lower, less controlled temperature. The interaction in the powder spreader is therefore between particles of different temperatures.

### 3.5.3 Automated powder spreader

Based on the previous version of the powder spreader, a new fully automated version is built. This updated version has several improvements over the semi-automated version. These improvements can split up into two categories: automation of the actions needed for the measurement and improved environmental control by full enclosure of the system.

The semi-automated powder spreader has several steps that required operator interference. The operator needed to (1) load the powder, (2) press the motor buttons to start the spreading and manually lift the spreading box to its starting position, (3) set the measurement platform to the correct height and (4) note down the observed weight. These steps lead to operator variability, such as a varying amount of powder being loaded and a varying time between layers. Moreover, the manual actions of the operator require strict safety precautions, especially when the IR heaters are active. The goal of the automated set-up is to remove these manual steps and create a continuous measurement that can measure up to 50 layers without operator interference. The next paragraphs describe how each of the four manual steps is implemented in the new design. General dimensions of the set-ups, such as the size of the measurement platform and spreading speed are kept the same as in the original design, to minimise differences between the two set-ups. The full design is shown in Figure 3-42.

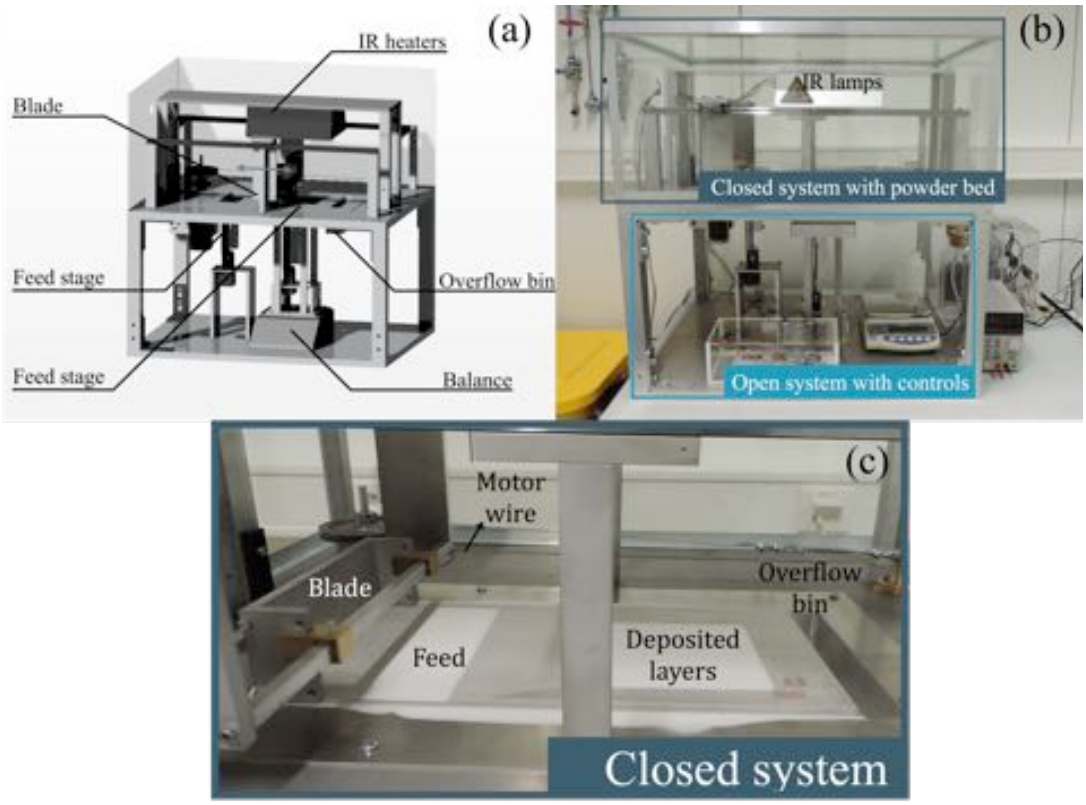


**Figure 3-42:** Schematic (a) and pictures (b-c) of the automated powder spreader.

Loading of the powders is achieved by a vertical stage that pushes up powder in front of the spreading blade. This is similar to the feeding mechanism of DTM Sinterstations, as discussed in Section 2.1.3. A feed stage, loaded with powder, moves up a pre-defined increment prior to spreading. This way a controlled and reproducible amount of powder is used in each cycle. A bipolar stepper motor, controlled by an Easy Driver, which is connected to an Arduino Uno board, controls

the linear feed stage. A program written in Arduino synchronises the movement of all mechanical parts in the set-up.

The blade movement is operated by a similar control system. A stepper motor connected to a pulley system creates a translational movement for the blade at 14 cm/s. The blade, which is fully attached to the pulley system, thereby scrapes from the feeding platform over the measurement platform to an overflow bin before it returns to its starting position. The spreading blade is similar to the spreader box, which is used for the semi-automated spreader. The front wall of the box is removed to facilitate the powder feeding in front of the blade. As no operator interference is needed anymore for the powder spreading operation, the measurement platform and feed stages can now be completely encased, enabling better temperature control. Furthermore, this improves safety for the operator, who no longer needs to interact with the blade or heaters.

The measurement platform is controlled in a similar fashion as the feed stage. Its precision enables a controlled movement to create layers of 100 µm. As the blade moves back to the starting position, the feed stages lowers another 500 µm to avoid interaction between the deposited powder and the returning blade. After the blade has returned, the platform raises 400 µm to create the desired layer height of 100 µm for the next spreading step. The automation of the measurement platform aids in the thickness control of the layers, which are no longer dependent on the precision applied by the operator.

Finally, the weighing is automated. The balance below the measurement platform is connected to a PC to provide a live feed of the layer weight, which records the weight every two seconds. Fluctuations in the weight are seen as the blade passes and delivers additional pressure to the balance. Therefore, in post-processing, the equilibrium weight at fixed time intervals needs to be extracted from the raw data.

To ensure that all results in this thesis are directly comparable, all spreading measurements in this thesis are performed on the same device. As the fully automated powder spreader was created near the end of the research, all data was already available on the semi-automated set-up. A proof of concept was performed on the new fully automated spreader, which was able to spread PA 2200 with a similar quality as the semi-automated version.

## 3.6 Conclusions

Three newly build set-ups for assessing powder flowability have been successfully tested on both sintering PA and spherical reference systems. Table 3-6 summarises the most important aspects of the three set-ups.

**Table 3-6:** Summary of the advantages and disadvantages of the developed powder flow measurements.

| | **A-DAoR/ T-DAoR** | **Powder rheometer** | **Powder spreader** |
|---|---|---|---|
| **Sample volume** | 12 ml | Ca. 80 ml* | Ca. 200 ml |
| **Measurement time**** | 2 min | Ca. 50 min | 30-60 min |
| **Thermal control** | Yes, charging issues | Yes, strong control | Yes, limited accuracy |
| **Temperature range** | 20°C – 150 °C | -20 °C^ – 150 °C | 20 °C – 200 °C |
| **LS relevance** | Medium | Medium (absolute indices) High (*T* changes) | High |
| **Ease of use** | High | High | Medium |
| **Triboelectrification issues** | Yes | No | No |
| **Humidity control** | Pre-conditioning, sealed container | No | No, implementation available^^ |
| **Main selling point** | Fast and easy first screening | Accurate and precise *T* control | High relevance for LS |

*40 g of sample. The corresponding volume thus varies.

**For one measurement at ambient conditions, not counting overhead time for starting up or referencing the device.

^Complications with moisture at decreased temperatures.

^^Cf. Appendix B for more details on the available on-line humidity control set-up.

The dynamic angle of repose set-up is able to indicate general trends on powder flowability, including the assessment of flow improvers. However, it is not able to give a definitive ranking for the resulting behaviour in spreading. Some powders, such as the PA Orgasol, scored poorly in the DAoR set-up, but managed to spread into smooth and dense layers. A thermally controlled DAoR is built, but the extensive friction in an insulating measurement cell gives rise to severe triboelectrification issues.

A commercial liquid rheometer is expanded with a powder cell set-up to include the measurements of powder flowability at an elevated temperature. The accurate temperature control enables the study of relative changes in the flowability, which

may affect the thermal window for the powder bed. The conductive powder cell used in this set-up managed to avoid triboelectrification issues. PA 2200 showed a steady increase in the flow resistance with increasing temperature past its glass transition temperature. The increase was small, however, as expected from its use in LS machines at elevated temperatures.

The powder spreader, which is newly developed for this research, is able to mimic the flow field within an EOS-type sintering machine. Two versions are built, namely a semi-automated and a fully automated set-up, and temperature control is added to both. The higher sample volume and operating time make this technique the most suited for a final ranking of powder flowability prior to full-scale sintering tests. The thermal control provides a reasonable indication of thermal effects, but its temperature control is less accurate than that of the powder rheometer.

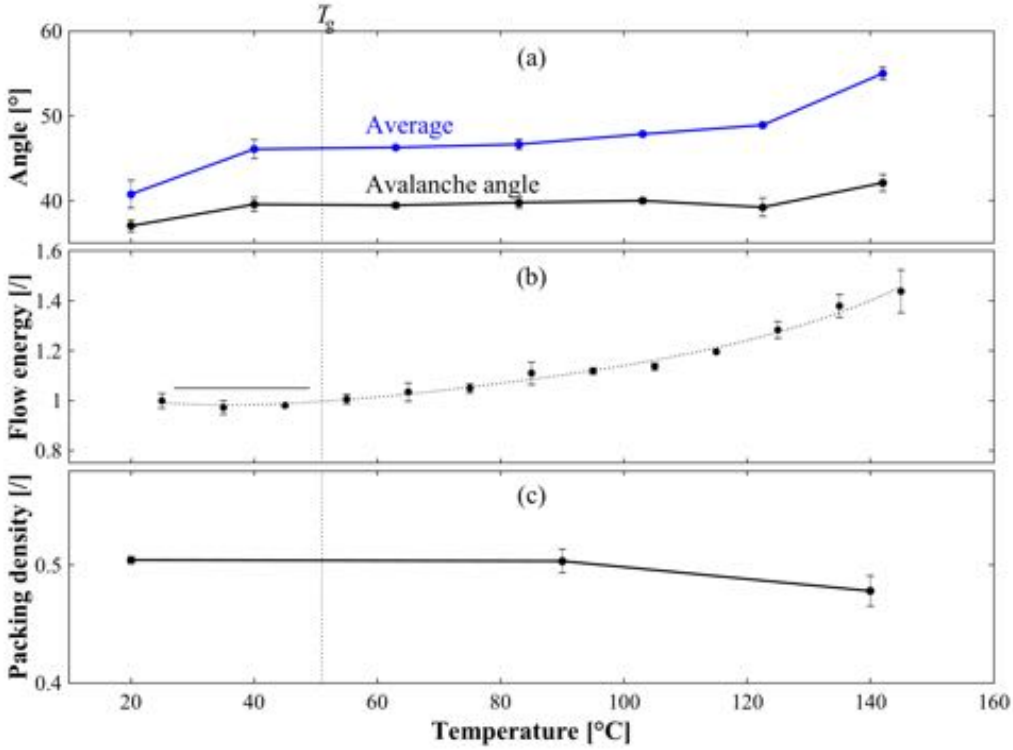


**Figure 3-43:** Comparison of the thermal results for the T-DAoR (a), powder rheometer (b) and powder spreader (c).

Figure 3-43 summarises the thermal effects the powder flowability of PA 2200, measured by the T-DAoR, powder rheometer and powder spreader. All three techniques give a similar result, namely a slight decrease in flowability, but the onset temperature differs. As discussed in the previous paragraph, the powder rheometer predicts a slight increase in flow resistance above the glass transition temperature. This effect is also seen in the T-DAoR, as especially the avalanche angle shows a steady increase. However, it is hard to quantitatively separate this

effect from tribo-electricication to determine the exact onset. The powder spreader shows a similar decrease in flowability in function on the powder bed temperature. This loss in flowability namely translates to a decrease in the packing density. The onset of this decrease is, however, at higher temepratures, compared to the powder rheometer. A possible explanation for this shift is the inherent non-isothermal nature of the spreading. The powder in the feed is at a much lower temperate than the powder bed, and has thus not increased in stickiness yet.

The next two chapters utilise these flowability measurements, together with measurements that assess coalescence, solidification and recyclability, on new powders intended for LS. Chapter 3 assesses the flowability of new grades of current LS polymers, namely PA and TPU. These new grades are introduced as cryogenically milled powders. Chapter 4 then expands the LS material palette with polymers that are currently not commercially used, such as polybutene-1 (PB-1) and polylactic acid (PLA).

# Chapter 4

# Cryomilled powders in laser sintering

This chapter further investigates the use of cryogenic milling, further referred to as cryomilling, for the creation of LS powders. Many cryomilled materials are assessed during the course of this research. This chapter focuses on polymers that are commonly used in laser sintering, namely polyamide (PA) and thermoplastic polyurethane (TPU). This way, a comparison is made between the commercial "smooth" powders, which often result from precipitation, and the powders obtained by cryomilling. Chapter 5 then looks at some newer materials for LS, such as polylactic acid (PLA), polybutene-1 (PB-1) and a copolyamide (coPA).

Section 4.1 provides a brief overview of the cryomilling process. It details the needed background to assess this production technique for use in LS. Section 4.2 then describes the additional lab measurements that are used to assess the powders of this chapter. The measurements that are described in Chapter 3, such as DSC and rheometry, are further applied with the same protocols, unless specifically stated otherwise. Finally, Sections 4.3 and 4.4 discuss the materials that are evaluated. Section 4.3 focuses on the most relevant material for LS, namely PA. The section examines the differences between a cryomilled and a precipitated powder of similar grades. Section 4.4 discusses cryomilled TPU. A wide variety of grades within this material class is evaluated in order to add new TPU grades to the LS market.

## 4.1 Powder production – Cryogenic milling

Various production routes exist for creating powders. Some polymers are formed as a powder directly in the reactor after polymerisation [172,173]. This generally yields quite smooth powders. However, most commercial thermoplastic polymers are not available as a reactor powder, but rather as pellets. Hence, further processing to a powder is needed. Two main strategies exist for doing this. These are referred to as constructive or destructive strategies [7]. The constructive strategy "builds up" the particles. Precipitation is a typical example of a constructive strategy. This process dissolves the polymer and then precipitates it again in powdered form. Depending on the system, strongly elevated temperatures or pressures may be required [174]. Examples of implementation of this process are spray drying [175,176] and precipitation by rapid expansion of a supercritical solvent [177]. The destructive strategy starts from a larger mass of material and breaks it down to the desired particles. Mechanical grinding/milling is a common example of this strategy [178]. Typical milling set-ups are ball-milling, a batch technique in which metal balls are added to a vial of polymer pellets prior to intensive agitation [179,180,176], and rotor milling, a (semi-) continuous technique in which the pellets are broken down by high speed rotor blades [176].

Each of the two strategies for obtaining a powder has both its merits and disadvantages. The solution-based strategies typically yield smoother powders, which in return provide better flowability properties. The big drawback is, however, the availability of usable solvents. Many polymers only dissolve in very specific solvents or conditions, meaning that a new dissolution process has to be chosen and optimised for each new polymer. Furthermore, most of these solvents pose serious health, safety and environmental issues, restricting their use in practice. This is in contrast to the milling strategies, which inherently lead to very irregular, and typically broad, particle size and shape distributions, as illustrated in Figure 4-1, which as a result pose a strong limitation for good powder flowability and resulting part quality [178,181]. However, none of the aforementioned solvent-issues apply for these strategies, resulting in a more generally applicable method for a wide variety of polymers. For this reason, the milling strategy is chosen within this research. The study of powder flowability for these inherently irregular powders is thus fundamental to obtain quality products.

Milling has, however, one big limitation. Due to the strong mechanical deformation and friction, a lot of heat is added to the system. The (local) temperature increase due to this heating results in softening, plastic deforming and, worst-case, melting of the polymer, which is detrimental for the final particle shape, as illustrated in Figure 4-1c. A solution to this problem is cryogenically cooling the system during milling. This is known as cryogenic milling or cryo-milling. In this process, the decrease in

temperature promotes brittle fracture and prevents melting of the polymers [182]. Cryogenic processing conditions usually refer to the use of temperatures around -196 °C (77 K), typically obtained by liquid nitrogen [183].

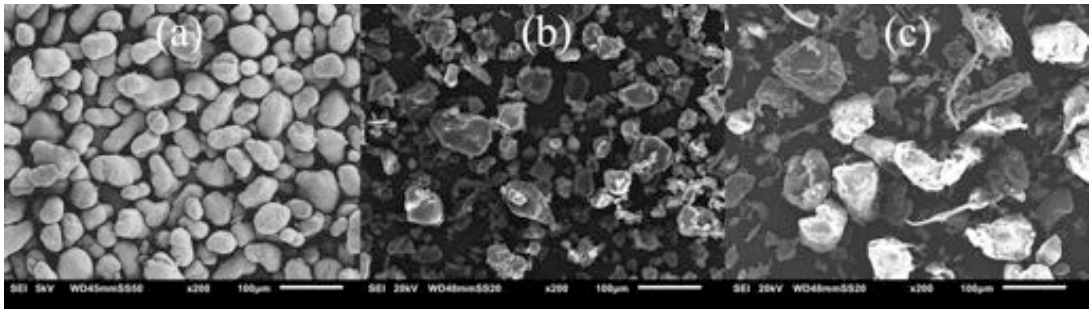


**Figure 4-1:** (a) typical smooth reactor powder, (b) rough cryo-milled powder and (c) cryomilled powder with strong plastic deformation.

An external partner performed all the cryomilling work for this research on an industrial scale. A strong collaboration was, however, set-up to optimise the milling parameters as efficiently as possible based on lab-scale measurements such as Differential Scanning Calorimetry (DSC). Exact milling parameters are not taken up in this text due to the intellectual property belonging to the industrial partner.

To obtain the correct particle size (range) a sieving step is necessary at the end of the milling line. Practice learns that this is the limiting step in the process from a powder flow perspective. Some powders tend to clog the fine sieve mesh, thus stopping the production. This problem is increased by water condensation as a result of the decreased temperatures. To solve the issue, flow improvers are added to the material. These are typically small silica-based particles, which not only sit between particles to change the contacts, but also tend to preferably take up the moisture. These foreign particles will not only have an effect on the flowability in laser sintering, but also on other sintering properties. They thus need to be taken into account for the assessment.

## 4.2 Methods

Three additional lab measurements are used to assess the powders in this chapter. Firstly, hot stage microscopy (HSM) measurements aid in the validation of the coalescence behaviour of the powders. Secondly, mechanical testing methods are added to provide an estimate of the attainable product properties. The description of the other techniques that are used in this chapter are found in Section 3.1.

### 4.2.1 Hot stage microscopy (HSM)

Hot stage microscopy (HSM) aids in the evaluation of coalescence behaviour. The used set-up consists of a CSS450 shear cell (Linkam Scientific), which is applied without any shear. Powder is loaded on a heated borosilicate glass plate, after which a lid closes off the system, thereby creating a micro-environment in the cell. The maximal attainable heating rate of 30 °C/min is applied. There is some thermal lag present at these heating rates, which is dependent on the temperature range of the test. This lag is, however, limited to a few degrees for all measurements described in this work. The HSM measurements are intended to provide a mainly qualitative evaluation of the coalescence behaviour, which complements the quantitative results of the melt rheology tests (cf. Section 3.1.4).

### 4.2.2 Tensile testing

Tensile tests are performed on compression moulded tensile bars to provide an estimation on the attainable product properties. These properties are then compared to those of sintered bars in the case of sinterable materials. The tensile tests are performed on an Instron 5567 Load Frame with a 1 kN load cell at ambient conditions. The dimensions of the tensile bars are shown in Figure 4-2. Two sizes of tensile bars are used. The first version (Figure 4-2a) is a small bar, which minimises the required material. To provide comparable results, this bar is used for all materials except for the TPU. For the TPU, a larger bar (Figure 4-2b) is chosen. This specimen is the recommended geometry for non-rigid plastics according to ASTM D 638 [184]. As indicated by ISO 37, which handles on vulcanised and thermoplastic rubbers, smaller tensile bars tend to give an overestimation on the tensile strength and elongation at break [185]. This standard recommends similar testing specimens as the ASTM counterpart, i.e. the larger bar, but suggests a larger width for the grip ends. The larger bar is therefore deemed the most suited for the TPU samples.

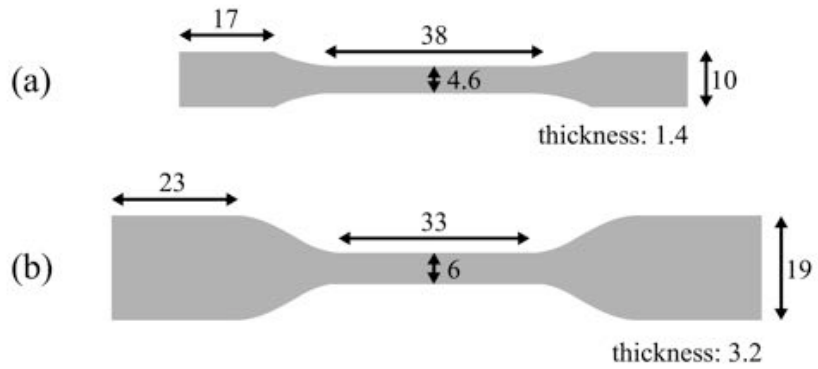


**Figure 4-2:** Schematic of the used tensile bars: standard bar (a) and larger bar for rubbers (b). All dimensions are in mm.

Depending on the elongation properties of the sample, an adequate strain rate is chosen. A too high strain rate results in sudden, uncontrollable fracture. A too low strain rate, on the other hand, results in creep, which provides a strong overestimation of the actual attainable strains. ASTM D 638 recommends the use of a rate that results in fracture of the material within 0.5 min to 5 min [184]. As a result, the strain rate is adjusted between 1 mm/min and 50 mm/min, dependant on the elongational properties of the sample.

## 4.3 Polyamide (PA)

The first material of this chapter is polyamide (PA). As stated in Chapter 2, PA is the reference material for LS applications. Many grades of this material are already commercially available and are thus extensively investigated in literature [3,73]. The goal of this section is therefore not to add a new material to the LS palette, but rather to evaluate whether a PA powder that is obtained via cryomilling can compete with the already available PA powders. A positive evaluation of the cryomilling processing route opens the possibility to apply it to other polymers.

The PA grade that was chosen is FS 3300PA, which is a commercial sintering PA12 powder by Farsoon Technologies. This particular grade is interesting for this research as it is available in both powder and pellet form, which makes it an ideal material to evaluate the cryogenic milling route. The commercial powder is likely created via a precipitation process, resulting in a smooth morphology, as illustrated in Section 4.3.1. To distinguish both samples, the commercial sintering powder is further referred to as the smooth powder, Farsoon-S, and the milled grade is referred to as Farsoon-M.

### 4.3.1 Powder characterisation

Table 4-1 and Figure 4-3 summarise the particle and material properties of both Farsoon PA powders. SEM images (Figure 4-3b) prove that Farsoon-S contains smooth particles, similar to other typical sintering PA, such as PA 2200. The milled sample, on the other hand, has a much rougher and more irregular morphology, which is likely to negatively impact flow properties, as further investigated in Section 4.3.2. Particle size analysis shows that Farsoon-S has a relatively narrow PSD, which is comparable to that of PA 2200. The low amount of fines, i.e. particles below 30 µm, is expected to have a positive effect on flowability. Furthermore, no particles larger than the layer thickness (100 µm) are present. Farsoon-M has a slightly wider distribution, including about 10 % of particles below 30 µm, which generally have a negative impact on flowability, as discussed in Chapter 3.

**Table 4-1:** Summary of the particle properties of the PA powders.

| Sample | $D_{10}$ [µm] | $D_{50}$ [µm] | $D_{90}$ [µm] | relative span [/] | $\Psi$ [/] | Bo [/] |
|---|---|---|---|---|---|---|
| **PA 2200 (Chapter 3)** | 39.5 | 63.4 | 82.2 | 0.67 | 0.86 | 1.49 |
| **Farsoon-S** | 36.9 | 55.1 | 78.7 | 0.76 | 0.87 | 1.83 |
| **Farsoon-M** | 31.3 | 63.3 | 92.7 | 0.97 | 0.81 | 1.57 |

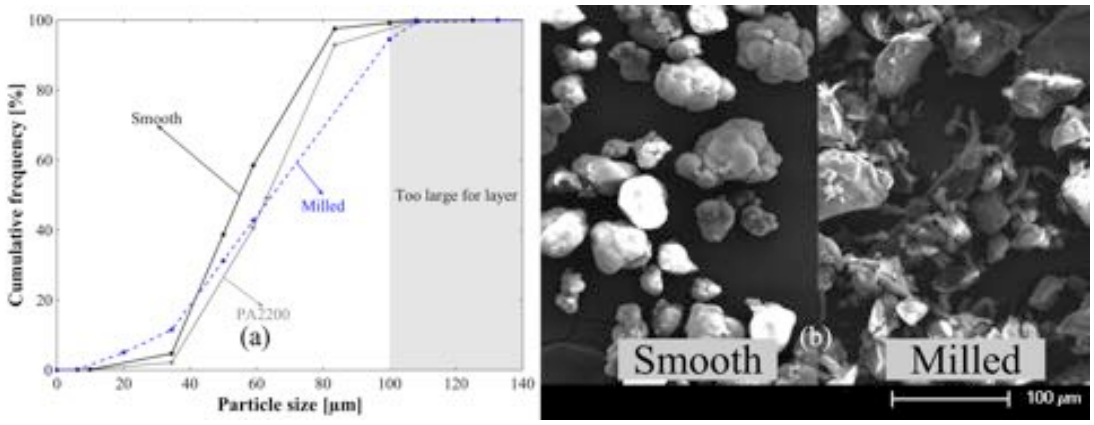


**Figure 4-3:** PSD of both Farsoon PA samples, compared to PA 2200, (a) and their corresponding SEM images (b).

Next the material density of both samples is determined via Archimedes' method (Table 4-2). Farsoon-S has a density of 1.08±0.005 g/cm$^3$, which is slightly higher than the density of the milled powder, which is 1.05±0.002 g/cm$^3$. The difference may be due to a difference in crystallinity, which in turn originates from the difference in production route. Furthermore, some undisclosed alterations to the chemical structure may have been performed by the manufacturer to facilitate their powder creation process.

**Table 4-2:** Summary of the physical properties of the PA powders. The Hamaker constant is taken for a generic PA to allow comparison of the Bond number.

| Sample | $\rho_m$ [kg/m$^3$] | $A_h$ [J/10$^{20}$] |
|---|---|---|
| **PA 2200 (Chapter 3)** | 1.07 ± 0.001 | 7.9 [87] |
| **Farsoon-S** | 1.08 ± 0.005 | 7.9 [87] |
| **Farsoon-M** | 1.05 ± 0.002 | 7.9 [87] |

The difference in crystal structure is further shown in DSC measurements (cf. Figure 4-4). As a result, the thermal processing window for both materials differs slightly. Both materials have a relatively sharp crystallisation peak at roughly the same temperature. As both materials contain an unknown amount of flow improvers, these are likely to effect the location of the crystallisation peak due to nucleating effects. The melting peaks are, however, quite different. Farsoon-S has a sharp melting peak with a relatively wide onset. Farsoon-M, in contrast, has a smaller melting peak, but it contains a shoulder that stretches to the crystallisation temperature. A priori, it is uncertain whether this shoulder negatively influences powder flowability. Thermal treatments may be able to remove this shoulder, as is demonstrated for different materials in Chapter 5. However, as further indicated in Sections 4.3.3 and 4.3.4, post-condensation, combined with the relatively high starting viscosity of the milled grade, hinders the use of thermal pre-treatments. The thermal windows estimated from DSC measurements are only around 10 °C for both materials, which is very small for a sintering material. They may, however, be larger if no severe powder stickiness is induced within the melting onset.

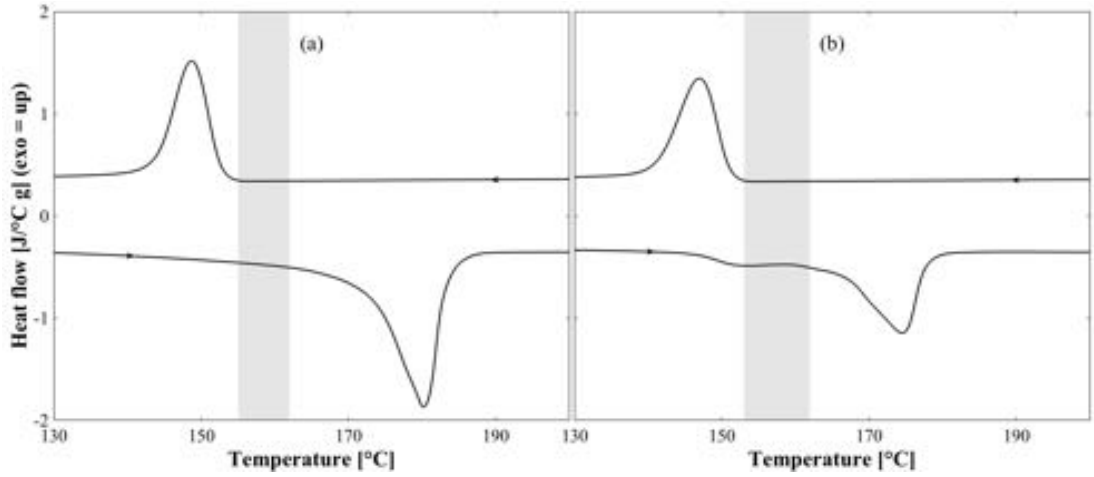


**Figure 4-4:** DSC measurements Farsoon-S (a) and Farsoon-M (b) at 10 °C/min. The grey zones indicate the available thermal window for the powder bed.

## 4.3.2 Powder flowability

Based on A-DAoR measurements, the Farsoon-S powder exhibits slightly better flow properties than the PA 2200 reference, as shown in Table 4-3. Not only does it possess very low heap angles, the avalanche and average angle are very close together, which indicates smooth continuous flow. This is expected from the smooth particle morphology and the lack of fine particles, as shown in Figure 4-3. The smooth flow translates to a relatively straight and constant powder interface in the rotating drum (Figure 4-5a). Farsoon-M on the other hand, shows much higher

angles. The average angle is around 45°, which is common for cryomilled materials, as further illustrated in Section 4.4.4. The flow is much more irregular, as lumps of powder slide down during the test (Figure 4-5b).

**Table 4-3:** Powder flowability indices based on the dynamic angle of repose (A-DAoR) and spreading experiments for PA Farsoon and PA 2200.

| | $\widehat{\phi}$ [°] | $\widehat{\phi_a}$ [°] | $\rho_{pk,geom}$ [%] | $\rho_{pk}$ [%] |
|---|---|---|---|---|
| **PA 2200 (Chapter 3)** | 36.6 ± 0.3 | 40.0 ± 0.3 | 51 | 44 ± 5 [73] |
| **Farsoon-S** | 34.1 ± 1.5 | 36.9 ± 1.9 | 54 | 48 ± 3 |
| **Farsoon-M** | 45.9 ± 1.3 | 53.1 ± 2.0 | 56 | 44 ± 3 |

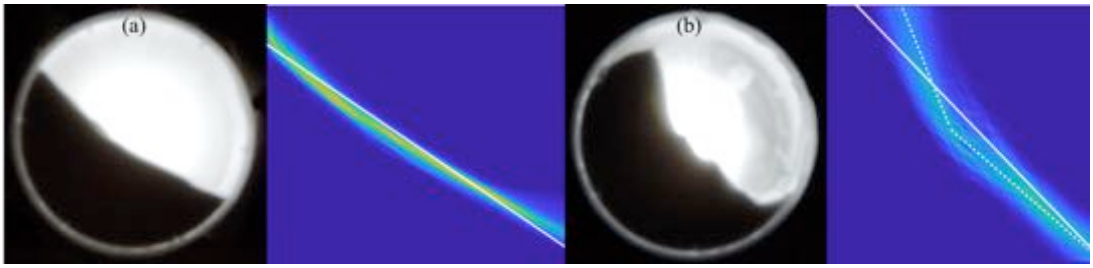


**Figure 4-5:** Representative A-DAoR frames of Farsoon-S (a) and Farsoon-M (b) and the respective edge heat maps of the full measurement.

The poorer flow results of Farsoon-M in the A-DAoR, however, do not translate into inadequate spreading properties, as illustrated in Figure 4-6. Farsoon-S and Farsoon-M have a tapped density of 0.574 g/cm$^3$ and 0.600 g/cm$^3$ respectively. The ratio to the material density of each material (Table 4-2) yields maximal packing densities of 56 % and 55 % respectively, which are not significantly different. When spreading the material into layers, however, the Farsoon-S powder has a packing density of 48 %, but Farsoon-M only reaches 44 %. The deviations reported in Table 4-3 are those for the inter-layer variability. When comparing different spreading experiments that all consist of at least 20 layers, the found packing densities are fully reproducible. As a result, the difference in the packing density is significant. This means that the reduced flowability of Farsoon-M hinders the material to approximate its densest packing. However, this reduced packing is still comparable to that of the reference PA 2200 and is thus deemed sufficiently high for LS. Furthermore, no defects are noted in any of the deposited layers of either sample. The experiment thus proves that the rough particle morphology obtained via cryomilling is not problematic for the required powder flowability in LS.

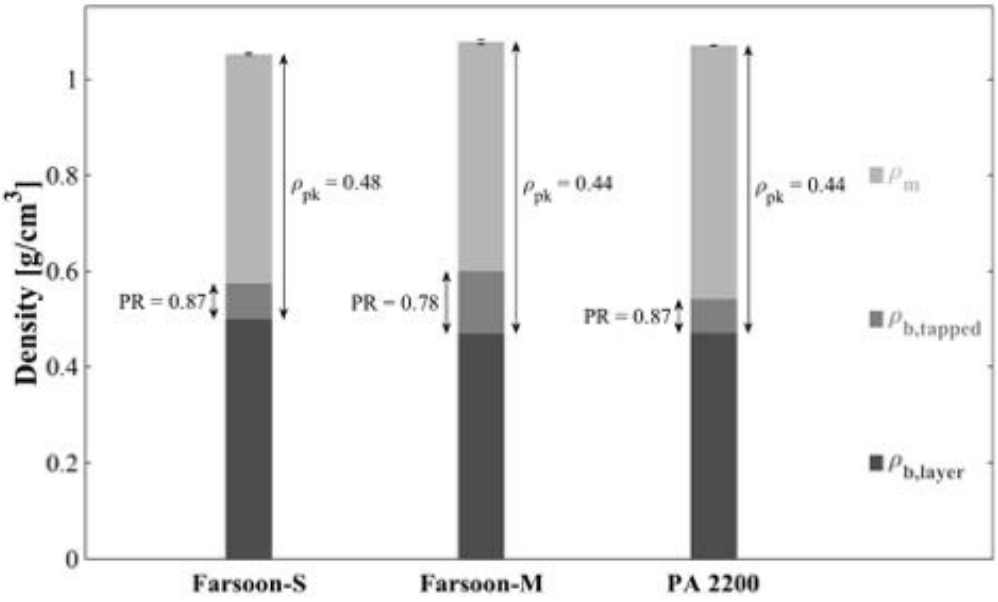


**Figure 4-6:** Summary of the measured densities and resulting ratios in spreading experiments of the examined PA grades.

As the current set-up of the powder rheometer is not able to achieve temperatures above 150 °C, it is not possible to determine the powder stickiness of these samples via this technique. No steep increase in flow energy is seen below 150 °C, as shown in Figure 4-7. The Farsoon-S sample shows a slight, continuous increase in flow resistance with increasing temperatures above the glass transition temperature. This result is similar to the findings of PA 2200 (Section 3.4). Furthermore, the experiment independently shows the decreased flowability of the milled sample, as the flow energy for Farsoon-M is about 40 % higher.

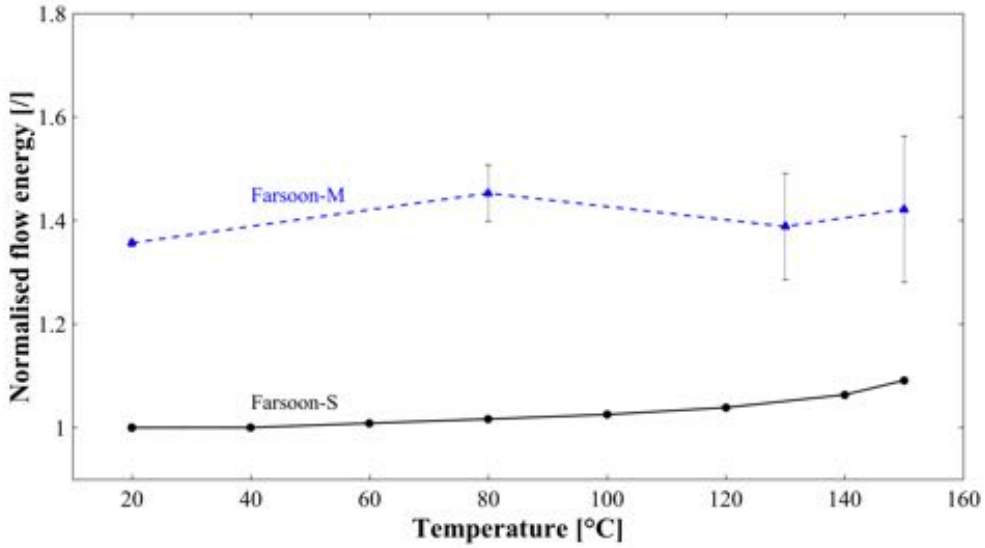


**Figure 4-7:** Powder rheometry results of Farsoon-S and Farsoon-M. All flow energies are normalised to the value of Farsoon-S at 20 °C.

### 4.3.3 Coalescence and solidification

As discussed in Section 2.1.3, a low zero-shear viscosity is desirable for LS materials as it facilitates coalescence. To create a fair comparison, the zero-shear viscosity is evaluated as a function of the temperature difference with the melting peak (180.0 °C for Farsoon-S, 174.6 °C for Farsoon-M and 186.2 °C for PA 2200). The viscosity of the Farsoon powders is measured at 0.1 $s^{-1}$, which is on the zero-shear plateau for both materials. The results are shown in Figure 4-8. The viscosity of Farsoon-S is significantly lower than that of PA 2200. Consequently, good coalescence is expected. Furthermore, the temperature dependence of the viscosity is much higher, which translates to a higher activation energy (72 kJ/mol) in the Arrhenius viscosity relation (Eq. 1.1.). As a result, an increase in laser energy will decrease the viscosity more than for the reference PA 2200. Farsoon-M shows a similar viscosity dependence ($E_a = 78$ kJ/mol), but is significantly more viscous. This viscosity increase likely follows from post-condensation, as further discussed in Section 4.3.4. HSM measurements, as a result, show much slower coalescence for the milled grade (Figure 4-8). Furthermore, the created melt of the milled sample is slightly less smooth, which may be due to contaminations or large amounts of non-melting additives.

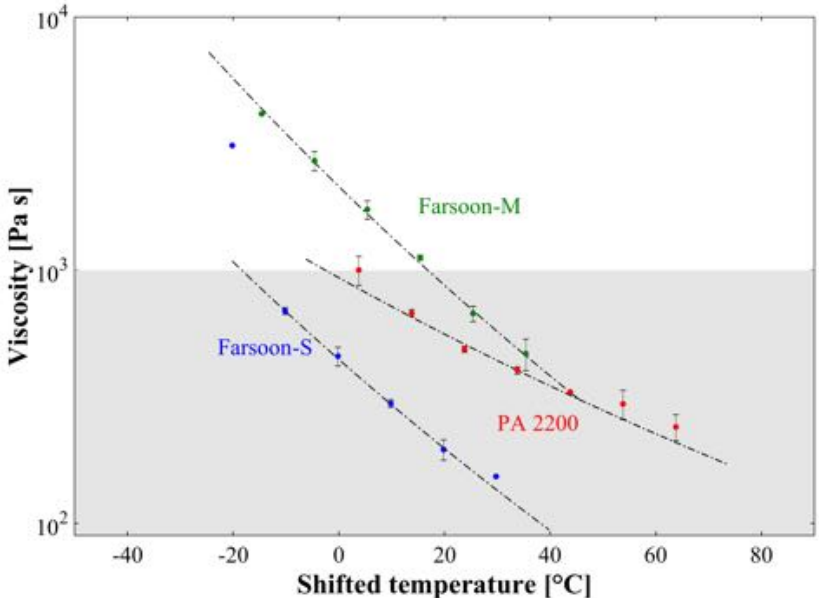


**Figure 4-8:** Zero-shear viscosity of PA 2200 [73] and Farsoon PA in function of the temperature difference with the melting temperature.

To enable the needed heating for coalescence, the stable sintering region needs to be sufficiently large. TGA measurements show that the degradation onset of the Farsoon powders is far above the needed temperature for coalescence (Figure 4-10). Application of the 1 % degradation onset discussed in Section 2.1.3, yields a stable sintering region of 182 °C and 124 °C for Farsoon-S and Farsoon-M respectively.

Both regions are wider than that of the reference PA 2200, which has a stable sintering region of 115 °C under the same criterion. Therefore, no severe issues with degradation upon sintering are expected. In practise, the stable sintering regions for all three materials may even be larger, as the weight loss due to post-condensation affects the 1%-degradation limit.

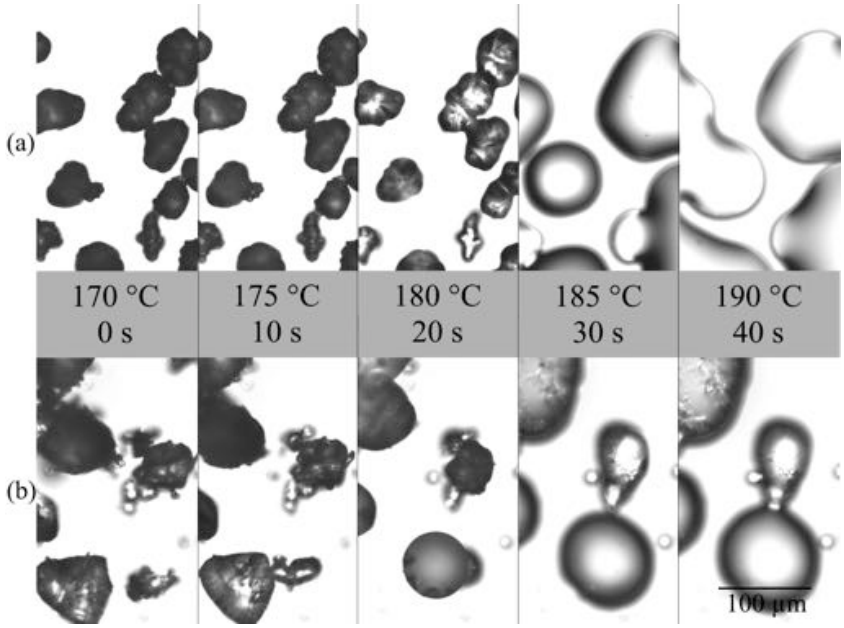


**Figure 4-9:** Hot stage microscopy of Farsoon-S (a) and Farsoon-M (b).

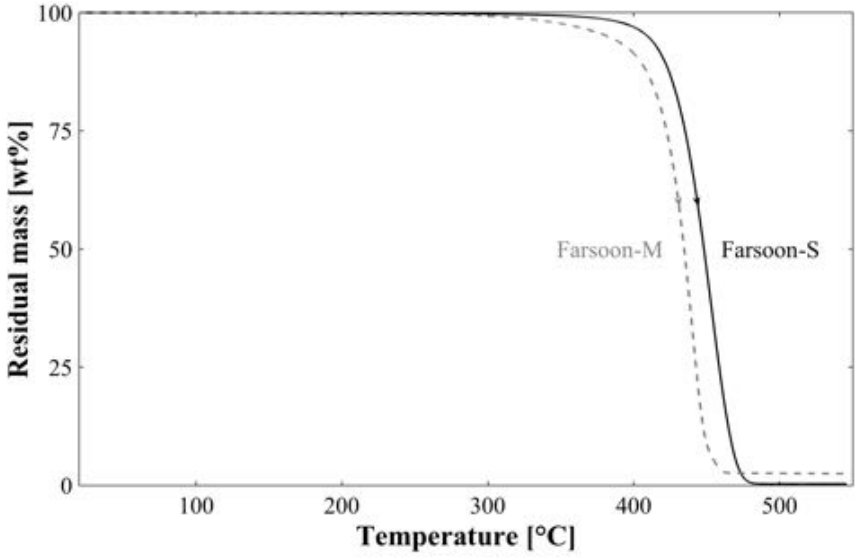


**Figure 4-10:** TGA curves of Farsoon-S and Farsoon-M.

### 4.3.4 Recyclability

As briefly touched upon in the previous section, the Farsoon powders exhibit post-condensation similar to PA 2200. The viscosity increase that results from this post-condensation limits the recyclability of the powder. The post-condensation is likely the cause behind the increased viscosity of the Farsoon-M. This hypothesis is further supported by the similar results for post-condensing TPU, which are discussed in Section 4.4.5. As discussed in Section 2.1.3, this increase in viscosity may lead to coalescence issues and "orange peel" formation upon re-use of the material.

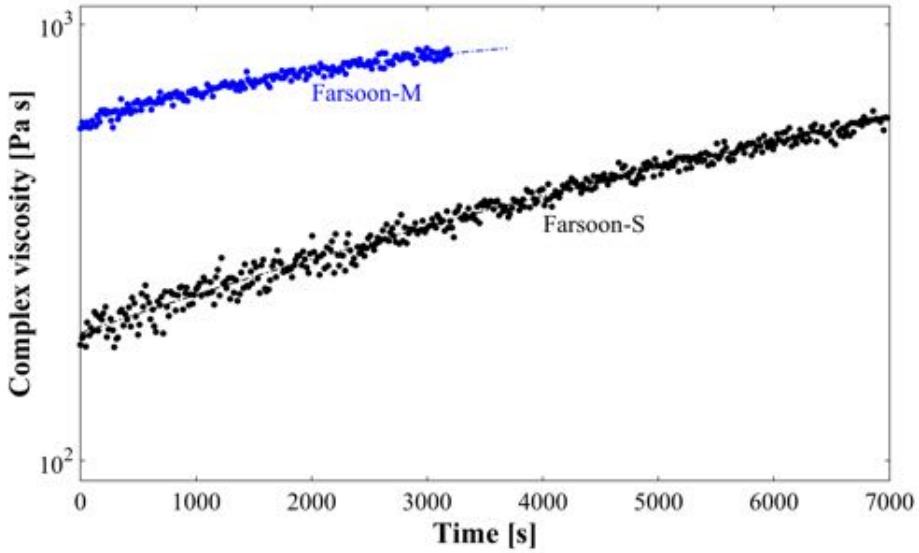


**Figure 4-11:** Post-condensation of PA Farsoon shown in dynamic viscosity measurements at 200 °C, 0.1 % strain and 1 rad/s.

Furthermore, strong yellowing was seen for the recycled powder from an LS build. This yellowing is expected to have a lesser influence on the product properties, compared to the post-condensation. However, it poses a commercial problem, as the yellow part colour is typically undesired for aesthetics. This problem may be alleviated by the addition of whitening agents, such as $TiO_2$.

### 4.3.5 LS proof of concept

Test builds of both powders are created on an EOS sintering machine. However, within the timeframe of the project, no suitable thermal window was found in these tests.

The negative result is unexpected, as Farsoon-S is sold as a commercial sintering powder for Farsoon eForm sintering machines. The powder bed can be heated up to 169 °C, which is well-within the broad melting onset seen in DSC measurements.

This result shows that DSC measurements alone are insufficient for the determination of the thermal window for the powder bed. Therefore, in Chapter 5, powder rheometry is used to aid in the correct prediction of the upper limit of the thermal window for the powder bed. However, at 169 °C, significant part curling is seen. The shift of this crystallisation onset is likely due to the slow cooling rate within LS. A fixed cooling rate of 10 °C/min is applied for all DSC measurements in this text. This rate is chosen for practical reasons and to enable the fast screening of many grades in early stage development and to allow a direct comparison to other studies [5,41,73]. Furthermore, the exact cooling rate within the LS build is undefined and dependent on the part location in the build. As a result, it is not possible to mimic this rate exactly. Verbelen et al. also found a similar cooling rate dependency for the crystallisation of other commercial sintering PA [5]. The viscosity measurements, which are kept at a constant temperature rather than a ramp, also indicate a sudden increase in viscosity for the measurements at 160 °C. This increase is the results of crystal formation, which indicates the thermal window is smaller than expected from DSC.

Farsoon-M shows similar results for the thermal window. The powder bed can be heated up to 168 °C, which illustrates that the broad shoulder in the DSC curve does not negatively impact the powder flowability. However, similar issues with curling arise. On the other hand, the powder recoating was quite good, which is in line with the lab scale spreading experiments. The inherently rough particle morphology of cryomilled powders is thus not problematic for the LS process. Furthermore, good coalescence was seen for single layers, which illustrates that the reported viscosity increase is low enough to still allow sintering.

### 4.3.6 Conclusions

Though final sintering tests were unsuccessful, the trials on the cyomilled PA powder have successfully demonstrated the viability of cryomilled powders for laser sintering. The issues with the material result primarily from the poor thermal window for the powder bed, which is inherent to the material, rather than the powder morphology. The thermal windows are summarised in Figure 4-12. A thermal window for the powder bed of roughly 10 °C is seen for both materials, but the slow cooling rates in LS shift up the crystallisation peak significantly. This is further illustrated in the isothermal viscosity measurements that show a sudden viscosity increase within the thermal window of Farsoon-S that is predicted from DSC. As a result, for the following materials in research, only materials with a sufficiently large thermal window in DSC are selected to allow for this effect.

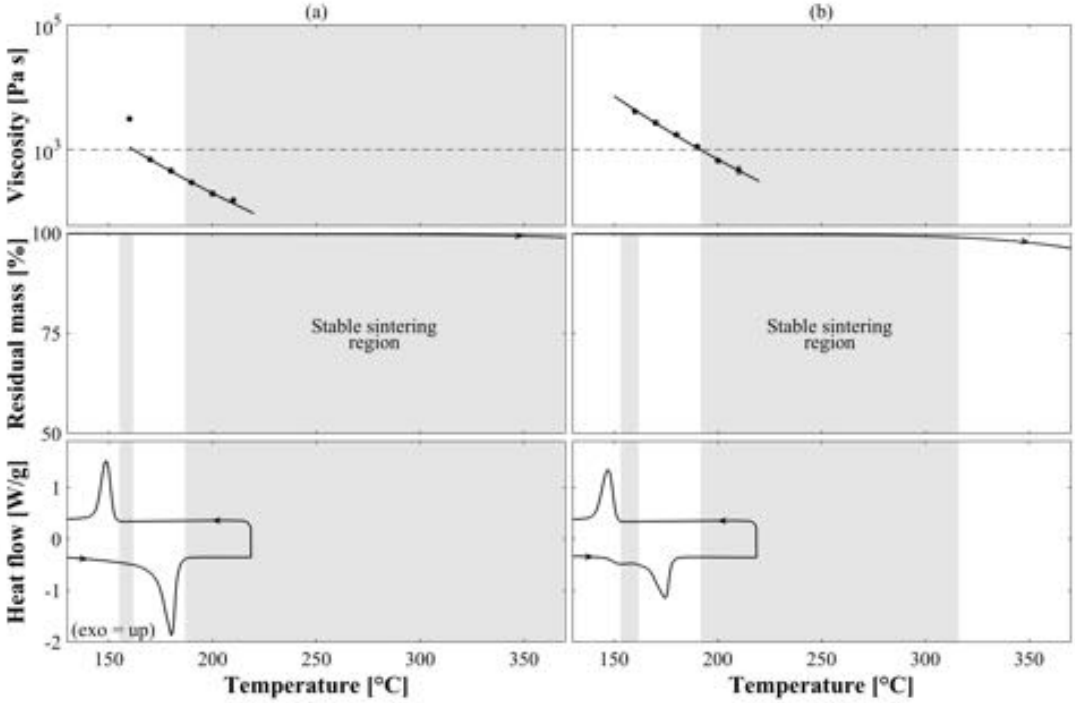


**Figure 4-12:** Thermal processing windows for Farsoon-S and Farsoon M.

Powder flowability is deemed adequate for the milled Farsoon sample. High avalanche angles are seen, as well as a significant increase in the flow energy compared to Farsoon-S. However, the material spreads into smooth, defect-free layers that possess a packing density that competes with that of the reference PA 2200. The next section therefore applies the cryomilling route to TPU samples.

## 4.4 Thermoplastic polyurethane (TPU)

This section discusses the use of cryogenically milled thermoplastic polyurethanes (TPU) for LS. As commercial sintering TPU grades already exist, the goal of this chapter is to evaluate new grades within this broad material family, as well as further prove the viability of the cryomiling process for obtaining LS powders. Furthermore, this section provides a thorough overview on the entire grade selection procedure, going from pellets to a powder.

### 4.4.1 General introduction on TPU

Thermoplastic polyurethanes (TPU) are a specific subset of the polyurethane family that do not form permanent crosslinks. This enables melt processing of the material, while still having a product with elastomeric, i.e. rubber-like, properties. This unique feature makes them especially interesting for applications that require flexibility [186].

The name TPU does not refer to one single molecular structure, but rather a family of linear segmented copolymers that all possess a urethane group (-NHCO-O-) in their backbone [186,187]. Typically, they contain three major building blocks: (1) a long chain diol, also called a macrodiol, which is typically a polyether or polyester, (2) a diisocyanate, which can be aromatic or aliphatic, and (3) a chain extender, which can be a diol or diamine [186]. The reaction between the cyanate (-NCO) and alcohol (-OH) groups creates the urethane bond (cf. Figure 4-13). The reaction of a cyanate and amine group gives a urea bond and thus a polyurea. However, even when some or most of the bonds in the molecule are urea bonds, the polymer is often still referred to as polyurethane [188].

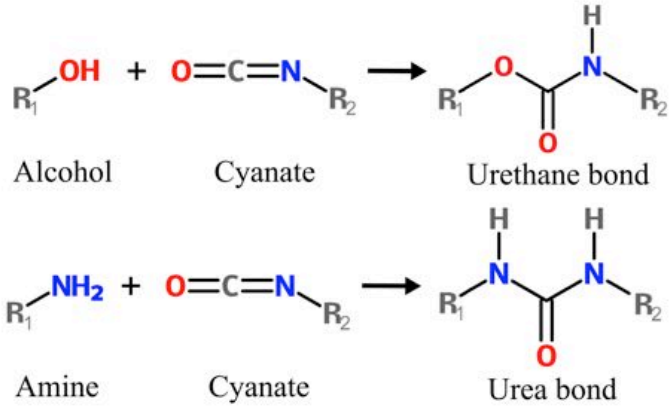


**Figure 4-13:** Urethane and urea reaction from an alcohol and amine with a cyanate.

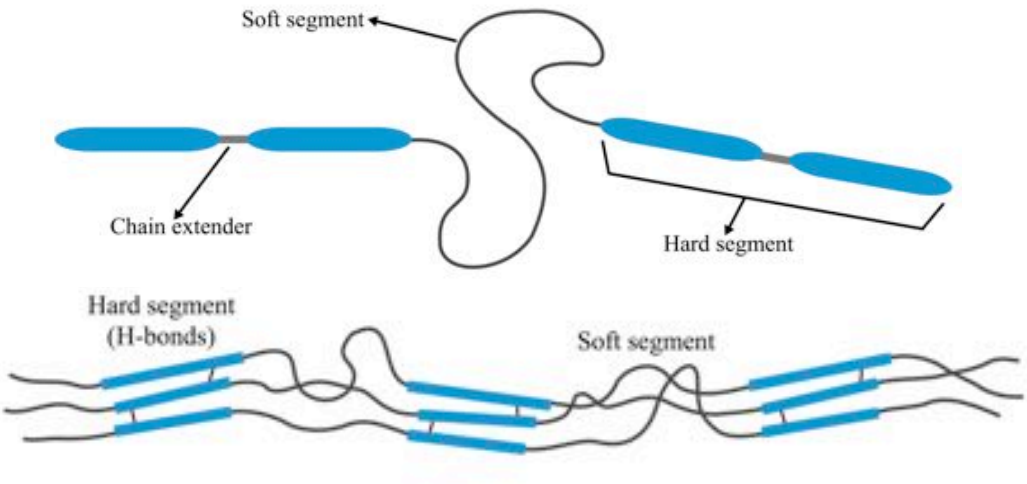


**Figure 4-14:** Schematic illustration of the soft and hard segment structure within TPU's, adapted from Priscariu [186].

The elastomeric properties of a TPU result from the interaction between the aforementioned building blocks. The macrodiols form the so-called soft segments of the TPU. They are long, relatively movable segments, which gives flexibility to the

material. In between two soft segments of the same chain, a hard segment is found, consisting of the diisocyanate and the chain extender (cf. Figure 4-14). These hard segments are able to form strong hydrogen bonds, which, together with crystallisation, results in the formation of hard domains. These hard domains work as thermo-reversible, physical cross-links, thus allowing re-processing of the polymer [186].

TPU's are divided into many subcategories based on their specific building blocks. The type of macrodiol often forms the basis for categorising the TPU. The most common macrodiols for TPU's are either ester or ether based. The choice between them has a strong effect on the final product properties. Ester TPU's are typically stronger than ether TPU's, as a consequence of stronger hydrogen bonding between the -NH and ester carbonyl group, compared to the –NH ether oxygen bond. For this reason, the glass transition of ester based TPU's is typically higher. Ether TPU's, however, hold an important advantage over their ester counterparts. The ether linkage is much less susceptible to hydrolytic cleavage than the ester linkage. As a result, ether based TPU's are able to sustain their mechanical properties much longer, especially in moist conditions [186]. A typical example where this comes into play is the use of TPU in footwear. Ester based TPU's degrade much faster in this application due to the combination of sweat and body heat. Other macrodiols, such as poly(alkylene carbonate), are used to create TPU [187]. These are, however, much less common than the ether or ester based grades. LS TPU's are typically ester based. This research therefore assesses whether also the other TPU types are sinterable.

Another distinction between TPU's is possible, based on the nature of the diisocyanate. This component mainly affects the mechanical properties of the resulting polymer. An aromatic diisocyanate typically leads to a stiffer TPU than its aliphatic counterpart [189]. Seidenstücker et al. noted that when all other parameters are kept the same, the aromatic or aliphatic nature of the diisocyanate does not significantly influence degradation properties of the polymer [190].

Due to the nature of the aforementioned reaction mechanism, post-condensation is an issue for some TPU grades. As each of the aforementioned building blocks has a reactive group on both ends, the polyaddition reaction is able to continue after the actual polymerisation process. This post-condensation reaction is stimulated by an increase in temperature. As a result, the heated bed in the LS machine strongly influences this post-condensation reaction during processing. Post-condensation is also seen in some commercial LS powders, such as PA 2200, as discussed in Sections 2.1.3 and 4.3.4.

The multitude of chemical compositions possible within the TPU family results in a wide range of attainable material properties. A review of the commercially available data of 520 different grades of some of the major TPU producers was performed. Figure 4-15 summarises the result of this review for hardness, tensile strength and elastic modulus.

A wide range in hardness is found, from around 30 Shore A to 87 Shore D. As the Shore A scale stops at 100 A (= 58 D), stiffer grades are plotted at 100 A for comparison. Soft TPU grades typically contain softening agents, which complicate the sintering process and analysis. These grades are therefore further avoided in this study.

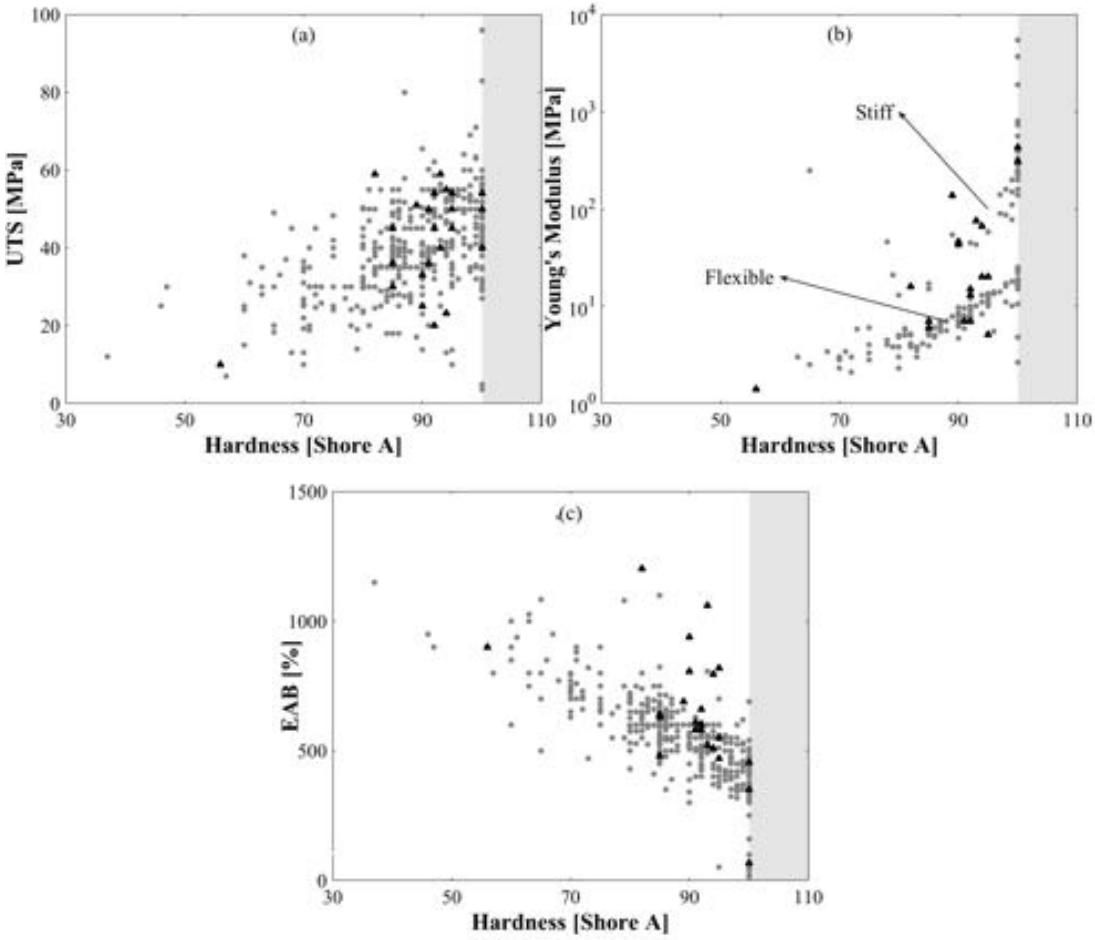


**Figure 4-15:** TPU property maps for commercial TPU grades (•) and all grades examined in this work (▲): strength (a), modulus (b) and elongation at break (c).

Besides hardness, also the strength of the TPU grades varies strongly (Figure 4-15a). Ultimate tensile strength (UTS) values range from below 10 MPa to almost 100 MPa. Harder TPU grades on average have higher strengths, which is a secondary argument to base the preliminary selection on harder TPU's. Degradation and part porosity resulting from the LS process tend to decrease the tensile strengths

of TPU significantly. Therefore, high-strength grades may be required to achieve mechanically viable final parts. From a commercial standpoint, the final parts require a tensile strength of at least 10 MPa.

The stiffness varies over four orders of magnitude (Figure 4-15b), which further illustrates the broad property variation within this material class. Two distinct subgroups, a stiff and a flexible branch, are visible in the property map, which are possibly the result of the aromatic versus aliphatic chain extenders. Both ester and ether TPU are found in each subgroup. Within each subgroup, the stiffness generally increases with increasing hardness. The average elongation at break, on the other hand, decreases with increasing hardness (Figure 4-15c). This trend is expected, as higher stiffness typically results in lower elongation properties. High values, up to several times the original length, are common. This is one of the main selling points of TPU materials. As a result of this wide range of tuneable properties, TPU has found its way into many flexible applications, ranging from medical devices to footwear to automotive industry [191].

Based on the literature review and grade availability, 26 TPU commercial grades are examined in detail. These grades span most of the property space, as indicated on Figure 4-15. The grades are further labelled by a capital letter that signifies the type of macrodiol and a number that represents their hardness. Table 4-4 lists all 26 grades and their mechanical properties. The list includes 14 ester type TPU (S), 9 ether type TPU (T), 2 caprolactam based TPU (L) and 1 carbonate TPU (C). All hardness values are expressed on the Shore A scale, except for the hardest TPU, namely TPU T-61D, which is expressed on the higher Shore D scale.

All examined grades are available in pellet form and are commercially used in various processing applications, not including LS. Most grades are injection-moulding (IM) grades, as this application requires a relatively low melt viscosity, compared to, for instance, extrusion based processes. As a result, better coalescence is expected from these grades. To provide a directly useful analysis for LS, these new grades are compared to TPU Luvosint X92A-1 (Lehmann & Voss), further referred to as TPU Luvosint. This grade is a commercial ester-based LS powder and is thus proven to be sinterable. Investigations on this grade have been published in earlier research [41].

The following sections discuss the further selection procedure for all TPU grades. Section 4.4.2 assesses the grades based solely on properties that are measurable on the pellets. Based on this assessment, several grades are milled and further evaluated in Sections 4.4.3 to 4.4.4. As the goal of this chapter is to evaluate the cryogenic milling route for LS, mostly the general trends in the pellet and powder measurements are discussed.

**Table 4-4:** Examined TPU grades and their mechanical properties: S = ester, T = Ether, L = caprolactam and C = carbonate. * denotes values obtained from commercial datasheets as opposed to the aforementioned testing methodologies.

| Sample | $T_m$ (peak) [°C] | UTS [MPa] | E [MPa] | EAB [%] | $\rho_m$ [g/cm$^3$] |
|---|---|---|---|---|---|
| **Luvosint** | 160 | 33 | 46 | 939 | 1.23 ± 0.007 |
| **S-56** | 165* | 10* | 1.4* | 900* | 1.14* |
| **S-82** | 136 | 59 ± 2 | 15.9 ± 0.4 | 1203 | 1.17 ± 0.006 |
| **S-85a** | 170 | 30* | NA | 480* | 1.20* |
| **S-85b** | 152 | 36* | 6* | 630* | 1.20 ± 0.001 |
| **S-85c** | 167* | 45* | 6* | 640* | 1.20 ± 0.010 |
| **S-89** | 204 | 51 ± 3 | 138 ± 5 | 690 | 1.19 ± 0.023 |
| **S-90** | 157 | 25* | 43* | 807 | 1.23 ± 0.007 |
| **S-91a** | 164 | 36* | NA | 580* | 1.21 ± 0.002 |
| **S-91b** | 219 | 50* | 7* | 610* | 1.21* |
| **S-92** | 53 | 20* | 7* | 660* | 1.16 ± 0.000 |
| **S-93a** | 195 | 40* | NA | 520 | 1.21 ± 0.001 |
| **S-93b** | 177 | 59 ± 1 | 75.8 ± 0.6 | 1060 | 1.20* |
| **S-94** | 162 | 23.2 ± 0.9 | 66.6 ± 9.8 | 795 | 1.25 ± 0.006 |
| **S-97** | 113 | 42* | NA | 562* | 1.28 ± 0.023 |
| **T-85** | 138* | 45* | ~7* | 640* | 1.12 ± 0.001 |
| **T-92a** | 175* | 45* | ~13* | 600* | 1.13* |
| **T-92b** | 198* | 54* | 15* | 580* | 1.13 ± 0.000 |
| **T-95a** | 214* | 45* | NA | 550* | 1.14 ± 0.009 |
| **T-95b** | 184 | 50* | ~20* | 470* | 1.13* |
| **T-95c** | 177 | 54 ± 4 | 5.1 ± 0.4 | 819 | 1.14 ± 0.001 |
| **T-61D** | 213 | 40* | NA | 350* | 1.16 ± 0.007 |
| **L-94** | 211 | 55* | ~20* | 510* | 1.22 ± 0.012 |
| **L-95** | 175 | NA | NA | NA | 1.20 ± 0.012 |
| **C-95** | 208 | NA | NA | NA | 1.17 ± 0.017 |

### 4.4.2 First selection: general sintering criteria

Five different tests are possible for the pellets. These tests are DSC, TGA, melt rheometry, TMA and mechanical testing. The results of the mechanical tests are listed in Table 4-4. The other measurements are discussed in the following sections.

**Thermal window of the powder bed**

As discussed in Section 2.1.3, a first important cut-off for many grades is the thermal window for the powder bed. As no measurements on powder stickiness are possible at this stage, the thermal window is solely based on DSC measurements. This yields some limitations in the accuracy of the window, as discussed for PA in Section 4.3. Moreover, many of the examined TPU grades, such as T-85, do not show a sharp melting peak, but rather a broad melting region, as illustrated in Figure 4-16a. As no clear onset for the melting peak is seen, the prediction of the thermal window is much less certain. Not only is it unclear at what point the peak starts, but it is also uncertain whether entering the broad melting peak gives rise to stickiness issues for the powder. This question also arises for other materials with a broad melting onset, as further discussed in Chapter 5. Some TPU grades, such as TPU S-97, on the other hand, show clear melting and crystallisation peaks (Figure 4-16b). This behaviour is similar to the PA grades discussed in Sections 2.1.3 and 4.3. As a result, the DSC measurement indicates a clear upper and lower limit for the thermal window of the powder bed for the latter subset of TPU.

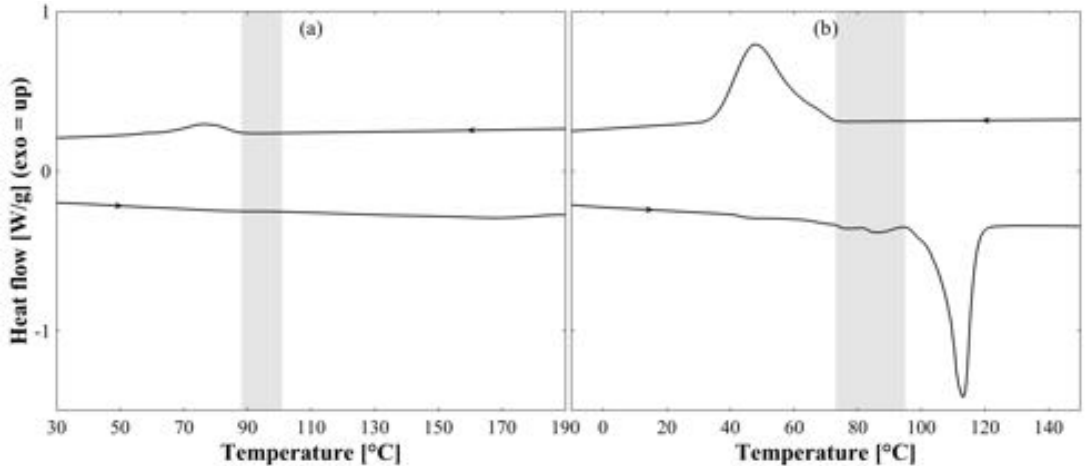


**Figure 4-16:** DSC curves of T-85 (a) and S-97 (b).

The resulting thermal windows are reported in Table 4-5. Underlined values for the DSC peaks denote sharp, clear onsets. Other values are estimated from relatively broad onsets. The TPU Luvosint reference has a clear thermal window of roughly 41 °C. Various other TPU show similar or larger windows, which is required for good powder spreading and the avoidance of warpage. However, many samples show insufficiently large or even non-existent windows. Even though the crystallisation of TPU grades is typically much smaller than that of PA, as discussed in the next section, this lack of a thermal window is likely to lead to processing issues. Furthermore, observations show that the thermal window obtained from DSC is often an overestimation of the real window, as discussed in the next paragraphs of this section. This observation is similar to that of the Farsoon PA in Section 4.3.5.

**Table 4-5:** Available thermal window for the powder bed for the TPU grades, based on DSC. Underlined values denote a clear melting or crystallisation peak. Other values are estimates for broad peaks. LL = lower limit, UL = upper limit. Underlined values for the DSC peaks denote sharp, clear onsets. Shaded cells denote poor results for LS.

| | Thermal window powder bed | | | Stable sintering region | | | |
|---|---|---|---|---|---|---|---|
| **Sample** | **LL [°C]** | **UL [°C]** | **Width [°C]** | **LL (DSC) [°C]** | **LL (Visc.) [°C]** | **UL [°C]** | **Width [°C]** |
| **Luvosint** | 86 | 127 | **41** | 174 | **177** | 286 | **109** |
| **S-56** | 145 | 136 | **0** | **185** | 184 | 259 | **74** |
| **S-82** | 75 | 120 | **45** | 185 | **192** | 289 | **97** |
| **S-85a** | 92 | 102 | **10** | 200 | **202** | 289 | **87** |
| **S-85b** | 55 | 104 | **49** | **178** | 170* | 286 | **108** |
| **S-85c** | 111 | 136 | **25** | **198** | **198** | 290 | **92** |
| **S-89** | 146 | 160 | **14** | **225** | 196 | 234 | **9** |
| **S-90** | 93 | 124 | **31** | **180** | 139 | 252 | **72** |
| **S-91a** | 78 | 78 | **0** | 184 | **200** | 288 | **88** |
| **S-91b** | 158 | 174 | **16** | **245** | 183 | 295 | **50** |
| **S-92** | 29 | 38 | **9** | 62 | **159** | 279 | **120** |
| **S-93a** | 62 | 134 | **72** | **202** | 166 | 259 | **57** |
| **S-93b** | 70 | 126 | **56** | **202** | 185 | 286 | **101** |
| **S-94** | 89 | 152 | **63** | **180** | 148 | 260 | **80** |
| **S-97** | 73 | 95 | **22** | 120 | **124** | 285 | **161** |
| **T-85** | 88 | 101 | **13** | **200** | 171 | 286 | **86** |
| **T-92a** | 121 | 103 | **0** | **210** | 187 | 294 | **84** |
| **T-92b** | 130 | 163 | **33** | **244** | 211 | 291 | **47** |
| **T-95a** | 118 | 204 | **86** | **220** | 198 | 294 | **74** |
| **T-95b** | 116 | 127 | **11** | **202** | 201 | 292 | **90** |
| **T-95c** | 107 | 112 | **5** | 204 | **232** | 300 | **68** |
| **T-61D** | 129 | 171 | **42** | **238** | 219 | 274 | **36** |
| **L-94** | 112 | 185 | **73** | **245** | 191 | 282 | **37** |
| **L-95** | 102 | 105 | **3** | 195 | **217** | 292 | **75** |
| **C-95** | / | 176 | **/** | **259** | 196 | 286 | **27** |

*extrapolated value

Two effects negatively influence the thermal window estimated from DSC by either shifting the crystallisation onset to higher temperatures or lowering the onset for powder stickiness. Firstly, some materials exhibit stickiness far below the melting onset. The pellets of TPU S-56 became unusually sticky upon drying at 60-70 °C, which is far below the melting onset of 136 °C. This stickiness may be related to the low hardness of the polymer. As the material is heated, it softens even more, which

results in higher deformability. When the pellets are then pressed together, their contact surface increases and the Van der Waals interaction between the pellets becomes much higher. The large surface to volume ratio of powder particles likely increases this issue compared to the pellets. Since DSC measurements also predicted a non-existent thermal window, this increased stickiness does not change the conclusion for this material. However, this effect should be taken into account for future grade selection.

A second reduction to the thermal window is related to the onset of the crystallisation peak. Three different causes play a role. Firstly, the onset of crystallisation is dependent on the cooling rate, as discussed in Section 4.3.5. Figure 4-17 illustrates this effect for TPU T-95a. Upon decreasing the cooling rate from -10 °C/min to -3 °C/min, the crystallisation peak shifts 12 °C and thus significantly reduces the thermal window. The second cause that is the addition of additives further shifts the crystallisation peak to higher temperatures. In Figure 4-17 this effect is seen as a shift in the crystallisation temperature curve upon the addition of 1 % silica based flow additive to the pure material. As discussed in Section 4.1, the addition of flow additives is unavoidable to facilitate the milling process. This shift thus has to be taken into account for all materials. As the exact amount of flow additives needed for cryomilling is not known a priori, it is difficult to measure this shift by adding the silica particles to the pellet. Therefore, a useful rule of thumb is to subtract around 5 °C from the thermal window of the pellet as a safety factor. Section 4.4.5 further illustrates the effect of flow improver with examples of milled powders. It shows how this rule of thumb is insufficient for polymers that do not show a clear crystallisation peak for the pure material.

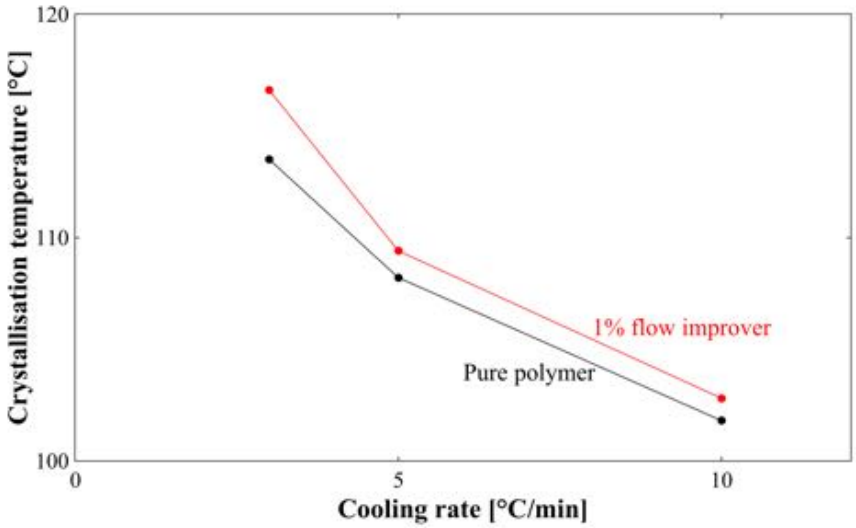


**Figure 4-17:** Dependence of the crystallisation peak location on the cooling rate and presence of nucleating agents for TPU T-95a.

A third cause for a shift in the lower limit of the thermal window for the powder bed arises from the thermal history of the material. This effect is illustrated by zero-shear viscosity measurements on TPU Luvosint and T-95a (Figure 4-18). Both materials are heated roughly 10 °C and 30 °C above their respective melting peaks. Upon cooling, a sudden viscosity increase is seen due to crystallisation. In the measurements that only heated the polymer 10 °C above their melting peaks, this viscosity increase starts at much higher temperatures, reducing the thermal window to zero. This observation means that at these temperatures there is still some degree of order present in the samples, which facilitates crystallisation. The effect needs to be taken into account, as in the LS process the temperatures attained by the polymer melt are often poorly defined. However, as this effect is present in the sinterable reference material (Luvosint), it is unlikely detrimental in the LS process. However, it implies that the stable sintering regions needs to be sufficiently large to allow for this temperature overshoot. The stable sintering region for the TPU grades is further discussed in the next section.

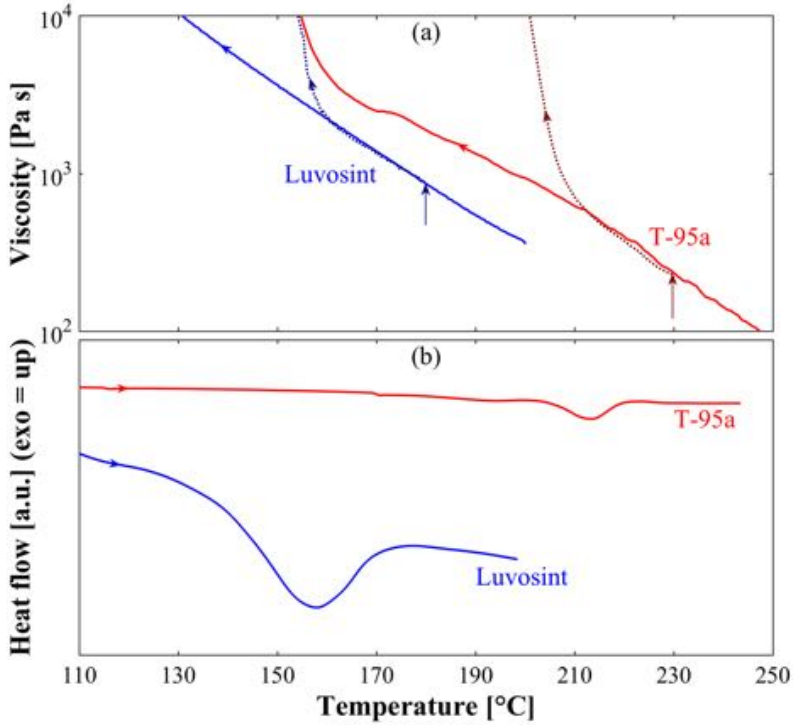


**Figure 4-18:** Shifted crystallisation onset seen in melt viscosity measurements at various initial melt temperatures (a) above the melting peak shown in DSC (b).

### Coalescence and solidification

A second screening criterion, besides the available thermal window for the powder bed, is the viscosity of the polymer melt. To create a fair comparison between polymers with strongly different melting temperatures, the viscosity is evaluated in function of the shifted melting temperature, i.e. the temperature increase above the melting peak. The expected powder bed temperature forms a more relevant

reference temperature than the peak location due to the vast difference in peak width for the different TPU grades. However, as discussed in the previous section, this temperature is more uncertain. Therefore, the location of the melting peak maximum is used to provide a first screening. For most materials, this change in reference temperature does not affect the polymer ranking, except for the grades with exceptionally broad melting onsets.

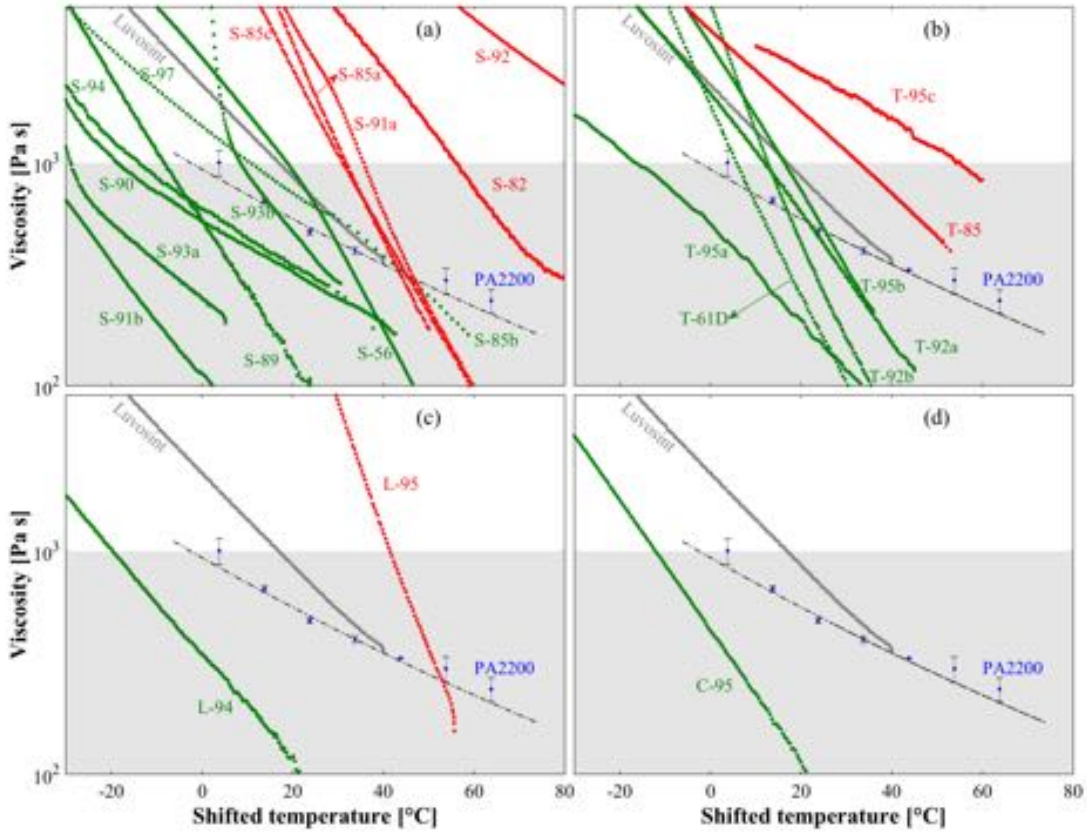


**Figure 4-19:** Zero-shear viscosity of the TPU grades in function of the temperature difference with the melting temperature: ester (a), ether (b), caprolactam (c) and carbonate (d) TPU grades. PA 2200 [73] and TPU Luvosint [41] are plotted as a reference.

As stated in Section 2.1.3, a viscosity similar to that of PA 2200, i.e. 1000 Pa s or less, is desired. The zero-shear viscosity of each TPU is measured during a continuous cooling ramp at -5 °C/min. The zero shear plateau is determined beforehand to select a correct shear rate for each measurement. The results of the viscosity measurements are shown in Figure 4-19 and compared to both TPU Luvosint and PA 2200. TPU S-85a, S-85c, S-91a, S-92, T-85, T-95c and L-95 are more viscous than the reference materials, which influences their coalescence behaviour. TPU S-92 scores exceptionally poor, compared to the other grades, as it requires a temperature increase of more than 100 °C above its melting temperature. TPU S-92 is a rather unique TPU, with an exceptionally low melting temperature of 53 °C. As a result, the absolute temperature needed for the powder melt is not that

much higher than for other TPU grades. This example further illustrates the need to look at the viscosity on a shifted temperature scale, rather than an absolute scale. Most TPU's also show a much stronger temperature dependence, compared to the reference materials. As a result, laser overshoots drop the viscosity much more and cooling effects of the surrounding powder bed will further limit the coalescence time. A too strong viscosity drop may lead to polymer bleeding into the surrounding bed, resulting in a poor part finish. As a result, process control and optimisation may be more difficult for these materials.

Next, the stable sintering region is determined. The DSC and viscosity measurements provide the lower limit of the stable sintering region. This lower limit is determined as the maximum of the end of the melting peak and the viscosity at which the melt viscosity reaches 1000 Pa s. The 1%-degradation criterion resulting from TGA forms the upper limit. The results are shown in Table 4-5. A sufficiently large stable sintering region is required to allow for the laser overshoot as well as ensure full melting, as discussed in the previous section. The reference TPU Luvosint has a stable sintering region of 109 °C. Only TPU S-85b, S-92 and S-97 show similar or wider regions. However, a slightly smaller stable sintering region may still be usable. TPU S-89, S-91b, T-92b, T-61D, L-94 and C-95 show stable sintering regions of 50 °C or lower, which are deemed problematic.

Solidification measurements on various TPU's have shown that they typically exhibit limited shrinkage compared to PA [41,73]. Additionally, TMA measurements have been performed on S85a, S-92, T-95a, L-95 and C-95 to further assess this observation for a strongly varying set of TPU grades. None of these materials showed significant crystallisation shrinkage, which is in line with earlier findings on other TPU grades [41]. Some slight gas formation during the measurement, however, hinders the exact determination of the shrinkage. Crystallisation shrinkage is, however, deemed less problematic for most TPU grades.

### 4.4.3 First selection and milling

As a result of the previous selection criteria, a selected set of TPU grades is milled. The summary of the selection is provided in Table 4-6. The grades that score well on all the assessed criteria are milled, as well as some poorer scoring grades. The latter are chosen as a proof of concept for the screening obtained in the lab-scale experiments. The milled grades are then further assessed for their powder properties, including powder flowability.

**Table 4-6:** First selection of the TPU grades based on pellet properties: thermal window of the powder bed (TWPB), zero-shear viscosity and the stable sintering region (SSR).

| Sample | TWPB | Viscosity | SSR | Result | Selection |
|---|---|---|---|---|---|
| **Luvosint** | good | good | good | pass | Reference |
| **S-56** | poor | good | good | x | / |
| **S-82** | good | poor | good | x | / |
| **S-85a** | poor | poor | good | x | Milled |
| **S-85b** | ok | good | good | pass | Milled |
| **S-85c** | ok | poor | good | x | / |
| **S-89** | poor | good | poor | x | Milling issues |
| **S-90** | good | good | good | pass | Milled |
| **S-91a** | poor | poor | good | x | / |
| **S-91b** | poor | good | poor | x | / |
| **S-92** | poor | poor | good | x | Milled |
| **S-93a** | excellent | good | good | pass | Milled |
| **S-93b** | good | good | good | x | Milled |
| **S-94** | good | good | good | pass | Milled |
| **S-97** | ok | good | excellent | pass | Milled |
| **T-85** | poor | poor | good | pass | Milled |
| **T-92a** | poor | good | good | x | / |
| **T-92b** | good | good | poor | x | Milling issues |
| **T-95a** | excellent | good | good | pass | Milled |
| **T-95b** | poor | good | good | x | / |
| **T-95c** | poor | good | good | x | Milled (issues) |
| **T-61D** | good | good | poor | x | / |
| **L-94** | excellent | good | poor | x | Milled |
| **L-95** | poor | good | good | x | / |
| **C-95** | excellent | good | poor | x | / |

The resulting PSD and morphology of the milled powders are shown in Table 4-7 and Figure 4-20. The milled grades show PSD ranges closer to that of PA 2200, than the reference TPU Luvosint. TPU Luvosint contains much larger particles, even above 100 µm. This material is therefore typically deposited in thicker layers than PA 2200. The larger particle size results in better flow behaviour for TPU Luvosint, as further elaborated on in Section 4.4.4. Two TPU powders, S-90 and S-94, have significantly more fine particles than the other grades. This is expected to influence their flow and packing behaviour.

**Table 4-7:** Summary of the particle properties of the milled TPU powders.

| Sample | $D_{10}$ [µm] | $D_{50}$ [µm] | $D_{90}$ [µm] | relative span [/] |
|---|---|---|---|---|
| **PA 2200 (Chapter 3)** | 39.5 | 63.4 | 82.2 | 0.67 |
| **Luvosint** [41] | 36.2 | 68.6 | 134.15 | 1.43 |
| **S-85a** | 35.8 | 64.6 | 94.5 | 0.91 |
| **S-85b** | 47.3 | 74.6 | 102.1 | 0.73 |
| **S-90** | 17.9 | 46.1 | 75.5 | 1.25 |
| **S-92** | 37.9 | 63.7 | 87.7 | 0.78 |
| **S-93a** | 32.7 | 61.6 | 89.8 | 0.93 |
| **S-93b** | 29.0 | 59.7 | 90.2 | 1.02 |
| **S-94** | 14.8 | 39.4 | 58.5 | 1.11 |
| **S-97** | 19.2 | 51.0 | 91.3 | 1.41 |
| **T-85** | 36.5 | 65.9 | 97.4 | 0.92 |
| **T-95a** | 28.4 | 57.1 | 82.4 | 0.95 |
| **T-95c** | 33.0 | 60.2 | 91.3 | 0.97 |
| **L-94** | 34.0 | 65.2 | 97.1 | 0.97 |

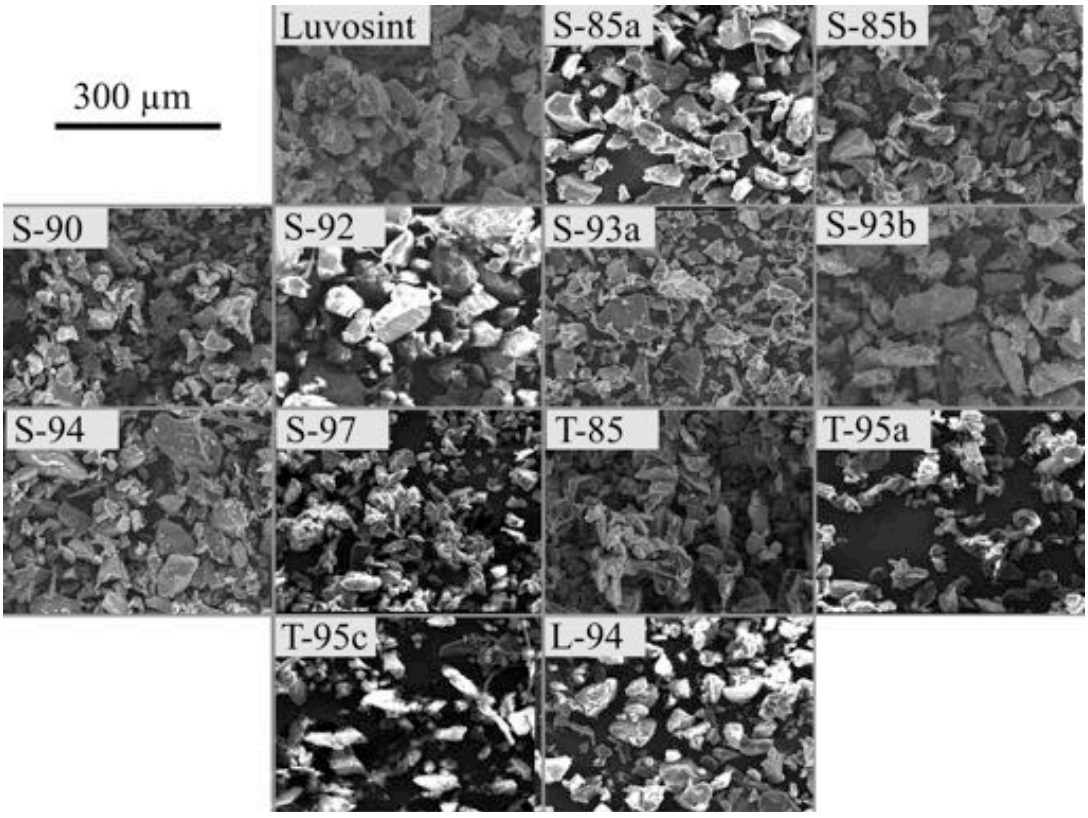


**Figure 4-20:** SEM images of all milled TPU powders compared to the reference TPU Luvosint.

All milled TPU share a similar rough morphology, as illustrated in the SEM images of Figure 4-20. All particles are quite irregular and show rough fracture edges, which result from the milling process. TPU S-94 and S-95c furthermore show a significant amount of elongated or string-like particles. This type of morphology is also seen in other milled materials, as further discussed in Chapter 5. These elongated particles are likely the result of strong local heating and plastic deformation in the milling process.

### 4.4.4 Powder flowability

The A-DAoR performs a first quick screening of the powder flowability. The results are listed in Table 4-8. Most TPU samples, including the reference TPU Luvosint, show similar angles. The average angles are typically around 42-45° and the avalanche angles are 7-10 ° higher. Remarkably, TPU Luvosint has the highest angles of all samples. The variability on the angle of TPU Luvosint is also much higher. This variability is the result of multiple batches of TPU Luvosint that were tested during the course of the research. For the milled batches, on the other hand, only one batch was available, thus limiting flow variability that is inherent to variability in the powder PSD and morphology.

**Table 4-8:** Powder flowability indices based on the dynamic angle of repose (A-DAoR) and spreading experiments for the examined TPU powders.

| Sample | $\widehat{\phi}$ [°] | $\widehat{\phi_a}$ [°] | $\rho_{pk,geom}$ [%] | $\rho_{pk}$ [%] |
|---|---|---|---|---|
| **Luvosint** | 44.2 ± 3.7 | 56.1 ± 3.6 | 53 | 45 [41] |
| **S-85a** | 45.0 ± 1.0 | 52.1 ± 1.1 | / | / |
| **S-85b** | 42.5 ± 1.3 | 50.0 ± 0.4 | / | / |
| **S-90** | 44.5 ± 1.8 | 50.7 ± 2.2 | 58 | 44 |
| **S-92** | 38.7 ± 0.6 | 41.7 ± 0.5 | 55 | 42 |
| **S-93a** | 42.7 ± 0.2 | 48.4 ± 0.1 | 50 | 36 |
| **S-93b** | 41.2 ± 0.1 | 50.0 ± 0.4 | 52 | 42 |
| **S-94** | 46.0 ± 0.2 | 52.8 ± 0.4 | 58 | 42 |
| **S-97** | 46.9 ± 0.1 | 55.9 ± 0.2 | 52 | 36 |
| **T-85** | 42.1 ± 0.5 | 49.4 ± 0.4 | / | / |
| **T-95a** | 42.3 ± 1.1 | 50.6 ± 1.6 | 48 | 40 |
| **T-95c** | 48.5 ± 1.1 | 56.1 ± 1.8 | / | / |
| **L-94** | 40.5 ± 1.1 | 46.4 ± 1.0 | 50 | 36 |

At such high angles, the ranking of the different powders becomes more difficult. This is further illustrated in spreading experiments of several powders. In spite of the high angles, all tested powders are spreadable into smooth defect free layers. Furthermore, higher avalanche angles do not always correspond to poorer packing. This observation further illustrates the need for powder flowability measurements that reflect the flow field of the intended application, such as the powder spreader set-up.

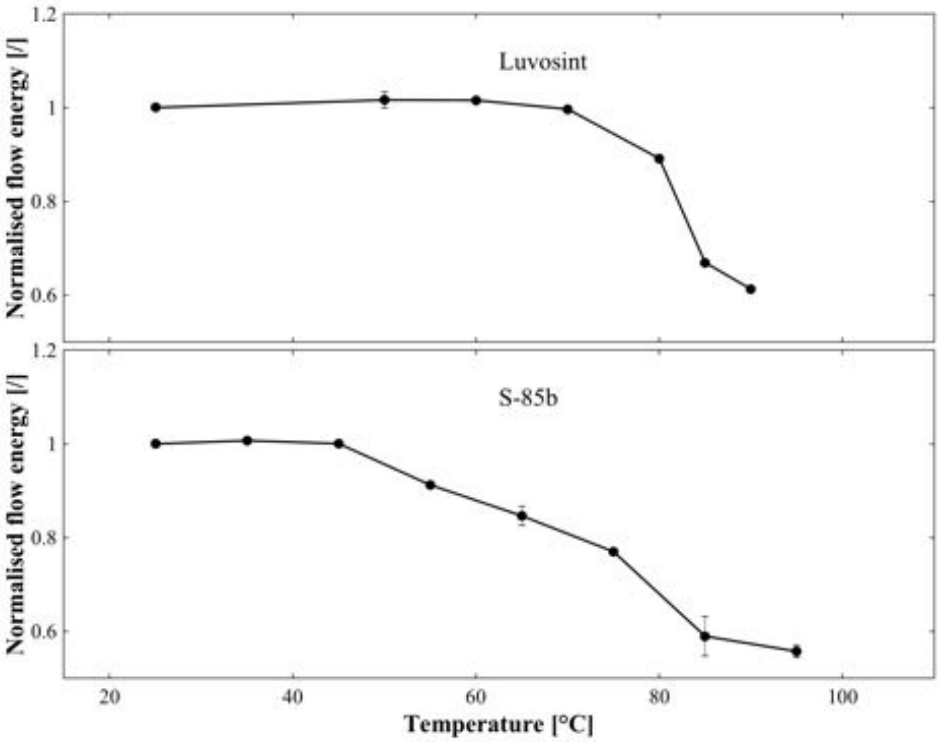


**Figure 4-21:** Powder rheometry results of TPU Luvosint and S-85b.

The powder rheometer provides unexpected results for all examined TPU materials. Unlike other materials, a drop in the flow energy with increasing temperature is seen for all examined samples. This observation is illustrated for TPU Luvosint and S-85b in Figure 4-21. TPU Luvosint shows a drop in the flow energy around 70 °C. This temperature is much lower than the attainable bed temperature of 100 °C [41]. TPU S-85b shows similar behaviour above 45 °C. A possible explanation lies in the stronger tendency of these materials to form porous, fluffy networks. This translates to high values of the Hausner ratio for many of these grades, up to 1.45. As the powder is heated, the powder bed expands even more, resulting in more limited contact between the particles. This contact is then locally broken by the blade, with limited movement of the rest of the powder bulk. As a result, fewer particles are in practise affected by the blade movement, compared to a more densely packed powder. The energy needed to move this reduced powder mass is thus also smaller. This hypothesis is visually supported during the measurement, as not only a strong

bed expansion is seen, but also a relatively still powder surface upon deeper penetration of the propeller. None of the other material families within this research exhibited similar behaviour.

### 4.4.5 Evaluation of cryomiling process for TPU

Based on the previous section, the cryomiling process has proven to produce usable powder for the application of laser sintering. The inherently irregular shape of the particles has some negative influence on the flowability, but in many cases is not deemed a limiting factor for LS. There are, however, still some drawbacks for this production route. Firstly, though the process was successful on most samples, not all polymer grades tested in this research were cryogenically millable to the desired PSD in the given timeframe. However, it is likely that with sufficient process optimisation, milling should be feasible for all materials. Due to the limited time of the project and the need for large amounts of pellets (ca. 100 kg) for the industrial scale milling, this was not fully optimised.

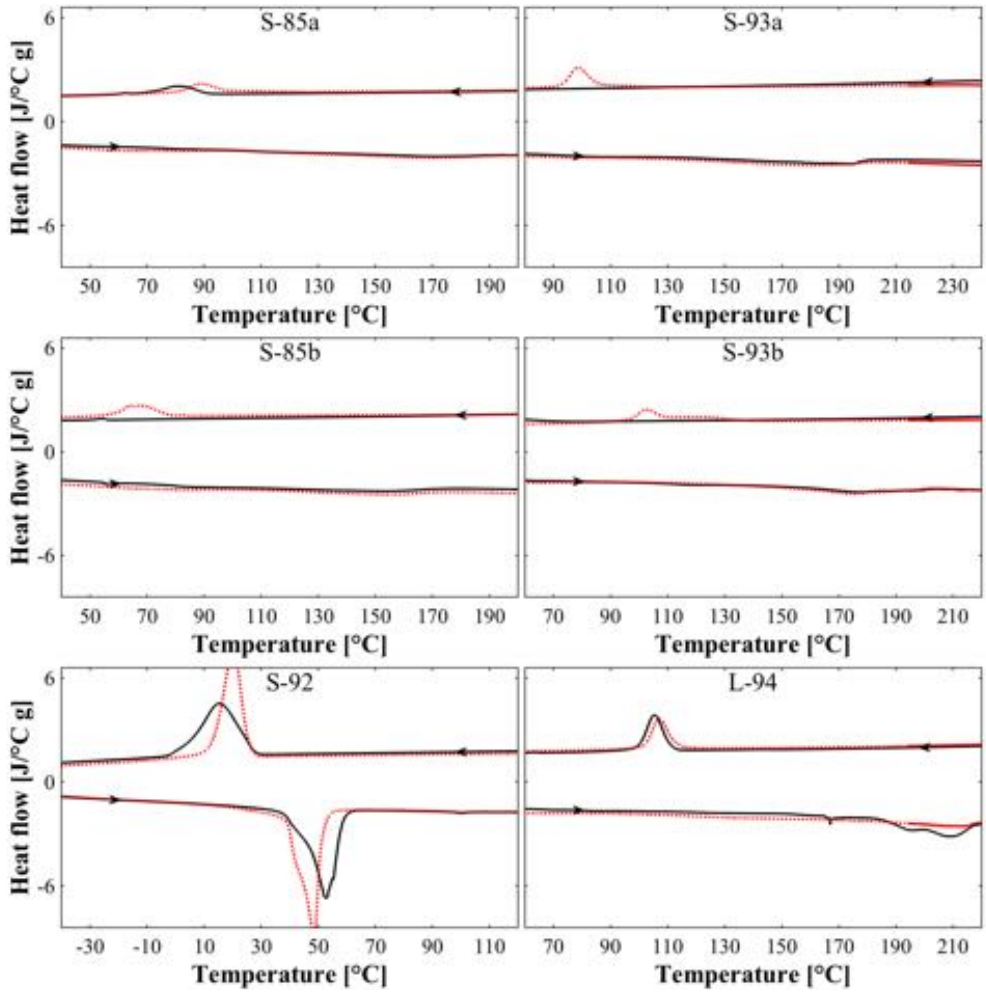


**Figure 4-22:** Effect of the addition of flow improvers on the DSC curves of TPU: pellet, pure (—) and powder with additives (----).

Secondly, relatively large amounts of flow improvers are added during the milling process. This addition prevents clogging of the sieves in the milling set-up. As shown in Figure 4-22, the additives typically act as a nucleating agent for crystallisation, thus raising the lower limit of the thermal window for the powder bed and thus introducing more issues with warpage, as discussed in Section 4.4.2. For pure TPU with a visible crystallisation peak, such as TPU S-85a and L-94, this addition results in a shift of the peak for a few degrees. Other materials, such as TPU S-93a and S-93b barely show any crystallisation peak for the pure material, but form a notable peak upon the addition of flow improvers. This newly formed peak strongly limits the thermal window for both grades.

Thirdly, significant post-condensation is present due to the cryomilling process, as seen in a substantial increase in the viscosity. To illustrate this effect, viscosity measurements are performed on various grades before and after milling. Figure 4-23 shows the viscosity measurements for two TPU grades that do not post-condense, namely S-85b and S-92. As seen in dynamic time-sweep measurements at 180 °C and 140 °C respectively (Figure 4-23a), the complex viscosity of both grades is stable in time. As a result, no significant change in the zero-shear viscosity is seen between the pellets and the powder (Figure 4-23b). Figure 4-24, on the other hand, shows the same measurements for two TPU grades that post-condense, namely S-93a and L-94. The time-sweep measurements reveal a significant increase of the complex viscosity in time (Figure 4-24a). Consequently, the milled powders show a viscosity that is 70 % to 100 % higher than their respective pellets (Figure 4-24b). This effect is seen for all post-condensing materials in this research.

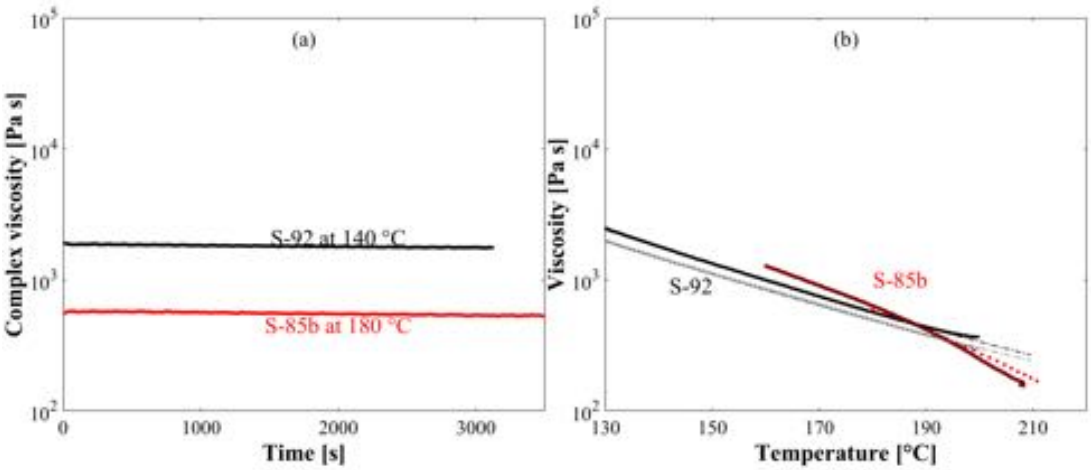


**Figure 4-23:** Viscosity measurements of TPU grades that do not post-condense, S-85b and S-92: (a) Dynamic time-sweep measurements at 1 % strain and 1 rad/s on the powder. (b) Steady zero-shear viscosity measurements on both the pellets (•) and powder (▲) at 0.05 $s^{-1}$ and -3 °C/min.

Prior to the viscosity measurements, the pellets and powders need to be melted into a plate-shape to allow the measurement. This preparation step has been mimicked exactly for the pellet and powder material, thus no significant difference is expected to arise from this preparation step. The difference in viscosity is therefore attributed to the milling procedure. The exact mechanism behind this viscosity increase is uncertain. The cryomilling process is cryogenically cooled, so no prolonged temperature elevation is expected. There may, however, be quite significant local heating upon particle deformation. The additional post-condensation is not necessarily problematic. It, however, needs to be taken into account when selecting pellets based on their viscosity and coalescence properties. A grade that is known to post-condense thus requires a viscosity that is significantly lower than that of the reference TPU and PA to allow for the currently unavoidable increase upon milling.

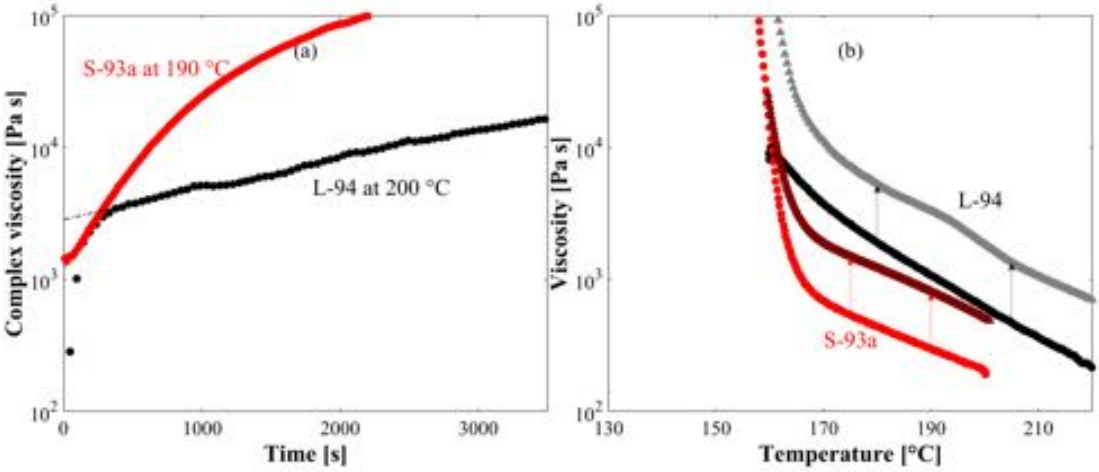


**Figure 4-24:** Viscosity measurements of TPU grades that post-condense, S-93a and L-94: (a) Dynamic time-sweep measurements at 1 % strain and 1 rad/s on the powder. (b) Steady zero-shear viscosity measurements on both the pellets (•) and powder (▲) at 0.02 $s^{-1}$ and -3 °C/min.

### 4.4.6 Proof of concept

As a proof of concept for the results obtained in the lab experiments, all milled grades except TPU T-95c are sintered on an industrial scale. TPU 95c was not tested due to the limited throughput created in the milling trials. The results are grouped in the following paragraphs to highlight the most important conclusions of these sintering tests.

**Poor grades: TPU S-85a, S-92 and T-85**

The first set of TPU grades are those that scored poorly on the lab screening and are deemed unsuccessful in industrial scale sintering tests. These grades are TPU S-85a, S-92 and T-85. All three grades show a lack of a usable thermal window for the

powder bed, as well as a high melt viscosity (cf. Table 4-6). The underperformance of these three grades in sintering tests thus proves the effectiveness of the screening methodology. In the sintering tests, both TPU S-85a and S-92 mainly show issues with the thermal window for the powder bed. In the case of TPU S-92, this small window is marked by a sharp melting and crystallisation peak (cf. Figure 4-22). As a result, no usable bed temperature is found at which the powder bed does not melt and the sintered layer does not curl. For TPU S-85a, on the other hand, the thermal window was much more ill-defined, due to the absence of a clear melting onset. Different bed temperatures between 105 °C and 120 °C have been tested, but either issues with curling or powder stickiness occur. Furthermore, many imperfections are present in the polymer melt pool, which are likely the result of the high material viscosity. TPU T-85 additionally showed a strongly incoherent melt pool, which is in line with the expectations from the viscosity measurements. As a result, no parts could be produced from any of these three grades.

**Unexpected coalescence issues: S-85b, S-93a and L-94**

The second set of results contains materials that scored quite well to excellent on the lab screening, but ran into unexpected coalescence behaviour. These grades are TPU S-85b, S-93a and L-94. TPU S-85b and S-93a passed all screening methods and TPU L-94 only shows issues due to its small stable sintering region. Sintering tests confirmed this degradation finding by strong yellowing of the parts. All materials showed adequate powder flowability, which supports the findings of the spreading experiments. As a result, the irregular particle morphology of the cryomilled powders is not deemed problematic to create sinterable powders.

The main issue with these materials is, however, their melt behaviour. Upon melting within an LS machine, the materials form distinct droplets rather than a homogenous melt pool. This behaviour is unseen in any other polymer class tested thus far. These issues are not observed in hot stage measurements at lab scale, as illustrated in Figure 4-25 for TPU S-93a and L-94. In these experiments the material coalesces similarly to any other TPU grade in this chapter. The coalescence of TPU L-94 is quite slow, which is likely the result of strong post-condensation during milling, as discussed in Section 4.4.5. No conclusive explanation of this behaviour is known at this time. The difference in behaviour between the HSM and sintering tests is expected to result from a different interfacial behaviour between the polymer melt and the unsintered powder bed, compared to the interaction between the melt and the glass substrate in HSM measurements. Another explanation is the possible degradation of the material due to the high-energy input by the laser. The degraded material may show a different interaction with the unsintered powder. Finally, segregation of the different segments in the structure of the TPU may occur upon melting. This may change the interaction with the underlying powder. Currently no screening tool is available to predict this behaviour.

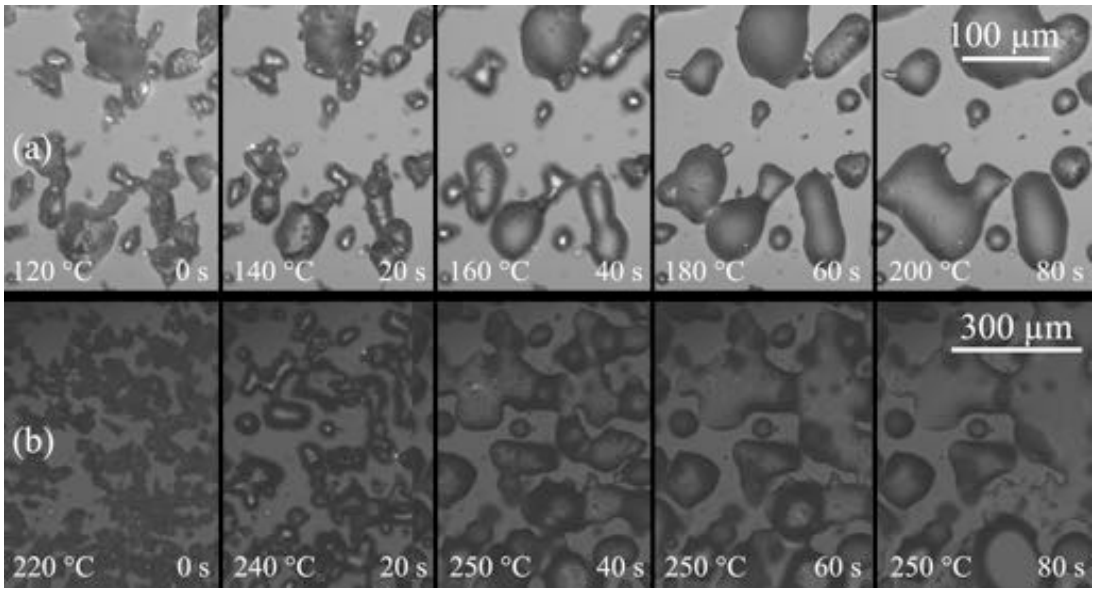


**Figure 4-25:** HSM measurements of S-93a (a) and L-94 (b).

**Sinterable grades: TPU S-90, S-93a, S-94, S-97 and T-95a**

TPU S-90, S-93a, S-94, S-97 and T-95a have been sintered to multilayer test parts. This further indicates the effectiveness of the screening methodology, as most of these materials have a perfect score on the lab screening. Only TPU S-93a shows a strongly decreased thermal window after cryomilling (Figure 4-22), but due to its limited shrinkage this is not problematic in sintering tests. However, for all four materials a strong drop in mechanical strength is seen upon sintering the material. All sintered parts, except TPU S-97, show tensile strengths around or below 10 MPa, which limits their commercial viability. TPU S-97 also shows a loss in material strength down to 15 MPa. Strength loss is also present for commercial sintering TPU, such as Luvosint. Verbelen et al. showed a 50% strength loss between the moulded and sintered parts [41]. The reason for this strength loss upon sintering is further investigated in the next paragraph. Furthermore, the similar results for the ester and ether TPU within this subgroup indicate that there is no fundamental difference in the sinterability of ester or ether grades.

TPA-95a has been sintered with the process parameters listed in Table 4-9. Two bed temperatures of 140 °C and 148 °C respectively have been tested. These temperatures lie well within the thermal window defined in Section 4.4.2. The layer thickness is selected based on the settings for commercial sintering TPU to provide a direct comparison in performance. As shown in Table 4-7, the reference TPU Luvosint has a $D_{90}$ value above 130 µm. As a result, a layer thickness of 150 µm is required for this material. The milled TPU grades, however, have a significantly smaller particle size, thus a smaller layer thickness is possible. This is further proven by the successful spreading tests with a layer thickness of 100 µm. The laser power is varied to obtain a range of ED values.

**Table 4-9:** Sintering parameters of TPU T-95a and S-92.

| | T-95a | | | S-92 |
|---|---|---|---|---|
| | **Set 1** | **Set 2** | **Set 3** | **Set1** |
| **Bed temperature [°C]** | 140/148 | 140/148 | 140/148 | 102 |
| **Layer thickness [mm]** | 0.15 | 0.15 | 0.15 | 0.15 |
| **Laser power [W]** | 12 | 20 | 36 | 40 |
| **Scan spacing [mm]** | 0.1 | 0.1 | 0.1 | 0.1 |
| **Scan speed [mm/s]** | 4000 | 4000 | 4000 | 5000 |
| **Energy density (Eq. 1.3a) [J/mm$^2$]** | 0.05 | 0.07 | 0.09 | 0.08 |

Tensile bars are printed in the xy-plane and their mechanical properties are measured. The results are shown in Figure 4-26 and Figure 4-27. To evaluate the mechanical properties of the sintered parts, the results are compared to tensile bars created via compression moulding. These compression-moulded parts are made from the raw pellet, the milled powder and the sintered material of each processing parameter set. The moulding temperature strongly affects the structure of the formed TPU part. As a result, the mechanical properties are strongly dependent on the processing parameters. Therefore, all compression-moulded parts are made by the same protocol. The material is melted at 240 °C and 50 bar, followed by a fast cooling by a water flow at ambient conditions. Tests on various TPU samples have shown that a change in the moulding protocol can result in strength changes up to 50 %.

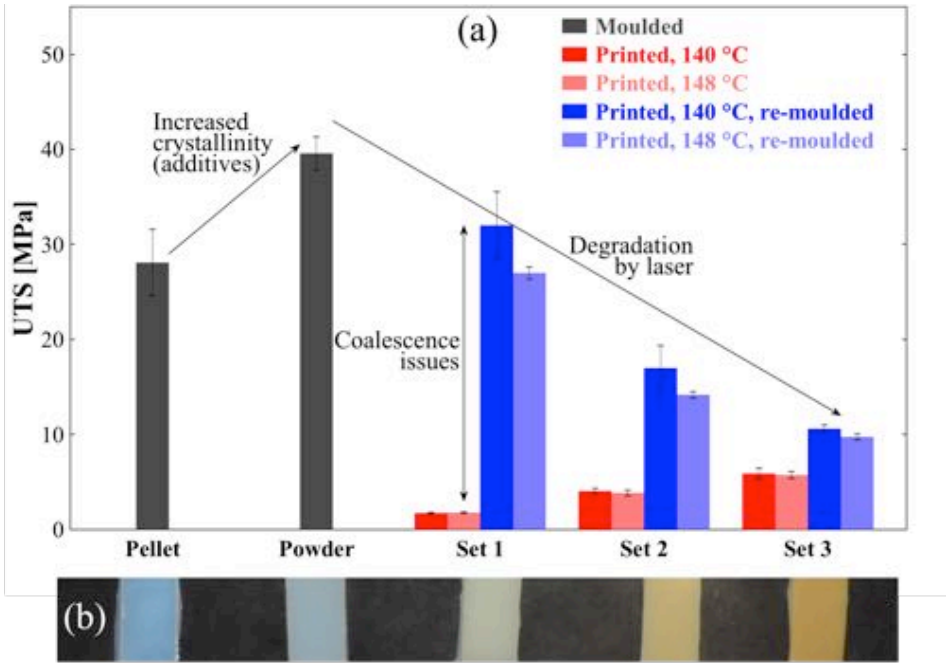


**Figure 4-26:** Ultimate tensile strength of sintered and moulded TPU T-95a parts (a) and pictures of the moulded tensile bars (b).

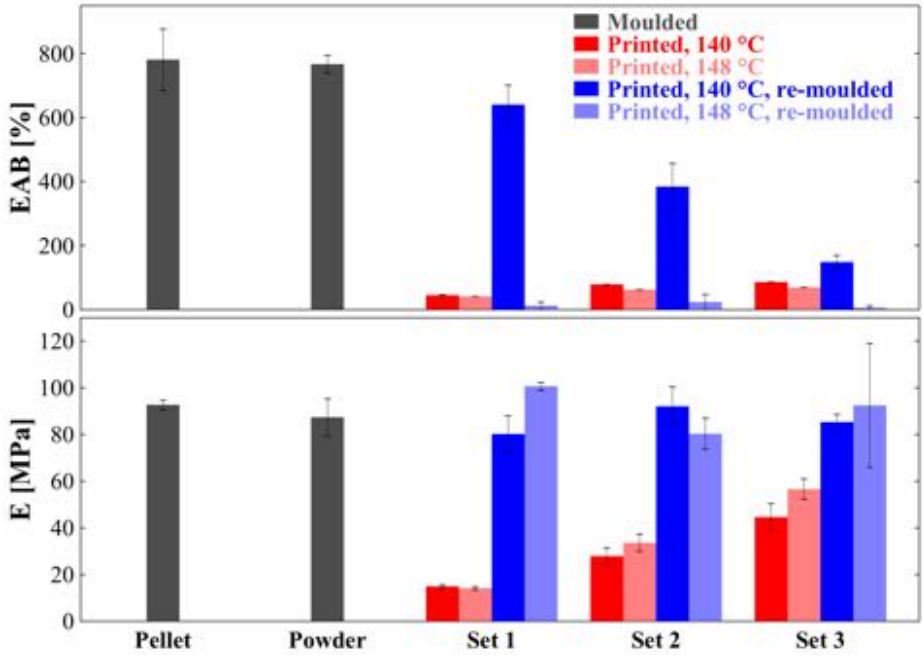


**Figure 4-27:** EAB and Young's modulus of sintered and moulded TPU T-95a parts.

Firstly, it is seen that the moulded parts created directly from the pellets have a lower strength than that indicated by the manufacturer (cf. Table 4-4). This is the result of a different moulding process. The material also undergoes a strongly different thermal history in LS, compared to the moulding process. This difference may result in different crystallisation, which may partially explain the loss in mechanical strength. Secondly it is seen that the moulded parts created from the powder have a 40% higher strength, which is likely due to an increase in crystallinity caused by the flow additives. This change in structure is also seen in the decreased transparency of the tensile bars. The sintered parts, however, show strengths that are up to 20 times lower than that of the powder reference. The bed temperature, which is varied between 140 °C and 148 °C, has no significant effect on this result. Increasing the ED, on the other hand, does have a positive effect. This increase is due to the improved coalescence, which lowers the final part porosity. Computed tomography scans support this finding, as the porosity decreases from 46 % to 21%, which is still quite high. The porosity at low ED is mainly due to insufficient coalescence. At 0.09 J/mm$^2$, however, large spherical pores are seen, which are likely formed due to gas formation upon degradation. Another contributing factor to the high porosity may be high powder bed porosity prior to sintering. As shown in the spreading experiments, the bed porosity of the cryomilled grades is much higher than that of the smooth PA powders of the Section 4.3. As a result, the melt coalescence has to compensate much more.

Re-moulding of the sintered parts further illustrates the degradation issue. Parts that were sintered at the lowest ED values recover most of their strength upon re-moulding. This recovery indicates that the polymer was not severely damaged by the laser. At the higher ED values, however, the strength recovery decreases, which indicates that the material has irreversibly degraded. This degradation is also visually present, as the material shows increased yellowness at elevated ED values. This may form an indication that the stable sintering regions up to 74 °C are insufficient. The stable sintering regions of the reference TPU and PA 2200 are each above 100 °C (cf. Table 4-5 and Figure 2-5). The results are similar for the elongation at break and the elastic modulus (Figure 4-27). The modulus is, however, much less affected by degradation.

TPU S-97 has proven to be the most successful material. Sintering tests at various processing parameters have been tested. Sintered parts at the most optimal parameter set, listed in Table 4-9, possessed a tensile strength of around 15 MPa. This is deemed a viable result for the material. Furthermore, the sintered parts show limited to no yellowing, as shown in Figure 4-28, which indicates fewer degradation issues. A possible explanation for this result is the extraordinarily large stable sintering region of 161 °C. Increasing the energy density further, however, did not improve the part properties and even resulted in a slight loss of strength.

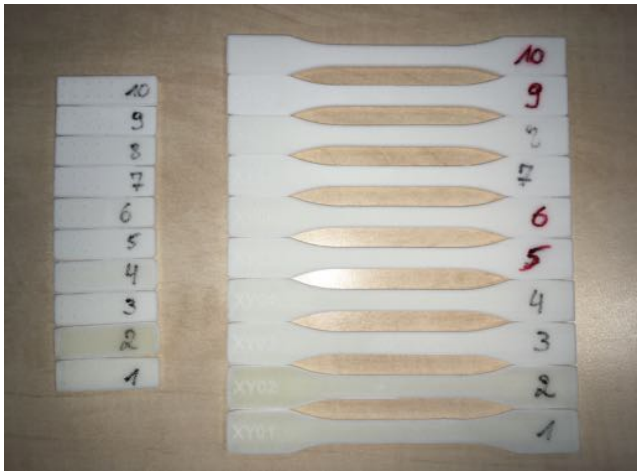


**Figure 4-28:** Sintered parts of S-97.

The attainable bed temperature is slightly higher than that predicted by DSC. A possible explanation for this observation is that at this temperature not enough of the polymer crystals have melted to induce powder stickiness. The effect of temperature on powder flowability is further elaborated on in Chapter 5, which introduces some new materials that are strongly influenced by thermal effects.

### 4.4.7 Conclusions

The screening methodology has successfully found some sinterable TPU grades among various TPU families and correctly indicated sintering issues for other grades. Loss of mechanical properties upon sintering, however, remains an issue for many TPU grades. Degradation and coalescence play an important role as well as the high powder bed porosity upon powder deposition. Though the packing density of deposited layers is significantly lower for these cryomilled powders, all powders managed to spread into smooth and defect-free layers.

TPU S-97 is deemed the most promising grade of this section, as sintering tests created multi-layer parts with limited yellowing and the highest strength of all tested TPU grades. The screening results of this material are summarised in Figure 4-29. A main advantage of this grade is the wide stable sintering region, which may be the cause of the increased strength compared to the other grades. Furthermore, the viscosity of this grade is similar to that of the reference TPU and PA grades.

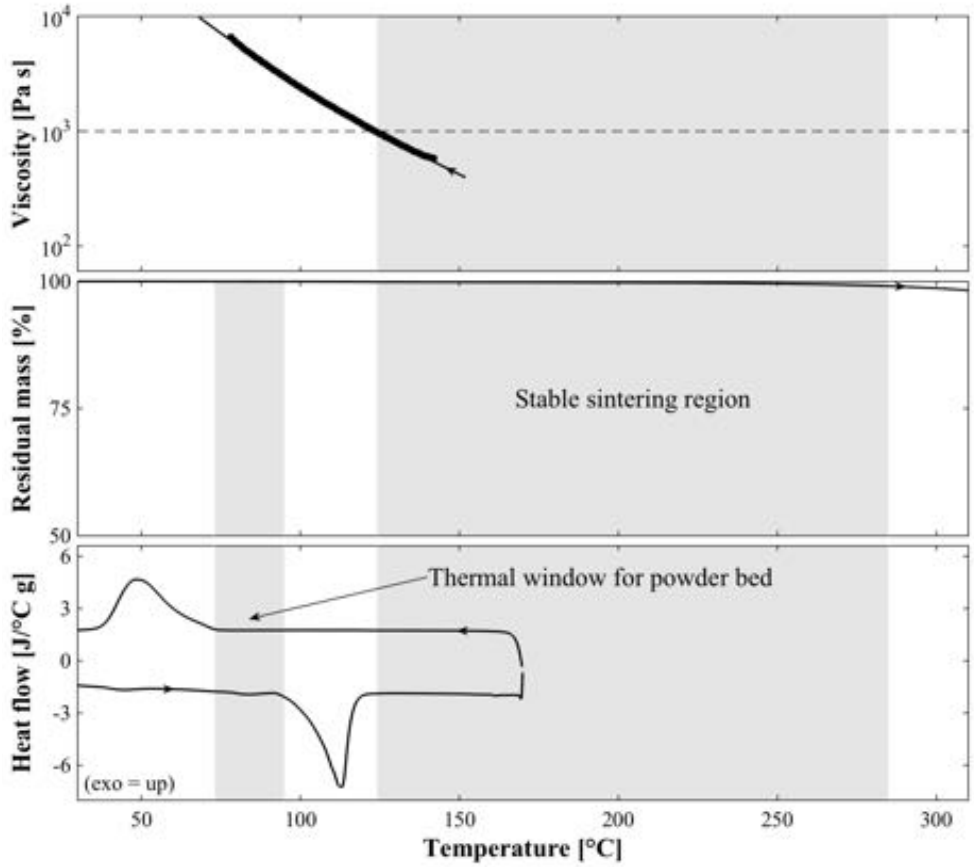


**Figure 4-29:** Thermal processing windows for TPU S-97.

## 4.5 Conclusions

This chapter illustrated the successful application of the cryomilling process to add new grades of existing sintering polymers, namely PA and TPU, to the LS material palette. Even though a rough and irregular morphology is obtained, the flowability of all grades is still sufficient to produce homogenous and defect-free powder layers. In direct comparison to "smooth" powder alternatives, a decrease in flowability is seen however. This decreased flowability results in slightly lower packing densities for the milled materials, which needs to be accounted for by good coalescence.

The cryomilling processing route as well as the polymer screening methodology demonstrated in this chapter are further utilised in the following chapter to create and evaluate new materials for laser sintering.

# Chapter 5

# New materials for LS: flow at elevated temperature

The previous chapter introduced new grades of common LS polymers by applying the cryomilling route. As this production process proves to be viable for creating sinterable powders, it is further applied to add new polymers to the LS material palette. Powder flow behaviour at elevated temperature has proven to be an important factor for many of the materials proposed in this chapter. As a result, the powder flowability techniques discussed in Chapter 3 form an important tool for assessing these materials. Section 5.1 briefly summarises the materials of this chapter and the additional measurement protocols that are applied to assess them. The protocols that were applied in Chapters 3 and 4 are further utilised on these new materials and their details are found in the respective chapters. Sections 5.2 to 5.4 then each assess a new material for its applicability in LS.

## 5.1 Materials & methods

This section discusses the new materials and methods, compared to the previous chapters. Section 5.1.1 summarises the material parameters and particle properties of the milled powders. Sections 5.1.2 to 5.1.4 then discuss three additional screening methods that are used throughout this chapter. The first method is the Hausner ratio test, which is introduced in Chapter 2. The second method is wide-angle X-ray scattering, which evaluates the crystal structure of polymers. The third method is dilatometry, which determines the shrinkage behaviour of the materials upon solidification.

### 5.1.1 Summary of materials

During this research, various new polymers have been evaluated for their applicability in LS. This chapter discusses three of them: polylactic acid (PLA, Section 5.2), polybutene-1 (PB-1, Section 5.3) and a copolyamide (coPA, Section 5.4). All these materials are available in pellet form and are thus cryomilled to a powder in the desired size range. Each of these materials is assessed for every step in the LS process, with a focus on powder flowability and thermal treatments to improve their flow behaviour. To provide a useful frame of reference, the results of PA 2200 (Chapter 3) are repeated throughout this chapter.

All materials have been successfully cryomilled. The resulting powder properties are summarised in Table 5-1. The material properties of each polymer are shown in Table 5-2. Thermal treatments have been applied to the PLA and PB-1 powders, resulting in additional samples. The details of these treatments are further discussed in their respective sections. In general, the cryomilled samples show slightly broader PSD's, which is in line with the other cryomilled powders that are discussed in Chapter 4. Furthermore, their particle size is slightly lower than that of PA 2200, especially in the case of the PB-1 powders, which leads to higher Bond numbers. Furthermore, as all the cryomilled powders show the typical, rough powder morphology that is inherent to the process, mediocre powder flow is expected. The material density of each sample is measured by the same protocol as the previous chapters. The Hamaker constants are taken from literature to provide an estimation for the Bond number. In the case of coPA, the value for polyamide was taken to provide a comparison. This leads to approximate Bond numbers that serve mainly to assess the PSD of the powders. However, as shown in Chapter 4, the irregular shape of the particles and the uncertain amount of flow improvers present in the sample due to cryomilling strongly hinder the prediction of flow behaviour based on the Bond number alone. As no representative Hamaker constant is found for the PLA powder, the Bond number is not computed.

**Table 5-1:** Summary of the main properties of the powders used in Chapter 5.

| Sample | $D_{10}$ [µm] | $D_{50}$ [µm] | $D_{90}$ [µm] | relative span [/] | $\Psi$ [/] | Bo [/] |
|---|---|---|---|---|---|---|
| **PA 2200 (Chapter 3)** | 39.5 | 63.4 | 82.2 | 0.67 | 0.86 | 1.49 |
| **PLA** | 35.9 | 66.5 | 95.7 | 0.90 | 0.76 | NA |
| **PLA-HT** | 37.9 | 66.8 | 96.4 | 0.88 | 0.76 | NA |
| **PB-1u** | 16.3 | 43.7 | 72.6 | 1.29 | 0.78 | 2.70 |
| **PB-1a** | 18.4 | 46.5 | 75.2 | 1.22 | 0.80 | 2.28 |
| **PB-1m** | 22.2 | 55.4 | 87.6 | 1.18 | 0.82 | 1.61 |
| **coPA** | 30.4 | 61.0 | 91.1 | 1.00 | 0.77 | 1.63 |

**Table 5-2:** Physical properties of the different samples used in Chapter 4.

| Sample | $\rho_m$ [kg/m$^3$] | $A_h$ [J/10$^{20}$] |
|---|---|---|
| **PA 2200 (Chapter 3)** | 1.07 ± 0.001 | 7.9 [87] |
| **PLA** | 1.23 ± 0.008 | NA |
| **PLA-HT** | 1.22 ± 0.018 | NA |
| **PB-1u** | 0.95 ± 0.011 | 5.6 [192] |
| **PB-1a** | 0.94 ± 0.001 | 5.6 [192] |
| **PB-1m*** | 0.89 ± 0.003 | 5.6 [192] |
| **PB-1m**** | 0.94 ± 0.001 | 5.6 [192] |
| **coPA** | 1.06 ± 0.001 | 7.9$^{\blacklozenge}$ |

*samples taken immediately after solidification

**samples taken >72 hours after solidification

$^{\blacklozenge}$value for PA taken

### 5.1.2 Hausner ratio

The Hausner ratio, described in Section 2.3.2, is used to evaluate the compaction properties of the powders. The measurements are performed on a JV 1000 Tapped Density Tester (Copley Scientific) with a 100 ml borosilicate glass cylinder with a 28 mm diameter. The device applies a tapping rate of 250 taps/min with a drop height of 3 ± 0.2 mm. To ensure a consistent filling procedure, a sieve with a mesh of 1.7 mm and a funnel are mounted at a fixed height directly above the glass cylinder. Powder is scooped in manually in amounts of a few grams. The cylinder is filled as close as possible to 100 ml, but never higher, and the starting volume is noted. The change in volume is recorded in function of the amount of taps. After tapping, the weight of the sample is measured to enable the computation of the density at each measurement point.

### 5.1.3 Wide angle X-ray scattering (WAXS)

*Passages from this sub-section have been adapted from an own, published journal paper [193].*

Wide angle X-ray scattering (WAXS) is used to determine the crystal structure of the polymers when relevant. A XeuSS (Xenox) with a Mo-source (λ = 0.7107 Å) and a MAR345 (MARresearch) image plate detector are used. The flight path between source and sample is kept under vacuum, while the flight path between the sample and detector is flushed with helium. Heating of the powder samples is performed on a Linkam DSC600 hot stage with a T95-PE controller and an LNP95

cooling system. First, the powder is measured at ambient condition, prior to heating. Next, immediately after melting, the powder is measured again. And finally, the sample is cooled at 1 °C/min to 25 °C, during which the sample is measured every 33 minutes.

The sintered samples are measured on a non-commercial sample holder. This holder hangs the parts in front of the beam at ambient conditions. The sample positions of both the hot stage and the sintered part holder are calibrated with an AgBeh powder with known scattering angles. The raw scattering data is transformed to a 1D pattern using azimuthal averaging. Two software programs, Fit2D and Conex, aid in this processing.

### 5.1.4 Dilatometry

*Passages from this sub-section have been adapted from an own, published journal paper [193].*

Shrinkage properties are measured by dilatometric measurements under atmospheric conditions, as the LS process operates at atmospheric pressure. These measurements are performed on a modified Q400 TMA (TA Instruments). The protocol for these measurements was developed in earlier studies [5] and has been applied in literature for research on PA [73]. As discussed in Section 2.1.3, low shrinkage is desired to avoid warpage issues during the build. The focus lies on the crystallisation shrinkage, as this is deemed the most significant contribution to these warpage issues.

The expansion of the Q400 TMA consists of a cylindrical, glass container. The sample is placed within the container and submerged in viscous silicon oil. Prior to the measurement, the filled container is placed in a vacuum oven at 50 °C to remove entrapped air bubbles. A glass lid rests on top of the oil and is able to move freely in the vertical direction. As a result, the volumetric expansion of the sample and the oil is converted into a linear motion of the lid. The TMA then applies a heating rate of 0.5 °C/min and a subsequent cooling rate of -0.5 °C/min. Before each ramp, the sample is equilibrated for 5 minutes. The same thermal profile is applied to a reference cell that only contains the silicon oil. This measurement is used to subtract the oil expansion from the final results.

## 5.2 Polylactic acid (PLA)

The first polymer is a polylactic acid (PLA). PLA is a synthetic thermoplastic aliphatic polyester, which is biodegradable [194]. It is created via a condensation polymerisation of lactic acid, during which water is set free (cf. Figure 5-1) [195].

Within the additive manufacturing material palette, it is the second most common material for FDM, only surpassed by acrylonitrile butadiene styrene (ABS) [14,196]. However, for LS its use is still limited. Some sources discuss PLA as a usable material for biomedical applications that focus mainly on porous scaffolds [197]. The reason for this application lies in the biocompatibility and biodegradability of the polymer. Its use in mechanical, full-dense end-parts is, however, scarce [14].

Recently, Bai et al. have performed research on low temperature sintering of PLA and PLA composites. They managed to sinter a pure PLA grade at a powder bed temperature of 80 °C, which is far below the melting point of 160 °C for their chosen grade [42]. The resulting parts had, however, a high porosity, which is likely the result of poor coalescence. The limited coalescence is possibly due to the fast cooling of the polymer melt by the cold surrounding powder or the excessive temperature increase that needs to be achieved by the laser energy. This problem was partially solved by applying a double scan.

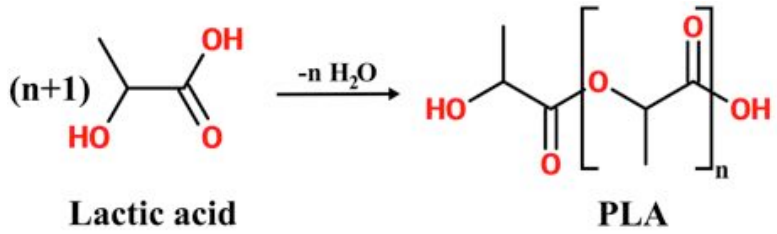


**Figure 5-1:** Molecular structure of lactic acid and PLA.

In this work, a pure PLA grade, namely Ingeo Biopolymer 3251D (NatureWorks), is examined for its sinterability. This specific grade is designed for injection moulding, thus low viscosity and, as a result, good coalescence is expected [198]. The grade is, however, currently not used as a sintering polymer. Some issues with powder flow at elevated temperatures are seen with this grade, as discussed more in detail in Section 5.2.1. A heat treatment is therefore proposed to improve processability. The heat-treated sample is labelled as PLA-HT throughout this text.

### 5.2.1 Powder characterisation

The PLA powder, which results from cryomilling, has a similar PSD to PA 2200, as illustrated in Figure 5-2a and Table 5-1. However, large fibre-like particles are present in the sample (cf. Figure 5-2b). These fibre-like particles are likely the result of the local heating during cryomilling, as discussed in Chapter 4. This heating results in strong plastic deformation when the material hits the milling pins. The PLA sample has an average sphericity of 0.76, which is lower than that of PA 2200, but is still relatively high. There are two reasons for the limited influence of the fibre-like particles on the sphericity. The first reason is the low amount of fibre-like particles that are present. As a result, their contribution to the average sphericity is

limited, even though they have extremely low sphericity values. For example: a 100 µm fibre with a 5 µm diameter results in a sphericity of 0.06, according to Eq. 1.11. The second reason is the fixed protocol of the device, which uses the projected area to determine the sphericity. The more the fibre is curled up or aligned with the camera lens, the higher its apparent sphericity is.

The material has a density of 1.23±0.008 g/cm$^3$. It is thus one of the denser polymers assessed in this work, which has a positive effect on inter-particle interaction due to the increase of the inertia force. As no representative value for the Hamaker constant is found in literature, the Bond number is not computed.

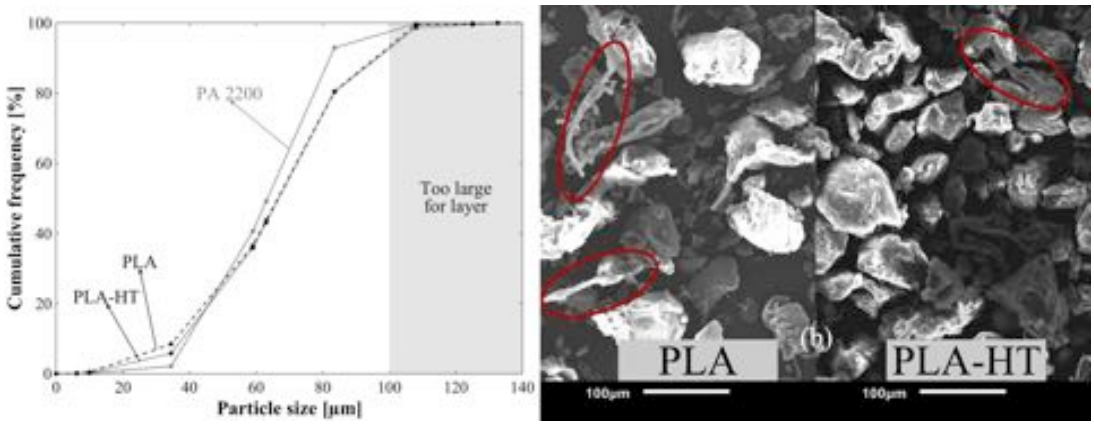


**Figure 5-2:** PSD (a) and SEM (b) image of cryomilled PLA powder and the heat-treated powder (PLA-HT). Long fibre-like structures are indicated in red.

DSC measurements provide a first indication on the thermal window for the powder bed. Figure 5-3 shows the DSC curve of the PLA grade in comparison to PA 2200. The PLA has a glass transition temperature of around 53 °C. During the heating cycle, a significant peak is seen around the glass transition. This type of peak is typically the result of annealing a glassy polymer below its glass transition temperature. During this annealing, the enthalpy drops. This enthalpy loss is then again recovered upon heating, resulting in the endothermic peak [199]. The peak is thus a result of the history of the polymer and it is not seen in a subsequent second heating cycle. During HSM measurements, the PLA particles tend to move strongly and occasionally even jump during heating at low temperatures around the glass transition. This movement is likely related to some stored stress that is relieved upon passing the glass transition. This behaviour is likely to affect its flowability properties.

The melting peak of the PLA is located at 167.3 °C. The sharpness of this peak defines a clear upper limit for the thermal window for the powder bed at roughly 150 °C. However, even at temperatures below the melting onset, issues with powder stickiness arise. These stickiness issues are further discussed for lab-scale measurements in Section 5.2.2 and for industrial sintering tests in Section 5.2.6.

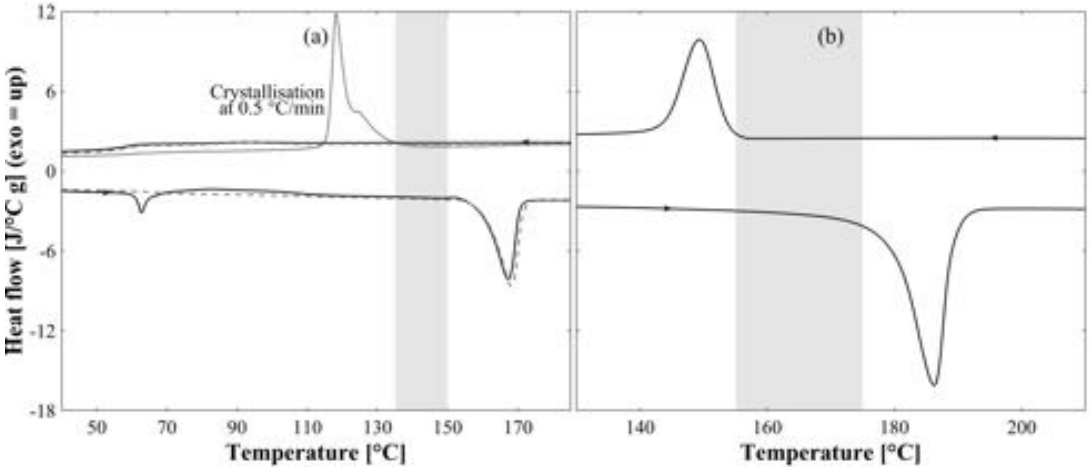


**Figure 5-3:** DSC measurements of PLA (—) and PLA-HT (- - -) (a) and PA 2200 (b) at 10 °C/min. The grey zones indicate the available thermal window for the powder bed.

A thermal treatment is proposed to solve these flow issues at elevated temperatures. This thermal treatment consists of annealing the PLA at 100 °C for at least 3 hours. Shorter annealing times are possible, provided that the entire powder mass reaches 100 °C before the end of the treatment. This treatment does not only dry the sample, it also removes the enthalpic peak around the glass transition temperature, which indicates that the material is in a different state. Furthermore, in HSM measurements of the treated sample, no powder movement is seen up until the melting onset, which further indicates that the state of material has changed. A glassy polymer is, however, able to continuously evolve toward this lower energetic state by structural relaxation, which is also called physical aging[200]. DSC tests show no reappearance of the endothermic peak around the glass transition within 2 weeks. However, samples that have aged for more than a year again show the same DSC result as the original powder. Some caking occurs during the proposed thermal treatment, which is in correspondence to the powder flow measurements of Section 5.2.2. However, no unbreakable agglomerates are formed and, as a result, after sieving the heat-treated sample retains the same PSD as the untreated sample, as shown in Figure 5-2. The string-like particles also remain in the sample. Furthermore, no significant difference was found in the material density before and after annealing.

Upon cooling from the melt at 10 °C/min, the polymer forms its amorphous state, as shown in Figure 5-3a. The absence of crystallisation and corresponding shrinkage yields no strict lower limit for the thermal window for the powder bed, as discussed in Chapter 3. However, in LS the cooling rate is much lower. DSC measurements at 0.5 °C/min show a crystallisation onset at 135 °C. As a result, the thermal window for the powder bed, based solely on DSC, is roughly 15 °C wide. This is slightly smaller than that of PA 2200, which is about 20 °C. The measurements of Section 5.2.2 further evaluate this thermal window from a flowability perspective. Hamad et

al. describe a melting enthalpy of 93.1 J/g for pure crystalline PLA homopolymers [201]. Based on DSC measurements, the selected grade has a melting enthalpy of 44.7 J/g. This corresponds to a degree of crystallisation of about 48 %.

An important property of any PLA is its degradation mechanism. PLA degrades in the presence of moisture and/or at elevated temperatures. The degradation mechanisms include hydrolysis and thermolysis up to the reformation of the lactic acid monomer [202]. Drying of the sample is therefore crucial. The manufacturer recommends drying the pellets for at least 3 hours at 100 °C or 10 hours at 50 °C [198]. Thermogravimetric measurements show that the PLA sample has a moisture content of 0.73 ± 0.05 wt% prior to drying. After drying for 24 hours at 50 °C under vacuum the moisture content was too low to measure by this thermogramitric technique. However, the removal of moisture does not completely prevent the degradation of PLA. Studies have shown that at temperatures as low as 10 °C above the melting point of PLA thermal degradation is seen due to chain splitting, rather than hydrolysis [195,203].

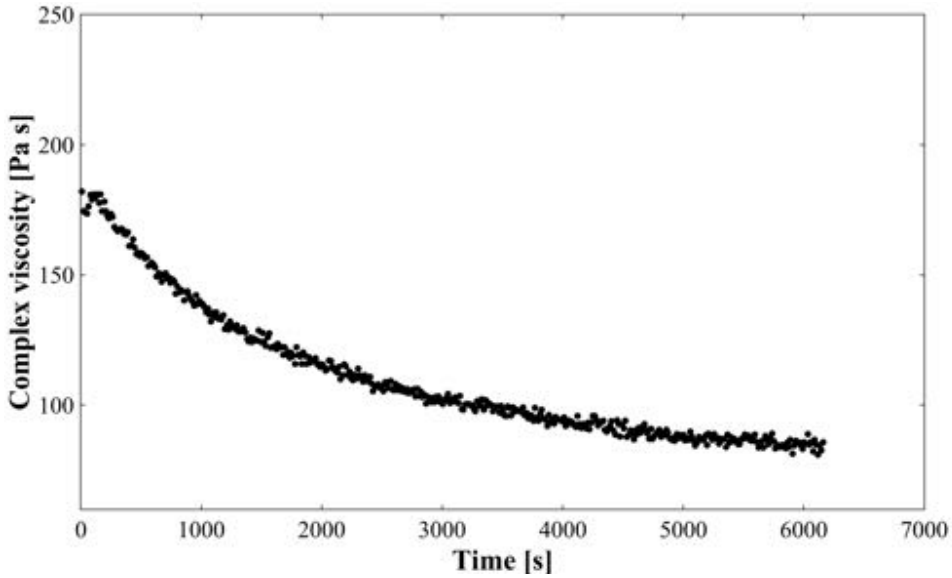


**Figure 5-4:** Viscosity degradation of PLA at 180 °C after drying 18 hours at 50 °C (measured at 1 % strain, 1 rad/s).

Figure 5-4 illustrates the thermal degradation of the PLA sample after drying for 24 hours at 50 °C. The complex viscosity of the sample, which is measured at 180 °C, 1 rad/s and 1 % strain, continuously drops in time. This viscosity drop is the result of the reduction of the molecular weight due to thermolysis. The thermal overshoot caused by the laser in LS is therefore expected to significantly affect the molecular weight and thus the resulting strength of the sintered part.

### 5.2.2 Powder flowability

As expected from the irregular particle morphology, the powder exhibits generally poor flowability. Similar to most cryogenically milled powders in this research, angles well above 45° are present in the A-DAoR measurement (cf. Table 5-3). In the spreading experiments, the powder exhibits an average packing density that is similar to that of PA 2200. Also, the geometrical packing limit is quite similar, which may be the direct result of the nearly identical PSD. However, when looking at individual layers, a remarkable difference is seen. The layer density of the PLA sample varied extraordinary strong, resulting in a large standard deviation on the packing density. However, in independent spreading measurements of PLA samples, roughly the same average density is always found after the deposition of 20 or more layers. The inherently strong inter-layer density variation may result from poor powder flowability, which is partially caused by the fibre-like particles. Another explanation lies in the elastic recovery of the powder bed, which is seen in LS tests of Section 5.2.6. In these tests it is demonstrated that the bed shows strong elastic relaxation after the blade has passed. As a result, the actual thickness of the deposited layer is impossible to determine in the current set-up. As a constant layer thickness of 100 µm is assumed in the computations, this could result in a false apparent density that strongly fluctuates. Finally, some layers also showed surface defects. These layers were not included for the density determination, but further illustrate the flowability issues.

**Table 5-3:** Powder flowability indices based on the dynamic angle of repose (A-DAoR) and spreading experiments for PLA and PA 2200.

| | $\widehat{\phi}$ [°] | $\widehat{\phi}_a$ [°] | $\rho_{pk,geom}$ [%] | $\rho_{pk}$ [%] |
|---|---|---|---|---|
| **PA 2200 (Chapter 3)** | 36.6 ± 0.3 | 40.0 ± 0.3 | 51 | 44 ± 5 [73] |
| **PLA** | 47.2 ± 0.7 | 53.9 ± 0.8 | 49 | 42 ± 12 |
| **PLA-HT** | 40.9 ± 0.6 | 45.5 ± 0.6 | 49 | NA |

PLA-HT shows significantly better powder flow. Both the average and avalanche angle drop roughly 7-8°. The positive effect on flowability is also visualised by a much smoother powder surface and smaller deviation on the edge location (cf. Figure 5-5). A similar result is seen in the powder rheometer. At ambient conditions, an improvement of the powder flowability of PLA-HT is noticeable by the decreased flow energy. The effect at elevated temperatures is even more pronounced. Around 100 °C the flow energy of the untreated PLA sample starts to increase. At 140 °C the stickiness becomes so strong that cohesive lumps of powder are formed, which results in strong variations in the measured flow energy. The

heat-treated powder, however, does not show this behaviour, as the flow energy remains relatively constant up to 145 °C. The increased stickiness of the PLA sample at temperatures well-below the sharp melting onset corresponds with observations in industrial sintering tests (Section 5.2.6).

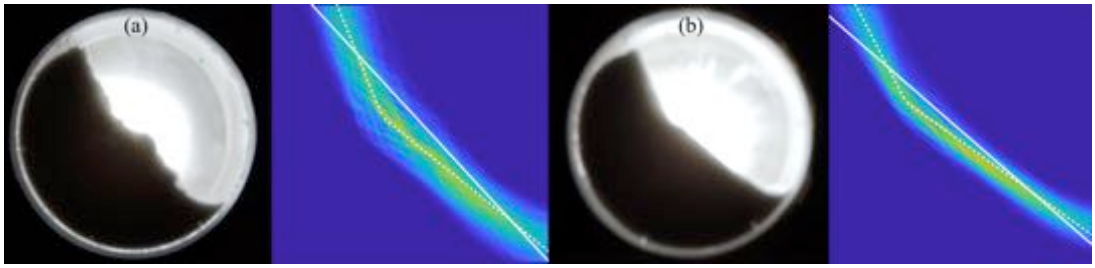


**Figure 5-5:** Representative A-DAoR frames of PLA (a) and PLA-HT (b) and the respective edge heat maps of the full measurement.

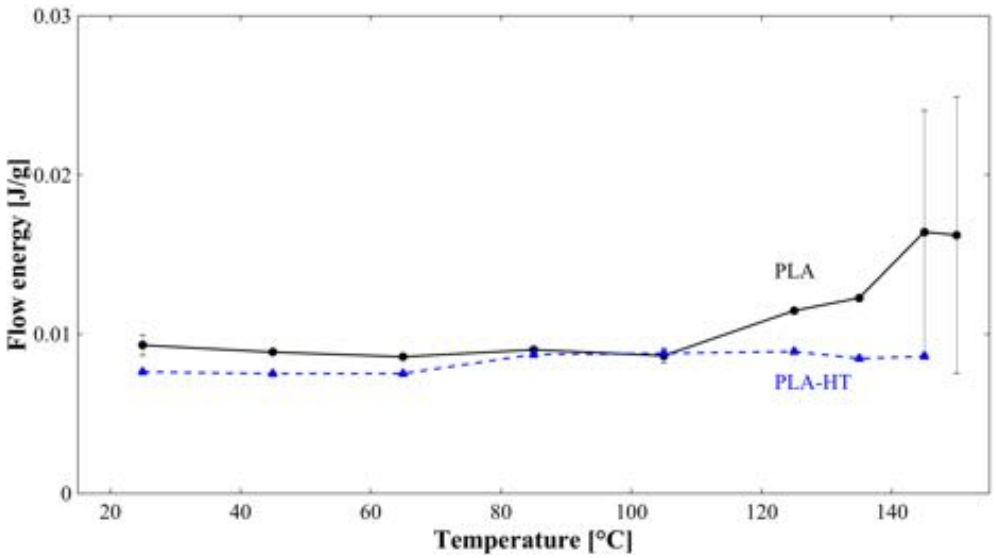


**Figure 5-6:** Powder rheometry results of PLA and PLA-HT.

The PLA powder further showed some notable caking issues during storage at ambient conditions, which further indicates flowability issues. This effect of time consolidation is further assessed by the Hausner ratio of the material. The Hausner ratio was measured at a tapping frequency of 250 taps/min and a drop height of 3 ± 0.2 mm. As shown in Figure 5-7, the Hausner ratio of PLA is significantly higher than that of PA 2200. PLA and PA 2200 have a Hausner ratio of 1.29 and 1.09 respectively. This corresponds to the high compaction seen during the storage of the PLA grade. The Hausner ratio measurement, however, is unable to detect a difference between the untreated and annealed PLA samples. The addition of flow additive C, which was introduced in Chapter 3, reduces the Hausner ratio of PLA to 1.25. Though this is a significant improvement, it does not fully solve the compaction issue. The addition of flow improvers did not show a measurable improvement on the A-DAoR measurements of this material.

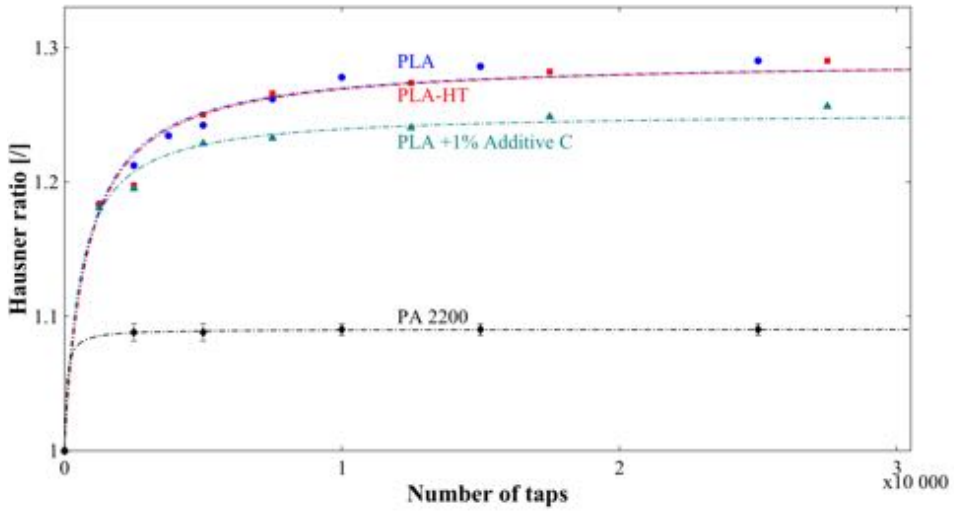


**Figure 5-7:** Hausner ratio of PLA, PLA-HT and PLA with additive C. The dotted lines are fitted by the Kawakita equation (Eq. **1.17**).

### 5.2.3 Coalescence

The chosen PLA grade has a viscosity that is comparable to that of PA 2200. Figure 5-8a shows the zero shear viscosity of both materials as a function of the temperature difference relative to the melting peak (167.3 °C for PLA and 186.2 °C for PA 2200). Above the melting peak, the viscosity of the PLA is already well below the 1000 Pa s limit and is even lower than that of PA 2200. The slope of the curve is, however, significantly steeper for PLA. As a result, a strong overshoot in the temperature may decrease the viscosity too much, causing leaks through the powder bed. On the other hand, upon cooling, the viscosity raises fast as well, thus limiting the coalescence time. The slope of the viscosity curve is quantified by the activation energy in Eq. 1.1. The assessed PLA grade has an activation energy of 100 kJ/mol K, compared to 11.8 kJ/mol K for PA 2200. The low viscosity results in fast and complete coalescence, as illustrated in HSM measurements (cf. Figure 5-8b).

A small remark on the degradation behaviour of PLA is needed. As the powder needs to be pressed into a disk to enable the viscosity measurements, some degradation has likely taken place during this preparation step. All disks were pressed at 180 °C and 50 bar for 3 minutes. Based on Figure 5-4, limited degradation takes place within this timeframe. Alternatively, the powder could be melted directly on the rheometer. This, however, typically takes more time than the plate-pressing step. As the viscosity is very low, the slight underestimation due to degradation in the plate press is not deemed significant.

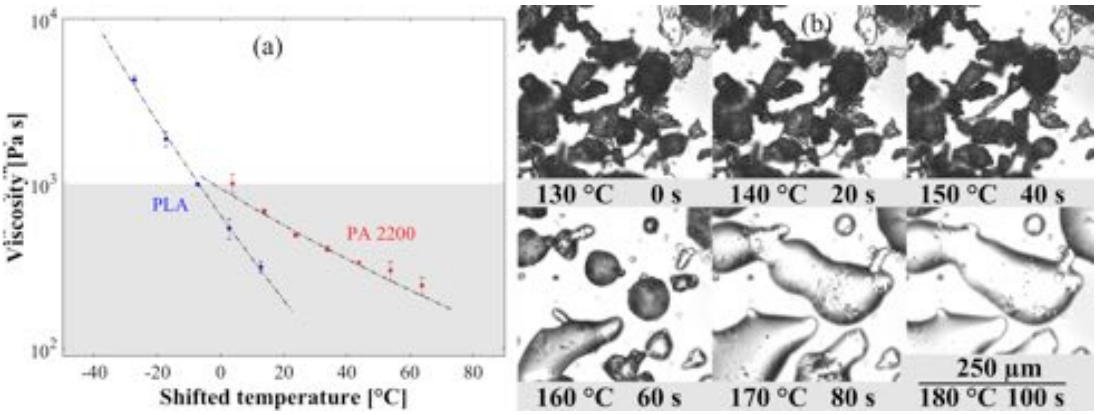


**Figure 5-8:** Zero-shear viscosity of PA 2200 [73] and PLA in function of the temperature difference with the melting temperature. (b) Coalescence of PLA in hot stage microscopy at a heating rate of 30 °C/min.

TGA measurements show a small, continuous degradation of the polymer upon heating. This is in correspondence with the earlier discussion on the viscosity degradation. However, significant degradation only occurs above 290 °C, which is well above the melting temperature of the materials. Therefore, no issues are expected for the stable sintering region. As melting the polymer erases all thermal history, the TGA curves of PLA and PLA HT overlap perfectly.

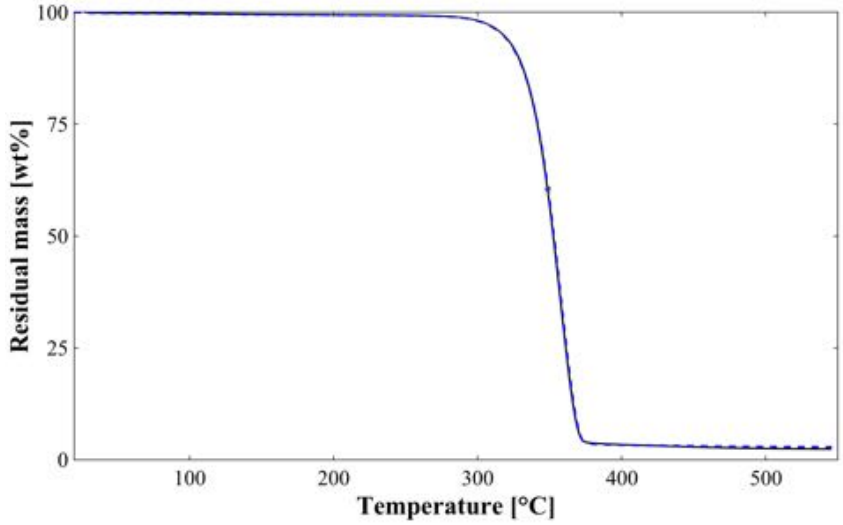


**Figure 5-9:** TGA of PLA (—) and PLA-HT (- - -) at 10 °C/min.

### 5.2.4 Solidification

Dilatometry tests on the PLA pellets at low cooling rates (0.5 °C/min) show clear crystallisation shrinkage at 100 °C, as shown in Figure 5-10. This crystallisation is expected from the DSC curve at the same cooling rate (cf. Figure 5-3a). The onset is, however, postponed, compared to the DSC measurement, in which crystallisation

already starts at 135 °C. As the DSC curve of Figure 5-3a is measured on the powder, the difference in the crystallisation onset is explained by the amount of flow improvers that are present and act as a nucleating agent. The total amount of shrinkage, however, is expected to be similar for the powder and the pellet. The PLA pellets have a crystallisation shrinkage of 2.7 %, which is significantly lower than that of PA 2200. The reasonable shrinkage, combined with the wide thermal window for the powder bed, predicts no significant warpage issues during the LS build.

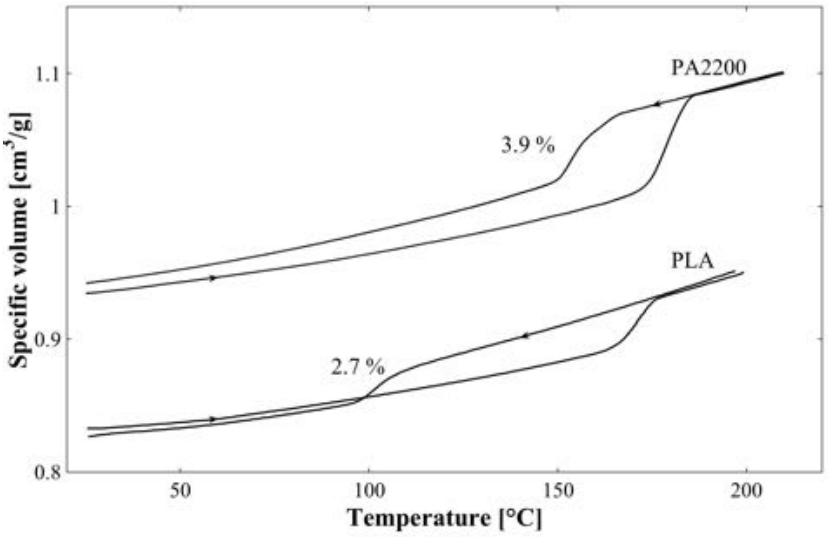


**Figure 5-10:** Dilatometric measurements on PLA (pellets) and PA 2200 [73].

## 5.2.5 Recyclability

The aforementioned viscosity degradation due to thermolysis and hydrolysis is also present in the solid state, which thus limits the recyclability on unsintered powder for subsequent LS builds. This effect is tested by aging the PLA rheometer disks for 90 hours at 140 °C. As dictated by the thermal window for the powder bed based on DSC and powder rheometry, 140 °C is a realistic temperature for the powder bed. To avoid variability in the plate pressing step, the comparison is performed on disks of the same plate pressing batch. Half of the disks are used to measure the viscosity that is reported in the previous section. The other half was aged in the annealing oven prior to the viscosity measurement. The viscosity of the PLA dropped 30-35 % as a result of this annealing step, as shown in Figure 5-11.

The solid state degradation thus also occurs for the unsintered powder in the LS machine, which is kept at a similar temperature for several hours to days. The result of the degradation is opposite to the post-condensation effect of certain PA and TPU grades. In the case of PLA, the thermolysis lowers the molecular weight and viscosity, which will yield faster coalescence but deteriorating product properties

with increased powder re-use. As a result fresh powder needs to be added to again increase the average molecular weight and a full renewal of the powder is required after several builds. At too low viscosities the powder also leaks into the pores of the underlying layers, which results in poor surface finish for the parts.

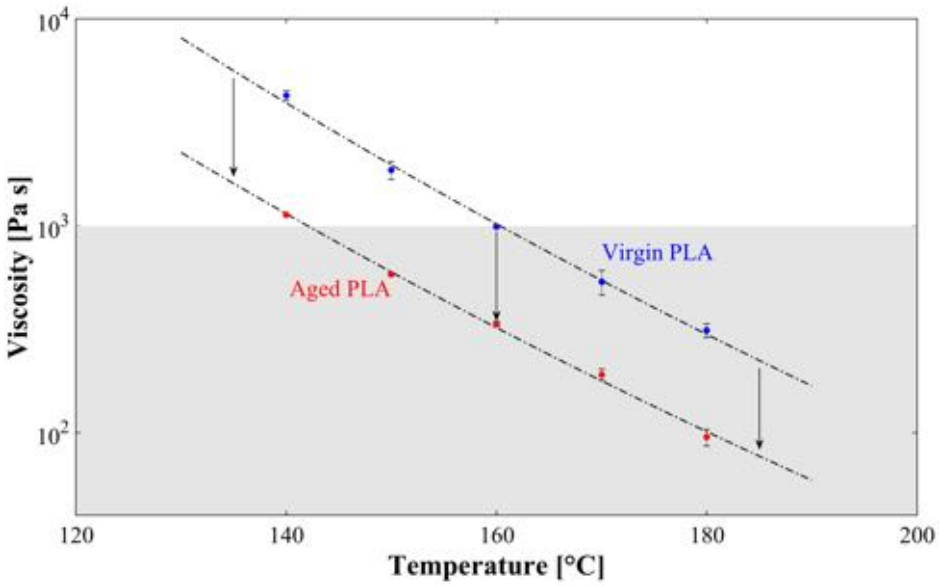


**Figure 5-11:** Viscosity degradation upon aging (93 hours at 140 °C).

As seen in Chapter 4, the cryomilling step introduces post-condensation in all tested post-condensing materials. Similarly, the processing conditions in cryomilling are expected to induce some viscosity degradation in the PLA due to the possibly large local heating on the one hand and the excessive presence of moisture due to condensation under the cryogenic conditions on the other hand. The viscosity of the PLA pellets, measured at 180 °C, is roughly 20-25 % higher than that of the powder, when measured at the same temperature. This indicates that, as expected, some viscosity degradation has already occurred. This effect needs to be accounted for in the future selection of other grades that exhibit similar degradation behaviour. It may therefore be beneficial to start from a PLA grade with a slightly higher viscosity. The observation of viscosity degradation in cryomilling is in correspondence to the reduction of the molecular weight of PLA upon cryomilling, observed by Nugroho [204].

### 5.2.6 LS proof of concept

Sintering tests have been performed on an industrial-scale sintering device with a spreader blade set-up. Both the thermal treatment and the addition of flow additive C show a qualitative improvement to the general flowability and the high temperature

stickiness, which is in correspondence to the lab results. However, the overall flowability of the material remains too poor to enable consistent spreading. This observation reflects the occurrence of defects in the lab-scale spreading tests, as well as the extreme fluctuations in layer density, which are unseen in any other material in this research. As a result, the examined powder is not deemed viable for LS in its current form. This unviability is mainly due to the poor particle properties resulting from the cryogenic milling process. This does not rule out the material for future use in LS, but indicates that there is still a need for optimising the cryomilling procedure.

Furthermore, a problem is seen due to the elastic relaxation of the powder bed. When the blade passes, it compresses the powder bed. However, some of this compression is recovered once the blade has passed. As a result, the top of the powder bed, and thus also the location of the sintered layer, are higher than expected. This forms a problem for the subsequent recoating step, as the blade then drags the sintered cross section with it. This unexpected bed re-expansion is in line with the strong variation of the apparent layer density in the flowability measurements of Section 5.2.2. For this reason only single layer sintering tests were further evaluated.

A third issue arises from single layer tests, namely excessive shrinkage of the sintered layers. This shrinkage is not expected from the dilatometric measurements. Therefore, the hypothesis for this shrinkage is that it is partially a result of poor deposition. As the bed is deposited with rather low quality and density, a large void fraction needs to be filled upon coalescence. As a result, the coalesced melt pool reduces in size. All these findings further stress the high importance of powder flowability for the LS process.

The results obtained in this section are, however, still valuable for future research on PLA. The thermal window obtained for the material, which is comparable to PA 2200, and the good coalescence properties show that PLA is still an interesting material for creating functional LS parts. Optimisation is, however, required for the milling process. As was discussed in Chapter 4, the millability of a material is strongly dependent on the milling temperature and does not always improve with decreasing temperature. An optimisation of this milling temperature, combined with other factors such as rotor speed, could therefore strongly affect the final particle morphology. Another approach for the milling optimisation is to look at the effect of the thermal treatment on the pellets. As the pellets exhibit a similar endothermic peak around $T_g$, this may affect their behaviour upon local heating due to the large shear introduced during milling. Pre-treating the pellets may therefore also have an effect on the final particle morphology.

Finally, the positive effect of the thermal treatment on powder flowability is a valuable discovery for the assessment of other materials. As annealing of the powder or pellets is a rather simple and low-cost methodology for the improvement of the material properties, this methodology may also be applied to other materials that exhibit a strongly history-dependent structure. A similar annealing methodology is therefore applied to PB-1 in Section 5.3.

### 5.2.7 Conclusions

DSC, TGA and melt rheology measurements indicate good LS processability for the chosen PLA grade. Figure 5-12 summarises these measurements and the resulting thermal window for the powder bed and stable sintering region. Powder flowability issues are noted at elevated temperatures. Therefore, an annealing procedure is proposed to successfully improve this flow behaviour. This methodology of improving powder flowability through an annealing procedure may improve other, currently unviable polymers as well.

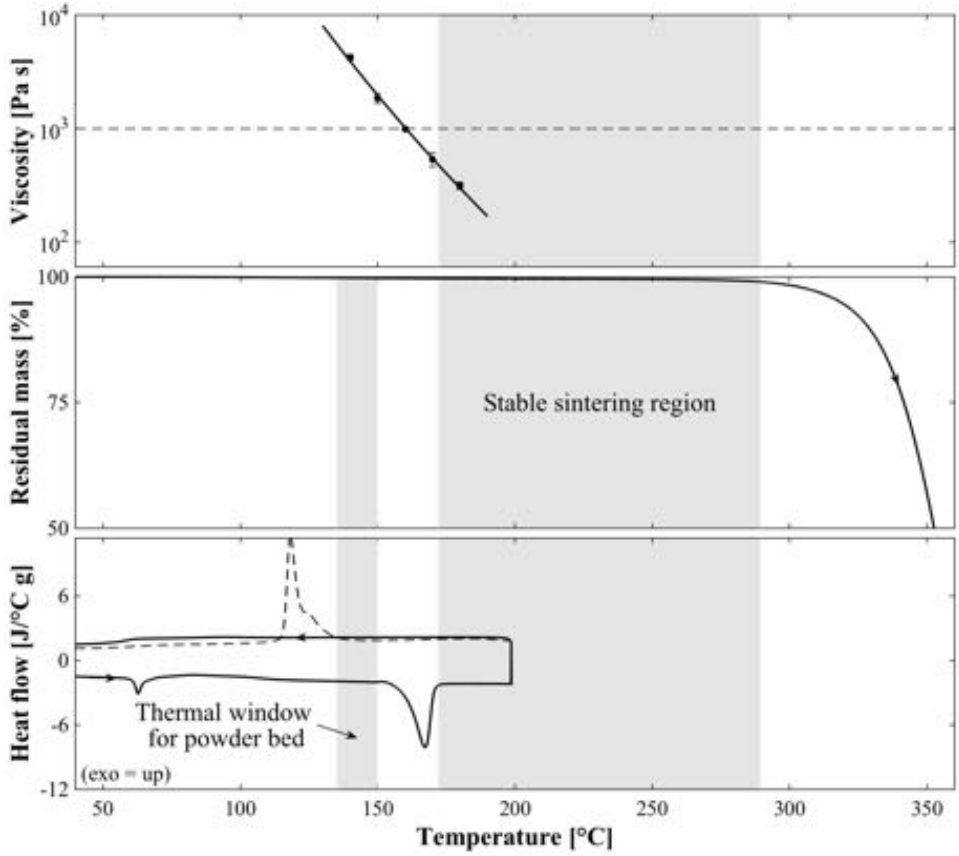


**Figure 5-12:** Thermal processing windows for PLA.

However, several issues remain and prevent the material's viability for LS. These issues include limited recyclability due to degradation and elastic relaxation of the powder bed. The strongest problem remains the overall powder flowability of the milled samples due to their poor powder morphology. Further optimisation of the milling procedure is therefore required to make this grade usable for LS.

## 5.3 PB-1

*Passages from this section, including figures, have been adapted from an own, published journal paper [193].*

Next, a cryogenically milled polybutene-1 (PB-1) powder is tested. PB-1 is an interesting polymer from a thermal point of view, as a different thermal history can lead to a different crystal structure. Based on preliminary studies on multiple PB-1 samples, a grade with a number molecular mass of 85 kg/mol and a polydispersity of 5.1 was selected. A strong selling point for this grade is its low viscosity, as further discussed in Section 5.3.3, which promotes the coalescence step. The grade is only available in pellet form, thus it is cryogenically milled to a powder.

The next sections look further into the applicability of the PB-1 grade for laser sintering. Section 5.3.1 discusses its polymorphism in further detail. Two thermal treatments are proposed to alter the crystal structure of the powder to improve sinterability. Together with the untreated sample, this thus yields three different powder samples. Sections 5.3.2 to 5.3.5 then assess all powder samples for the different steps in LS. Finally, Section 5.3.6 provides a proof of concept by creating sintered parts.

### 5.3.1 PB-1 polymorphism and thermal treatments

Four crystal forms of PB-1 are known in literature. As some of these forms differ in melting temperature and density, they are expected to behave differently in LS. The next section discusses the general theory behind the different forms of PB-1. Based on this theory, two thermal treatments are then proposed to optimise the LS behaviour of the sample.

**Polymorphism: general theory**

The four different crystal forms of PB-1 are summarised in Table 5-4, including their melting temperature and the location of the peaks in WAXS. The first form holds a hexagonal crystal structure. Two variants of this form exist: a twinned form, which is referred to as form I and an untwinned form, which is referred to as I'. This distinction in literature is typically made for single crystals [205]. Form I is usually obtained from the melt, via the intermediate form II, which is discussed in the next

paragraph. Form I' is obtained via various routes, including crystallisation from solution, directly upon polymerisation or after annealing form III, which is discussed further on in this section [205,206,207]. Both forms differ strongly in melting temperature, which affects the thermal windows for the powder bed. For typical crystallinity degrees of around 50-60 % the resulting material has a density of 0.95 g/cm$^3$ [208,209].

**Table 5-4:** Melting temperature and scattering vector of the different PB forms, based on Shieh et al. [210]. Melting ranges are for typical PB-1 grades of the corresponding form, including single crystals. The material density is taken for typical semi-crystalline samples [208].

| Form | Crystal structure | $T_m$ [°C] | $q$ [Å$^{-1}$] | $\rho_m$ [g/cm$^3$] | Stability (ambient) |
|---|---|---|---|---|---|
| **I** | Hexagonal (twinned) | 120-135 | 0.72, 1.23, 1.45 | 0.95 | stable |
| **I'** | Hexagonal (untwinned) | 90-100 | 0.72, 1.23, 1.45 | 0.95 | stable |
| **II** | Tetragonal | 110-120 | 0.83, 1.19, 1.29 | 0.89 | ➔ I |
| **III** | Orthorombic | 90-100 | 0.87, 1.22, 1.32 | NA | stable |

The second form, form II, has a tetragonal structure. It is typically obtained by the crystallisation of a PB-1 melt at atmospheric pressure [205,35]. The form is, however, unstable at ambient conditions and converts to the twinned hexagonal form I in a few days. Goldbach et al. mention a transformation time of 3 days [205], but references up to 7-10 days exist as well [35,211]. The tetragonal structure is much less dense (0.89 g/cm$^3$) and mechanically weaker than the hexagonal form [208]. As the tetragonal form will be formed upon melting in the LS process, the post-production shrinkage needs to be taken into account.

The final form is the orthorhombic form, also described in literature as form III. This form is typically created when the powder is obtained directly from precipitating the polymer from a solvent [212]. It is one of the lower melting forms, with a melting temperature of 90 °C to 100 °C [212,210]. This form is stable at ambient conditions, but annealing for several hours at 94 °C has been proven to create the untwinned hexagonal form I' [205].

**Thermal treatments**

Based on the considerations of the previous paragraphs, three samples were created. The first sample is obtained by directly cryomiling the provided pellets. It is further referred to as the untreated sample (PB-1u). The WAXS pattern of this sample,

shown in Figure 5-13, shows clear peaks at scattering vector values of 0.72, 1,25 and 1.44-1.47 $Å^{-1}$. As listed in Table 5-4, this pattern is typical for the hexagonal forms. The particle density, determined by Archimedes' method, is $0.95 \pm 0.011$ $g/cm^3$, which further indicates that it indeed possesses the hexagonal crystal structure. Similar to most other cryomilled samples, the PB-1 also shows a relatively broad PSD and irregular particle shape, as seen in Figure 5-14 and Table 5-1. It contains more fine particles than the PLA sample, but no fibre-like particles are present. Literature provides a Hamaker constant of 5.6 for typical PB-1 grades [192]. Combined with the PSD, this yields a computed average Bond number of 2.70 for the untreated powder.

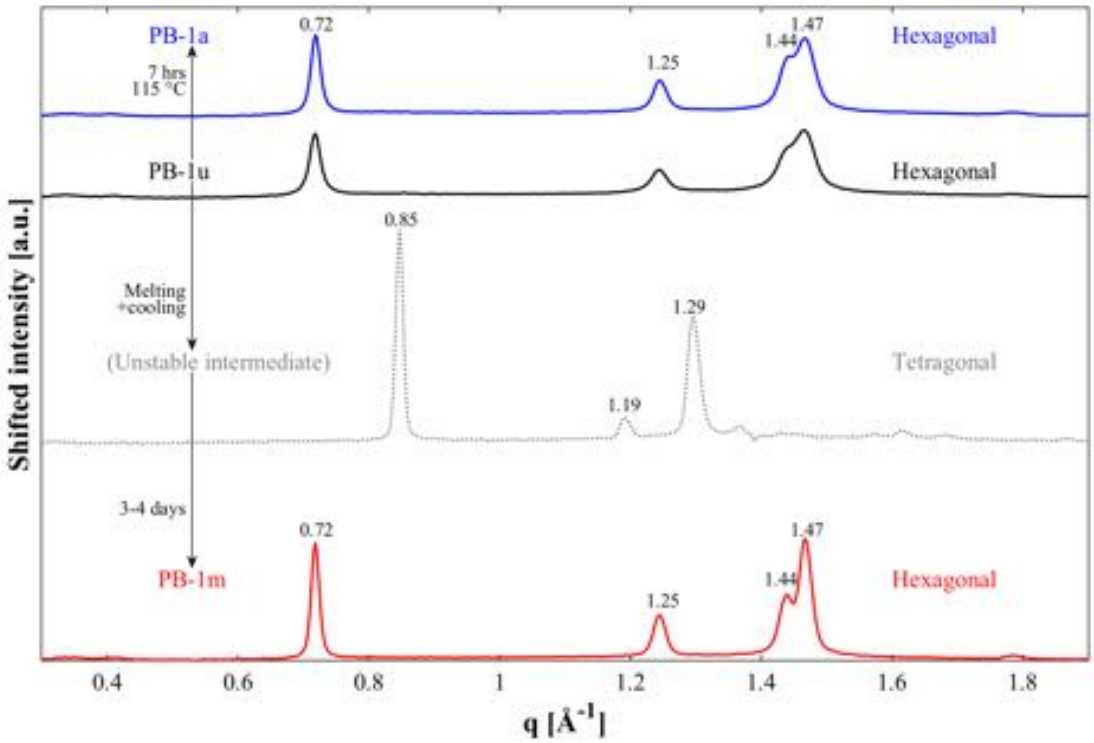


**Figure 5-13:** WAXS diffraction peaks for the different PB-1 samples.

One of the major drawbacks of this sample is the wide onset of the melting peak, which results in a small thermal window for the powder bed. Within this melting onset, issues with powder stickiness arise, as further discussed in Section 5.3.2. As a result of this stickiness, the PB-1u sample only has a thermal window of 5 °C, as shown in Figure 5-15a. This is significantly smaller than the window of 20 °C for the PA 2200 reference. As a result, thermal control within the LS machine is extremely difficult and warpage issues are expected. Therefore, two thermal treatments of the cryomilled powders are proposed to sharpen this onset or shift it to higher temperatures.

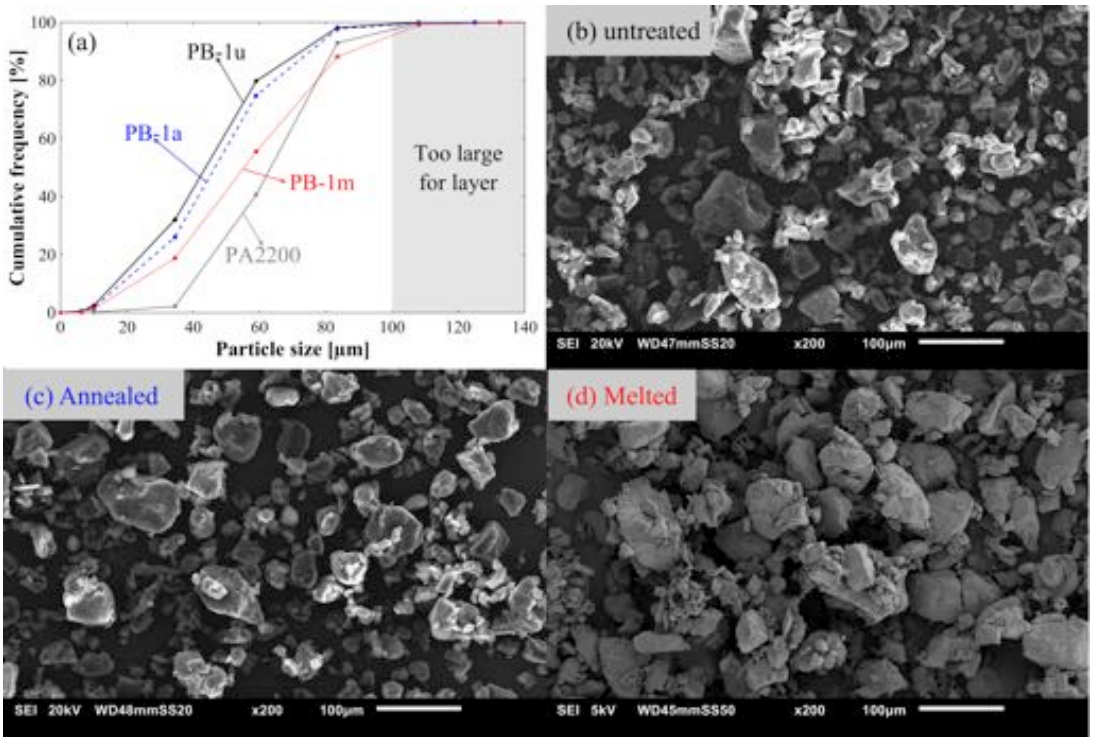


**Figure 5-14:** (a) PSD and (b) SEM image of the cryomilled PB-1 powder.

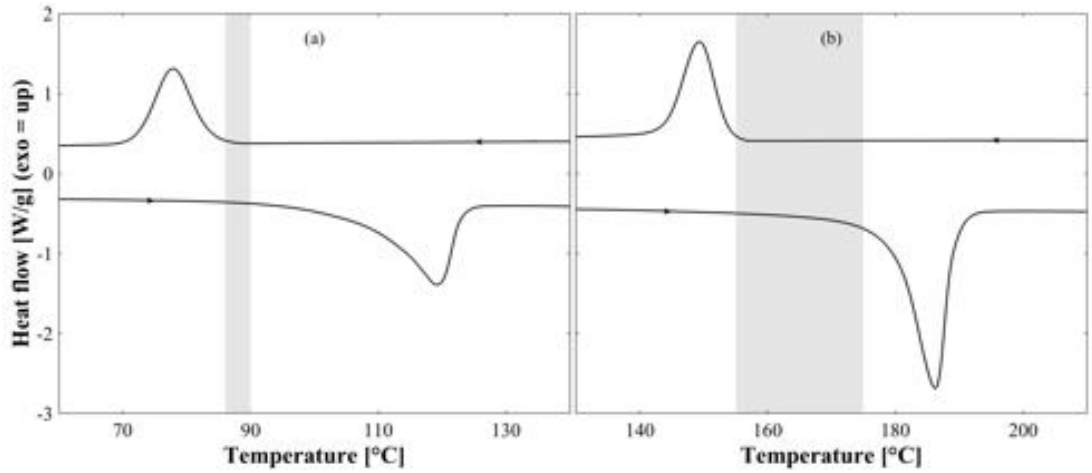


**Figure 5-15:** DSC measurements of PB-1 (a) and PA 2200 (b) at 10 °C/min. The grey zones indicate the thermal window for the powder bed.

The first thermal treatment is an annealing step at 115 °C for 7 hours in a pre-heated oven. The resulting sample is further referred to as the annealed sample (PB-1a). The time of 7 hours is chosen to ensure that the entire powder bulk has equilibrated at 115 °C. Tests show that increasing the treatment time does not have any visible effects on the DSC results of the sample. As shown in Figure 5-15a, the applied temperature sits below the peak melting temperature. As a result the powder does not fully melt, nor coalesces. Some caking is, however, visible. Therefore, the powder is sieved with a 150 µm mesh to break the formed agglomerates. The

particle size and shape thus remain unchanged compared to the untreated sample, as is proven in the PSD and SEM images (Figure 5-14). A small shift to larger particles is seen, which may also be the result of some remaining agglomerates or segregation during the powder handling.

The hexagonal crystal structure is retained, as shown by the unchanged location of the diffraction peaks in the WAXS pattern ( Figure 5-13). The increased sharpness of the peaks, however, indicates crystal perfection. This crystal perfection is desirable to sharpen the melting onset to a value of 108 °C, as illustrated in Figure 5-16a. Upon melting, the thermal history of the sample is removed. As a result the crystallisation peak perfectly coincides with that of the untreated sample. Therefore, the thermal window for the powder bed increases to about 20 °C, which is a significant improvement and a similar window size as that of PA 2200. To ensure that the entire powder bulk has received the same improvement, samples at multiple locations were taken. All DSC curves overlapped well. The upper limit of the thermal window shifted a few degrees, which is most likely the result of temperature fluctuations in the oven. A small melting peak is seen around 130 °C, which indicates that a limited fraction of the crystals has transformed into a higher melting hexagonal structure.

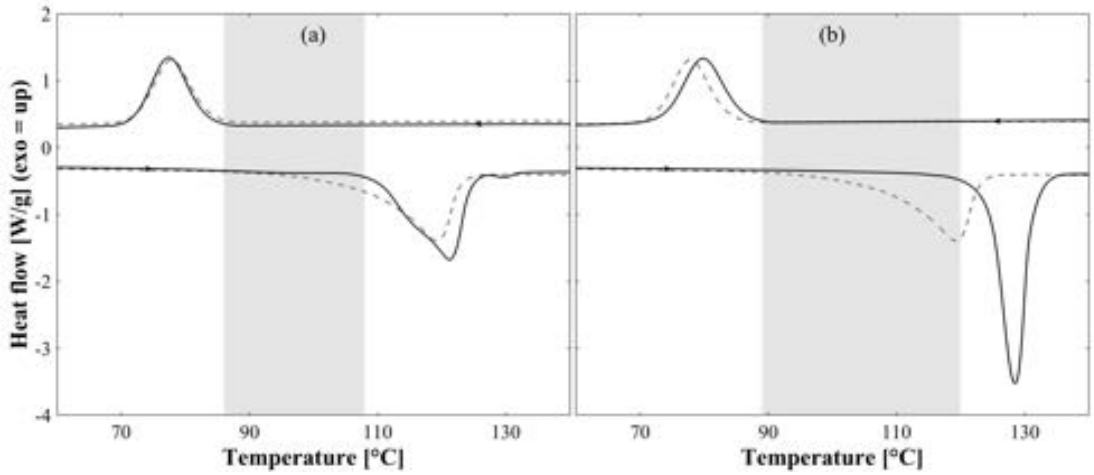


**Figure 5-16:** DSC curves for the applied treatments (—) compared to the untreated PB-1 sample (- - -): annealing (a) versus melting and re-milling (b). The melted sample is measured several weeks after the treatment. The grey zones indicate the thermal window for the powder bed.

The second treatment fully melts the sample, unlike the annealing treatment. This sample is therefore referred to as the melted sample (PB-1m). After melting, the powder slowly cools at ambient conditions. The hypothesis is that this treatment will create a higher melting hexagonal structure via the tetragonal form, as indicated in Table 5-4. The formed block of PB-1 is then industrially shredded to large flakes and re-milled under cryogenic conditions. As the flakes were more difficult to mill

and the small amount of available material hindered the optimisation of the milling parameters, a much wider PSD was obtained, as shown in Figure 5-14. This melting and solidification procedure yields the tetragonal form, as shown in the shift of the diffraction peak in WAXS to 0.87, 1.22 and 1.32 $Å^{-1}$ (cf. Figure 5-13). These peaks again correspond well with the values from literature, listed in Table 5-4. The tetragonal form transforms into the hexagonal form within 3 days, as expected. This recrystallised hexagonal form has a much higher melting temperature of about 130 °C and a much sharper onset, as seen in Figure 5-16a. The improvement in the melting temperature is most likely the result of an increase in the lamellar thickness compared to the hexagonal form in the untreated powder. Earlier studies on pellets of this PB-1 grade prove via SAXS measurements that there is indeed an increase in the lamellar thickness [5]. However, the interference of the large amounts of flow additives present in these milled samples hinders SAXS analysis. As the systems and noted results in DSC are very similar, it is likely that the increase in lamellar thickness is also present in these samples. The melting peak of PB-1m is at the same location as the small extra peak that was created in the annealing procedure. It is therefore likely that some of the lower-melting crystals undergo the same transition via the tetragonal structure in the annealing treatment.

A small shift of the crystallisation onset to higher temperatures is also present for PB-1m. This shift results from the increased amount of additives that are added in the re-milling process. These additives work as nucleating sites, thus promoting crystallisation. However, this increase is limited, compared to the increase in the melting temperature. A net increase of the thermal window to 30 °C is therefore seen.

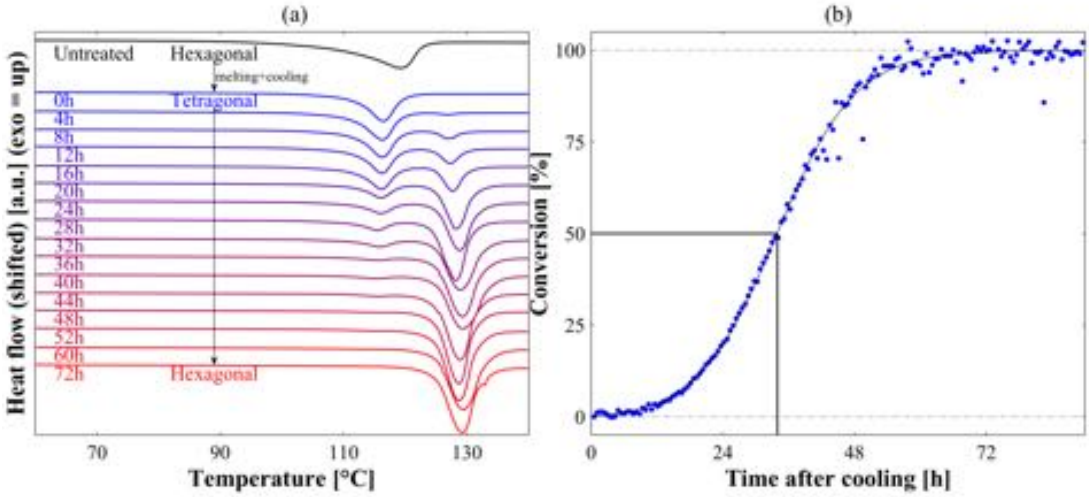


**Figure 5-17:** Evolution of the melting peaks with time during the transformation from the tetragonal to the hexagonal form (a) and the corresponding conversion in time obtained from WAXS (b).

The transformation of the tetragonal to the higher melting hexagonal structure is clearly visible in DSC and WAXS, as shown in Figure 5-17. In the DSC measurements, this is seen by the melting peak at around 115 °C of the tetragonal structure that disappears with the formation of the melting peak at 130 °C. Controlled melting experiments under lab-conditions, show that 50 % of the tetragonal structure transforms to the hexagonal structure within 34 hours. Within 3 days, full conversion is reached. The conversion was determined by the relative increase in peak area of the WAXS diffraction peak at 0.72 Å. The transformation speed is in good correspondence with the results of Goldbach et al. [205], but it is thus significantly faster than that reported by other sources [35,211]. This difference in the kinetics may result from a difference in molar mass or it could be affected by the presence of the aforementioned flow enhancers. Additives are known to have an effect on the transformation kinetics [213,214]. Due to the fast conversion speed to the hexagonal form, it is deemed unrealistic to use tetragonal powder in the LS process. Furthermore, the thermal window for the high-melting hexagonal form is preferable over the tetragonal form.

The improvement of the thermal window described in this section is confirmed by the sintering tests of Section 5.3.6. Both the annealing and melting procedures show a similar improvement to the attainable bed temperatures. Therefore, the annealing procedure is deemed preferential, as it requires the fewest additional processing steps. The melting procedure namely requires shredding and re-milling steps, which not only needs a lot more time, but also specific equipment, which is not available for most LS part producers. As a result, the melting procedure adds a significant cost to the powder creation.

The three PB-1 samples, the untreated, annealed and melted sample, are evaluated for each of the aforementioned steps of the sintering process: powder flowability, coalescence, solidification and recyclability in Sections 5.3.2 to 5.3.5.

### 5.3.2 Powder flowability

The powder flow of PB-1 was examined via the DAoR, powder spreader and powder rheometer. Table 5-5 shows the results of the A-DAoR and powder spreader tests at ambient conditions and compares these indices to the reference PA 2200, described in Chapter 3. The PB-1 samples score less well than the PA 2200 reference, most likely due to the rough particle morphology and the larger amount of fine particles, which are known to possess poorer flow properties. Angles above 45° are found, which are common for cryogenically milled powders, as seen in Section 5.2.2 and Chapter 4.

**Table 5-5:** Powder flowability indices based on the dynamic angle of repose (A-DAoR) and spreading experiments for PB-1 and PA 2200.

| | $\widehat{\phi}$ [°] | $\widehat{\phi_a}$ [°] | $\rho_{pk,geom}$ [%] | $\rho_{pk}$ [%] |
|---|---|---|---|---|
| **PA 2200 (Chapter 3)** | 36.6 ± 0.3 | 40.0 ± 0.3 | 51 | 44 ± 5 [73] |
| **PB-1u** | 45.9 ± 0.9 | 57.1 ± 1.4 | 50 | 35 ± 2 |
| **PB-1a** | 45.4 ± 0.8 | 56.4 ± 1.9 | 50 | 32 ± 3 |
| **PB-1m** | 47.9 ± 0.8 | 61.7 ± 0.1 | 53 | 25 ± 6 |

The annealing procedure has no significant effect on the powder flowability at ambient conditions in the A-DAoR. Both the average and maximum angles remain unchanged. This result is expected, as there is no significant difference in the particle morphology or PSD, as shown in Figure 5-14. Also the change in the degree of crystallinity is deemed limited, thus no effect on elasticity or hardness of the particles is expected. PB-1m, on the other hand, shows a slight increase in both angles. As the PSD contains fewer fine particles and the corresponding Bond number is lower, this change is most likely due to the more irregular particle morphology. This is in line with the knowledge that smoother and more round particles intrinsically exhibit better flow properties [50]. Another possible explanation is that the amount of flow additives has become too high after the re-milling procedure. As shown in Chapter 3, the addition of flow improvers often shows an optimum in concentration.

The powder spreading results are quite similar to those of the A-DAoR. The packing density is considerably lower than that of PA 2200. Again PB-1u and PB-1a score similar and the melted sample scores the poorest. The poorer score of PB-1m results from the decreased flowbility, as its tapped density is even higher than that of the other two samples. This negative effect of flow is similar to the results found for the milled PA (Section 4.3.2). All samples were, however, spreadable without any visual defects in the deposited layers. The geometrical packing limit of the PB-1 samples is very similar to that of PA 2200. The reduced packing density in the deposited layers thus results from their poorer powder flowability.

Finally, powder rheometry tests provide insights into the powder flowability at elevated temperatures and the expected caking in the LS process. Again, PB-1u and PB-1a score very similar at ambient conditions, as seen in Figure 5-18. This observation corresponds well with the A-DAoR and powder spreader measurements and further illustrates how all three measurements are able to indicate the same trends when applied to similar materials. At elevated temperatures, however, the difference becomes noticeable. The untreated sample becomes sticky at much lower temperatures than the annealed sample and reaches higher energy values. This thus

indicates an improvement of the attainable powder temperature in LS. PB-1m again scores poorer at ambient conditions, which is also in line with the other flowability measurements. However, no improvement is seen at elevated temperatures, compared to the untreated sample. The test was repeated for multiple samples, but all showed the same result. Laser sintering tests, discussed in Section 5.3.6, on the other hand do show an improvement in the attainable powder temperatures. The difference in the flow field between the powder rheometer and the powder spreader may thus still lead to some different particle interactions. This is in strong contrast to the PLA sample, for which the thermal improvements were clearly visible in the rheometry tests.

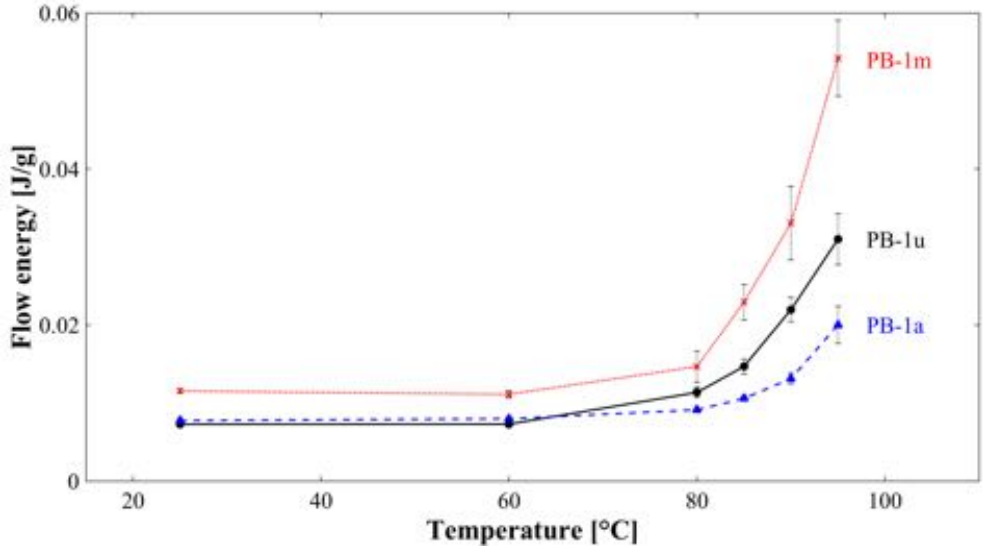


**Figure 5-18:** Flow energy determined by powder rheometry in function of temperature.

A similar result was seen for the untreated powder in the T-DAoR set-up. Up to 60 °C, a constant value for the average and avalanche angles is found, of 41.8 ± 1.8° and 54.1 ± 1.0° respectively. These values are slightly lower than those of the A-DAoR, which is in correspondence to the findings of Section 3.3.4. At 80 °C the powder becomes sticky and lumps of powder roll down or stick to the container walls during the measurement. As a result, it is not possible to attach a meaningful value to the angles anymore. As both the powder rheometer and T-DAoR provide the same qualitative result but the powder rheometer is able to quantify the increase better, the T-DAoR is not further examined for this powder.

### 5.3.3 Coalescence

The coalescence properties are determined via melt rheometry and HSM. As melting the powder removes all thermal history, these measurements are only shown for the untreated sample. The melting onset in HSM will, however, be different for the three samples.

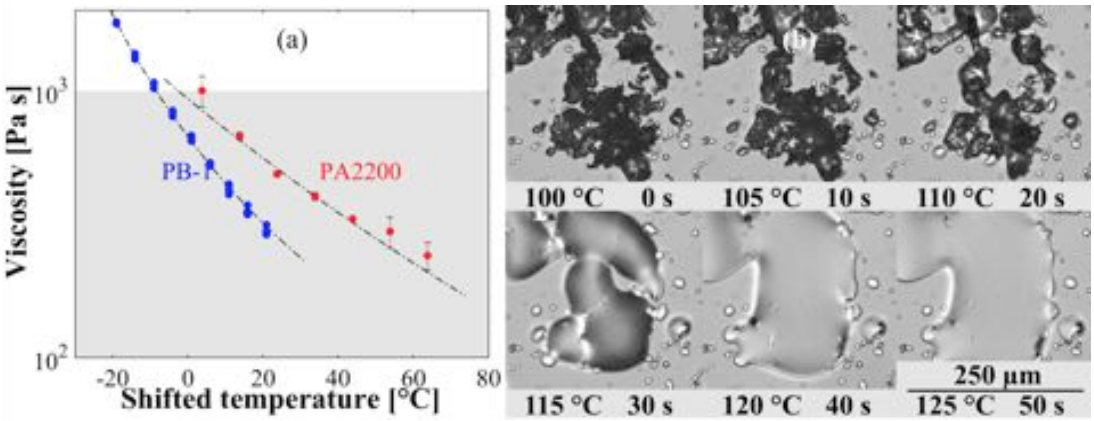


**Figure 5-19:** Zero-shear viscosity of PA 2200 [73] and PB-1u in function of the temperature difference with the melting temperature. (b) Coalescence of PB-1u in hot stage microscopy at a heating rate of 30 °C/min.

Figure 5-19a shows the zero shear viscosity as a function of the temperature increase relative to the melting peak (119.1 °C for PB-1u and 186.2 °C for PA 2200). The viscosity curve of PB-1u is very similar to that of PA 2200, which translates to fast and complete coalescence upon passing the melting endotherm (cf. Figure 5-19b). The fit of the Arrhenius relation between viscosity and temperature (Eq. 1.1) yields an activation energy of 58.5 kJ/mol, which is significantly higher than that of PA 2200 [73]. Finally, upon reaching the fully molten state for all three PB-1 samples, no notable difference in the viscosity was seen. This indicates that neither the thermal treatments nor the shredding degrade the material. The low viscosity is expected to aid in creating denser parts, thereby counteracting the effect of the low powder bed densities, described in the previous section.

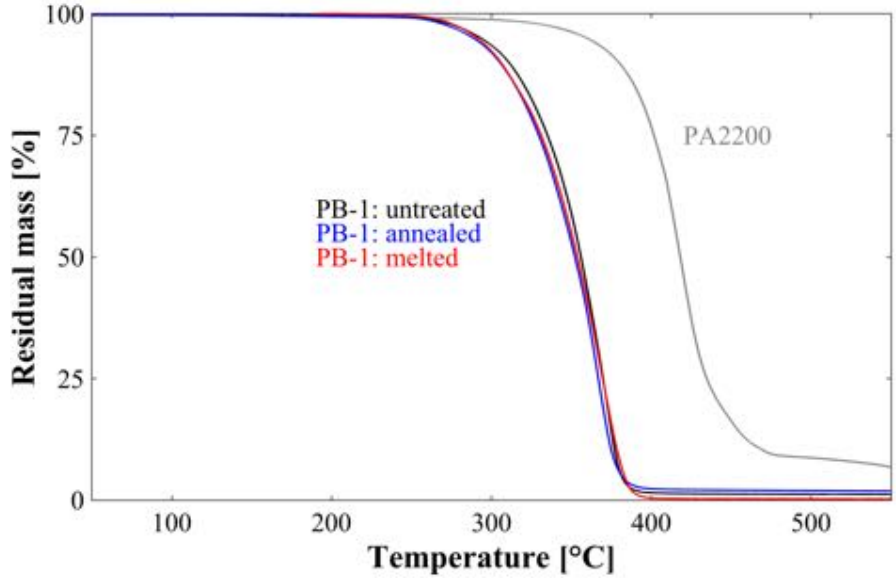


**Figure 5-20:** TGA measurements of the PB-1 and PA 2200 samples.

The degradation temperature, indicated by TGA, is sufficiently above the melting temperature, as shown in Figure 5-20. This enables a wide stable sintering region up to 258 °C. Furthermore, all three samples show exactly the same degradation behaviour, which is expected as no viscosity degradation was seen in the previous experiments and the three samples are thus identical once entering the molten state.

### 5.3.4 Solidification

As shown in Table 5-2, the different forms of PB-1 exhibit different densities. The untreated hexagonal powder has a density of $0.95 \pm 0.01$ g/cm$^3$. Upon melting and re-solidification, the density reduces to $0.89 \pm 0.003$ g/cm$^3$ for the tetragonal form. In the subsequent 72 hours, this density increases again to $0.94 \pm 0.001$ g/cm$^3$ for the higher melting hexagonal structure. This transformation is thus expected to create significant shrinkage in the part.

This change in density is also seen in dilatometric measurements (cf. Figure 5-21). Upon melting, PB-1u expands 8.8 %, which is larger than the expansion of the standard PA 2200, i.e. 6.9 % [73]. This large volumetric change is in correspondence with reports from literature [215]. PB-1a and PB-1m have similar material densities, as both powders possess the hexagonal crystal form. They thus show similar volumetric expansion. Upon cooling, however, the shrinkage is much lower, at only 2.9 %. This value is even lower than that of the reference PA 2200, thus limiting the expected warpage issues in processing. The limited shrinkage is due to the formation of the tetragonal structure, which is much less dense. The remainder of the volume change happens post-build, as the tetragonal form converts into the hexagonal structure. An additional 5.9 % shrinkage thus needs to be taken into account in the design of the final product.

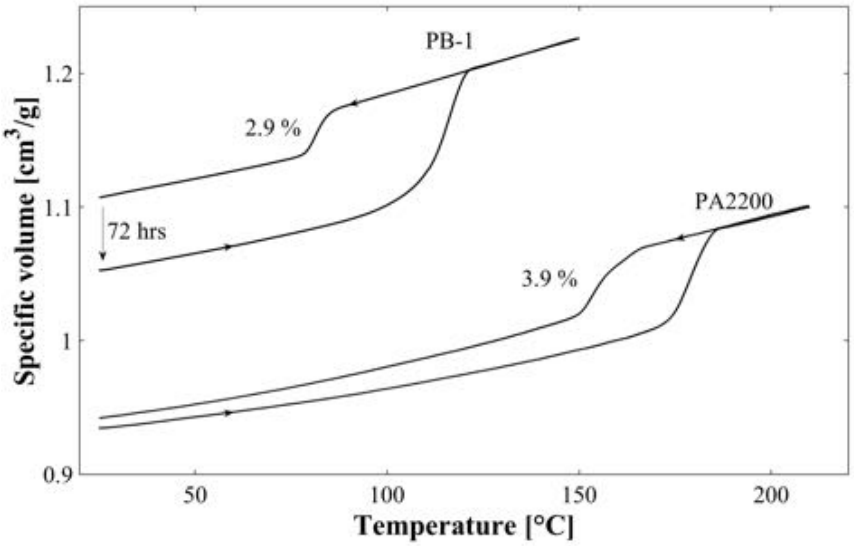


**Figure 5-21:** Dilatometric measurements on PB-1u and PA 2200 [73].

### 5.3.5 Recyclability

The recyclability is only discussed briefly, as not that many problems are expected with the powder. As with other polyolefins, the polymerisation mechanism does not rely on reactive end groups in the monomer. As a result, after the polymerisation process has completed, there is no possibility for a condensation reaction to occur in the powder. TGA further proves that there is no degradation issue noticeable below 258 °C. Furthermore, rheology measurements did not show any viscosity degradation or increase with time.

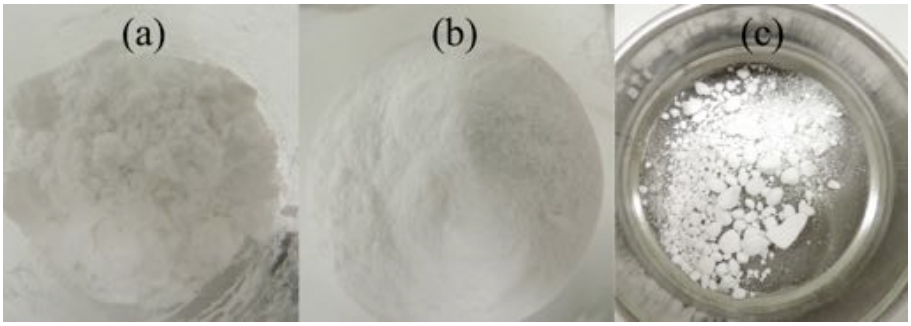


**Figure 5-22:** Caking phenomenon for PB-1u: Powder bed at 80 °C before (a) and after mild stirring (b) and agglomeration > 85 °C (c).

The only recyclability issue is the strong caking phenomenon that happens in the powder bed. Below 85 °C the powder gets a slight flour-like texture upon prolonged heating, as shown in Figure 5-22a. However, upon mild stirring the powder regains its original texture (cf. Figure 5-22b). Above 85 °C increased caking is seen with temperature, resulting in large agglomerates shown in Figure 5-22c. This is in strong correspondence with the powder rheometry measurements, that also indicate a significant increase in the flow energy above 85 °C. Strong mechanical agitation, such as high intensity sieving, is able to break up these agglomerates. As a result, no significant issues with the powder recyclability are expected.

### 5.3.6 LS proof of concept

Finally, to validate the results discussed in Sections 5.3.2 to 5.3.5, sintering tests were performed. The thermal windows obtained from DSC and the powder stickiness onset determined by powder rheometry form a basis for the bed temperature optimisation.

The small scale, multilayer tests are performed on a Sinterstation 2000 (DTM), equipped with a 100 W $CO_2$ laser (Synrad) with a Gaussian beam diameter of 450 µm, $N_2$ atmosphere and a roller coater. Rectangular bars with xy-dimensions of 50 mm by 200 mm are produced with a scan speed of 1000 mm/s, a scan spacing of 150 µm and a layer thickness of 100 µm. Preliminary large-scale sintering tests on a

faster scanning EOS machine, however, show that scan speeds up to 2800 mm/s are achievable for this material. After 5 layers, the build is aborted and the build chamber cools down to 50 °C, prior to removing the parts. Parts were processed at laser powers of 3, 4, 5 and 6 W. These settings yield energy densities of 0.02, 0.027, 0.033 and 0.04 J/mm$^2$ respectively, according to (Eq. 1.3b). These ED values are in the same range as those needed to sinter PA parts [3,216,217]. Table 5-6 shows the optimised bed temperatures for the single layer tests. These results are in line with the expectations, as a strong increase in the attainable bed temperature is enabled by the thermal treatments. PB-1u gets sticky above 107.5 °C, but the annealing treatment raises this onset to 118 °C. The melted sample was even spreadable up to 126 °C. The difference in the onset values, compared to the rheometry measurements, likely results from the difference in the lower temperature of the powder in the feed, as discussed in Chapter 3. The powder that is spread therefore has a significantly lower temperature than the bed onto which it is deposited.

**Table 5-6:** Usable bed and feed temperatures applied in test part production for single layer tests.

| | **Bed temperature [°C]** | **Feed temperature [°C]** |
|---|---|---|
| **PB-1u** | 107.5 | 50 |
| **PB-1a** | 118 | 56 |
| **PB-1m** | 126 | 56 |

The thermal improvement is also seen on the pre-heating temperature of the powder feed cylinders, which can be set a few degrees higher for the treated powders. This increase improves the quality of the final parts, as it reduces the thermal fluctuations upon deposition of the next layer. As a result, the produced parts showed minimal warpage upon removal from the build. However, due to the crystal transformation in the subsequent days, high shrinkage was noted. This observation is in line with the WAXS and DSC measurements of Section 5.3.1.

The effect of caking was limited due to the limited amount of layers that are deposited. This affects both the weight that is applied to the underlying bed, as well as the time the bed is compressed by its own weight. In contrast, during preliminary full-scale sintering tests, the weight of the powder bed induced a strong caking in the material. This observation corresponds to the stickiness described by the powder rheometry measurements.

At an ED of 0.02 J/mm$^2$ (3 W) the parts did not sinter sufficiently. All other applied energy densities, however, did succeed in creating multilayer parts. As a proof of

concept, the part sintered at 0.033 J/mm$^2$ (5 W) was further examined in detail. The following discussion focuses on the part sintered from the PB-1a powder, though the results for parts made from PB-1m powder are similar. Good coalescence is seen in the produced parts. Figure 5-23 shows the cross-section of a sintered part of PB-1a at 0.33 J/mm$^3$ in SEM. Good coalescence is seen both within the individual layers and between different layers of the same part. This proves that the low melt viscosity is able to counteract the poor packing density upon layer deposition. It should, however, be noted that as the used DTM sinterstation uses a roller rather than a blade, the powder layer density may be higher than that reported in Table 5-5.

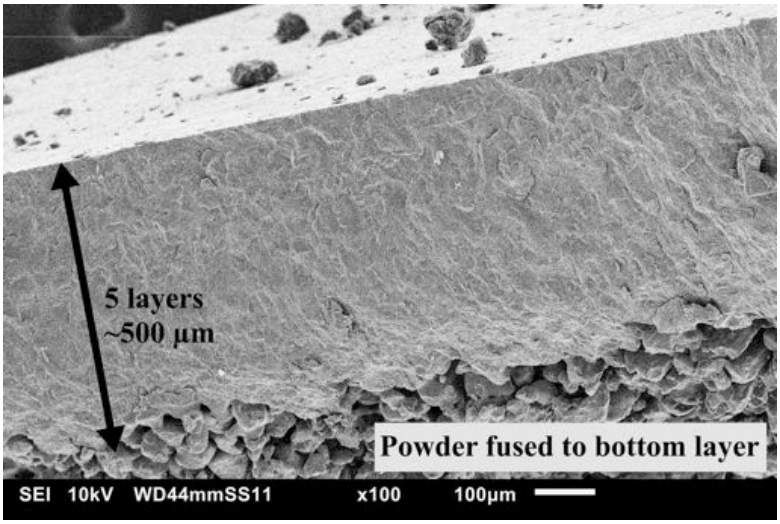


**Figure 5-23:** Sideview cross-section of a sintered part (annealed powder, 0.033 J/mm$^2$).

Right after the build is cooled down to 50 °C, the sample is removed and loaded into the WAXS set-up. The resulting diffraction pattern in time (cf. Figure 5-24) shows a similar sigmoidal conversion curve to the conversion curve reported in 5.3.1. There are, however, a few differences. Firstly, already a significant fraction (15 %) of the hexagonal form is present at the start of the measurement. Two possible explanations exist. (1) As shown in Figure 5-23, a significant amount of unsintered powder is fused to the bottom layer of the part. This powder has thus retained its hexagonal form. (2) The part cools down much slower and less controllable in the sintering machine. During this time, part of the transformation may already occur. A second difference is seen in the transformation rate. The transformation rate of the present tetragonal form is slightly faster than that of the lab experiments. 24 hours after the part removal from the build, already 50 % of the present tetragonal structure has converted to the hexagonal form. The reason for this increase again lies in the different cooling time of the LS machine versus the lab experiments. As shown in Figure 5-17, the conversion rate in the first few hours after the build is close to zero. For the sintered part, however, a non-zero conversion rate is already visible at the first measurement points. This means the curve is shifted to lower

times, due to the cooling down time in the printer. Furthermore, as the powder has been kept at an elevated temperature below the melting peak for a prolonged time, the thermal history of the sample is slightly different. Chvátalová et al. also indicated that temperature has a strong effect on the transformation rate [209].

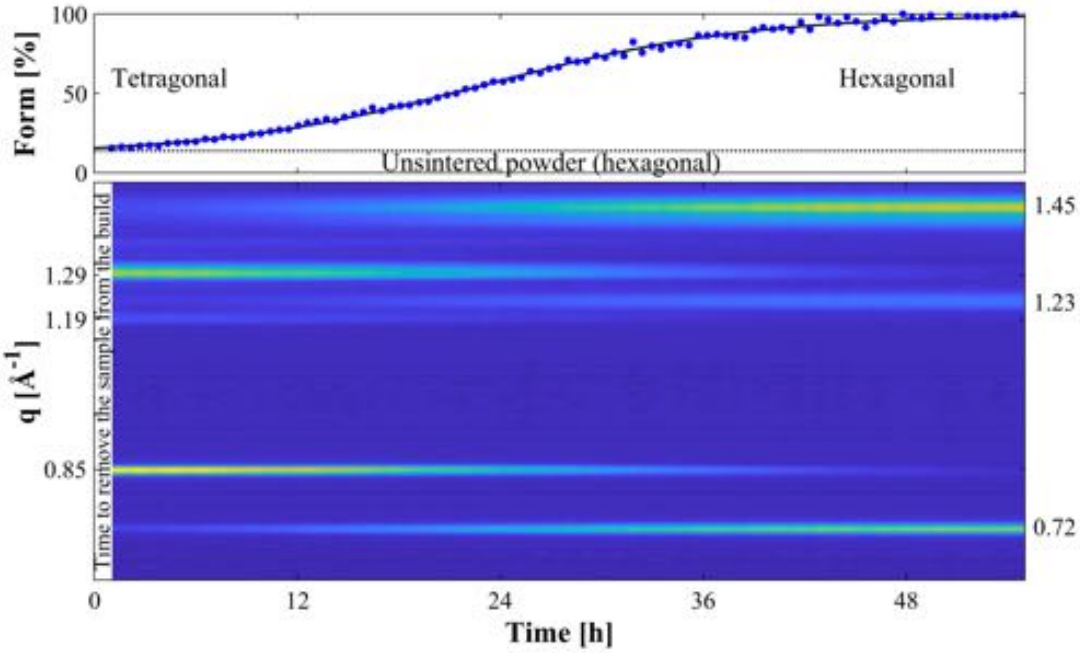


**Figure 5-24:** WAXS signal in time for a sintered part of PB-1a (0.33 J/mm$^3$) directly after removal from the build.

The same procedure was performed on parts produced from the untreated and melted samples. No notable differences were observed. The presence of post-build shrinkage during the first 48 hours after the build thus needs to be taken into account for all samples. This includes allowing for the shrinkage in the design phase of the product, as well as performing the final quality control tests at least two days after removing the parts from the build.

## 5.3.7 Conclusions

PB-1 was deemed a usable material for LS. The thermal window for the original sample was, however, too small for practical applications. The proposed thermal treatments, i.e. melting and annealing, significantly improved this thermal window and made the material viable for LS. The improvement of the thermal window for the melted sample is slightly larger. However, as both treatments have a sufficient positive effect, the annealing procedure was deemed the most applicable from a practical standpoint. The melting procedure adds a lot more processing steps, which as a result cost more time and money. As a commodity polymer, pricing of the powder is important from a competitive standpoint. Figure 5-25 summarises the thermal windows for processing the annealed PB-1 powder.

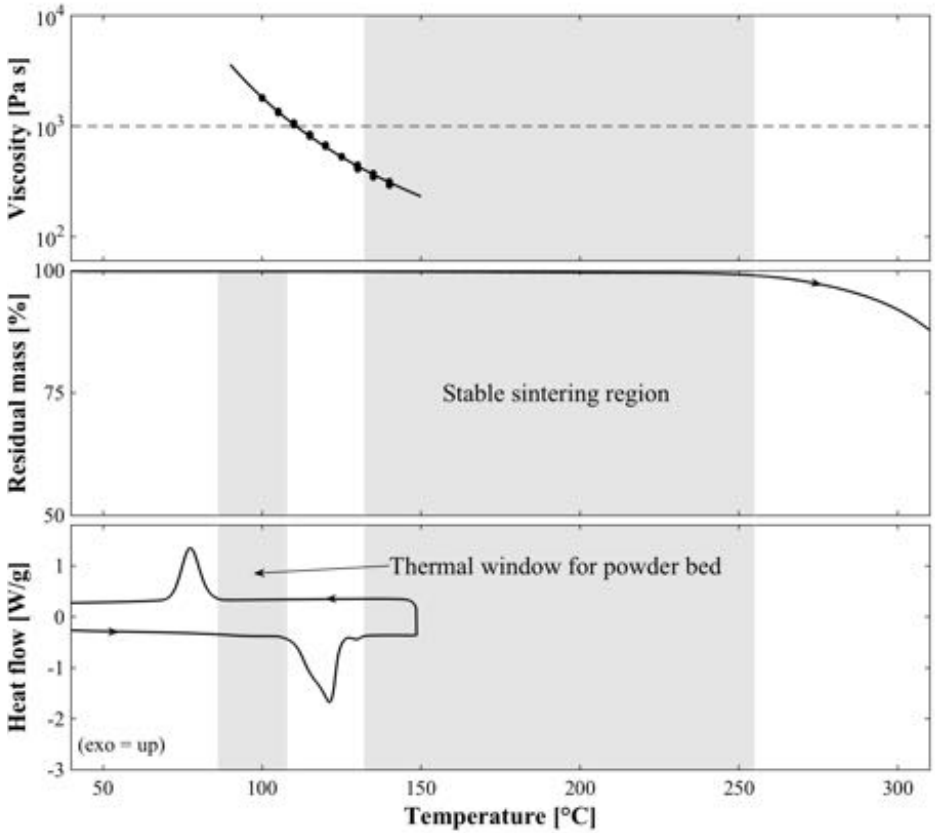


**Figure 5-25:** Thermal processing windows for PB-1a.

## 5.4 Copolyamide (coPA)

Copolyamide (coPA) is chosen as a new competitor for TPU in flexible applications. There are two reasons behind this choice. (1) The material is low cost. Typical copolyamide powders used in adhesive applications are in the price range of $ 4-6. (2) coPA grades typically have large elongation at break, competing with many TPU grades, as illustrated in Table 5-7. The biggest difference with TPU, besides chemical composition, is the decreased elastic recovery for coPA.

The chosen grade is a caprolactam based copolyamide which is currently used in adhesive applications. It has a Shore A hardness of 96, which is similar to the harder TPU's discussed in Chapter 4. The tensile strength (34 MPa) and elongation at break (789 %) of moulded coPA parts are very similar to the TPU sintering reference (TPU Desmosint) and Ir A 95 p 4657, which is discussed in Chapter 4. The coPA grade is however much stiffer, and thereby competes with the high stiffness TPU's. Figure 5-26 localises the coPA grade within the TPU property maps that were defined in Section 4.4.1.

**Table 5-7:** Mechanical properties of coPA, compared to common sintering TPU, based on injection moulded tensile bars.

| | Hardness [Shore A] | E [MPa] | UTS [MPa] | EAB [%] |
|---|---|---|---|---|
| **coPA** | 96 | 223 | 34 | 789 |
| **TPU Luvosint** | 89 | 46 | 33 | 939 |
| **TPU T-95a** | 95 | 92 | 28 | 780 |

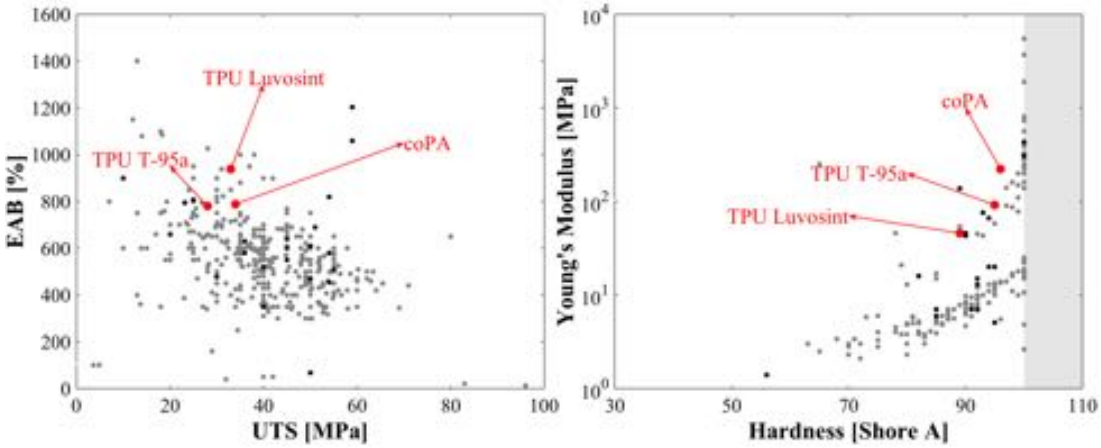


**Figure 5-26:** Localisation of coPA within the TPU property maps.

## 5.4.1 Powder characterisation

Upon cryomilling the coPA pellets, a quite similar average particle size is obtained compared to PA 2200, as shown in Figure 5-27a. The percentage of smaller particles around 20-30 µm is, however, slightly larger, which is expected to yield poorer powder flowability. Also slightly more large particles around the layer thickness of 100 mm are present. These are, however, not deemed problematic due to their limited presence. As seen in SEM images (Figure 5-27b), some fibre-like particles are also present, but their abundance is much smaller than in the case of the PLA. Besides these fibre-like particles, the typical rough morphology for cryomilled powders is seen.

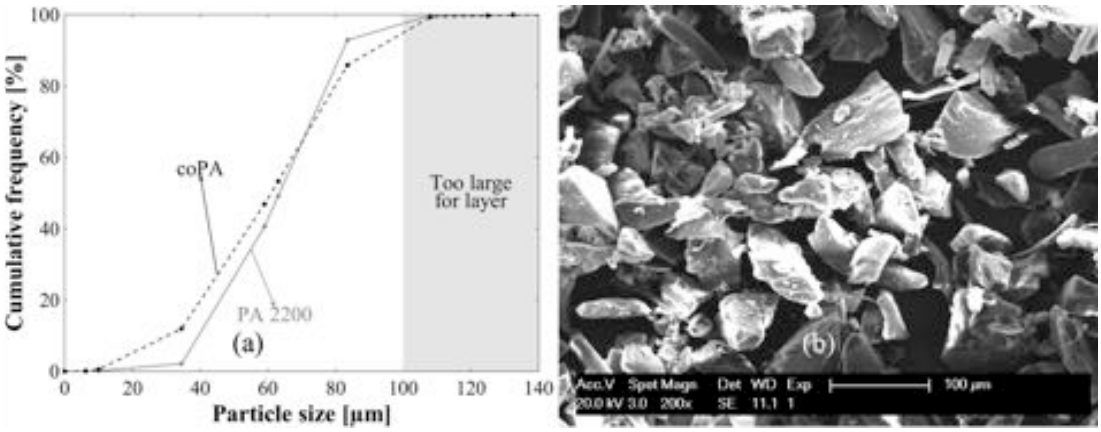


**Figure 5-27:** (a) PSD and (b) SEM image of the cryomilled coPA powder.

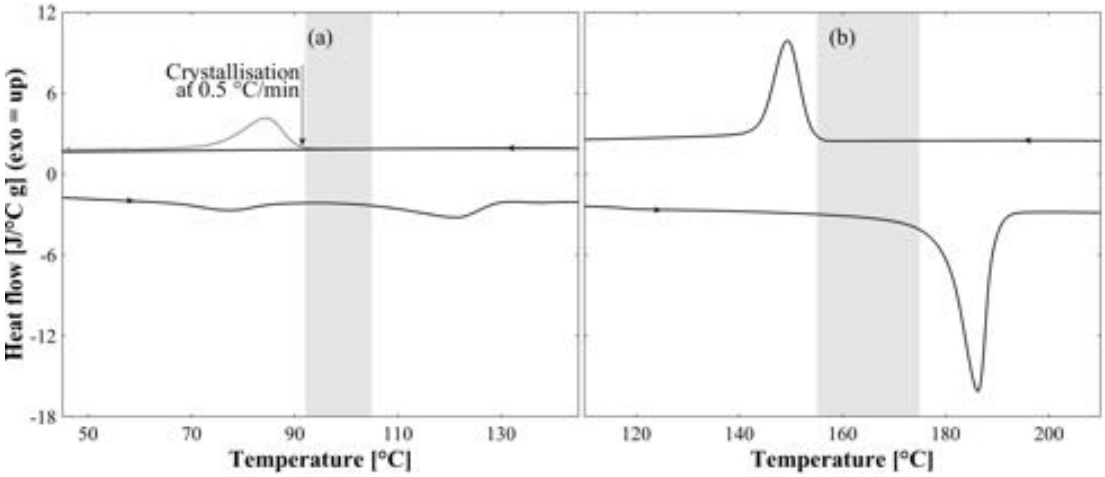


**Figure 5-28:** DSC measurements of coPA (a) and PA 2200 (b) at 10 °C/min (—) and 0.5 °C/min (---). The grey zone indicates the thermal window available as bed temperature in a laser sintering process.

DSC measurements, shown in Figure 5-28, do not clearly indicate a thermal window. In standard procedure with a ramp rate of 10 °C/min, the coPA sample shows two wide melting peaks at roughly 75 °C and 120 °C. This melting behaviour makes it unclear at which temperature the powder bed can be kept. Firstly, it is uncertain whether passing the first melting peak already induces sufficient stickiness in the powder. Secondly, as the peaks have quite broad onsets, it is difficult to determine an exact upper limit to the thermal window for the powder bed based on either peak. Section 5.4.2 creates clarity on the exact upper limit of this window, based on powder flowability. Also the lower limit of the thermal window is unclear from the standard measurement protocol. At the standard cooling rate of 10 °C/min, the grade solidifies in an amorphous form, similarly to the PLA sample, discussed in Section 5.2. At a lower cooling rate of 0.5 °C/min, however, a crystallisation peak with an onset around 92 °C appears. Similarly to the PLA sample, this crystallisation at low cooling rates limits the thermal window for the powder bed, as this is the most representative cooling rate for LS.

### 5.4.2 Powder flowability

A-DAoR, powder rheometry, powder spreading experiments and the Hausner Ratio determine the powder flowability of coPA. The latter test is mainly used to evaluate the recyclability of the powder and is thus discussed in Section 5.4.4. Table 5-8 shows the results of the A-DAoR and powder speading measurements in comparison to PA 2200. The coPA grade scores slightly worse than the PA 2200 reference. Its angles are roughly 5° higher and a similar difference was noted in the spreading experiments. The packing limit of the coPA is quite similar to that of PA 2200. However, the powder flowability of coPA hinders it strongly from reaching this densest packing. As a result, the PR of coPA is significantly lower than that of PA 2200. This limited packing due to flowability rather than the geometrical packing limit seems to be present in all cryomilled powders assessed in this chapter. However, no defects were observed in any of the lab-scale spreading experiments. Therefore, the flowability of coPA is deemed sufficiently high to enable LS.

**Table 5-8:** Powder flowability indices based on the dynamic angle of repose (A-DAoR) and spreading experiments for coPA and PA 2200.

| | $\widehat{\phi}$ [°] | $\widehat{\phi}_a$ [°] | $\rho_{pk,geom}$ [%] | $\rho_{pk}$ [%] | PR [%] |
|---|---|---|---|---|---|
| **PA 2200 (Chapter 3)** | 36.6 ± 0.3 | 40.0 ± 0.3 | 51 ± 6 | 44 ± 5 [73] | 87 |
| **coPA** | 40.6 ± 0.2 | 45.5 ± 0.4 | 53 ± 2 | 39 ± 2 | 73 |

As discussed in Section 5.4.1, the double melting peak of the coPA hinders the prediction of the thermal window for the powder bed. Based solely on the DSC data it is unclear if the powder is still spreadable past the first melting peak or if the powder becomes too sticky at this point. To aid in this analysis, powder rheometry tests are performed, as shown in Figure 5-28. At around 100 °C the flow energy increases. This increase corresponds to the onset of the second melting peak. The presence of the first melting peak, however, did not seem to significantly affect powder flowability. The thermal window for the powder bed is therefore larger than predicted by DSC. This result again illustrates how powder flowability measurements are able to aid in the correct prediction of the thermal window.

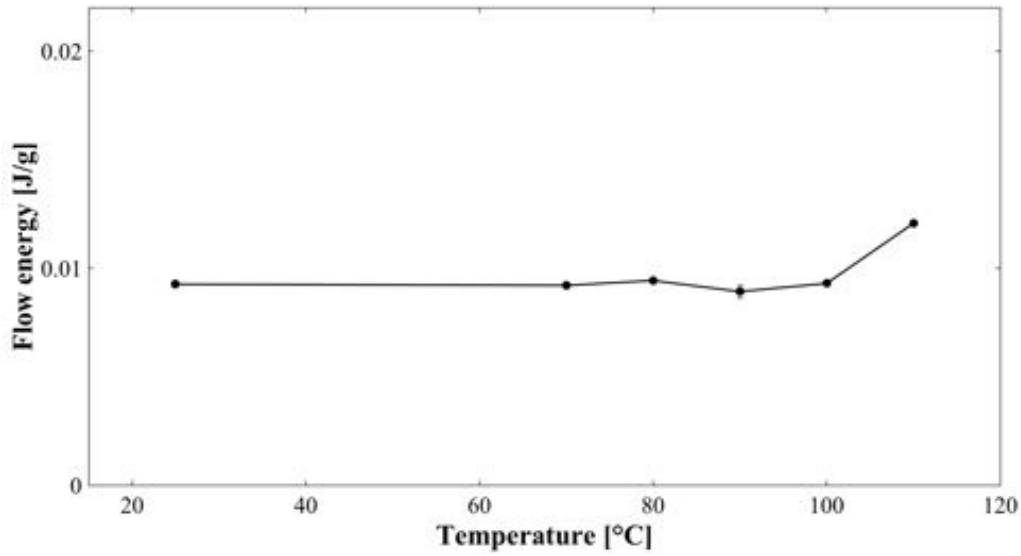


**Figure 5-29:** Powder rheometry measurements for coPA.

### 5.4.3 Coalescence and solidification

The viscosity of coPA was measured during a continuous cooling ramp of 1 °C/min in steady shear. Figure 5-30a shows the viscosity of the coPA grade, relative to the temperature difference with the melting peak (121.4 °C for coPA and 186.2 °C for PA 2200). The viscosity of the coPA grade is slightly larger than that of PA 2200, which results in slower coalescence, as illustrated in Figure 5-30b. Furthermore, the temperature dependence of the viscosity is significantly larger. This strong dependence is quantified in the large activation energy in the Arrhenius equation (Eq. 1.1), which equals 82.7 kJ/mol. As a result, slight heating past the melting peak is sufficient to enter the viable viscosity range for LS.

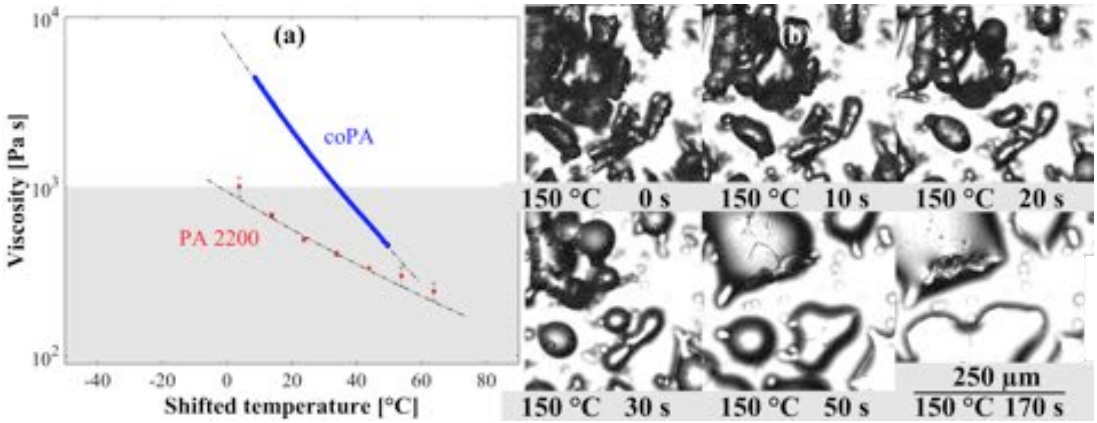


**Figure 5-30:** Zero-shear viscosity of PA 2200 [73] and coPA in function of the temperature difference with the melting temperature. (b) Coalescence of coPA in hot stage microscopy at a heating rate of 30 °C/min.

TGA measurements (Figure 5-31) show a continuous mass decrease with temperature. However, no effects of post-condensation or viscosity degradation with temperature were seen in melt viscosity measurements. By applying the 1% degradation onset as the upper limit of the stable sintering region, a stable sintering region of only 50 °C is found. However, most of the degradation does not occur below 350 °C, which is possibly a more correct upper limit for the stable sintering region.

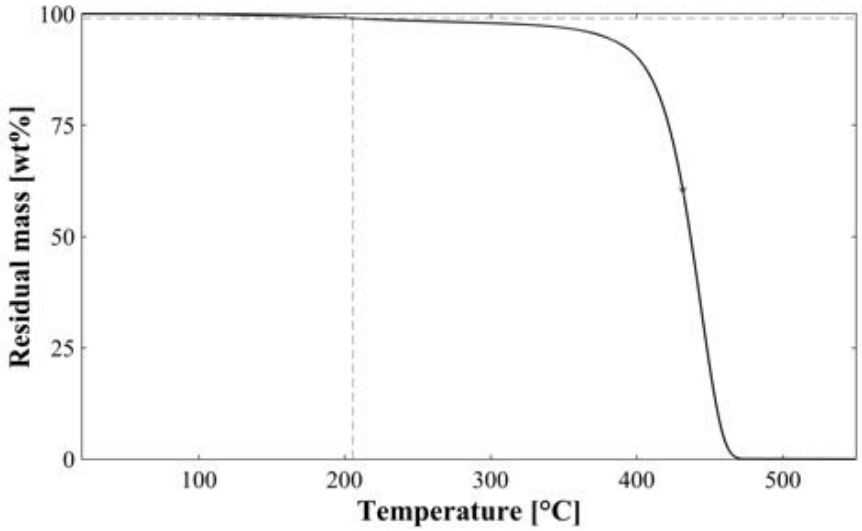


**Figure 5-31:** TGA of coPA.

No shrinkage measurements were performed on this grade. The shrinkage is, however, expected to be minimal, similar to TPU. The sintering tests of Section 5.4.5 show a feasible thermal window with no issues with warpage.

### 5.4.4 Recyclability

The coPA grade does not post-condense, which facilitates powder recycling. The absence of post-condensation was tested by an oscillatory shear measurement at 160 °C, 1 rad/s and 1% strain. The viscosity remained constant during the entire measurement of 2 hours.

**Table 5-9:** Powder flowability indices based on the dynamic angle of repose (A-DAoR) and spreading experiments for coPA and PA 2200.

| | $\widehat{\phi}$ [°] | $\widehat{\phi}_a$ [°] | HR [/] |
|---|---|---|---|
| **coPA** | 40.6 ± 0.2 | 45.5 ± 0.4 | 1.22 |
| **coPA recycled** | 48.4 ± 0.3 | 55.0 ± 0.7 | 1.28 |
| **coPA rec + additive C** | 41.6 ± 0.9 | 49.6 ± 1.0 | 1.22 |

However, some recyclability issues were noted during the large-scale sintering tests, which are discussed in Section 5.4.5. Upon recycling, the powder became increasingly sticky, resulting in a lower dense, fluffy powder mass. As the powder flow issues had a clear effect on the bulk density, a Hausner ratio measurement was used to assess the severity and possible solution to the problem. These results are then compared to an angle of repose measurement. Figure 5-32 shows the results of a Hausner ratio measurement with a tapping frequency of 250 taps/min and a drop height of $3 \pm 0.2$ mm. The virgin sample has a HR of 1.22. Upon recycling this value increases to 1.28, marking a significant decrease in flowability. The addition of 1 wt% of flow additive C is able to lower the HR to the initial value of 1.22. This trend is also reflected in A-DAoR measurements (cf. Table 5-8). The recycled powder shows an increase in the average and avalanche angle of more than 7°. The increase is also counteracted almost completely by the addition of flow additive C. The same improvement was seen qualitatively within the sintering tests.

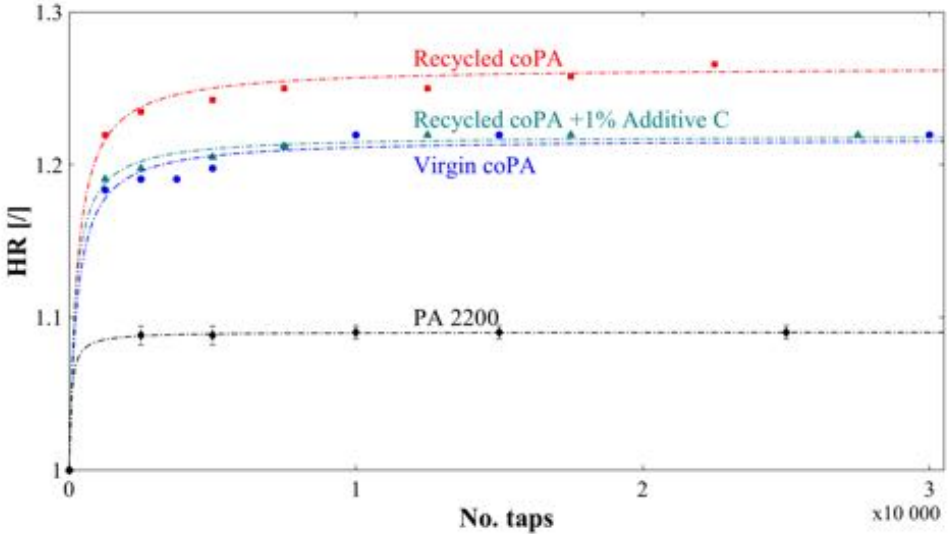


**Figure 5-32:** HR measurement of coPA and PA 2200. The dotted lines are fitted by the Kawakita equation (Eq. **1.17**).

The deterioration of the flow properties upon recycling can have several reasons. One possibility is the change of additive content during processing. This change can result from segregation on the one hand, or immobilisation of the freely moving additives on the coPA particle surface due to partial melting of the coPA on the other hand. The addition of new flow additives may therefore make up for the loss during processing, resulting in the regain of flow properties. Another possible explanation lies within the thermal properties of the polymer. As the powder bed is kept at a temperature above the first melting peak, the structure of the material changes, as illustrated in Figure 5-33. The annealing effect of the elevated powder bed temperature removes the first melting peak and adds to the total enthalphy of the second peak.

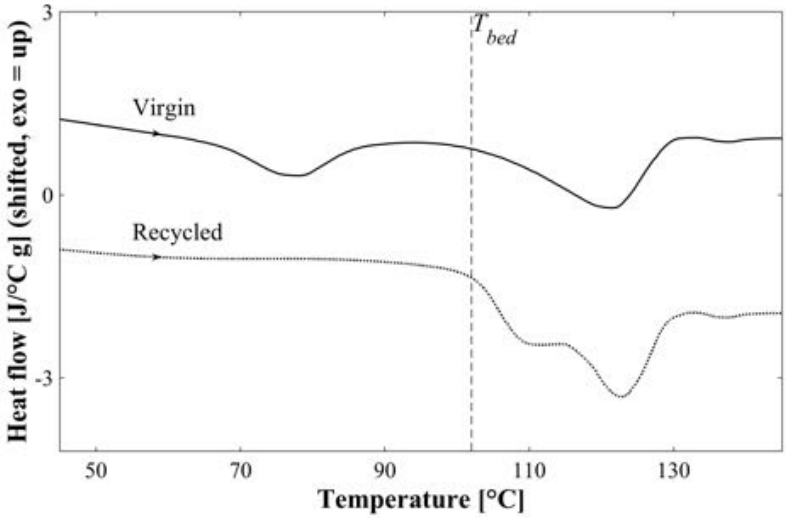


**Figure 5-33:** DSC heating ramps of the virgin and recycled coPA.

### 5.4.5 LS proof of concept

Sintering tests provide a proof of concept for the sinterability of the coPA grade. First, small-scale sintering tests are performed, according to the protocol of Section 5.3.6 with optimised processing parameters, as listed in Table 5-10. Next, the material is tested on a full-scale industrial EOS sintering machine.

**Table 5-10:** LS processing parameters applied in the sintering tests of coPA.

| | Small-scale | Full-scale | | |
|---|---|---|---|---|
| | | Set 1 | Set 2 | Set 3 |
| **Bed temperature [°C]** | 115 | 100 | 98 | 96 |
| **Feed temperature [°C]** | 55 | NA | NA | NA |
| **Laser power [W]** | 9 | 12.6 | 9.0 | 13.5 |
| **Scan spacing [mm]** | 0.15 | 0.3 | 0.15 | 0.15 |
| **Scan speed [mm/s]** | 1000 | 2800 | 1000 | 1500 |
| **Energy density (Eq. 1.3a) [J/mm$^2$]** | 0.06 | 0.015 | 0.06 | 0.06 |

In the small scale sintering tests, a bed temperature of 115 °C is attainable. This is larger than the value of 105-110 °C, predicted in Section 5.4.2. The difference may lie in the lower feed temperature, as was also discussed in Section 5.3.6. Furthermore, some issues with the exact temperature calibration of the LS device may have been present. All parts are sintered with a scan spacing of 0.15 mm and a scan speed of 1000 mm/s. Various laser powers are tested, ranging from 3 to 27 W. The parts sintered at 3W (0.02 J/mm$^2$) have not fully sintered. High porosity is seen, which influences the mechanical strength of the sintered multilayers. Above 15 W (0.1 J/mm$^2$) the density of the parts drops again, likely due to degradation by the laser. An optimal laser power of 9 W (0.06 J/mm$^2$) is therefore chosen.

Tensile bars are printed with the processing parameters of Table 5-10. Two sets of bars are created in the small-scale sintering tests. One set lies flat in the powder bed; the other is placed on its side. Both sets score very similar, though the bars placed sideways seem to perform slightly better. A reduction in all mechanical properties is seen, which is common for sintered parts, due to the increase in porosity or the limited molecular diffusion between particles. The resulting mechanical properties are, however, still quite high.

**Table 5-11:** Tensile properties of printed tensile bars (small-scale sintering procedure), compared to the injection moulded (IM) bars.

| | **E [MPa]** | **UTS [MPA]** | **EAB [%]** |
|---|---|---|---|
| **IM (**Table 5-7**)** | 223 | 34 | 789 |
| **Sintered, flat** | 93 ± 21 | 15 ± 1 | 221 ± 31 |
| **Sintered, side** | 126 ± 44 | 18 ± 2 | 287 ± 37 |

Based on the successful small-scale sintering tests, the material was tested on a full-scale industrial sintering machine. The lab results and small-scale sintering tests provided in the previous sections formed the basis for determining the process parameters, which are added in Table 5-10. Three parameter sets were tested. Set 1 is based on typical processing parameters of commercial TPU. Set 2 uses the same parameters as the small-scale sintering tests. Set 3 uses the same ED, but tries to speed up the process by increasing the laser power and scan speed.

Tensile bars were produced to determine the mechanical properties that are attainable in LS for the different parameter sets. The parameters of set 1 created parts with sub-optimal density. This is in line with the small scale sintering tests that did not create viable parts below 0.02 J/mm$^2$. Set 2 was able to create tensile bars with a median UTS of 32 MPa and a median EAB around 400 %. The results are, however, very sensitive to the bed temperature, as at 96 °C the parts did not sinter successfully. The faster parameter set of set 3 managed to obtain similar results as set 2, but the bed temperature could be effectively lowered to 96 °C.

All tested bars had a UTS between 20 MPa and 30 MPa, which is slightly higher than the values that were attainable in the small-scale sintering tests. Furthermore, they are close to the ideal limit of the injection moulded parts (34 MPa). An EAB of 200-400 % was attainable, which is rather high for sintered materials. As a final qualitative test, fully three-dimensional parts were sintered, as shown in Figure 5-34. No defects were seen in these parts and, as opposed to TPU, no smoke formation was seen during the build. As a result, coPA may be an interesting competitor for flexible applications in LS.

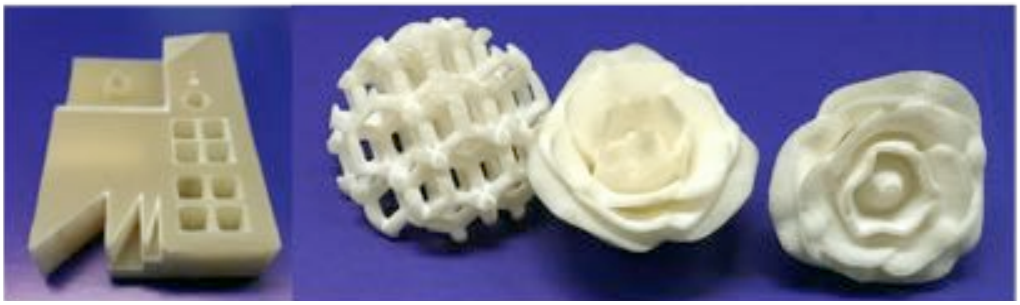

**Figure 5-34:** Sintered coPA parts.

The only remaining downside for the coPA sample is the low building speed. It builds about two to three times slower than the PB-1 grade. In literature, scanning speeds up to 4000 mm/s to 5000 mm/s are reported for PA 2200 [218] and similarly high scan speeds are found for the TPU in Section 4.4.6. At higher speeds, the powder does not coalesce. The low building speed of coPA adds a significant production cost, which is undesirable as the material is meant as a low cost TPU competitor. The reason for this slow building speed is not yet fully understood. One hypothesis states that is may be due to the extremely low absorption of coPA at the laser wavelength, as shown in Figure 5-35. The absorbance spectra, measured in transmission mode on plate pressed films, show a strong valley around the laser wavelength of 10.6 µm. As discussed in Section 2.1.3, this does not account for the entire absorbance in LS, as internal reflection in the powder bed plays a large role in the total absorption. The near-zero absorbance in transmission mode, however, does indicate qualitatively that the material interacts much less with the laser beam, compared to the reference powders, i.e. PA 2200 or TPU Desmosint. More studies are, however, required on the kinetics of laser absorption to fully explain this phenomenon.

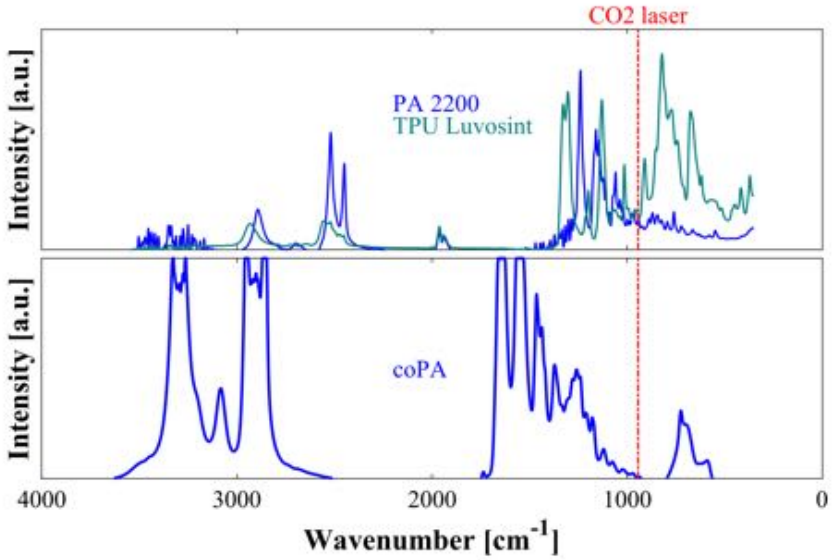


**Figure 5-35:** Absorbance spectra of the examoned coPA grade, compared to PA 2200 and TPU Luvosint.

In an attempt to improve the absorbance, carbon black is added to the powder and a preliminary sintering test of multilayers is performed. The carbon black, however, gives off sparks in the sintering process, indicating a strong energy loss due to burning of the carbon black. Therefore, the addition of carbon black was not further evaluated.

### 5.4.6 Conclusions

Both the lab measurements and the sintering tests have proven that coPA is an interesting material for LS. The thermal window for the powder bed and the stable sintering region, which are determined from lab experiments, are summarised in Figure 5-36. Sintering experiments provided proof of the sinterability of the material as a low-cost competitor for TPU. Its mayor selling points are its low price, good strength and elongation and the absence of smoking during the build. As the material is very flexible, but exhibits less elastic recovery than most TPU grades, it could potentially fill additional market needs. The major downside of the material is, however, its low building speed due to the strongly limited scan speeds. As a result, this hinders its viability from an economical standpoint. Further research on improving the laser absorption by additives or even the modification of the base polymer is therefore needed to obtain the full potential of this material.

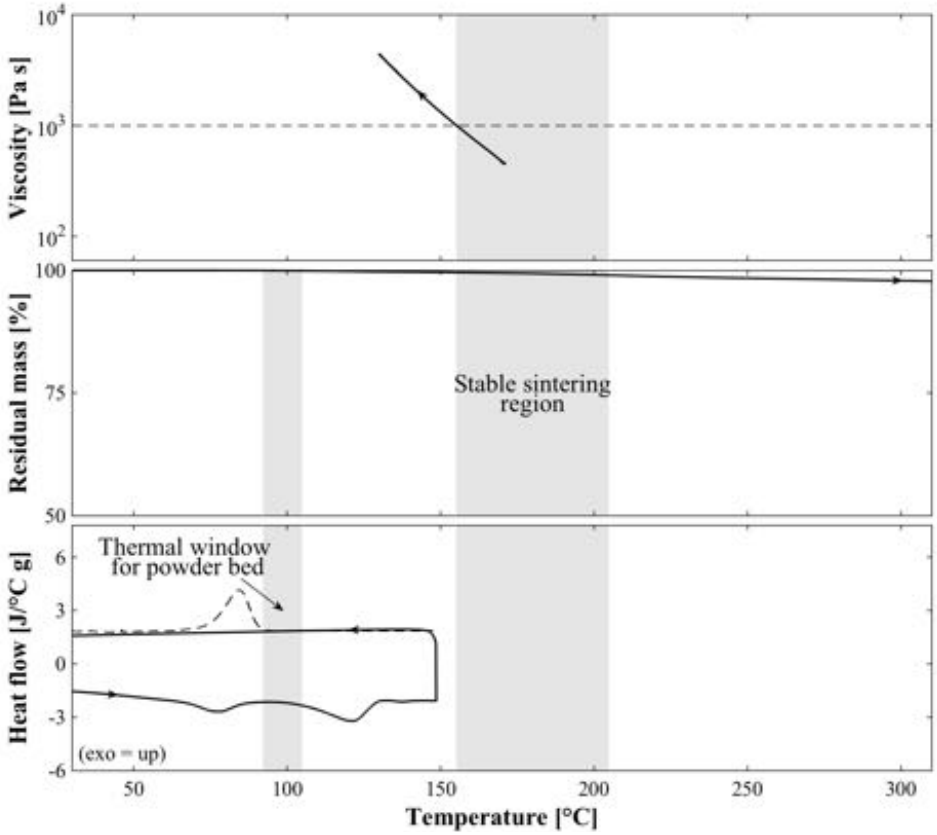


**Figure 5-36:** Thermal processing windows for coPA. The worst case 1 % degradation limit is shown for the stable sintering region.

## 5.5 Conclusions

Four major conclusions follow from the research shown in this chapter. Firstly, the provided material screening methodology proves useful to assess new materials for LS. The results obtained in lab experiments provided directly useful input for the LS process, such as applicable bed temperatures and whether issues are expected in any of the LS processing steps.

Secondly, the importance of powder flowability at elevated temperatures and adequate methodologies to assess this effect is highlighted with three different examples. The PLA grade exhibits stickiness, which is not predictable from the thermal window obtained in DSC. The PB-1 grade shows a wide melting onset, which hinders the exact prediction of the attainable bed temperature. And finally, the coPA grade exhibits two distinct melting peaks, which complicates the localisation of the upper limit of the powder bed temperature. Powder rheometry is deemed the most useful technique for predicting the flow behaviour at elevated temperatures, due to its strong thermal control and clear increase in flow energy, which corresponds to the flow issues encountered in full-scale sintering tests. The powder rheometer is therefore a useful tool to complement the insights obtained from DSC.

Thirdly, thermal treatments have proven to increase the viability of the PB-1 and PLA grades. For the PB-1 grade, a simple annealing step made the unsinterable base powder sinterable. This methodology may impact other materials and grades, which are currently deemed non-viable for LS.

Finally, two materials, PB-1 and coPA, were successfully assessed for LS. Parts were sintered for both materials, indicating their viability for the LS process. Some further optimisation in the processing speed of coPA is, however, still desirable to make this material economically viable. The cryomilled PLA was deemed non-viable due to the current particle morphology. Additional research into improving the millability of this material is therefore required.

# Chapter 6

# Conclusions and outlook

The first half of this chapter summarises the most important conclusions of this work, spanning all previous chapters. The second half then formulates some remaining questions for follow-up research, based upon the findings of the previous chapters.

## 6.1 Final conclusions

The three main aims of this work, as stated in Section 1.3, are successfully met, namely (1) expansion of the screening methodology with a focus on powder flowability, (2) evaluation of the cryomilling process as a viable powder production route for LS and (3) addition of new polymers to the LS material palette via the cyromilling process.

### 6.1.1 Successful expansion of the screening methodology

The screening methodology has been successfully expanded with three powder flowability measurements, namely the dynamic angle of repose, the powder rheometer and the powder spreader. The dynamic angle of repose and powder spreader set-ups are built specifically for this research and the powder rheometer set-up is a new expansion of a commercial stress-controlled rheometer. In the case of the dynamic angle of repose, software is written to enable a user-friendly and operator independent analysis of the powder heap. All three techniques have been

validated on existing reference materials (Chapter 3) as well as on new cryomilled polymer powder grades, intended for LS (Chapters 4 and 5). The tests illustrate two central needs for the flowability assessment: (1) the direct link to the flow field within LS and (2) the inclusion of a high-temperature powder flowability assessment.

The most direct link to the LS flow field is obtained in the powder spreader set-up (cf. Section 3.5), which mimics the spreading step of an industrial LS machine. Firstly, it is able to qualitatively screen poorly flowing powders by the presence of defects in the layers. Next, for the powders that pass this qualitative screening, a quantitative ranking is possible by assessing the layer density. This density is directly relevant for the LS process, as higher density promotes denser final parts. The need for this direct link to the LS flow field is proven by comparison to other, more general flowability, such as the dynamic angle of repose. On the one hand, the dynamic angle of repose indicates the same trends as the powder spreader, such as the effect of flow enhancers and the distinction between spherical, smooth and irregular powders. However, within subsets of powders, the relation with the layer density is limited. This is further illustrated for the subset of cryomilled powders, which commonly have average angles around 45°, but still score differently in the spreading tests (Chapter 4 and 5).

Temperature control is added to all three flowability measurements to determine the onset of powder stickiness. This knowledge is crucial for setting the upper limit of the thermal window for the powder bed, as DSC measurements alone have proven to be insufficient. Some materials, such as various TPU grades (Section 4.4) and the PB-1 grade (Section 5.3) exhibit broad melting peaks, which makes it difficult to predict how high the powder can be heated. Other materials, such as the PLA grade (Section 5.2) and TPU S-56 (Section 4.4) show strong stickiness before the onset of the melting peak. In these cases, the DSC provides an overestimation of the thermal window. Finally, some materials such as the examined coPA (Section 5.4) show multiple melting peaks. Flowability measurements help to assess whether heating above one or more of these peaks creates powder stickiness issues. In the case of coPA this means the difference between a nearly non-existent thermal window for the powder bed and a viable window. The powder rheometer is deemed the most useful technique for assessing this stickiness onset, as its precise temperature control and high sensitivity enable the most accurate measurement. The biggest drawback of this technique is, however, its current inability to correctly assess powders, such as TPU, which form a very fluffy, low dense network.

In conclusion, each of the three added techniques fills a specific niche in the testing protocol. The dynamic angle of repose is useful for quickly screening trends, such as the addition of additives, due to its ease of use, limited sample mass and short

measurement time. In this measurement, the trends related to particle size are clearly linked to the estimated Bond number for the spherical powders, but the roughness, unknown amount of additives and estimation of the Hamaker constant make it unable to fully compare the other samples. The powder spreader is the most relevant technique for the assessment of flowability in an actual LS machine and, as a result, provides the most informative data for ranking individual powders. It is, however, also the most labour-intensive technique. Therefore, an automated version is developed for future use. Finally, the powder rheometer provides the most accurate temperature control, which enables it to predict the stickiness onset of most powders quite well. Except for the TPU grades, it enabled a much more accurate prediction of the thermal window for the powder bed, compared to DSC measurements alone. The current rheometer set-up can withstand temperatures up to 150 °C, which was deemed sufficient for most materials, except for the PA grades. However, for possible research on higher-melting materials, an expansion to this temperature range is beneficial.

### 6.1.2 Viability of cryomilling

Cryomilling is able to create powders that are viable for laser sintering. PA, TPU, PLA, PB-1 and a coPA have been milled to a desirable particle size range. All powders show a relatively rough morphology and high angles in the dynamic angle of repose, which indicate poor powder flowability. However, upon spreading, most materials create smooth, defect-free layers. The packing density of the layers, on the other hand, varied more strongly and was typically much lower than that of the commercial, smooth LS powders. This hinders coalescence, but is not deemed an insurmountable limitation for LS applicability. An additional compression step after spreading, such as a co-rotating roller, may help to further densify the layers, as illustrated by Niino et al. [62]. The only exception to this conclusion is the milled PLA grade (Section 5.2). In industrial LS trials, the grade shows strong flowability issues, which are likely related to the exceptionally poor particle morphology, which includes a large fraction of string-like particles. Further optimisation of the milling process is thus required to avoid this morphology in future powders.

Even though the cryomilling trials have been successful, there are still several limitations for the use of cryomiling for LS. While the technique is considered universal for all polymers, e.g. no polymer-specific solvent or other components are necessary, there are some hurdles for milling certain samples such as TPU S-89, S-92b and T-95c (cf. Section 4.4.5). This problem is not confined to TPU grades, as other, non-elastomeric polymers, which have not been discussed further in this text, showed similar problems. This milling issue is further discussed in the future outlook (Section 6.2.1).

### 6.1.3 Evaluation of three new polymers and various new TPU grades

This work succeeded in the evaluation of three materials that have not commonly been used in mechanical LS applications before this research, as well as various new TPU grades. This evaluation provided new insights into the needs of LS materials and hopefully further opens the LS market to even more materials.

Various TPU grades that have not previously been applied to LS have been tested (Section 4.4). Several grades failed the lab-scale screening methodology and also failed in industrial sintering trials in accordance to the lab predictions. This predicted failure demonstrates the usefulness of the screening methodology to correctly predict powder behaviour in LS. Though many grades did not pass the evaluation, there have been some promising results. TPU S-97 was the most successful, as non-yellowed tensile bars with adequate tensile strength are created. Furthermore, TPU S-90, S-93a, S-94 and T-95a show good sintering behaviour, but lose too much of their mechanical strength in the process due to a combination of porosity and degradation. Additional process optimisation may partially remedy this problem, but is limited by polymer degradation upon further increasing the energy density. Finally, some grades showed unexpected sintering behaviour, as they formed separate droplets rather than a homogenous melt pool. This previously unseen issue thus requires further investigation and a lab-scale screening procedure.

PB-1 (Section 5.3) is successfully sintered. Utilising the knowledge of the polymorphism of the material, a sinterable powder form is found and processed into tensile bars. A major concern is, however, the post-build shrinkage, which needs to be taken into account. Also the coPA grade (Section 5.4) shows promising results, as final parts with good elastic properties have been sintered. However, the low processing speed still limits economic viability. A new PLA grade (Section 5.2) has also been investigated. Even though the base grade shows promising results, the inadequate particle morphology hinders successful sintering, as discussed in Section 6.1.2. This result, however, does not exclude PLA as a usable polymer for future work, provided that the powder morphology issues can be remedied.

### 6.1.4 Thermal treatments to improve LS viability

This research has shown that some powders that are originally unviable for LS can become usable after a thermal treatment. This finding creates a novel approach to the evaluation of LS polymers, as it may re-introduce polymers that have previously been deemed unsinterable. The effect of such thermal treatments has been illustrated for PLA and PB-1 (Chapter 5). Both materials showed severe issues with powder stickiness at elevated temperatures, which rendered their thermal windows too small. In both cases, an annealing treatment improved the flow behaviour and thus made

them more viable for LS. This process is easily applied on an industrial scale and does not give rise to a large increase in the material cost.

A similar thermal treatment may also be beneficial for the flowability of the investigated Farsoon PA powder. This powder, like the PB-1 grade, exhibited a too wide onset for the melting peak (Cf. Section 4.3). However, the strong post-condensation of the material hinders the effective use of any annealing procedure. This example illustrates how the application of thermal treatments is only viable for polymers that either do not post-condense or that show only a limited increase in their viscosity during the intended thermal treatment.

## 6.2 Future outlook

Even though promising results have been made regarding the aims that have been set for this work, there are still many opportunities for future research to expand upon these findings and address some new research questions that arose.

### 6.2.1 Cryomilling optimisation and deeper understanding

This research has proven the viability of cryomilling as an industrial-scale processing route for the creation of LS powders. However, as stated in Section 6.1.2, there are still some limitations that require attention. Firstly, as some materials have not been milled successfully to the desired PSD, more insight into this current inability is needed. Preliminary Sharpy impact tests have been performed to evaluate the toughness of the problematic materials at their cryomilling temperature, but no distinct trends are found. Both the problematic materials as well as millable reference grades show a strong variation from brittle fracture to plastic deformation without breaking in these tests. Furthermore, no trends in hardness or other mechanical properties are seen. Within the limited set of available materials, the only noteworthy observation is the difference between the glass transition and the attempted milling temperature. More issues are seen if these temperatures sit closer together, even leading to an improvement by raising the milling temperature in some cases. However, this has been tested on too few materials to draw conclusions at this stage. A more systematic and fundamental analysis of the cryomilling process is therefore required.

Secondly, many of the exact processes that occur during the milling procedure are at this point poorly understood. This lack of knowledge includes the fracture dynamics, which in some cases result in cleanly fractured particles and in other cases yield undesired elongated, string-like particles, as is illustrated in Sections 4.4.3 and 5.2.1. These deformations may be linked to strong local heating effects, which in turn

could also explain the post-condensation (cf. Section 4.4.5) and viscosity degradation (cf. Section 5.2.5) that is noted in the cryomilling process.

Finally, large and uncontrolled amounts of additives have been added to the material to enable the sieving step. As shown in Section 4.4.5, these additives have a largely negative effect on the thermal window of the powder bed. Furthermore, this influences also the flowability assessment, as it is currently unknown whether these materials could be viable with a smaller amount of flow additives. Besides a general reduction of the additive requirement in cryomilling, also a better control of the amount of additives that are in the final powder is needed to minimise batch variability. Currently it is poorly known what fraction of the additives ends up in the LS powder, and how much additive is situated in the waste fractions.

### 6.2.2 Investigation of unexplained sintering issues

Two unprecedented LS processing problems have been encountered during this research. The first is the problem of droplet formation upon melting, as seen in Section 4.4.6. Thus far it has only been encountered in a few TPU grades, but its origin is unknown. Hypotheses are that this is either a surface tension issue or the result of the low powder packing densities found for some of these materials, which limits the desired coalescence. As this problem is currently not screened in the lab-scale testing, it creates strong issues during the industrial scale sintering trials.

The second problem relates to the processing speed of the investigated coPA (cf. Section 5.4.5). Scanning speeds thus far could only be raised to 1500 mm/s, which is significantly lower than the attainable scanning speeds of the tested TPU grades, i.e. 4000 – 5000 mm/s. This limits the viability of coPA as a low-cost competitor for TPU, as the increase in production time brings a strong increase in production cost. Further studies are needed on the exact interaction of the laser with the powder material. Some preliminary tests have been performed on the absorption of the base material. These tests should, however, be expanded to a full analysis of the laser interaction with the powder.

### 6.2.3 Further expansion of the material palette

The work in this thesis has focussed mainly around two sets of materials: the commodity or low-cost polymers (PLA, PB-1 and the coPA grade) and the engineering class polymers (PA, TPU). A third class of materials, namely the specialty or high temperature polymers is also included in the intended market aims of the WAVE project. However, limitations with temperature control in the available sintering machines, as well as some milling issues with some harder materials within this class prevented a full investigation of these materials.

Furthermore, the work presented in this thesis provides a systematic base for the evaluation of many more materials within the entire available polymer portfolio.

## 6.3 Concluding statement

This work created a deeper understanding on polymer powders for LS. The close collaboration with industry resulted in a unique opportunity to directly validate the results for practical applications. As a result, the claimed innovations in the screening methodology, cryomilling applicability and proposed materials have been shown in industrial sintering trials. Finally, even though many questions have been addressed during this work, a lot of possibilities are left to expand upon the findings of this research and create a strong added value for the Flemish AM industry.

# Appendix A

# Circular Hough transform

A circular Hough transform is utilised to determine the drum location within the first frame of a DAoR measurement (Section 3.3.1). A Hough transform algorithm transforms the edge points of an image into the parameter space to find objects of any predefined shape. In the case of a circle, Eq. A.1 in the cylindrical coordinate space is used, with $r$ the circle radius [219,220].

$$r^2 = (x - \mathrm{b}_1)^2 + (y - \mathrm{b}_2)^2 \tag{A.1}$$

The algorithm then finds the object defined by the equation via the following steps. First, as the algorithm works only on edges, preliminary edge detection on the entire frame is performed via the algorithm described in Section 3.3.1. Next, the radius $r$ in Eq. A.1 is set, thus only circles of one specific radius are searched. Then, the image edge is transformed to the parameter space, i.e. the coordinates (x,y) for each edge point are used as the parameter set ($b_1$,$b_2$) in Eq. A.1. This can be seen as drawing a circle of radius $r$ through each point of the edge image. This step is visualised in Figure A-7-1 for three exemplary points. Finally, as all these circles per definition cross in the centre of the original image, an intensity profile of the new circles provides a maximum at this centre. This location, combined with the predefined radius, fully determines the detected circle [219,220].

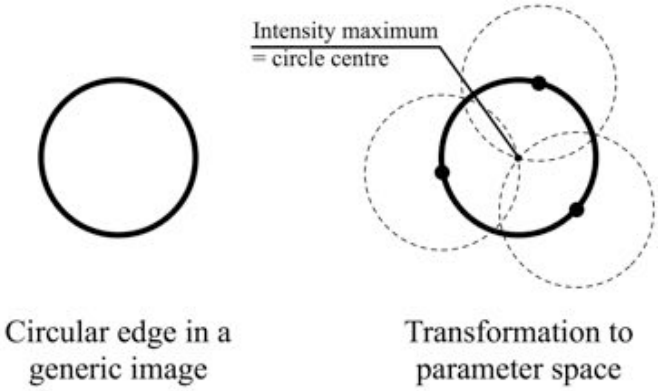


**Figure A-7-1:** Illustration of a circular Hough transform analysis for a generic image (adapted from. Pedersen [219]).

In the case of the rotating drum, only one clear circle is present in the image, namely the drum circumference. However, due to the variable distance to the camera lens, the radius of this drum in pixels is unknown. To find the drum, the Hough transform algorithm thus needs to be applied for a range of radii. The larger this range is, the longer the algorithm takes. In the DAoR software, the upper limit of this range is taken as half the minimal image dimension, as the entire drum needs to be within the frame. The lower limit is taken as half of the upper limit, which allows for quite some variation in the camera distance.

# Appendix B

# Humidity controller on the automated powder spreader

The powder spreader has been automated to optimise user-friendliness and minimise operator variability. The base principle of the device, as well as the IR heating mechanism, is kept the same as for the semi-automated version (Cf. 3.5.1). Due to the automatic movement of the blade and platforms, the upper half of the powder spreader can now be fully sealed of, as shown in Section 3.5.3. This enables environmental control during the measurement. A humidity controller has been designed to regulate humidity within this chamber.

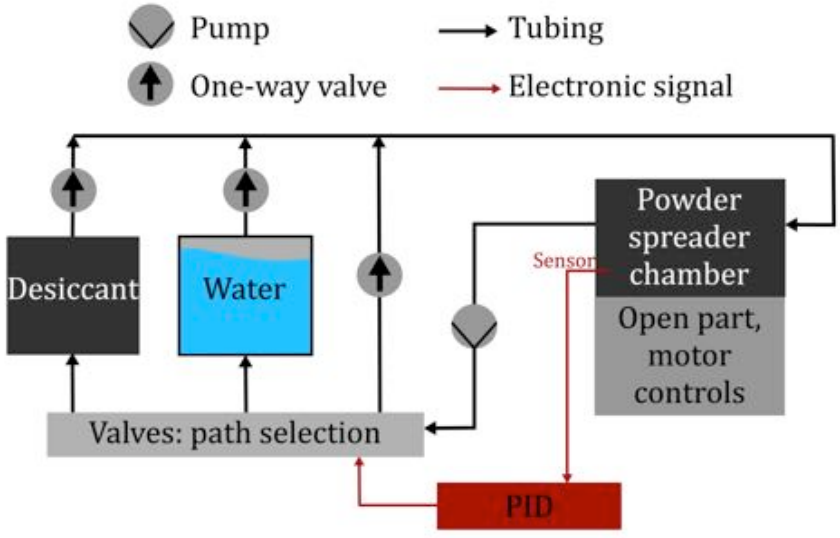


**Figure B-8-1:** Schematic representation of the humidity controller.

The humidity controller consists of a standalone device that can be mounted to any sealed chamber with an in- and outlet hole. A schematic of this set-up is shown in Figure B-8-1. The controller blows either humid or dry air through the chamber to raise or lower humidity, respectively. A proportional-integral-derivate (PID) controller determines what type of air is needed via a relative humidity sensor. The PID controller sends an electrical signal to a series of valves that guide the air path through a water reservoir or a silica based desiccant. Once the desired humidity is obtained, the air goes through a bypass, until the PID registers a humidity content outside of the chosen alarm limits.

The humidity controller has been tested in an environment of 55 % relative humidity and 20 °C. In this environment it is possible to create a stable minimal humidity of 33 % and a maximal humidity of 82 %. The humidity was kept constant for ±1 % over the course of 1 hour.

# References


1. Chua, C. K. & Leong, K. F., *3D printing and additive manufacturing: principles and applications*, 4th ed. (World Scientific, Singapore, 2015).
2. Wohlers Associates Inc., *Wohlers Report 2016* (2016).
3. Goodridge, R. D., Tuck, C. D. & Hague, R. J. M., Laser sintering of polyamides and other polymers. *Prog. in Mater. Sci.* **57**, 229-267 (2012).
4. Kruth, J.-P., Levy, G., Schindel, R., Craeghs, T. & Yasa, E., *Consolidation of polymer powders by selective laser sintering*, presented at Proc. of PMI2008, Ghent, Belgium, 2008 (unpublished).
5. Verbelen, L., in *Towards scientifically based screening criteria for polymer laser sintering (Doctoral thesis)* (KU Leuven, 2016).
6. SIM-Flanders, About SIM-FLANDERS, Available at www.sim-flanders.be (accessed: 01/08/2018).
7. Castellanos, A., The relationship between attractive interparticle forces and bulk behaviour in dry and uncharged fine powders. *Adv. in Phys.* **54** (4), 263-376 (2005).
8. Wu, A. & Sun, Y., *Granular dynamic theory and its applications* (Springer, Heidelberg, 2008).
9. Wong, K. V. & Hernandez, A., A review of additive manufacturing. *ISRN Mech. Eng.* (2012).
10. Gibson, I., Rosen, D. & Stucker, B., *Additive Manufacturing Technologies*, 2nd ed. (Springer, New York, 2010).
11. Hopkinson, N., Hague, R. & Dickens, P., in *Rapid manufacturing: an industrial revolution for the digital age*, edited by Hopkinson, N., Hague, R. & Dickens, P. (John Wiley & Sons, 2006), pp. 1-4.
12. Pham, D. T. & Gault, R. S., A comparison of rapid prototyping technologies. *Int. J. of Mach. Tools & Manuf.* **38**, 1257-1287 (1998).
13. Wendel, B., Rietzel, D.; Kühnlein, F.; Feulner, R., Hülder, G., Schmachtenberg, E., Additive processing of polymers. *Macromol. Mater. for Eng.* **293**, 799-809 (2008).
14. Van den Eynde, M. & Van Puyvelde, P., in *Advances in polymer science* (Springer, 2017).
15. Horn, T. J. & Harrysson, O. L. A., Overview of current additive manufacturing technologies and selected applications. *Sci. Prog.* **95** (3), 255-282 (2012).
16. Hopkinson, N. & Erasenthiran, P., *High speed sintering - Early research into a new rapid manufacturing process*, presented at Solid Freeform Symposium, 2004 (unpublished).
17. Majewski, C. E., Oduye, D., Thomas, H. R. & Hopkinson, N., Effect of infra-red power level on the sintering behaviour in the high speed sintering process. *Rapid Prototyp. J.* **14** (3), 155-160 (2008).
18. Brucks, A., Arndt, T., Ottino, J. M. & Lueptow, R. M., Behavior of flowing granular materials under variable g. *Phys. Rev. E* **75**, 032301 (2007).
19. Ruffo, M., Tuck, C. & Hague, R. J. M., Cost estimation for rapid manufacturing - laser sintering production for low to medium volumes. *Proc. IMechE, Part B: J. of Eng. Manuf.* **220** (9), 1417-1427 (2006).
20. Ko, H., Moon, S. K. & Otto, K. N., Design knowledge representation to support personalised additive manufacturing. *Virtual and Phys. Prototyp.* **10** (4), 217-226 (2015).
21. Duan, B. & Wang, M., Selective laser sintering and its application in biomedical engineering. *MRS Bulletin* **36**, 998-1005 (2011).
22. Amado, A., in *Characterisation and prediction of SLS processability of polymer powders with respect to powder flow and part warpage (doctoral thesis)* (Zurich, 2016).
23. Yang, S. & Evans, J. R. J., Metering and dispensing of powder; the quest for new solid freeforming techniques. *Powder Technol.* **178**, 56-72 (2007).
24. Crawford, R. H. & Beaman, J. J., Solid freeform fabrication. *IEEE Spectrum* **36** (2), 34-43 (1999).

25. Bagsik, A., *Mechanical properties of fused deposition modeling parts manufactured with Ultem*9085*, presented at ANTEC, Boston, 2011 (unpublished).

26. Bourell, D. L., Perspectives on additive manufacturing. *Anuu. Rev. Mater. Res.* **46**, 1-18 (2016).

27. Vasquez, G. M., Majewski, C. E., Haworth, B. & Hopkinson, N., A targeted material selection process for polymers in laser sintering. *Addit. Manuf.* **1-4**, 127-138 (2014).

28. Goodridge, R. D., Dalgarno, K. W. & Wood, D. J., Indirect selective laser sintering of an apatite-mullite glass-ceramic for potential use in bone replacement applications. *Proc. IMechE Part H: J. Eng. in Med.* **220** (2006).

29. Schmid, M., Amado, A. & Wegener, K., Materials perspective of polymers for additive manufacturing with selective laser sintering. *J. Mater. Res.* **29** (17), 1824-1832 (2014).

30. Kruth, J. P., Wang, X., Laoui, T. & Froyen, L., Lasers and materials in selective laser sintering. *Assem. Automation* **23** (4), 357-371 (2003).

31. Deckard, C. R. Patent No. US4863538A (1986).

32. United States Patent and Trademark Office, Trademark Electronic Search System (TESS), Available at http://tmsearch.uspto.gov/bin/jumpto?f=doc&state=4804:7ld8ug.3.113 (accessed 23/07/2018) .

33. Justia, Justia Trademarks, Available at https://trademarks.justia.com/782/32/sls-78232400.html (accessed 28/07/2018) (2018).

34. Justia, Justia Trademarks, Available at https://trademarks.justia.com/740/63/sls-74063298.html (accessed 28/07/2018) (2018).

35. Azzurri, F., Flores, A, Alfonso, G.C., Sics, I., Hsiao, B.S., Baltá Calleja, F.J., Polymorphism of isotactic polybutene-1 as revealed by microindentation hardness. Part II: correlations to microstructure. *Polym.* **44**, 1641-1645 (2003).

36. Pham, D. T., Dotchev, K. D. & Yusoff, W. A. Y., Deterioration of polyamide powder properties in the laser sintering process. *Proc. IMechE Part C: J. Mech. Eng. Sci.* **222**, 2163-2176 (2008).

37. Bourell, D. L., Watt, T. J., Leigh, D. K. & Fulcher, B., Performance limitations in polymer laser sintering. *Phys. Procedia* **56**, 147-156 (2014).

38. Wiria, F. E., Leong, K. F., Chua, C. K. & Liu, Y., Poly-ε-caprolactone/hydroxyapatite for tissue engineering scaffold fabrication via selective laser sintering. *Acta Biomaterialia* **3**, 1-12 (2007).

39. Partee, B., Hollister, S. J. & Das, S., Selective Laser Sintering Process Optimization for Layered Manufacturing of CAPA® 6501 Polycaprolactone Bone Tissue Engineering Scaffolds. *J. of Manuf. Sci. and Eng.* **128**, 531-540 (2006).

40. Yuan, S., Strobbe, D., Kruth, J.-P., Van Puyvelde, P. & Van der Bruggen, B., Production of polyamide-12 membranes for microfiltration through selective laser sintering. *J. of Membr. Sci.* **525**, 157-162 (2017).

41. Verbelen, L., Dadbakhsh, S., Van den Eynde, M., Strobbe, D., Kruth, J.-K., Goderis, B., Van Puyvelde, P., Analysis of the material properties involved in laser sintering of thermoplastic polyurethane. *Addit. Manuf.* **15**, 12-19 (2017).

42. Bai, J., Goodridge, R. D., Hague, R. J. M. & Okamoto, M., Processing and characterization of a polylactid acid/nanoclay composite for laser sintering. *Polym. Compos.* **38** (11), 2570-2576 (2017).

43. Berzins, M., Childs, T. H. C. & Ryder, G. R., The selective laser sintering of polycarbonate. *CIRP Annals* **45**, 187-190 (1996).

44. Ho, H. C. H., Cheung, W. L. & Gibson, I., Morphology and properties of selective laser sintered bisphenol A of polycarbonate. *Ind. Eng. Chem. Res.* **42**, 1850-1862 (2003).

45. Drummer, D., Rietzel, D. & Kühnlein, F., Development of a characterization approach for the sintering behavior of new thermoplastics for selective laser sintering. *Phys. Procedia* **5**, 533-542 (2010).

46. Wegner, A., New polymer materials for the laser sintering process: polypropylene and others. *Phys. Procedia* **83**, 1003-1012 (2016).

47. Arai, S., Tsunoda, S., Kawamura, R., Kuboyama, K. & Ougizawa, T., Comparison of crystallization characteristics and mechanical properties of poly(butylene terephthalate) processed by laser sintering and

injection molding. *Mater. and Des.* **113**, 214-222 (2017).

48. Ghita, O., James, E., Davies, R., Berretta, S., Singh, B., Flint, S., Evans, K.E., High Temperature Laser Sintering (HT-LS): An investigation into mechanical properties and shrinkage characterisics of Poly(Ether Ketone) (PEK) structures. *Mater. and Des.* **61**, 124-132 (2014).
49. Pohle, D., Ponader, S., Rechtenwald, T., Schmidt, M., Schlegel, K.A., Münstedt, H., Neukam, F.W., Nkenke, E., von Wilmowsky, C., Processing of three-dimensional laser sintered polyetheretherketone composites and testing of osteoblast proliferation in vitro. *Macromol. Symp.* **253**, 65-70 (2007).
50. Berretta, S., Ghita, O. & Evans, K. E., Morphology of polymeric powders in laser sintering (LS): from polyamide to new PEEK powders. *Eur. Polym. J.* **59**, 218-229 (2014).
51. Berretta, S., Wang, Y., Davies, R. & Ghita, O. R., Polymer viscosity, particle coalescence and mechanical performance in high-temperature laser sintering. *J. Mater. Sci.* **51**, 4778-4794 (2016).
52. Kim, H., Zhao, Y. & Zhao, L., *Process-level modelling and simulatio for HP's Multi Jet Fusion 3D printing technology*, presented at CPPS 2016 1st International Workshop on, 2016 (unpublished).
53. Materialise, Multi Jet Fusion, Available at http://www.materialise.com/en/manufacturing/3d-printing-technology/multi-jet-fusion (accessed 18/05/2018) (2018).
54. McIntyre, K. & Ortiz, J. A., in *Taking stock of industrial ecology*, edited by Clift, R. & Druckman, A. (Springer Open, 2016), pp. 317-330.
55. Bose, S., Vahabzadeh, S. & Bandyopadhyay, A., Bone tissue engineering using 3D printing. *Mater. Today* **16** (12), 496-504 (2013).
56. Utella, B., Storti, D., Anderson, R. & Ganter, M., A review of process development steps for new material systems in three dimensional printing. *J. of Manuf. Process.* **10**, 96-104 (2008).
57. Suwanprateeb, J. & Chumnanklang, R., Three-dimensional printing of porous polyethylene structure using water based binders. *J. of Biomed. Mater. Res. Part B: Appl. Biomater.* **78** (1), 138-145 (2006).
58. Verbelen, L., Dadbakhsh, S., Van den Eynde, M., Kruth, J.-P., Goderis, B., Van Puyvelde, P., Characterization of polyamide powders for determination of laser sintering processability. *Eur. Polym. J.* **75**, 163-174 (2016).
59. Rietzel, D., Kühnlein, F. & Drummer, D., Selektives Lasersintern van teilkristallinen Thermoplasten. *RTejournal Forum Rapid Technol.* **6** (2011).
60. Ziegelmeier, S., Christou, P., Wöllecke, F., Tuck, C., Goodridge, R., Hague, R., Krampe, E., Wintermantel, E., An experimental study into the effects of bulk and flow behaviour of laser sintering polymer powders on resulting part properties. *J. of Mater. Process. Tech.* (215), 239-250 (2015).
61. Lorrison, J. C., Goodridge, R. D., Dalgarno, K. W. & Wood, D. J., *Selective laser sintering of bioactive glass-ceramics*, presented at Proc. of the 13th Annual Int. Solid Freeform Fabrication Symp., Austin, 2002 (unpublished).
62. Niino, T. & Sato, K., *Effect of powder compaction in plastic laser sintering fabrication*, presented at Proc. Solid Freeform Fabrication Symposium, Austin, 2009 (unpublished).
63. Schmid, M., Amado, F., Levy, G. & Wegener, K., *Flowability of powders for Selective Laser Sintering (SLS) investigated by Round Robin Test*, presented at High Value Manufacturing: Advanced Research in Virtual and Rapid Prototyping: Proceedings of the 6th International Conference on Advanced Research in Virtual and Rapid Prototyping, Leiria, 2013 (unpublished).
64. Haworth, B., Hopkinson, N., Hitt, D. & Zhong, X., Shear viscosity measurements on polyamide-12 polymers for laser sintering. *Rapid Prototyp. J.* **19** (1), 28-36 (2013).
65. Bellehumeur, C. T., Bisaria, M. K. & Vlachopoulos, J., An Experimental Study and Model Assessment of Polymer Sintering. *Polym. Eng. and Sci.* **36** (17), 2198-2207 (1996).
66. Vasquez, M., Haworth, B. & Hopkinson, N., Methods for quantifying the stable sintering region in laser sintered polyamide-12. *Polym. Eng. & Sci.* **53** (6), 1230-1240 (2013).
67. Franco, A., Lanzetta, M. & Romoli, L., Experimental analysis of selective laser sintering of polyamide powders: an energy perspective. *J. of Clean. Prod.* **18**, 1722-1730 (2010).
68. Bael, V. E., Paggi, R. A., Salmoria, G. V. & Lago, A., Statistical evaluation of laser energy density effect

on mechanical properties of polyamide parts manufactured by selective laser sintering. *J. of Appl. Polym. Sci.* **113**, 2910-2919 (2009).

69. Vandenbroucke, B. & Kruth, J.-P., Selective laser melting of biocompatible metals for rapid manufacturing of medical parts. *Rapid Prototyp. J.* **13** (4), 196-203 (2007).
70. Laumer, T., Stichel, T., Nagulin, K. & Schmidt, M., Optical analysis of polymer powder materials for Selective Laser Sintering. *Polym. Test.* **56**, 207-213 (2016).
71. Tolochko, N.K., Khlopkov, Y.V., Mozzharov, S.E., Ignatiev, M.B., Laoui, T., Titov, V.I., Absorptance of powder materials suitable for laser sintering. *Rapid Prototyp. J.* **6** (3), 155-161 (200).
72. Gibson, I. & Shi, D., Material properties and fabrication parameters in selective laser sintering process. *Rapid Prototyping Journal* **3** (4), 129-136 (1997).
73. Verbelen, L., Dadbakhsh, S., Van den Eynde, M., Kruth, J.-P., Goderis, B., Van Puyvelde, P., Characterization of polyamide powders for determination of laser sintering processability. *Eur. Polym. J.* **75**, 163-174 (2016).
74. Gibson, I., Rosen, D. & Stucker, B., in *Additive Manufacturing Technologies: 3D Printing, Rapid Prototyping, and Direct Digital Manufacturing* (Springer, 2015).
75. Dotchev, K. & Yusoff, W., Recycling of polyamide 12 based powders in the laser sintering process. *Rapid Prototyp. J.* **15** (3), 192-203 (2009).
76. Acierno, S. & Van Puyvelde, P., Rheological behavior of polyamide 11 with varying initial moisture content. *J. of Appl. Polym. Sci.* **97**, 666-670 (2005).
77. Tontowi, A. E. & Childs, T. H. C., Density prediction of crystalline polymer sintered parts at various powder bed temperatures. *Rapid Prototyp. J.* **7** (3), 180-184 (2001).
78. Rietzel, D., Drexler, M., Kühnlein, F. & Drummer, D., *Incfluence of temperature fields on the processing of polymer powders by means of laser and mask sintering technlogy*, presented at Proceedings of the SFF Symposium, Austin, 2011 (unpublished).
79. Van den Eynde, M., in *16th European school on rheology, part 4: lab sessions* (Leuven, 2017), pp. 119-136.
80. Lumay, G., Boshini, F., Traina, K., Bontempi, S., Remy, J.-C., Cloots, R., Vandewalle, N., Measuring the flowing properties of powders and grains. *Powder Technology* **224**, 19-27 (2012).
81. Thanh, N. T., in *Particle-particle interaction in dry powder blending: Applying theoretical concepts to practical systems (doctoral thesis)* (2014).
82. Visser, J., Van der Waals and other cohesive forces affecting powder fluidization. *Powder Technol.* **58**, 1-10 (1989).
83. Kousaka, Y. & Okuyama, K., in *Powder technology handbook*, edited by Iinoya, K., Gotoh, K. & Higashitani, K. (Marcel Dekker, New York, 1991).
84. Forsyth, A. J., Hutton, S. R., Rhodes, M. J. & Osborne, C. F., Effect of applied interparticle force on static and dynamic angles of repose of spherical granular material. *Phys. Rev. E* **63** (2001).
85. Tomas, J. & Kleinschmidt, S., Improvement of Flowability of Fine Cohesive Powders by Flow Additives. *Chem. Eng. Technol.* **32** (10), 1470-1483 (2009).
86. Thio, B. J. R. & Meredith, J. C., Measurement of polyamide and polystyrene adhesion with coated-tip atomic force microscopy. *J. of Colloid and Interface Sci.* **314**, 52-62 (2007).
87. Zeng, X. M., Martin, G. P. & Marriott, C., *Particulate interactions in dry powder formulations for inhalation* (Taylor & Francis, London, 2001).
88. Masuda, H., Gotoh, K., Higashitani, K. & Matsusaka, S., in *Powder technology handbook*, edited by Masuda, H., Higashitani, K. & Yoshida, H. (CRC Press, 2006), pp. 157-170.
89. Matsusyama, T. & Yamamoto, H., Impact charging of particulate materials. *Chem. Eng. Sci.* **61**, 2230-2238 (2006).
90. Rowley, G., Quantifying electrostatic interactions in pharmaceutical solid systems. *Int. J. of Pharm.* **227**, 47-55 (2001).

91. Mukherjee, R., Gupta, V., Naik, S., Sarkar, S., Sharma, S., Peri, P., Chaudhuri, B.*l.*, Effects of particle size on the triboelectrification phenomenon in pharmaceutical excipients: experiments and multi-scale model. *Asian J. of Pharm. Sci.* **11** (5), 603-617 (2016).
92. Bailey, A. G., Electrostatic phenomena during powder handling. *Powder Technol.* **37**, 71-85 (1984).
93. Emery, E., Oliver, J., Pugsley, T., Sharma, J. & Zhou, J., Flowability of moist pharmaceutical powders. *Powder Technol.* **189**, 409-415 (2009).
94. Ireland, P. M., Triboelectrification of particulate flows on surfaces: Part I - Experiments. *Powder Technol.* **198**, 189-198 (2010).
95. Fasso, L., Chao, B. T. & Soo, L., Measurement of electrostatic charges and concentration of particles in the freeboard of a fluidized bed. *Powder Technol.* **33**, 211-221 (1982).
96. in *Electrification of particulates in industrial and natural multiphase flows* (Springer, 2017).
97. Stauffer, F., Vanhoorne, V., Pilcer, G., Chavez, P.-F., Rome, S., Schubert, M.A., Aerts, L., De Beer, T., Raw material variability of an active pharmaceutical ingedient and its relevance for processability in secondary continuous pharmaceutical manufacturing. *Eur. J. of Pharm. and Biopharm.* **127**, 92-103 (2018).
98. Coelho, M. C. & Harnby, N., Moisture Bonding in Powders. *Powder Technol.* **20**, 201-205 (1978).
99. Ackler, H. D., French, R. H. & Chiang, Y.-M., Comparisons of Hamaker constants for ceramic systems with intervening vacuum or water: from force laws and physical properties. *J. of Colloid and Interface Sci.* **179**, 460-469 (1996).
100. O'Melia, C. R., Chapter 18 - Fundamentals of particle stability. *Interface Sci. and Technol.* **10**, 317-362 (2006).
101. Levine, H. & Slade, L., Water as a plasticizer: physico-chemical aspects of low-moisture polymeric systems. *Water Sci. Rev.* **3**, 79-185 (1988).
102. Zafar, U., Vivicqua, V., Calvert, G., Ghadiri, M. & Cleaver, J. A. S., A review of bulk powder caking. *Powder Technol.* **313**, 389-401 (2017).
103. Zafar, U., Hare, C., Hassanpour, M. & Ghadiri, M., Drop test: a new method to measure the particle adhesion force. *Powder Technol.* **264**, 236-241 (2014).
104. Holdich, R. G., *Fundamentals of particle technology* (Midlandit, Shepsted, 2002).
105. Friedman, S. P. & Robinson, D. A., Particle shape characterization using angle of repose measurements for predicting effective permittivity and electrical conductivity of saturated granular media. *Water Resour. Res* **38** (11), 1236 (2002).
106. Endoh, S., in *Powder technology handbook*, edited by Masuda, H., Higashitani, K. & Yoshida, H. (CRC Press), pp. 33-48.
107. Mori, Y., in *Powder technology handbook*, edited by Masuda, H., Higashitani, K. & Yoshida, H. (CRC Press), pp. 115-124.
108. Davies, R., in *Handbook of powder science and technology*, edited by Fayed, M. E. & Otten, L. (Van Nostrand Reinhold Company, 1984), pp. 31-68.
109. Leturia, M., Benali, M., Lagarde, S., Ronga, I. & Saleh, K., Characterization of flow properties of cohesive powders: a comparative study of traditional and new testing methods. *Powder Technol.* **253**, 406-423 (2014).
110. Søgaard, S. V., Pedersen, T., Alleso, M., Garnæs, J. & Rantanen, J., Application of ring shear testing to optimize pharmaceutical formulation and process development of solid dosage forms. *Annu. Trans.of the Nordic Rheol. Soc.* **21**, 91-98 (2013).
111. Schwedes, J., Review on testers for measuring flow properties of bulk solids. *Granul. Matter* **5**, 1-43 (2003).
112. Schwedes, J., Consolidation and flow of cohesive bulk solids. *Chemical Engineering Science* **57**, 287-294 (2002).
113. Schwedes, J. & Schulze, D., Measurement of flow properties of bulk solids. *Powder Technol.* **61**, 59-68

(1990).

114. Fitzpatrick, J. J., Barringer, S. A. & Iqbal, T., Flow property measurement of food powders and sensitivity of Jenike's hopper design methodology to the measured values. *Journal of Food Engineering* (61), 399-405 (2004).
115. Grey, R. O. & Beddow, J. K., On the Hausner Ratio and its Relationship to Some Properties of Metal Powders. *Powder Technology* **2** (6), 323-326 (1969).
116. Abdullah, E. C. & Geldart, D., The use of bulk density measurements as flowability indicators. *Powder Technol.* (102), 151-165 (1999).
117. Santomaso, A., Lazzaro, P. & Canu, P., Powder flowability and density ratios: the impact of granules packing. *Chemical Engineering Science* **58**, 2857-2874 (2003).
118. Barbosa-Canovas, G. V. & Juliano, P., in *Advances in Food and Nutrition Research.* (Elsevier Academic Press, Boston, 2005), Vol. 49, pp. 233-301.
119. Kawakita, K. & Lüdde, K.-H., Some considerations on powder compression equations. *Powder Technol.* **4**, 61-68 (1971).
120. Ziegelmeier, S., Wöllecke, F., Tuck, C., Goodridge, R. & Hague, R., *Characterizing the Bulk & Flow Behaviour of LS Polymer Powders*, presented at Proceedings SFF Symposium, Austin, Texas, 2013 (unpublished).
121. Mullen, L., Stamp, R. C., Brooks, W. K., Jones, E. & Sutcliffe, C. J., Selective laser melting: a regular unit cell approach for the manufacture of porous, titanium, bone-ingrowth constructs, suitable for orthopedic applications. *J. of Biomed. Mater. Res. Part B: Appl. Biomater.* **89** (2), 325-334 (2008).
122. Vlachos, N. & Chang, I. T. H., Investigation of flow properties of metal powders from narrow particle size distribution to polydisperse mixtures though an improved Hall-flowmeter. *Powder Technol.* **205**, 71-80 (2011).
123. Choi, J.-P., Shin, G.H., Yang, S., Yang, D.Y., Lee, J.S., Brochu, M., Yu, J.-H., Densification and microstructural investigation of Inconel 718 parts fabricated by selective laser melting. *Powder Technol.* **310**, 60-66 (2017).
124. Khan, M. & Dickens, P., Selective laser melting (SLM) of gold (Au). *Rapid Prototyping J.* **18** (4), 81-94 (2012).
125. GranuTools, Application note using: Granuflow TM, Available at https://granutools.com/references/application-notes/highlighting-reproducibility-comparison-vs-hall-flowmeter/ (accessed 20/05/2018) .
126. Spears, T. G. & Gold, S. A., In-process sensing in selective laser melting (SLM) additive manufacturing. *Integr. Mater. and Manuf. Innov.* **5** (2) (2016).
127. Geldart, D., Abdullah, E. C., Hassanpour, A., Nwoke, L. C. & Wouters, I., Characterization of powder flowability using measurement of angle of repose. *China Particuology* **4** (3-4), 104-107 (2006).
128. McGlinchey, D., in *Characterisation of bulk solids*, edited by McGlinchey, D. (Blackwell Publishing Ltd, 2005), pp. 48-84.
129. Al-Hashemi, H. M. B. & Al-Amoudi, O. S. B., A review on the angle of repose of granular materials. *Powder Technol.* **330**, 397-417 (2018).
130. Lavoie, F., Cartilier, L. & Thibert, R., New Methods Characterizing Avalanche Behavior to Determine Powder Flow. *Pharmaceutical Research* **19** (6), 887-893 (2002).
131. Henein, H., Bribacombe, J. K. & Watkinson, A. P., Experimental study of transverse bed motion in rotary kilns. *Metall. Trans. B* **14B**, 191-205 (1983).
132. Ding, Y. L., Forster, R., Seville, J. P. K. & Parker, D. J., Granular motion in rotating drums: bed turnover time and slumping-rolling transition. *Powder Technol.* **124**, 18-27 (2002).
133. Liu, X. Y., Specht, E. & Mellmann, J., Experimental study of the lower and upper angles of repose of granular materials in rotating drums. *Powder Technology* **154**, 125-131 (2005).
134. Pirard, S. L., Lumay, G., Vandewalle, N. & Pirard, J. P., Motion of carbon nanotubes in a rotating drum: the dynamic angle of repose and a bed behaviour diagram. *Chem. Eng. J.* **146**, 143-147 (2009).

135. Amado, A., Schmid, M. & Wegener, K., in *Flowability of SLS Powders at Elevated Temperature (research report, https://doi.org/10.3929/ethz-a-010057815) (Accessed 14/07/2018*.
136. Hancock, B.C., Vukovinsky, K.E., Brolley, B., Grimsey, I., Hedden, D., Olofsky, A., Doherty, R.A., Development of a robust procedure for assessing powder flow using a commercial avalanche testing instrument. *J. of Pharm. and Biomed. Anal.* **35**, 979-990 (2004).
137. Amado, A., Schmid, M., Levy, G. & Wegener, K., *Advances in SLS powder characterization*, presented at Proc. of SFF, Austin (TX), 2011 (unpublished).
138. Salehi, H., Sofia, D., Schütz, D., Barletta, D. & Poletto, M., Experiments and simulation of torque in Anton Paar powder cell. *Part. Sci. and Technol.*, 1-12 (2018).
139. Hare, C., Zafar, U., Ghadiri, M., Freeman, T., Clayton, J., Murtagh, M.J., Analysis of the dynamics of the FT4 powder rheometer. *Powder Technol.* **285**, 123-127 (2015).
140. Gu, Z. H., Arnold, P. C. & McLean, A. G., Consolidation-related bulk density and permeability models for bulk solids. *Powder technol. 72*, 39-44 (1992).
141. Faqih, A., Chaudhuri, B., Muzzio, F. J. & Tomassone, M. S., Flow-induced dilation of cohesive granular materials. *AIChE J.* **52** (12), 4124-4132 (2006).
142. Bhadra, R., Rosentrater, K. A. & Muthukumarappan, K., Measurement of Sticky Point Temperature of Coffee Powder with a Rheometer. *Int. J. of Food Prop.* **16** (5), 1071-1079 (2013).
143. Lazar, M. E., Brown, A. H., Smith, G. S., Wong, F. F. & Lindquist, F. E., Experimental production of tomato powder by spray drying. *Food Technol.* **3** (1), 129-134 (1956).
144. Ozmen, L. & Langrish, T. A. G., Comparison of glass transition temperature and sticky point temperature for skim milk powder. *Drying Technol.* **20** (6), 1177-1192 (2002).
145. Boonyai, P., Bhandari, B. & Howes, T., Stickiness measurement techniques for food powders: a review. *Powder technol.* (145), 34-46 (2004).
146. Jaya, S. & Das, H., Glass transition ans sticky point temperatures and stability/mobility diagram of fruit powders. *Food Bioprocess. Technol.* **2**, 89-95 (2009).
147. Krantz, M., Zhang, H. & Zhu, J., Characterization of powder flow: Static and dynamic testing. *Powder Technol.* **194**, 239-245 (2009).
148. Tomasetta, I., Barletta, D., Lettieri, P. & Poletto, M., The measurement of powder flow properties with a mechanically stirred aerated bed. *Chem. Eng. Sci.* **69**, 373-381 (2012).
149. Schweiger, A. & Zimmermann, I., A new approach for the measurement of the tensile strength of powders. *Powder Technology* **101**, 7-15 (1999).
150. Li, Q., Rudolph, V., Weigl, B. & Earl, A., Interparticle van der Waals force in powder flowability and compactibility. *Int. J. of Pharm.* **280**, 77-93 (2004).
151. Molitch-Hou, M., HP and SIGMADESIGN lanch material development kit for 3D printing, Available at https://www.engineering.com/3DPrinting/3DPrintingArticles/ArticleID/14550/HP-and-SIGMADESIGN-Launch-Material-Development-Kit-for-3D-Printing.aspx (accessed 30/07/2018) (2017).
152. Alexander, A.W.,Chaudhuri, B., Faqih, A., Muzzio, F., Davies, C., Tomassone, M.S., Avalanching flow of cohesive powders. *Powder Technol.* **164**, 13-21 (2006).
153. Geldart, D., Abdullah, E. C. & Verlinden, A., Characterisation of dry powders. *Powder Technology* **190**, 70-74 (2009).
154. Tay, J. Y. S., Liew, C. V. & Heng, P. W. S., Powder flow testing: judicious choice of test methods. *AAPS PharmSciTech* **18** (5), 1843-1854 (2016).
155. Tsai, C.-J., Pui, D. Y. H. & Liu., B. Y. H., Elastic flattening and particle adhesion. *Aerosol. Sci. and Technol.* **15**, 239-255 (1991).
156. Richter, A., Franz, W., Renners, H. & Schiffer, T., US Patent No. US20060135670A1 (November 2004).
157. Ouvrard, T., Senninger, T., Loyen, K. & Senff, H., US Patent No. US20090075081A1 (November 2004).
158. Baumann, F.-E., Monsheimer, S., Grebe, M., Christoph, W., Schiffer, T., Scholten, H., Patent No. CA2444710A1 (October 2002).

159. Strobbe, D., Dadbakhsh, S., Verbelen, L., Van Puyvelde, P. & Kruth, J.-P., Selective laser sintering of polystyrene: a single layer approach. *Plast., Rubber and Compos* **47** (1), 2-8 (2018).

160. Canny, J., A computational appraoch to edge detection. *IEEE Trans. on Pattern Anal. and Mach. Intel.* **PAMI-8** (6), 679-698 (1986).

161. Vincent, O. R. & Folorunso, O., A descriptive algorithm for Sobel image detection. *In Proceedings of Informing Science & IT Education Conference (InSITE)* **10**, 97-107 (2009).

162. Ziou, D. & Tabbone, S., Edge detection techniques - an overview. *Pattern Recognition and Image Analysis C/C of Raspoznavaniye Obrazov I Analiz Izobrazhenii* **8**, 537-559 (1998).

163. Basu, M., Gaussian-based edge-detection methods - a survey. *IEEE Transactions on Systems, Man and Cybernetics, Part C (Applications and Reviews)* **32** (3), 252-260 (2002).

164. Mathues, M., in *Filament stabilisation in free-surface flows of complex fluids (PhD thesis)* (2015).

165. Liu, X. Y. & Zhang, Y. Y., Real-time detection of the repose angle of solids in rotating drum based on image processing. *Adv. Mater. Res.* **301-301**, 748-751 (2011).

166. Van den Eynde, M., in *Characterization of polymer powder flow for the laser sintering (LS) process (Master's thesis)* (2014).

167. Amado, A., Schmid, M. & Wegener, K., Flowability of SLS Powders at Elevated Temperature (Report, avalable at https://doi.org/10.3929/ethz-a-010057815) (2014).

168. Verkinderen, O., Baeten, D., Adriaensens, P., Van Puyvelde, P. & Goderis, B., Morphology - density relations in polyamide 12, in press.

169. Van den Eynde, M., Verbelen, L. & Van Puyvelde, P., Assessing polymer powder flow for the application of laser sintering. *Powder Technol.* **286**, 151-155 (2015).

170. Van den Eynde, M., Verbelen, L. & Van Puyvelde, P., *Influence of temperature on the flowability of polymer powders in laser sintering*, presented at Proc. of PPS-32, Lyon (France), 2016 (unpublished).

171. McGeary, R. K., Mechanical Packing of spherical Particles. *Journal of the American Ceramic Society* **44** (10), 513-522 (1961).

172. Kanamoto, T., Ohama, T., Tanaka, K. & Takeda, M., Two-stage drawing of ultra-high molecular weight polyethylene reactor powder. *Polymer* **28**, 1517-1520 (1987).

173. Loyen, K., Seniff, H. & Pauly, F.-X., US Patent No. US 8,124,686 B2 (Feb. 2012).

174. Baumann, F.-E. & Wilczok, N., US Patent No. US 5,932,687 (Aug. 1999).

175. Mys, N., Verberckmoes, A. & Cardon, L., Processing of syndiotactic polystyrene to microspheres for part manufacturing through selective laser sintering. *Polymers* **8** (11) (2016).

176. Mys, N., Van De Sande, R., Verberckmoes, A. & Cardon, L., Processing of polysulfone to free flowing powder by mechanical milling and spray drying techniques for use in selective laser sintering. *Polym.* **8** (150) (2016).

177. Lele, A. K. & Shine, A. D., Morphology of polymers precipitated from a supercritical solvent. *AIChE Journal* **38** (5), 742-752 (1992).

178. Drummer, D., Medina-Hernández, M., Drexler, M. & Wudy, K., Polymer powder production for laser melting through immiscible blends. *Procedia Eng.* **102**, 1918-1925 (2015).

179. Smith, A.P., Shay, J.S., Spontak, R.J., Balik, C.M., Ade, H., Smith, S.D., Koch, C.C., High-energy mechanical milling of poly(methyl methacrylate), polyisoprene and poly(ethylene-alt-propylene). *Polym.* **41**, 6271-6283 (2000).

180. Bai, C., Spontak, R. J., Koch, C. C., Saw, C. K. & Balik, C. M., Structural changes in poly(ethylene terephthalate) induced by mechanical milling. *Polym.* **41**, 7147-7157 (1999).

181. Schmidt, J., Sachs, M., Blümel, C., Winzer, B., Toni, F., Wirth, K.-E., Peukert, W., A novel process chain for the production of spherical SLS polymer powders with good flowability. *Procedia Eng.* **102**, 550-556 (2015).

182. Lim, J., Chong, M. S. K., Chan, J. K. Y. & Teoh, S.-H., Polymer powder processing of cryomilled polycaprolactone for solvent-free genereation of homogeneous bioactive tissue engineering scaffolds. *Small*

**10** (12), 2495-2502 (2014).

183. Kalia, S., Cryogenic processing: a study of materials at low temperatures. *J Low Temp Phys* **158**, 934-945 (2010).
184. ASTM International, in *Annual book of ASTM standards* (1994), Vol. 10.01, pp. 50-63.
185. ISO, in *ISO 37: Rubber, vulcanized or thermoplastic - Determination of tensile stress-strain properties* (2011).
186. Prisacariu, C., *Polyurethane Elastomers: From Morphology to Mechanical Aspects* (Springer, Dordrecht, 2011).
187. Eceiza, A., Martin, M.D., de la Caba, K., Kortaberria, G., Gabilondo, N., Corcuera, M.A., Mondragon, I., Thermoplastic polyurethane elastomers based on polycarbonate dials with different soft segment molecular weight and chemical structure: mechanical and thermal properties. *Polym. Eng. Sci.* **48** (2), 297-306 (2008).
188. Tang, D., in *Biobased thermoplastic polyurethanes synthesized by isocyanate-based and isocyanate-free routes (PhD thesis)* (Eindhoven, 2011).
189. Baudis, S., Ligon, S.C., Seidler, K., Weigel, G., Grasl, C.; Bergmeister, H., Schima, H., Liska, R., Hard-block degradable thermoplastic urethane-elastomers for electrospun vascular prostheses. *J. of Polym. Sci. Part A: Polym. Chem.* **50**, 1272-1280 (2011).
190. Seidenstücker, T. & Fritz, H.-G., Innovative biodegradable materials based upon starch and thermoplasric poly(ester-urethane) (TPU). *Polym. Degrad. and Stab.* **59**, 279-285 (1997).
191. Rogulsk, M., Kultys, A. & Lubczak, J., New thermoplastic polyurethane elastomers based on aliphatic-aromatic chain extenders with different content of sulfur atoms. *J. of Therm. Anal. Calorim.* **121** (1), 397-410 (2015).
192. Vial, J. & Carré, A., Calculation of Hamaker constant and surface energy of polymers by a simple group contribution method. *Int. J. Adhesion and Adhesives* **11** (3), 140-143 (1991).
193. Van den Eynde, M., Strobbe, D., Verkinderen, O., Verbelen, L., Goderis, B., Kruth, J.-P., Van Puyvelde, P., Effect of thermal treatments on the laser sinterability of cryogenically milled polybutene-1. *Mater. and Des.* **153**, 15-23 (2018).
194. Carbone, M. J., in *Poly(lactic acid) characterization and enhancement (PhD thesis)* (Leuven, 2015).
195. Garlotta, D., A literature review of poly(lactic acid). *J. of Polym. and the Environ.* **9** (2), 63-84 (2001).
196. Turner, B. N., Strong, R. & Gold, S. A., A review of melt extrusion additive manufacturing processes: I. Process design and modeling. *Rapid Prototyp. J.* **20**, 192-204 (2014).
197. Zhou, W. Y., Lee, S. H., Wang, M., Cheung, W. L. & Ip, W. Y., Selective laser sintering of porous tissue engineering scaffolds from poly(L-lactide)/carbonated hydroxyapatite nanocomposite microspheres. *J. of Mater. Sci.: Mater. in Med.* **19** (7), 2535-2540 (2008).
198. NatureWorks, Ingeo Biopolymer 3251 Techincal Data Sheet, Available at https://www.natureworksllc.com/~/media/Files/NatureWorks/Technical-Documents/Technical-Data-Sheets/TechnicalDataSheet_3251D_injection-molding_pdf.pdf (accessed 15/07/2018) .
199. Hodge, I. M., Effects of annealing and prior history on enthalpic relaxation in glassy polymers. 4. Comparison of five polymers. *Macromolec.* **16**, 898-902 (1983).
200. Yu, L., Amorphous ^haarmaceutical solids: preparation, characterization and stabilization. *Adv. Drug Deliv. Rev.* **48**, 27-42 (2001).
201. Hamad, K., Kaseem, M., Yang, H. W., Deri, F. & Ko, Y. G., Properties and medical applications of polylactic acid A review. *eXPRESS Polym. Lett.* **9** (5), 435-455 (2015).
202. Lehermeier, H. J. & Dorgan, J. R., Melt Rheology of poly(lactic acid): consequences of blending chain architectures. *Polym. Eng. and Sci.* **41** (12), 2172-2184 (2001).
203. Migliaresi, C., Cohn, D., De Lollis, A. & Fambri, L., Dynamic mechanical and calorimatric analysis of compression-molded PLLA of different molecular weights: Effect of thermal treatments. *J. of Appl. Polym. Sci.* **41** (1), 83-95 (1991).
204. Nugroho, N. R. W., Steric stabilization of polylactide acid particles achieved by covalent 'grafting-from'

with hydrophillic polymers. *KTH Fibre Polym. Technol.*, 1-54 (2013).

205. Goldbach, G. & Peitscher, G., Infrared investigations of the polymorphic modifications of polybutene-1. *Polym. Lett.* **6**, 783-788 (1968).
206. Holland, V. F. & Miller, L., Isotactic polybutene-1 single crystals: morphology. *J. of Appl. Phys.* **35** (11), 3241-3248 (1964).
207. Boor Jr, J. & Youngman, E. A., Polymorphism in poly-1-butene: Apparent direct formation of modification I. *J. of Polym. Sci. Part C: Polym. Lett.* **2** (9), 1542-6254 (1964).
208. Alger, M., *Polymer Science Dictionary*, 3rd ed. (Springer, 2017).
209. Chvátalová, L., Benícek, L., Berková, K., Cermák, R., Obadal, M., Verney, V., Commereuc, S., Effect of annealing temperature on phase composition and tensile properties in isotactic poly(1-butene). *J. of Appl. Polym. Sci.* **124**, 3407-3412 (2010).
210. Shieh, Y.-T., Lee, M.-S. & Chen, S.-A., Crystallization behavior, crystal transformation, and morphology of polypropylene/polybutene-1 blends. *Polym.* **42**, 4439-4448 (2001).
211. Hwo, C. C., Polybutylene blends as easy open seal coats for flexible packaging and lidding. *J. of Plast. Film & Sheeting* **3**, 245-259 (1987).
212. Choi, S. Y., Rakus, J. P. & O'Toole, J. L., Time dependent crystallinity of PB-1. *Polym. Eng. and Sci.* (1966).
213. Alfonso, G. C., Azzurri, F. & Castellano, M., Analysis of calorimetric curves detected during the polymorphic transformation of isotactic polybutene-1. *J. of Therm. Anal. and Calorim.* **66**, 197-207 (2001).
214. Kaszonyiova, M., Rybnikar, F. & Geil, P. H., Crystallization and transformation of polybutene-1. *J. of Macromol. Sci., Part B* **43** (5), 1095-1114 (2004).
215. Boor, J. J. & Mitchell, J. C., Kinetics of crystallization and a crystal-crystal transition in poly-1-butene. *J. of Polym. Sci.: Part A* **3**, 59-84 (1963).
216. Tontowi, A. E. & Childs, T. H. C., Density predictio of crystalline polymer sintered parts at various powder bed temperatures. *Rapid Prototyp. J.* **7** (3), 180-184 (2001).
217. Bourell, D., Kruth, J.-P., Leu, M., Levy, G., Rosen, D., Beese, A.M., Clare, A., Materials for additive manufacturing. *CIRP Annals* **66** (2), 659-681 (2017).
218. Erdal, M., Dag, S., Jande, Y. & Tekin, C. M., Manufacturing of functionally graded porous products by selective laser sintering. *Mater. Sci. Forum* **631-632**, 253-258 (2010).
219. Pederson, S. J. K., Circular Hough transform. *Allborg University, Vision, Graphics, and Interact. Syst.* **123** (2007).
220. Rizon, M.,Yazid, H., Saad, P., Shakaff, A.Y.M., Saad, A.R., Sugisaka, M., Yaacob, S., Mamat, M.R., Karthigayan, M., Object detection using circular Hough transform. *Am. J. of Appl. Sci.* **2** (12), 1606-1609 (2005).
221. Otsu, N., A threshold selection method from gray-level histograms. *IEEE Trans. on Syst. Man and Cybern.* **SMC-9** (1), 62-66 (1979).
222. Qu, M., Meth, J.S., Blackman, G.S., Cohen, G.M., Sharp, K.G., Van Vliet, K.J., Tailoring and probing particle-polymer interactions in PMMA/silica nanocomposites. *Soft Matter* **7** (18), 8401-8408 (2011).
223. Geldart, D., Harnby, N. & Wong, A. C., Fluidization of cohesive powders. *Powder Technol.* **37**, 25-37 (1984).
224. Schubert, H., Food particle technology. Part I: properties of particles and particulate food systems. *J. of Food Eng.* **6**, 1-32 (1987).
225. Petraccone, V., Pirozzi, B., Frasci, A. & Corradini, P., Polymorphism is isotactic poly-α-butene: Conformational analysis of the chain and crystalline structure of form 2. *Eur. Polym. J.* **12** (5), 323-327 (1976).
226. Natta, G., Corradini, P. & Bassi, I. W., Crystal structure of isotactic poly-alpha-butene. *Nuovo Cim* **15**, 52-67 (1960).

# Curriculum vitae



Michael Van den Eynde was born on 7 august 1991 in Vienna (Austria). After high-school graduation at the Sint-Jozefscollege in Aarschot, he set out for an engineering degree at KU Leuven. In 2012 he graduated magna cum laude in the bachelor of engineering. In his master, he specialised as a chemical engineer, during which he was introduced to the exciting topics of additive manufacturing and powder technology under the thesis supervision of prof. Peter Van Puyvelde. After graduating summa cum laude in 2014, he joined the division of Soft Matter Rheology and Technology (SMaRT) at the department of Chemical Engineering at KU Leuven as a PhD researcher. His main field of study became selective laser sintering, with a strong focus on powder flowability. In 2018, he finalised his PhD research and started as a scientist in particle and powder technology at Janssen Pharmaceutica (Beerse), thus continuing his interest in powder flow and characterisation.

During his years in Leuven, Michael was active in Sagio.be, a non-profit tutoring platform for students of KU Leuven. He started as a maths and science tutor in 2012 and entered the management in 2013 as the responsible for all students that are registered for tutoring sessions. In 2014 he joined the board of directors, of which he became the president for the academic year 2015-2016. After this, he continued his work with Sagio.be as a member of the general assembly.

# List of publications

## Articles in peer-reviewed international journals

**Van den Eynde M.**, Verbelen L., Van Puyvelde P., Assessing Polymer Powder Flow for the Application of Laser Sintering, *Powder Technol.* 286, 151-155 (2015)

Verbelen, L., Dadbakhsh, S., **Van den Eynde, M.**, Kruth, J. -P., Goderis, B., & Van Puyvelde, P., Characterization of polyamide powders for determination of laser sintering processability. *Eur. Polym. J.*, 75, 163-174 (2016)

Verbelen, L., Dadbakhsh, S., **Van den Eynde, M.**, Strobbe, D., Kruth, J. P., Goderis, B., & Van Puyvelde, P., Analysis of the material properties involved in laser sintering of thermoplastic polyurethane. *Addit. Manuf.*, 15, 12-19 (2017)

**Van den Eynde M.**, Strobbe D., Verkinderen O., Verbelen L., Goderis B., Kruth J.-P., Van Puyvelde P., Effect of thermal treatments on the laser sinterability of cryogenically milled polybutene-1, *Mater. & Design* 153, 15-23 (2018)

## Full-length articles in peer-reviewed conference proceedings

**Van den Eynde M.**, Verbelen L., Van Puyvelde P., Influence of temperature on the flowability of polymer powders in laser sintering, *PSS-32*, Lyon, 2016, AIP Conference Proceedings 1914, 190007 (2017)

## Book chapters

**Van den Eynde M.**, Van Puyvelde P., 3D Printing of Polylactic Acid, *Adv. Polym. Sci.*, Springer International Publishing AG (2017)

## Oral contributions to regional and international conferences (first author contributions only)

**Van den Eynde M.**, Verbelen L., Van Puyvelde P., Polymer powder flow characterisation for laser sintering, *PPS-2015*, Graz, Austria (2015)

**Van den Eynde M.**, Verbelen L., Van Puyvelde P., The study of powder flowability for the application of laser sintering, *51ème Congès Annuel du Groupe Français de Rhéologie*, Lille, France (2016)

**Van den Eynde M.**, Verbelen L., Van Puyvelde P., Flowability of laser sintering polymers at elevated temperatures, *PMI 2017*, Ghent, Belgium (2016)

**Van den Eynde M.**, Verbelen L., Van Puyvelde P., Influence of temperature on the flowability of polymer powder in laser sintering, *PPS 32*, Lyon, France (2016) – *Linked to corresponding article*

**Van den Eynde M.**, Van Puyvelde P., Flow behaviour of laser sintering powders at elevated temperatures, *PPS-2017*, Dresden, Germany (2017)

**Van den Eynde M.**, Van Puyvelde P. Flow behaviour of laser sintering powders at elevated temperatures, *SFF 2017*, Austin, Texas, United States (2017)

## Miscellaneous first author contributions

**Van den Eynde M.**, Verbelen L., Van Puyvelde P., Characterization of polymer powder flow for the laser sintering process, *SIM user forum*, Ghent, Belgium (2014) – *Poster presentation*

**Van den Eynde M.**, Verbelen L., Van Puyvelde P., Powder flow: 'a new characterization tool for the determination of powder spreadability in laser sintering', *SIM user forum*, Ghent, Belgium (2015) – *Oral presentation*

**Van den Eynde M.**, Verbelen L., Van Puyvelde P., Lab-scale powder flow evaluation applied to laser sintering, *SIM user forum*, Ghent, Belgium (2015) – *Poster presentation*

**Van den Eynde M.**, Van Puyvelde P., Analysing powder flow for laser sintering: a particular challenge, *BePCIS: a 359° view on 3D printing*, Leuven, Belgium (2016) – *Oral presentation*

**Van den Eynde M.**, Strobbe D., Verkinderen O., Verbelen L., Goderis B., Kruth J.-P., Van Puyvelde P., Thermal tuning of polybutylene powder for laser sintering, *SIM user forum*, Antwerp, Belgium (2017) – *Poster presentation*

**Van den Eynde M.**, Van Puyvelde P., Powder rheometry at elevated temperatures: an industrial challenge, *TA user meeting*, Antwerp, Belgium (2017) – *Oral presentation*

**Van den Eynde M.**, Strobbe D., Van Hooreweder B. , Kruth J.-P., Van Puyvelde P., Selection methodology for cryogenically milled thermoplastic polyurethanes (TPU) in laser sintering, *SIM user forum*, Ghent, Belgium (2018) – *Poster presentation*

**Van den Eynde M.**, Van Puyvelde P., Powders in 3D printing: a particular challenge, *Arenberg youngster seminar 13*, Leuven, Belgium (2018) – *Oral presentation*

FACULTY OF ENGINEERING SCIENCE
DEPARTMENT OF CHEMICAL ENGINEERING
SOFT MATTER RHEOLOGY AND TECHNOLOGY
Celestijnenlaan 200F box 2424
B-3001 HEVERLEE, BELGIUM
tel. +32 16 32 1347
michael.vandeneynde@kuleuven.be
https://cit.kuleuven.be/smart